Colloidal Self-assembly Approaches to Smart Nanostructured Materials

Zhiwei Li, Qingsong Fan, and Yadong Yin*

Department of Chemistry, University of California, Riverside, CA 92521 (USA)

*Corresponding Author: E-mail address: yadong.yin@ucr.edu

KEYWORDS: colloid particles, self-assembly, colloidal crystals, smart nanomaterials, responsive superstructures, photonic crystals, plasmonic, coloration, applications

ABSTRACT: Colloidal self-assembly refers to a solution-processed assembly of nanometer-/micrometer-sized, well-dispersed particles into secondary structures, whose collective properties are controlled by not only nanoparticle property but also the superstructure symmetry, orientation, phase, and dimension. This combination of characteristics makes colloidal superstructures highly susceptible to remote stimuli or local environmental changes, representing a prominent platform for developing stimuli-responsive materials and smart devices. Chemists are achieving even more delicate control over their active responses to various practical stimuli, setting the stage ready for fully exploiting the potential of this unique set of materials. This review addresses the assembly of colloids into stimuli-responsive or smart nanostructured materials. We firstly delineate the colloidal self-assembly driven by forces of different length scales. A set of concepts and equations are outlined for controlling the colloidal crystal growth, appreciating the importance of particle connectivity in creating responsive superstructures. We then present working mechanisms and practical strategies for engineering smart colloidal assemblies. The concepts underpinning separation and connectivity control are systematically introduced, allowing active tuning and precise prediction of the colloidal crystal properties in response to external stimuli. In the following section, various exciting applications of these unique materials are summarized with a specific focus on the structure-property correlation in smart materials and functional devices. We conclude this review with a summary of existing challenges in colloidal self-assembly of smart materials and provide a perspective on their further advances to the next generation.

Contents

1. INTRODUCTION

1.1 Stimuli-responsive Colloidal Assemblies

Colloidal particles are nanometer-/micrometer-sized, dispersed particles with defined size, size distribution, shape, and property.[1] They are stabilized by a layer of surfactants or by functional groups attached to their surfaces, which are organic molecules or charged terminating groups for preventing nanoparticles from physical agglomeration and chemical transformation.[2] These capping ligands, also named stabilizers or passivating ligands, facilitate the control over the particle size and shape during colloidal synthesis within the conventional kinetic size and shape control window, therefore allowing the easy arrest of desirable properties that are determined by particle composition, size, and shape.[3,4] Regulating the interactions between surface ligands, which in most cases interplays with other forces of different length scales, makes it possible to agglomerate the well-dispersed colloids in a controllable manner.[5,6] Depending on driving force magnitude and directionality, this sequence of events creates superstructures of different dimensions, sizes, phases, and symmetries, ranging from highly ordered colloidal crystals with perfect Bravais lattice to superstructures with pure orientational orders and colloidal clusters of a few nanoparticles.[7-11] Such self-assembly of colloidal particles into a secondary structure offers new opportunities in preparing functional materials with desirable collective properties. The colloidal particles possess useful physicochemical properties, while their connectivity within the resultant superstructures is mainly regulated by colloid surface chemistry and environmental property. These remarkable superstructures feature unique particle separation, allowing further processing to more complex hierarchical materials. In fact, the combination of size- and shape-dependent properties of colloids with the ease of fabrication and further processing to an even more complex superstructure makes colloidal self-assembly attractive and promising in creating smart materials and devices with highly tunable collective properties in response to external stimuli.

Colloidal crystals are occasionally referred to as "colloidal molecules" due to their apparent structural similarity with atomic and molecular crystals.[6,7,12,13] However, over the last three decades, it has been gradually recognized that colloidal crystals are analogous to atomic or molecular crystals, with preparative strategy, growth pathway, and crystal symmetry being similar in many ways to those that have been established in colloidal nanocrystal synthesis.[14] Treating dispersed colloids as reactive monomers allows for describing colloidal crystal growth through the classic nucleation-growth pathways.[15-17] In some carefully prepared reactions (e.g., self-assembly of Janus particles with a defined surface patch,[18,19] colloidal assembly driven by DNA base pair interaction or electrostatic attraction[20]), it allows precise prediction of size, shape, and stoichiometry of a colloidal crystal and the coordination number of interacting colloids within the crystal.[21-23] The growth of superlattices can also be visualized by solving the colloidal dynamics in quantum simulation or classical mechanics calculation, leading to direct observation of a dispersed phase growing into a superlattice of long-range order.[24-26] Because of the great similarities between colloidal and atomic crystals, these powerful tools benefit the understanding of extremely fast nucleation at the early stage of nanocrystal growth.[27,28] In another typical example, the self-assembly of binary colloids into perfect superlattices driven by electrostatic attraction helps explain the origin of ionic crystals because of the same driving force and similar assembly thermodynamics.[29] These considerations underpin the important role of colloidal assembly in understanding the atomic and molecular crystal formation, which in turn promotes the clarification of structure-property correlation in these two highly relevant but distinct systems focusing on mater-mater interactions in complementary length scales. While most colloidal crystals have perfect Bravais lattice, a few carefully prepared assembly produces superstructures without any atomic lattice equivalents[30-32] or quasicrystalline superlattices with only rotational symmetry.[33-35]

But the ability to realize and control colloidal assembly is not only of fundamental importance: easy access to a wide range of colloidal crystals is a prerequisite for exploiting their excellent properties and smart responses to external stimuli. A great benefit in this regard is the unique particle separation and regular spaces between highly ordered colloids, which serve as accessible sites to guest molecules.[36,37] One direct consequence of such guest molecule infiltration is many interesting property changes due to the ensuing alteration of surrounding dielectrics, like color changes in photonic crystals and plasmonic superstructures.[38,39] This advantageous structural property also allows further incubation of colloidal superstructures in a functional continuum material by a few established strategies such as the infiltration-polymerization process.[40,41] These practical strategies open the door to many unique smart materials by using colloidal superstructures as responsive constituents or removable templates, during which one may expect a great expansion of the structural complexity and potential applications of these remarkable materials. A few noticeable examples in this regard include inverse opals, hierarchical structures, integrated biomimetic materials, which have demonstrated great success in developing high-performance colorimetric sensors,[42] energy storage and conversion,[43-45] and smart soft robotics.[46-48] Another unique feature of colloidal superstructures is the weak coherent forces (e.g., van der Waals, DNA base pair interaction, hydrogen bonding, and dipole interaction) between assembled colloids, whose magnitude is much lower than covalent bonds in molecules. As a result, the particle connectivity inside a colloidal crystal is highly susceptible to external stimuli, enabling precise control over particle separation and thus crystal periodicity. One consequence of these dynamic events is the highly tunable optical and mechanical properties of the colloidal superstructures.[49-52] The working principles underlying these attractive phenomena are lattice-constant changes or even phase transitions driven by the employed external stimuli, including both local environmental changes (temperature, pH, ionic strength, depletant, humidity, solvent, etc.) and remote perturbation (electric field, magnetic field, mechanical force, gravity force, light, etc.). Responsive photonic crystals and active plasmonics are two compelling materials in this regard, which benefit from the intrinsic advantages of colloidal assemblies and their brilliant responses to various stimuli in natural settings.[52,53] In fact, chemists have developed even more exquisite approaches to responsive colloidal superstructures, with many of them having been used for fascinating applications. If anisotropic colloidal building blocks are used, it is possible to assemble them into colloidal liquid crystals and control their collective orientation in the liquid crystal phase while maintaining structural integrity and lattice identity.[54,55] Such orientational

control is operational to a unique set of building blocks, requires a long-range driven force for reversible and remote manipulation, and provides many distinctive properties. A highly relevant yet famous example is liquid crystals of polar molecules and various associated liquid-crystal phase transitions induced by an electric field.[56-58] Despite significant variations in the molecular structure and composition, there are a few criteria in their chemical and physical properties to form a liquid-crystal phase. A literature review of these common features is always a good starting place to design colloidal liquid crystals. For example, previous studies on liquid crystals have come to appreciate that discotic, conic, or rod-shaped molecules are perfect candidates for thermotropic liquid crystals.[59,60] This observation inspires researchers to assemble nanorods and nanoplates into liquid crystals, whose first effort was focused on graphene oxide nanosheets because of their similar structures to liquid crystal molecules and reduced sizes.[61,62] For larger anisotropic colloids, a few advanced techniques are now available to produce responsive colloidal liquid crystals, including nanoscale magnetic assembly, electric field-driven assembly, mechanical orientation control, DNA templating method, and colloidal self-assembly.[63-65] They have attracted considerable attention in producing photonic and liquid crystals with orientation-dependent optical responses and active plasmonic superstructures with linear and chiral optical effects.[66-68]

1.2 Scope of This Review

Colloidal superstructures comprise a set of colloidal particles arranged with regular spaces in well-defined interparticle separation or dispersed in a secondary continuum matrix, such as polymers, metal-organic frames, or inorganic functional materials. Photonic crystals are a unique type of colloidal superstructures with a periodic arrangement of nanoparticles in a long-range order. They feature photonic bandgaps and diffract brilliant structural colors corresponding to the bandgap frequency, which is determined by destructive and constructive interference of light within the periodic structures.[11,69] Their diffraction peak positions depend on crystal periodicity, orientation, and refractive index of constitutive nanoparticles and surrounding environments.[52] These remarkable materials have been extensively used as photonic pigments in anticounterfeiting, multicolor displays, color printing, and colorimetric sensing.[70,71] Compared with conventional organic dyes or pigments used for coloration, photonic crystals are much brighter and more stable because their structural color comes from the diffraction rather than absorption of organic molecules. They also provide a widely accessible range of spectral colors. More interestingly, their structural colors are highly tunable by controlling crystal periodicity, orientation, and surrounding dielectrics, allowing dynamic colorimetric responses to changing environments. Other emerging materials that benefit from the combination of low-cost self-assembly and solid-state performances are plasmonic superstructures featuring prominent plasmon coupling effects.[72-74] In a general sense, plasmonic nanoparticles are conductive inorganic nanoparticles stabilized by a layer of capping ligands.[75] The free electrons confined in the nanometer-sized particles can form resonant oscillation under the excitation of electromagnetic waves. The excited surface plasmon, the so-called localized surface plasmon resonance (LSPR), produces remarkable extinction and a sharp peak at the resonant wavelength, which is determined by particle composite, size, and shape.[75-78] If plasmonic nanoparticles self-assemble into close proximity, their LSPR couples mutually between adjacent nanoparticles so that the peak position can be further tuned by regulating the assembled superstructures.[79-81] The scope for these unique materials has promoted the intensive study of the self-assembly of responsive plasmonic nanostructures for desirable physical properties. The research in these two distinct but highly related materials is developing so rapidly that many new concepts, working mechanisms, and practical strategies have first been put forward for these materials but later been combined as a unified set of assembly control concepts. These empirical or/and theoretical principles are also applied to an extended category of smart materials, including responsive colloidal liquid crystals, advanced soft actuators, biohybrid materials, mechanical and electronic materials, and metasurfaces.

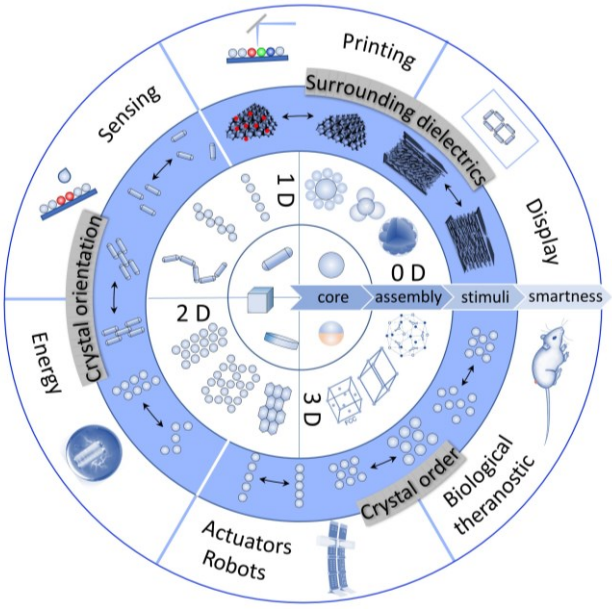

Figure 1. Colloidal self-assembly approach to smart nanostructured materials.

To explain the general concepts underlying these remarkable materials, it is necessary to comprehensively overview the developments and current stages of these materials within the centralized regime of stimuli-responsive nanostructured materials. Therefore, in this review, we outline a general set of concepts and working principles for creating smart nanostructured materials from colloidal self-assembly (**Figure 1**). In a general sense, smart nanostructured materials are nanomaterials that can change their physicochemical properties (optical, mechanical, electric, magnetic, catalytic properties, etc.) in a controllable manner in response to external stimuli, including local environmental changes and remote perturbation. Besides, the superstructures introduced in this review are assembled from colloidal particles using various solution processes, which covers colloidal crystals with known lattice symmetry, three-dimensional (3D) superstructures of liquid crystal phase (only with orientational orders), two-dimensional (2D) lattices, and colloidal chains (linear, helical, branched, cross-linked, etc.), as well as colloidal clusters or molecules. Colloidal self-assembly driven by underlying and entropic forces of different length scales is first introduced to elucidate the dependence of superstructure's

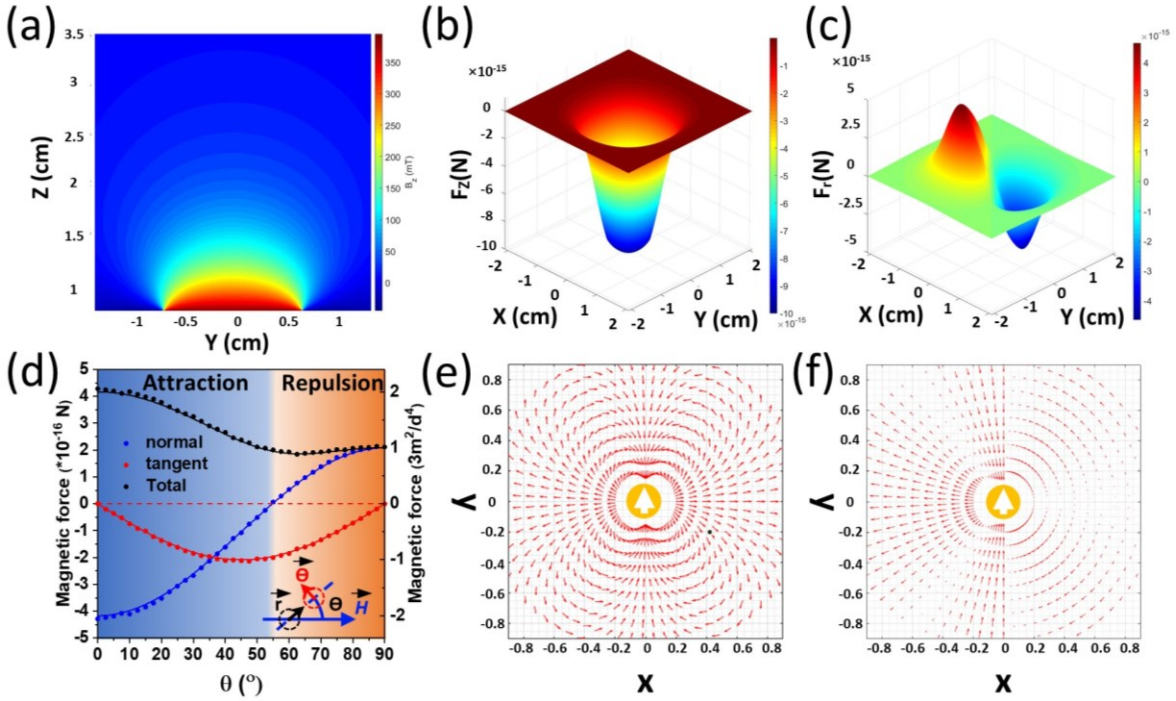

Figure 2. Magnetic dipole-dipole interactions in colloidal particles and the packing forces under external magnetic fields. (a) Simulated magnetic field distribution atop a cubic permanent magnet. (b) The z-component of the packing force. (c) The packing force of one nanoparticle in a magnetic field of the permanent magnet. Positive forces point to the positive direction of the coordinate. (d) The dipole-dipole interaction between two identical nanospheres. (e) The dipole-dipole force field between two interacting nanospheres with constant dipole moment and direction. (f) The tangent and normal components of the dipole-dipole interactions.

collective properties on the constitutive particle connectivity, focusing on quantitative description of these forces and their unique features in producing superstructures of different symmetries, sizes, and dimensions. Based on these theoretical considerations, we outline three unified sets of working principles for engineering smart colloidal assemblies, including tuning environmental physicochemical properties, actively controlling the interparticle separation, and regulating the superstructure orientation. These strategies have been extensively studied to tune the collective properties of superstructures and to control their responses to dynamic stimuli, leading to many interesting optical, mechanical, electrical effects, whose further developments inspire a broad spectrum of fascinating applications. As a result, the use of these remarkable materials is introduced in sequence to demonstrate their great potential in optical devices, biomedicine, energy conversion, and smart soft robotics.

2. COLLOIDAL ASSEMBLY OF SUPERSTRUCTURES

The driving forces play important roles in determining the interparticle connectivity and, most importantly, the responses of superstructures to external stimuli. Understanding these nanoscale interactions are therefore a primary requirement to create and manipulate smart colloidal assemblies for desirable physicochemical properties. The successful regulation of forces between interacting colloids provides a widely accessible range of secondary structures whose collective optical, electronic, mechanical, and thermal properties can be used for creating integrated devices and smart materials. The clarification of complex phase behaviors of colloidal assemblies under changing forces also enables exquisite control over superstructure responses under external perturbation, which is of fundamental importance and practical interest in developing smart colloidal assemblies. In this section, we introduce typical driving forces in assembling stimuli-responsive colloidal crystals and explain the dependence of superstructure size, symmetry, and collective properties on the force magnitude, length scale, and directionality. This property is also manifested and explained by a few carefully chosen superstructures that are unique to driving forces of different symmetries and length scales.

2.1. Nanoscale Magnetic Assembly

Magnetic nanoparticles have different magnetization properties depending on their composition, shape, size, and crystallinity. For example, ferromagnetic nanoparticles have a permanent magnetic dipole with preferential parallel alignment to a magnetic field, while paramagnetic or superparamagnetic nanoparticles have zero net magnetic dipole moment due to the random orientation of each magnetic domain. They can be magnetized under a magnetic field with an induced dipole moment of $m = \chi HV$, where χ, H, and V are the volume susceptibility, local magnetic field, and particle volume, respectively. The induced magnetic dipole will couple with the applied field, the so-called Zeeman coupling, which induces different assembly behaviors depending on the field uniformity. In a uniform magnetic field, the induced dipole in nanoparticles simply aligns themselves along the external field. Colloidal particles experience an additional packing force in an uneven magnetic field, which drags them toward regions with greater field strength and is responsible for the well-known magnetic separation and targeting.[82,83]

Consider a gradient magnetic field generated by a cubic permanent magnet and imagine one magnetized particle in such an uneven field. It is possible to resolve the field distribution of the magnet and its exerted packing force on the particle. As shown in **Figure 2a**, the field strength decays exponentially from the magnet surface, forming a smooth field gradient. The packing force in such a typical dipole magnetic field depends on the local field strength, which can be predicted by $\mathbf{F}=\mu(\mathbf{m}\bullet\nabla)\mathbf{H}$, with μ being the surrounding permeability.[84] This equation assumes an "equivalent" point dipole in the magnetized nanoparticle and requires access to the local field vector for a precise calculation. The dependence of packing force direction and magnitude is complicated due to the gradient of the dipole magnetic field. By decomposing the total force to a z-component (**Figure 2b**) and a complementary component in the x-y plane (**Figure 2c**), it is possible to reasonably describe the assembly of nanoparticles driven by the packing force. The z-component packing force is always negative with a maximum magnitude, predicting an attraction to the magnet surface (**Figure 2b**). The packing force tends to localize the particle to the cubic magnet center because of position-dependent attraction, as evidenced by the interesting force field in the x-y plane (**Figure 2c**). These two effects simultaneously separate the dispersed magnetic particles from a solution and attract them to the nearest place to the magnet surface.

In addition to the packing force, two adjacent magnetic nanoparticles can interact through dipole-dipole coupling. In a simple case of one nanosphere with an induced magnetic moment of *m*, its generated magnetic field at the position of a second particle can be calculated by $\mathbf{H}=[3(\mathbf{m}\bullet\mathbf{r})\mathbf{r}-\mathbf{m}]/d^3$, where **r** is the unit vector pointing along connecting line to the second particle and *d* is the interparticle separation (scheme shown in the inset of **Figure 2d**). If the second particle has the same moment, the magnetic potential energy can be given by $U=\mathbf{m}\bullet\mathbf{H}=(3\cos^2\Theta-1)m^2/d^3$, where Θ is the angle between the unit vector (**r**) and the external magnetic field and has a value between 0° and 90°. Clearly, the dipole-dipole interaction energy is a function of the azimuth and separation of the two particles, whose partial differential against Θ and d leads to the tangent (F_T) and normal components (F_N) of the dipolar force between them.

$$\boldsymbol{F_N(\theta,d)} = \frac{\partial U(\theta,d)}{\partial d} = \frac{3(1-3cos^2\theta)m^2}{d^4}\boldsymbol{r} \quad (1)$$

$$\boldsymbol{F_T(\theta,d)} = \frac{\partial U(\theta,d)}{\partial \theta} = \frac{-3\sin(2\theta)m^2}{d^3}\boldsymbol{\theta} \quad (2)$$

The force direction is defined by the unit vector, **r** and **Θ**, as illustrated in the inset of **Figure 2d**. These theoretical considerations lead to a quantitative description of the dipolar force between two magnetic nanoparticles, which is simply the vector sum of the normal and tangent components. Its magnitude first decreases and slightly increases as Θ changes from 0° to 90°. More interestingly, the tangent component vanishes at parallel (0°) and perpendicular (90°) alignment and approaches the maximum in the middle. Meanwhile, the normal component changes from a negative to a positive value with a critical angle of 54.74°, which implies a transition from attraction to repulsion between the two interacting nanoparticles. This position-dependent dipolar force drives the two particles into dimers, further growing into long chains with parallel alignment to the applied field (**Figure 2e**). This phase behavior is confirmed by the 2D mapping of the normal and tangent components of the dipolar force (**Figure 2f**). In the repulsive domain ($54.74^\circ < \Theta \leq 90^\circ$), the normal force drives particles to move away from each other while the tangent force causes it to assemble within the attractive domain ($0^\circ \leq \Theta < 54.74^\circ$) into a parallel linear chain. With finite element methods, it is possible to analyze the field distribution of one nanoparticle and assembled superstructures in a uniform magnetic field, which benefits understanding the complex coupling between nanoparticles and between particles and the field. In **Figure 3a**, the Zeeman coupling enhances the field strength at two poles of an induced dipole. Besides, the magnetic force between two nanoparticles in colloidal dimers depends on the dimer orientation: repulsion (**Figure 3b**) and attraction (**Figure 3c**) for perpendicular and parallel chains, respectively. If many nanoparticles are used in the nanoscale magnetic assembly, one may expect the formation of long chains with parallel alignment to the external field (**Figure 3d**).

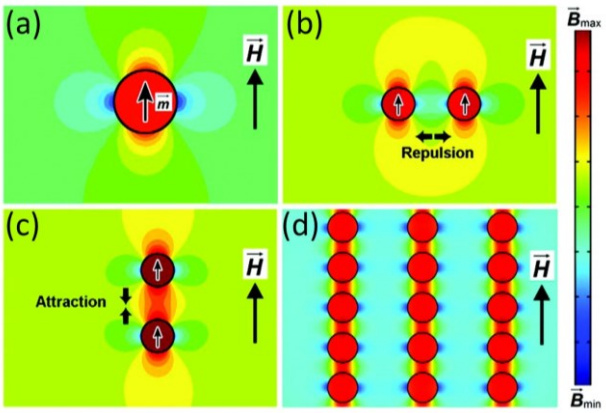

Figure 3. Magnetic field distribution of one nanosphere and two interacting nanospheres in a uniform magnetic field. (a) Magnetic field distribution of a superparamagnetic nanosphere with a parallel magnetic dipole to the magnetic field direction. The magnetic field distribution around (b) two repulsive and (c) two attractive dipoles. (d) The magnetic field distribution of linear chains formed by the dipole-dipole interactions. Reproduced with permission from ref [85]. Copyright 2012 American Chemical Society.

Although this simple calculation predicts the formation of one-dimensional (1D) chains, the onset of this nanoscale magnetic assembly is facing a few challenges, including the synthesis of monodisperse magnetic nanoparticles and methods to prevent magnetic aggregation. Based on distinct properties of magnetism, superparamagnetic nanospheres are a natural candidate for creating magnetically responsive superstructures. The zero net magnetic dipoles without magnetization allow them to disperse well in colloidal dispersion, while the induced magnetic dipole is strong enough to assemble them under an applied magnetic field.[86] According to the concept of magnetocrystallinity, the critical domain size for the superparamagnetic-ferromagnetic transition of Fe_3O_4 nanoparticles is ~30 nm; it is therefore becoming important to control the domain size of magnetite nanoparticles in colloidal synthesis. To this end, a high-temperature hydrolysis reaction has long been established to synthesize colloidal nanocrystal clusters (CNCs) of magnetite (Fe_3O_4) with widely tunable particle size (30-200 nm) and small domain size (~10 nm).[87,88] This superparamagnetic cluster is composed of small nanocrystals (**Figure 4a**) and has many polyacrylic acid

ligands so that they are negatively charged. Under a uniform magnetic field, they self-assemble into 1D photonic chains due to the interplay between magnetic attraction and long-range electrostatic repulsion (**Figure 4b**). Simply increasing particle concentration and field strength produces 2D photonic nanosheets (**Figure 4c**) and 3D photonic crystals (**Figure 4d**).[89]

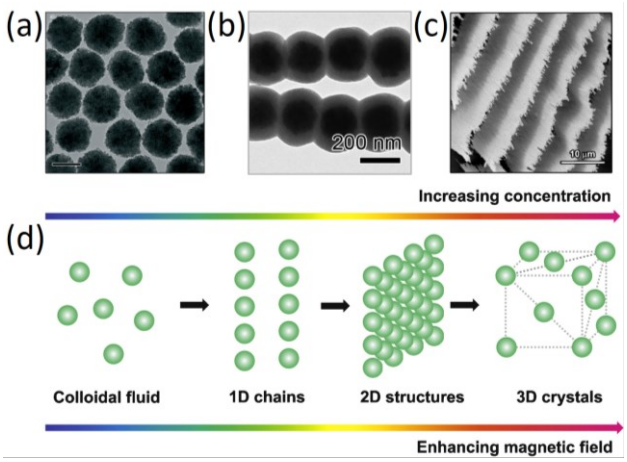

Figure 4. Magnetic assembly of superparamagnetic nanoparticles in a uniform magnetic field. (a) TEM image of superparamagnetic Fe_3O_4 colloidal nanocrystal clusters. Scale bar: 100 nm. Reproduced with permission from ref [88]. Copyright 2007 Wiley-VCH Verlag GmbH & Co. KGaA, Weinheim. (b) TEM image of colloidal chains from the magnetic assembly of the Fe_3O_4 colloids. Reproduced with permission from ref [90]. Copyright 2013 Elsevier Ltd. (c) SEM image of 2D nanosheets from the magnetic assembly of the high-concentration Fe_3O_4 colloids. Reproduced with permission from ref [89]. Copyright 2013 American Chemical Society. (d) Phase diagram of the magnetic assembly of superparamagnetic nanoparticles under a uniform magnetic field. Reproduced with permission from ref [90]. Copyright 2013 Elsevier Ltd.

Although the theoretical calculation predicts strong repulsion between parallel chains, the strong electrostatic repulsion between high-concentration chains enables chain coalescence into zigzag nanosheets. One interesting phenomenon is the bright structural colors from the 2D nanosheets due to light diffraction in the highly periodic structures (**Figure 5a**). If a non-magnetic template is introduced to modulate local field distribution in the nanoscale magnetic assembly (**Figure 5b**), it is possible to prepare more complex hierarchical superstructures. For example, a 2D array of circular relief patterns (SEM shown in **Figure 5c**) can greatly enhance the local field strength around the patterns, leading to further arrangement of 2D photonic nanosheets into a secondary labyrinth structure (**Figure 5d**).

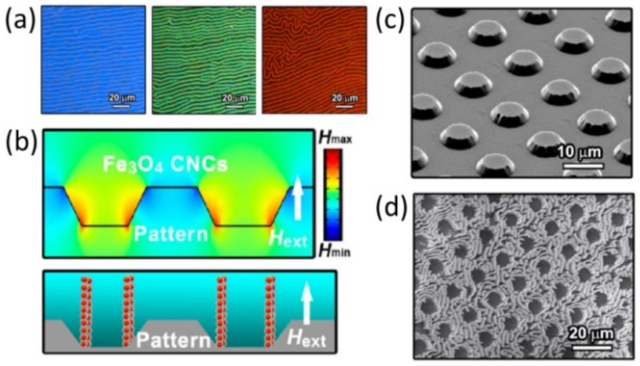

Figure 5. Magnetic assembly of superparamagnetic nanoparticles into 2D photonic crystals. (a) Optical microscopy images of 2D photonic structures from superparamagnetic colloids with increasing sizes from left to right samples. (b) Simulated magnetic field distribution on a templated that is immersed in a colloidal dispersion of Fe_3O_4 nanoparticles. (c) SEM image of a 2D array of circular relief patterns. (d) SEM image of the 2D photonic superstructures on the template. Reproduced with permission from ref [89]. Copyright 2013 American Chemical Society.

As particle concentration further increases, a formation of colloidal crystal array is confirmed by bright structural colors even under the absence of a magnetic field (**Figure 6a**).[91] This self-assembly of nanospheres into non-close-packed face-Centered Cubic (*fcc*) lattice is driven by concentrating effect, which often occurs in dense colloidal dispersions. Applying a magnetic field leads to a blueshift of the diffraction colors (**Figure 6b**), which is associated with a phase transition from polycrystalline to well-orientated, single-crystalline crystals (**Figures 6c** and **6d**).

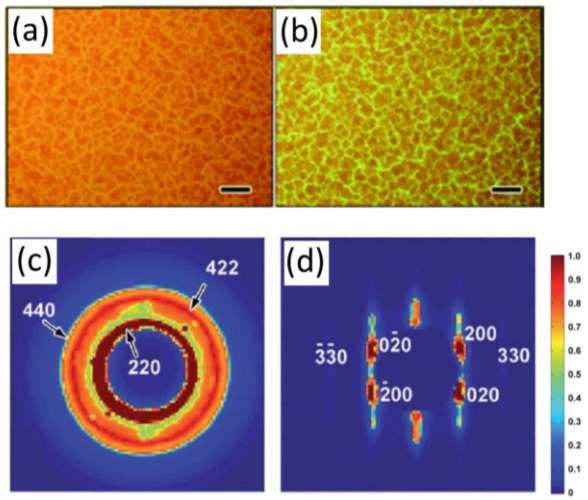

Figure 6. Magnetic assembly of superparamagnetic nanoparticles into 3D photonic crystals. (a) Optical microscopy images of 3D photonic crystals under a magnetic field with a field strength of (a) 0 G and (b) 120 G. Scale bars: 20 μm. Small-angle X-ray diffraction patterns of the 3D photonic crystals under a field strength of (c) 0 G and (d) 1600 G. Reproduced with permission from ref [91]. Copyright 2012 Royal Society of Chemistry.

Such the nanoscale magnetic assembly is also operational for assembling non-magnetic nanoparticles by introducing the so-

called "magnetic hole" effects. This interesting extension is experimentally achieved by dispersing guest non-magnetic particles in host ferrofluids; applying a magnetic field to the mixture provides the guest colloids with an opposite magnetic dipole. To understand this concept and its underlying mechanism, consider one non-magnetic particle in magnetized ferrofluids under a vertical magnetic field and imagine an equivalent volume of ferrofluids replaced by the non-magnetic colloidal hole. This replacement creates an effective magnetic dipole in the magnetic hole with a moment equal to the total moment of the replaced ferrofluid while being opposite to the applied field (**Figure 7a**). The dipole moment in the magnetic hole can thus be calculated by a similar equation as the one for magnetic particles, $m = -\chi_{eff}HV$, where χ_{eff} becomes the effective volume susceptibility of the ferrofluid.[92] Based on this explanation, one may expect a similar assembly behavior of the magnetic holes as with the magnetic nanoparticles. The effective magnetic dipole is repulsive and attractive when two non-magnetic colloids are perpendicular and parallel to the external field (**Figure 7b**), respectively, suggesting a parallel chain formation in response to an applied magnetic field.[85] However, one distinct property between these two systems is that a gradient magnetic field exerts a positive packing force and thus drives the movement of the magnetic hole to a region with lower field strength.[93] This opposite driving force has been quantitatively analyzed in a recent review that addresses the nanoscale magnetic assembly for functional materials.[66] Similarly to magnetic particles, it is also possible to pattens non-magnetic colloids using a non-magnetic template. For the 2D array of circular relief patterns shown in **Figure 5**, the simulation result demonstrates enhanced and reduced field strength around and above the circular relief, respectively. Therefore, the repulsive packing force of non-magnetic colloids drives them to assemble atop rather than around the relief. This different behavior has been verified by an interesting SEM image shown in **Figure 7c**, in which polystyrene beads assemble exclusively on the relief top with a high yield.[94] The magnetic assembly and patterning of general colloids further extend the potential of nanoscale magnetic assembly and its applications in producing smart materials, including photonic crystals (**Figure 7d**).

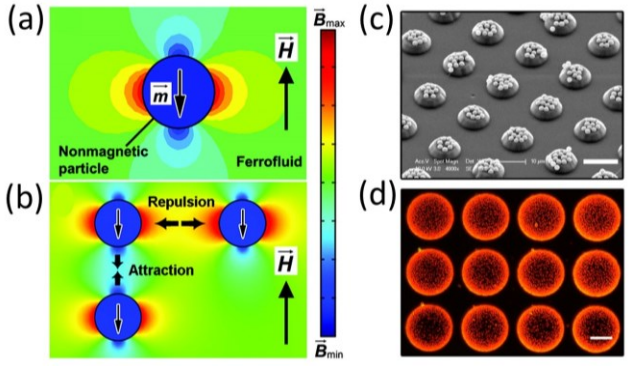

Figure 7. Magnetic assembly and patterning of general nanoparticles through nonmagnetic templates. (a) Magnetic field distribution round a nonmagnetic nanoparticle dispersed in ferrofluid with a permanent magnetic dipole. (b) Magnetic field distribution round three interacting nonmagnetic nanospheres demonstrating the attraction and repulsion among them. Reproduced with permission from ref [85]. Copyright 2012 American Chemical Society. (c) SEM image of the assembly and patterning of nonmagnetic beads in the ferrofluid. Scale bar: 10 μm. (d) Dark-field optical microscopy image of the photonic patterns formed by assembling polystyrene beads on circular relief patterns. Scale bar: 20 μm. Reproduced with permission from ref [94]. Copyright 2012 American Chemical Society.

The ability to control the colloidal magnetization property produces colloids with multipole symmetries and is also a key to developing even more complex superstructures. One practical approach in this regard is to assemble a mixture of colloids with different magnetic properties and sizes, which can be gradually extended to a diverse set of colloids for building hierarchical superstructures.[95] The fact that the repulsive packing force of non-magnetic particles drives their movement to the weak-field region guides the assembly behavior and determines the location of these magnetic holes. Consider a simple binary case where larger paramagnetic particles co-assemble with small non-magnetic ones. The smaller particles will assemble around the weak-field "equator" region of the large particles, leading to an interesting Saturn-ring configuration. If the size difference is opposite for these two types of magnetic dipoles, an inverse ring is produced, with large non-magnetic particles acting as cores and small magnetic counterparts as satellites. It is important to point out that all the self-assembly occurs in a ferrofluid, creating an effective opposite magnetic dipole in non-magnetic particles. This experimental onset enables precise control over the non-magnetic particles' magnetization, also making it possible to further tune the particle arrangement. Another alternative approach to fully exploiting possible assemblies is to add different types of building blocks. The magnetic assembly of trinary systems, for example, produces two-tone superstructures (**Figure 8**). In the first case, which involves 1.0-μm and 0.21-μm non-magnetic particles and 2.7-μm paramagnetic particles, the smaller and larger non-magnetic particles have a positive and negative dipole and therefore attach to the poles and equator of the magnetic particles, respectively (**Figure 8a**). In a second case using three types of particles with well-separated sizes, flower-like hierarchical structures are formed (**Figure 8b**).

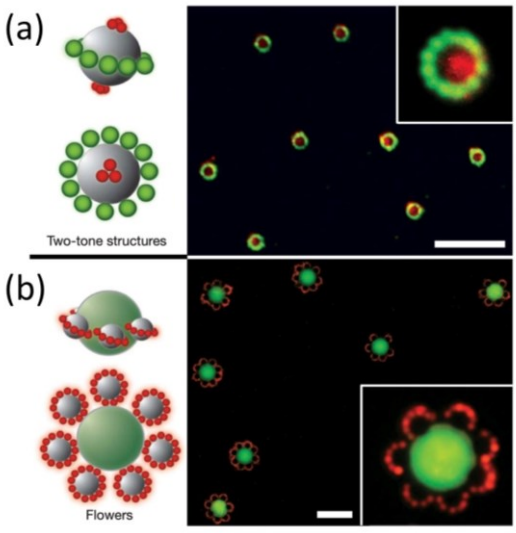

Figure 8. Magnetic assembly of colloidal superstructures with multipole symmetry. (a) Scheme (left panels) and fluorescent images

(right panels) of superstructures assembled from a four-component system: ferrofluid, 0.21-μm (red), and 1.0-μm (green) nonmagnetic polystyrene particles, and 2.7-μm paramagnetic core particles. (b) Scheme (left) and fluorescent image of superstructures assembled from the different four-component system: ferrofluid, 1.0-μm (red) and 9.9-μm (green) nonmagnetic polystyrene particles, and 2.7-μm magnetic core particles. Scale bars: 20 μm. Reproduced with permission from ref [95]. Copyright 2009 Springer Nature.

Extending the nanoscale magnetic assembly to anisotropic colloids provides an additional degree of freedom to control crystal symmetry and structural diversity, whose implementation yet requires further theoretical consideration of the concepts of magnetic shape anisotropy and magnetocrystalline anisotropy. In fact, anisotropic colloids have an associated demagnetizing field that is not directionally equal, creating one or more easy magnetization axes. Consider a dilute dispersion of magnetized nanoparticles in a uniform magnetic field, where only the Zeeman coupling is effective due to low particle density. The long-range packing force will assemble these nanoparticles so that their easy axes are parallel to the external field. This general property underpins the important role of magnetic shape anisotropy in assembling non-spherical nanoparticles (e.g., nanorods, nanocubes, and nanoplates). The demagnetizing field is opposite to the external magnetic field with a magnitude of $B=-\mu_0 N \bullet m$, where N and μ_0 are the demagnetizing tension and magnetic permeability of free space, respectively. The particle energy in the demagnetizing field is calculated by the following equation:

$$E = -\frac{1}{2}\int B \bullet m \, dV \tag{3}$$

This equation is further simplified based on a few assumptions to predict easy axes of typical shapes. For an infinitely long cylinder, its demagnetizing energy is given by $0.25\ \mu_0 m^2 \sin^2\Theta$, where Θ is the angle between the major axis and external magnetic field. Instead, for a considerably thin flat ellipsoid, its demagnetizing energy is given by $0.5\mu_0 m^2 \cos^2\Theta$, where Θ is the angle between the normal plane of the flat ellipsoid and the external field. Using these equations, one can easily predict that a nanorod or cylinder spontaneously organizes its major axis to the external field while a thin plate aligns its normal axis perpendicular to the field.[68]

The presence of an easy axis makes the magnetic assembly of non-spherical particles more complicated than the spherical counterparts but understanding the magnetic forces between two colloids is always a good starting place to access complex yet interesting assembly phases. One great benefit associated with magnetic shape anisotropy is the preferential parallel alignment of the easy axis of anisotropic particles to the field such that one may neglect the rotational degree of freedom in calculating their magnetic forces. For example, the magnetic interactions of simple nanorods can be calculated by rotating a second nanorod around the middle primary one from 0° to 90° (**Figure 9a**), with a constant surface-to-surface separation once a time. The magnetic forces are resolved based on finite element methods, with their magnitude depending on particle azimuth (Θ) and separation (**Figure 9b**). The force strength monotonically decreases with gradually increasing separation, but its dependence on the azimuth is much more complicated with a maximum value in a certain direction of the interaction. This interesting profile implies that moving the second rod from 90° to 0° has much more complex physical effects than a simple separation process and that interpreting the underlying physical principles needs further force analysis. To this end, the magnetic forces are decomposed into tangent (left panel in **Figure 9c**) and normal forces (right panel in **Figure 9c**) relative to the rod surface normal. With arrows indicating local force direction, it is easy to recognize a few important angles that define the force boundary. The normal component changes from repulsive to attractive force as Θ increases to 90°, leading to a separation-dependent force boundary. Within the attractive domain, the tangent force approaches zero at a critical angle, where the two nanorods only assemble to closer proximity while hardly shifting their relative position. Notably, this critical angle changes in coordination with the rod separation, whose physical meaning represents surface coating of a given thickness. In this way, it is straightforward to recognize the thermodynamic equilibrium position of two interacting nanorods. This finite element analysis further allows precise prediction of the critical angle and equilibrium binding direction of a set of nanorods, leading to a conclusion that the magnetic assembly of nanorods is dependent on size, aspect ratio, and coating thickness (**Figure 9d**).

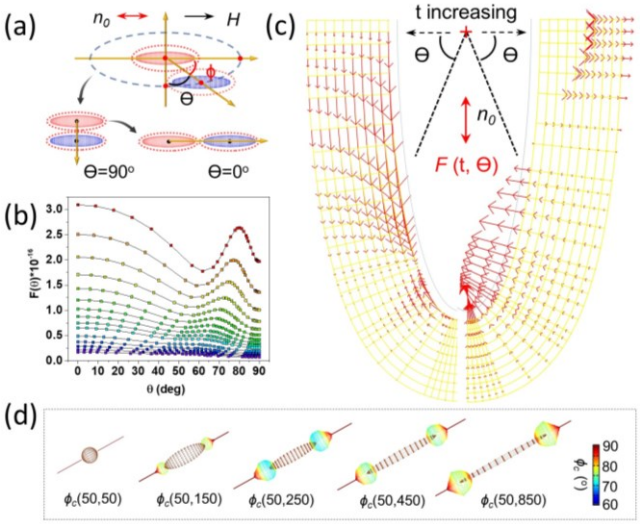

Figure 9. Magnetic assembly of nanorods and their dipole-dipole interactions. (a) Schematic illustration of the geometry for simulating the magnetic interactions between two nanorods. (b) Dependence of the dipole-dipole interactions between two nanorods with parallel alignment. (c) 3D mapping of tangent (left) and normal (right) components of the total magnetic force. The value of t is half the surface-to-surface distance between the magnetic nanorods. (d) 3D mapping of the equilibrium states in the magnetic assembly of nanorods, defined by a critical angle between two interacting nanorods. The $\phi_c(50, 150)$ represents the critical angle for assembling magnetic nanorods with a diameter of 50 nm and length of 150 nm.

The magnetic field distribution around two interacting nanorods provides visible tools to analyze their magnetic force dynamics. **Figures 10a** to **10d** show the field distribution of two nanorods at 0°, the force boundary, the critical angle, and 90°, respectively, whose corresponding local field magnitude and direction are systematically mapped from **Figure 10e** to **10h**. Clearly, their magnetic interaction changes in sequence from repulsion

to attraction at the force boundary and produces an optimal configuration at the critical angle.

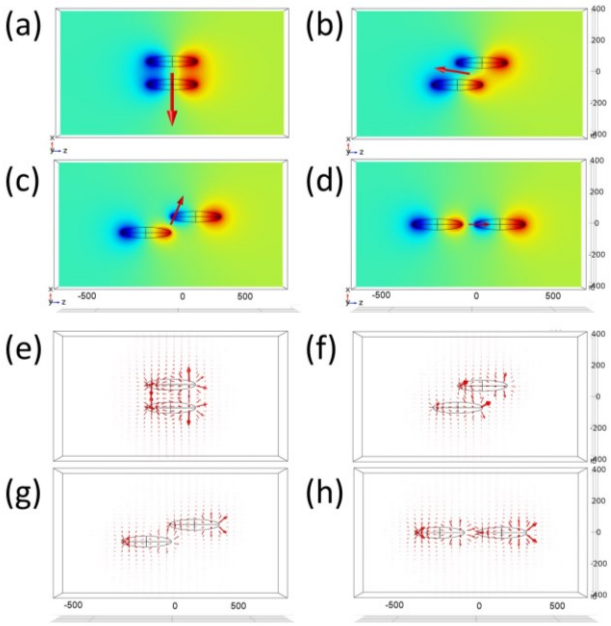

Figure 10. Magnetic assembly of nanorods and their magnetic field distribution. Magnetic field distribution (top) and mapping (bottom) during magnetic assembly of two nanorods: (a, e) at 90°; (b, f) at the repulsion-attraction boundary; (c, g) at the critical angle; and (d, h) at 0°. The angle is defined between the connecting line between two nanorod centers and the z-axis, where is also the magnetic dipole direction.

In experiments, this sequence of events creates exquisite 3D superstructures with perfect lattice and unique symmetry in the magnetic assembly of monodisperse nanorods, as revealed by the TEM images in **Figures 11a** and **11b**. The distinct 2D projection patterns suggest the reduced lateral symmetry of the colloidal crystals, leading to the unique orthorhombic 2D lattice in **Figure 11a** and layer-by-layer packing of nanorods in **Figure 11b**. A close analysis of this interesting lattice suggests a body-centered tetragonal colloidal crystal, with one rod in the unit cell center and eight rods in the unit cell vertex (**Figure 11c**).

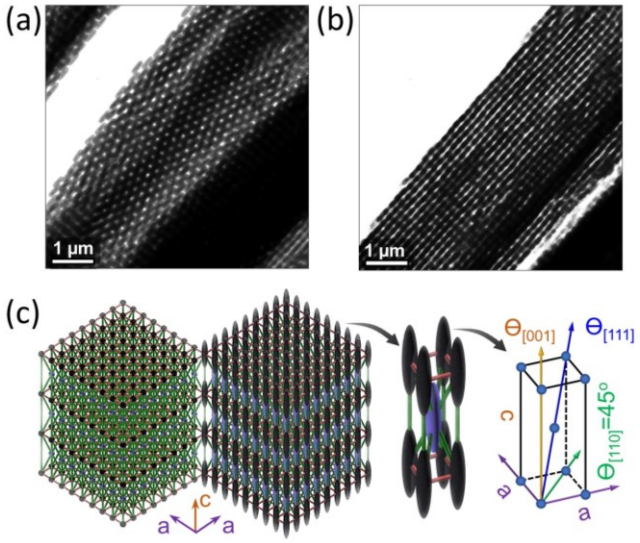

Figure 11. Magnetic assembly of nanorods into tetragonal colloidal crystals. (a, b) TEM images of the body-centered tetragonal colloidal crystals with crystal orientation of (100) and (110), respectively. (c) Schematic illustration of the body-centered tetragonal colloidal crystals.

Another different but related concept uses the magnetocrystalline anisotropy of magnetite nanocubes for assembling helical superstructures.[96] This remarkable magnetic assembly involves forming a thin nanocube dispersion between a liquid-air interface, followed by magnetic assembly upon evaporating the solvent. One unique feature of the cubic building block is that their easy axis is the [111] crystallographic direction, diverging from any geometric axes favoring close packing (**Figure 12a**). At a low particle surface concentration, 2D nanobelts of [100]-orientated nanocubes are formed but with a magnetic dipole in each nanocube varying with applied magnetic field strength due to the competition between dipole-dipole interactions and Zeeman coupling. Increasing the particle concentration to a moderate range, 2D belts with [110]-orientated nanocubes are the thermodynamic equilibrium product, as favored by both the Zeeman coupling and dipole-dipole interaction. However, in a high concentration, all the magnetite nanocubes tend to align their easy axes to the external field, thus leading to single-stranded helical structures (**Figure 12b**). A further analysis contributes such striking superstructures to the competition between magnetic and spatial symmetries, and the rearrange of belt structures to helix minimizes the system energy as suggested by Monte Carlo simulations (**Figure 12c**). A similar competing effect is also reported in the magnetic assembly of large nanocubes for orientation-dependent photonic responses.[97] In this study, the nanocubes are polycrystalline such that they only feature magnetic shape anisotropy with an easy axis along cubic [111] direction. The competition between Zeeman coupling, favoring [111] direction, and dipole-dipole coupling, favoring [100] direction, interestingly produce 1D chains containing [110]-orientated nanocubes.

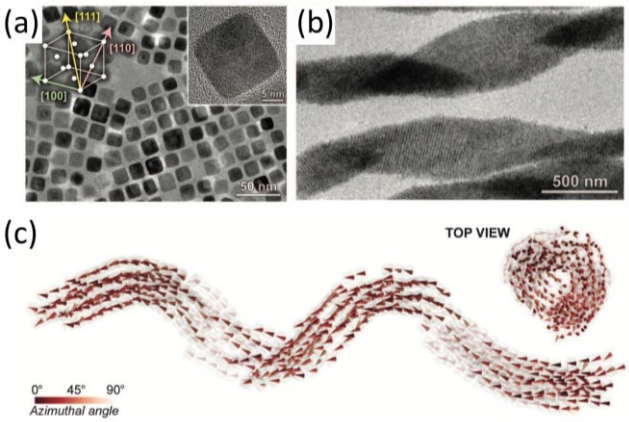

Figure 12. Magnetic assembly of nanocubes into helical superstructures. (a) TEM image of monodisperse magnetite nanocubes. (b) TEM image of the single-stranded helical superstructures from the magnetic assembly of nanocubes. (c) A snapshot of the helical superstructures predicted from computer simulation. Reproduced with permission from ref [96]. Copyright 2014 The American Association for the Advancement of Science.

2.2. Van der Waals Force

In addition to electrostatic interaction, van der Waals force is another primary contributor to the total potential energy of interacting colloids, according to DLVO theory.[98-100] It is a universal force between noncharged molecules from three different contributions, Keesom force (attraction between permanent dipoles), Debye force (attraction between permanent and induced dipoles), and London dispersion force (attraction between fluctuating and induced dipoles), which therefore has been extensively studied in regulating the collective properties of superstructures in response to external stimuli. Van der Waals force is a short-range force with its magnitude inversely proportional to the sixth order of molecular distance. It differs from the dipole-dipole attraction between polar molecules by considering the rotational degree of freedom of interacting molecules, whose magnitude is basically the ensemble average over all these configurations. Therefore, for two molecules with the dipole moments of m_1 and m_2, the angle averaged Keesom force and Debye force potential in k_BT can be given using the following two equations:[101]

$$V_{Keesom} = \frac{-m_1^2 m_2^2}{24\pi^2 \varepsilon_0^2 \varepsilon_r^2 r^6} \quad (6)$$

$$V_{Debye} = \frac{-m_1^2 \alpha_2}{16\pi^2 \varepsilon_0^2 \varepsilon_r^2 r^6} \quad (7)$$

where α is the polarizability. However, colloidal particles have given shapes and number of atoms, and calculating their van der Waals force is to integrate all interacting atoms over the entire volume, which makes the calculation dependent on particle shape. For example, in two interacting nanospheres, it is possible to derive the following formula to compute their van der Waals force potential:

$$V_{vdW} = -\frac{A}{6}\left(\frac{2}{R^2-4} + \frac{2}{R^2} + ln\frac{R^2-4}{R^2}\right) \quad (8)$$

In this equation, A is the Hamaker constant between particles[102] and $R=r/a$, where r and a are particle center-to-center distance and particle radius, respectively. Notably, the force integration is often simplified using the coarse grain method, which divides nanoparticles of a given shape into isolated domains. The van der Waals force is estimated by summing over the forces between all possible domain pairs instead of atom pairs.[96] Another noticeable variation in colloidal systems is the van der Waals force between surface capping ligands, which plays an important role in assembling colloidal particles because of their close contact. Particularly in the self-assembly of nanoplates, van der Waals force between neighboring alkyl chains is stronger than the nanoplate cores because of the interdigitated configuration of ligands adhered to adjacent plates (**Figure 13a**).[103] In fact, the van der Waals force between ligands on the edges of nanoplates is so effective that its competition with shape anisotropy of plates leads to interesting 2D superlattices with an alternating tessellation of nanoplates (**Figure 13b**). The deterministic roles of organic tethers in regulating effective nanoparticle interaction have also been discussed in the self-assembly of colloidal superlattices.[104-106] Obviously, such ligand-ligand interactions are more effective if the particle surface is flat rather than curved.[107]

Controlling the size, morphologies, and stoichiometry of superlattices is possible in a few defined self-assembly processes driven by van der Waals force. Because of the presence of repulsive forces between dispersed nanocrystals, like steric or electrostatic repulsion, their self-assembly usually starts with the destabilization of their colloidal dispersion, which typically involves nonsolvent addition,[108] depletant addition,[109] and micelle deposition.[110,111] In an elegant example, water-soluble semiconductor nanorods self-assemble into monodisperse superstructures via micelle deposition in diethylene glycol (**Figure 13c**).[110] A close investigation suggests that spherical superstructures made of >80000 nanorods contain a central cylindrical domain of close-packed rods capped by two domes (left panel in **Figure 13d**). The size of the spherical superstructures can be controlled by the number of surfactants present in the solution. These observations lead to a favorable growth mechanism of the superlattices driven by van der Waals force and dipole interaction, in which small rod domains below a critical radius of stable nuclei coalesce into the capped spherical superstructures. Destabilization of the rod dispersion by slow diffusion of polar nonsolvent allows kinetic control of leaving capping ligands, which creates facet-selective functionality of the nanorods. This sequence of events yields single-domain, elongated needle-like superstructures (right panel in **Figure 13d**) or superparticle platelets.[108] Several comprehensive studies of binary nanocrystal superlattices have jointed to appreciate that van der Waals force in combination with other driving forces creates copious superstructures with widely tunable stoichiometry, and that van der Waals is of particular importance in stabilizing these complex structures for characterization and further processing to smart materials. For comprehensively understanding self-assembly of small nanocrystals, we present the possible sixteen superstructures from binary nanocrystals in **Figure 14** and refer the readers to a nice review that focuses on all the aspects of nanocrystal superlattices.

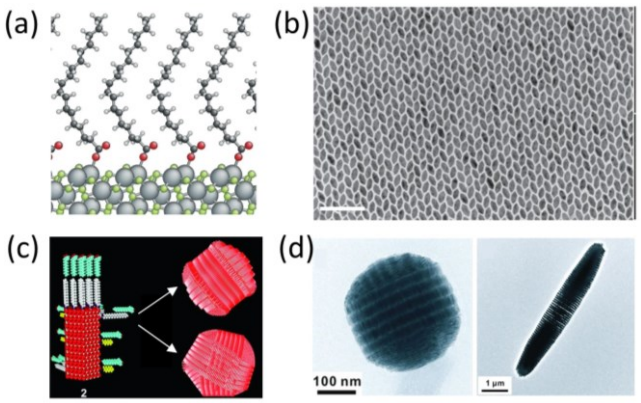

Figure 13. Self-assembly of superstructures driven by van der Waals force. (a). Calculated molecular structure of surface ligands on the (101) surface of nanocrystals. (b) TEM image of alternating arrangements of hexagonal nanoplates. Scale bar: 100 nm. Reproduced with permission from ref [103]. Copyright 2013 Springer Nature. (c) Scheme of the self-assembly of nanorods in colloidal dispersions. (d) SEM images of spherical (left) and ellipsoidal (right) colloidal crystals. Reproduced with permission from ref [110]. Copyright 2012 The American Association for the Advancement of Science.

2.3. Interactions between Ligands

It is well-known that chemical compounds or biomolecules have solvation shells if they are properly dissolved in a solvent. Similar to the solvent shells of any free molecules in a solution, there also exists a solvation layer surrounding colloidal particles due to the interactions between ligands and solvent molecules.[112,113] Depending on the ligands and solvents in the colloidal dispersion, the solvation layer exerts different forces between colloids, such as the steric repulsion between neutral ligands and the attractive van der Waals force that drives nanoparticle self-assembly. In addition to the physical interactions, some reactive ligands can form chemical bonds and thus drive the self-assembly of nanoparticles into diverse crystals, with the specific interaction between DNA as a representative example. Because colloidal assembly is the self-organization of dispersed nanoparticles, it is the surface ligands and the associated solvation layers that come in contact as the self-assembly proceeds. Therefore, the interactions between ligands are of great importance in mediating and understanding the assembly behaviors of nanoparticles in colloidal dispersions. Common interactions between surface molecules of colloids include the van der Waals forces, hydrogen bond, DNA base-pair interactions, chemical cross-linking.

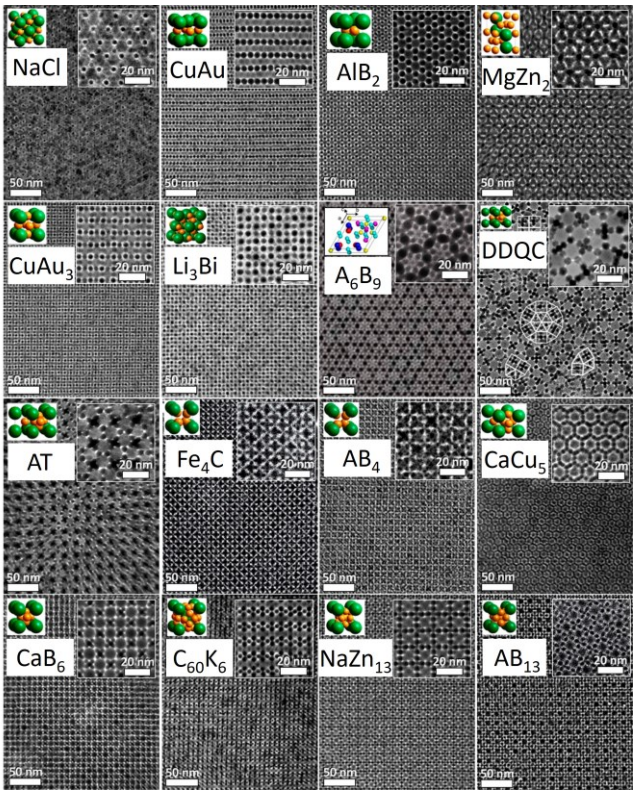

Figure 14. Self-assembly of binary superlattices. Each TEM image shows the crystal structure of a superlattice. Insets: schemes (left panels) and enlarged TEM images (right panels). Scale bars: 50 nm. Scale bars in insets: 20 nm. DDQC represents dodecagonal quasicrystal. Reproduced with permission from ref [114]. Copyright 2016 American Chemical Society.

2.3.1. Electrostatic Interaction

Like van der Waals force, electrostatic forces are ubiquitous at all scales for particles or molecules carrying charges (e.g., ions, colloids, macromolecules, and macroparticles), which can regulate particle separation for developing smart materials.[115-117] One unique feature that makes them distinct from van der Waals force is that electrostatic interactions can be either attractive or repulsive for oppositely charged and like-charged particles, respectively. For two-point charges with a separation of r, their electrostatic force can be simply calculated by Coulomb's law as $F=k_e q_1 q_2/r^2$, where k_e is the Coulomb's constant ($k_e \approx 8.988\times10^9\ N\cdot m^2\cdot C^{-2}$). The q_1 and q_2 are the magnitudes of the two charges. In the colloidal systems, however, the quantitative description of electrostatic forces between charged nanoparticles is much more complicated because the interaction magnitude, direction, and length scale are very sensitive to the shape-dependent charge distribution of nanoparticles, the presence of counterions, solvent effect, solution temperature, and particle concentrations. On the other hand, these dependencies also enable the controllable self-assembly of nanoparticles for desirable responses if the electrostatic forces between them can be carefully controlled. Therefore, it is critical to find analytical or numerical solutions to predict the dependence of electrostatic forces on these important parameters.

When charged nanoparticles are dispersed in water, some capping ligands will be dissociated while others remain neutral depending on the dissociation constant so that the nanoparticles have net surface charges to absorb oppositely charged counterions (**Figure 15a**).[118] These two physical processes create a double layer surrounding the nanoparticles, referring to two parallel layers of opposite charges, in which the first layer comprises charged ligands due to the dissociation of surface functional groups. In contrast, the second layer is made of the counterions attracted to the surface charges via electrostatic forces.[119,120] The association-dissociation equilibrium of such complex structures is determined by a constant K_{eq}, which is the intrinsic properties of specific ligand-ion pairs. Another important parameter to characterize the associated exponential decay of electrostatic potential (φ) in colloidal dispersions is called Debye screening length or simply Debye length (κ^{-1}).[121] In an equilibrium system, the Debye length can be calculated by $\kappa^{-1} = (\varepsilon_0 \varepsilon_s k_B T / 2000 e^2 N_A I)^{-1/2}$, where k_B, e, I, ε_0, ε_r, N_A, and T are the Boltzmann constant, the charge of the electron, the ionic strength of the solvent, permittivity of free space, the dielectric constant of the solvent, Avogadro constant, and absolute temperature, respectively. This critical Debye length makes it possible to compute the electrostatic potential energy via the following equation based on the Derjaguin-Landau-Verwey-Overbeek (DLVO) theory.[122-124]

$$V_{elec} = 2\pi\varepsilon_r\varepsilon_0 a\psi_0^2(T)\ln\left(1+\exp\left(-a\kappa(R-2)\right)\right) \quad (4)$$

In this equation, a and ψ^0 are the radius of the particle and the surface potential of the particle. R equals r/a with r as the particle center-to-center distance. This equation predicts that, in addition to the known deterministic parameters of electrostatic forces (e.g., ionic strength, surface charge density, solvent), the temperature is also important in determining the driving forces between interacting nanoparticles. In fact, it has been used to reversibly assemble and dissemble charged nanoparticles for responsive plasmonic superstructures.[123]

In a different but highly relevant theory that neglects the ion correlation effect, nanoparticles are assumed as point charges,[125,126] and the electrostatic potential energy can be calculated through analyzing the constant chemical potential in an equilibrium solution system. By substituting the derived local ion concentration and charge density into Poisson's equation, $\nabla^2\varphi = -\rho/\varepsilon_0\varepsilon$, it is possible to calculate the electrostatic potential energy using the Poisson–Boltzmann equation for a monovalent electrolyte.[127,128]

$$\nabla^2\varphi = \frac{2ec_s}{\varepsilon_0\varepsilon_r}\sinh\left(\frac{e\varphi}{k_BT}\right) \quad (5)$$

The C_s is the bulk salt concentration. Accurately describing the electrostatic potential energy requires three different boundary conditions to further characterize the surface of charged particles and to specify the electrostatics of the system. In this regard, the charged particle surfaces are divided into neutral surfaces absorbed by charged species and ionizable surfaces. Based on this simple approximation, three boundary conditions are recognized: constant charge, charge-regulating, and constant potential conditions. In an ideal case where all the particle surface functional groups are dissociated, the constant charge boundary condition is the natural choice since external stimuli may cause small changes in the surface charge due to its high equilibrium dissociation constant. In a middle state, the dissociation of surface ligands and the ionic equilibrium is comparable, and their completing effects lead to a charge-regulating boundary condition.[129,130] At a considerably low dissociation constant, however, the constant potential boundary condition is reasonable and adopted for calculation. Therefore, this theoretical consideration produces three different electrostatic potentials based on the involved boundary conditions (**Figure 15b**). Prior to using these equations, it is important to estimate the particle surface properties and the ionic strength in the solution so that an optimal condition and equation can be properly employed. Notably, these equations are operational for both electrostatic repulsive and attractive forces but with different magnitudes for any constant separation (**Figure 15b**) because the affinities of positively and negatively charged ligands with their counterions can be significantly different at the charge balance state. This situation is particularly true for charged nanoparticles surrounded by monovalent counterions with considerably different sizes.[131,132]

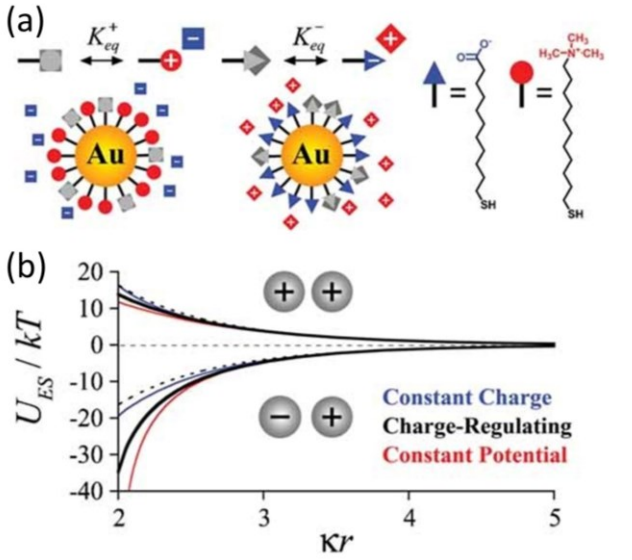

Figure 15. Electrostatic interactions between charged colloids. (a) Schematic illustration of dissociation of oppositely charged Au nanoparticles. (b) Electrostatic interaction potential between the Au nanoparticles. The dashed curve is the asymptotic approximation of electrostatic interaction potential between spherical particles. Reproduced with permission from ref [118]. Copyright 2009 John Wiley and Sons.

These equations are possible to be extended to anisotropic nanoparticles but with limited capability. This barrier is mainly caused by the structural complexity of anisotropic nanoparticles and their solvation layers, which makes many prerequisites unavailable. However, they can still provide considerable accuracy in predicting the self-assembly of a few common anisotropic particles, like nanorods. Consider a case where the Debye length is considerably smaller than particle size and imagine the electrostatic force is only dependent on the local curvature of interacting colloids near the contact. It is possible to predict a "side-on" attachment of nanospheres to oppositely charged nanorods, which is favored by a stronger attraction than the "end-on" attachment. For assembling nanoparticles with the same

charges, one may expect a stronger repulsion in "side-on" than "end-on" attachments, which suggests a favorable "end-on" attachment. In some cases, the polarization effect may be effective such that it imposes an additional limitation to the use of these equations.[133] Albeit the accuracy in predicting forces, determining the electrostatic force direction is particularly difficult for these equations. To this end, developing a new reliable method to overcome the existing barrier and precisely predict force directions is required to understand the colloidal self-assembly driven by electrostatic forces.

Coarse-grained simulation as an established methodology provides considerably accurate modeling of many complex systems, including the colloidal self-assembly problems. For demonstrating its unique capabilities, two nanorods with only orientational order and the same surface charges are used as a model system to predict their electrostatic interactions (**Figure 16a**). With the assumption of a homogeneous charge distribution, it is possible to divide rod surface into finite, sufficiently small domains carrying identical charges (periodic dots in **Figure 16a**) such that each domain can serve as a point charge. Based on the classic Coulomb's law, the electrostatic forces between any two domains can easily be calculated, the vector sum of which provides both force magnitudes and directions with reasonable accuracy. Notably, this method has been extensively used in Monte Carlo simulation to provide a numerical approach to the thermodynamic equilibrium states of colloidal self-assembly.[96,134,135] It is also operational to many underlying forces if there exist reliable equations to calculate the forces between grain pairs. In the case of electrostatic interactions, the rods experience both separation- and orientation-dependent repulsive force, whose direction changes simultaneously. The force magnitude decreases as the rod center-to-center distance increases, consistent with the prediction of classic Coulomb's law (**Figure 16b**). What is interesting is the dependence of force direction on the rod relative orientation. Colloidal particles with arbitrary shapes can be treated as point charges if their separation is relatively larger than their sizes, and their electrostatic forces have been demonstrated to be along the rod connection line (namely center to center).[136,137] When particle separation decreases from a value comparable with rod length, the electrostatic repulsion is gradually approaching the rod surface normal, whose dependence is difficult to predict based on empirical or numerical equations (**Figure 16c**). It allows to precisely calculate different forces between interacting colloids and predict their thermodynamic equilibrium state and superstructures by analyzing these forces. The accuracy that can be achieved is only limited to the characterization of particle properties (surface charges, ligand density, dielectric constant, etc.) and grain sizes.

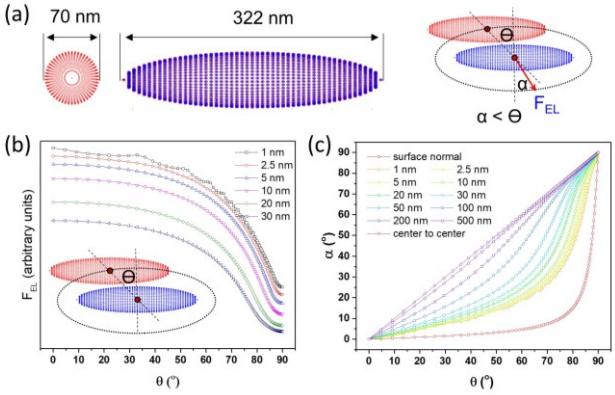

Figure 16. Electrostatic interactions between charged nanorods. (a) Scheme of the rod size. (b) Dependence of electrostatic repulsion on the azimuth angle (Θ). (c) Changes in the electrostatic repulsion direction (α) with the azimuth angle. The numbers indicate the surface-to-surface distance between the two nanorods. The curves labeled as "surface normal" and "center to center" are the predicted dependence of repulsion direction on the azimuth angle, assuming that the electrostatic repulsion is parallel to the surface normal and the center-to-center connecting line, respectively.

In the self-assembly of colloidal nanoparticles stabilized by surface charges, it is possible to assemble them into secondary structures by controlling the electrostatic repulsion. This strategy has been extensively used in the solution-processed assembly of responsive plasmonic nanoparticles motivated by their unique optical properties. A few associated attractive forces include underlying van der Waals force or emergent entropic force, which alone tends to assemble monodisperse nanoparticles into dense clusters or close packing crystals with broadband coupling in the visible spectrum. To achieve optimal optical properties, many elegant methods have been developed to control these interplaying forces and thus the assembled plasmonic structures.[138-140] A great benefit in this regard is that the electrical double layer is reconfigurable depending on the structural geometry.[141] In a colloidal oligomer from the self-assembly of a few nanoparticles, the electrical double layer reconfigures to wrap the whole oligomer due to the close arrangement of adjacent nanoparticles, which produces anisotropic electrostatic repulsion to its neighboring monomers. Therefore, the neighbors will experience a stronger electrostatic repulsion when approaching the oligomer from the side than from the end. This consideration is consistent with the discussion in the electrostatic forces between nanorods and nanospheres and leads to favorable "end-on" attachment of colloidal monomers into chain-like structures. When monomer is depleted, the number of oligomers increases, making the selective addition of chains difficult and enabling the formation of branched chains.[142] This interesting phase property has been observed in many solution-based self-assembly processes regulated by pH, salt, and temperature.[143-148] Producing perfect 1D chains without branches or other defects is possible by introducing strong anisotropic repulsion to prevent morphological isomer formation, which may change the assembly pathway of colloids.[138]

The fast developments of ligand-mediated self-assembly in the past two decades have come to appreciate that it somewhat re-

sembles a typical polymerization process, with assembly pathway, polydisperse intermediate, and the final product similar in many ways to those involved in organic polymerization.[149-155] As monodisperse nanoparticles have the same tendency to assemble, many solution-processed self-assembly processes favor the step-growth polymerization pathway.[149,151,156] That is, the colloid monomer first assembles into short chains, which further join through branching and addition to form large chains (left panel in **Figure 17a**). One feature of this pathway is that chain size increases slowly initially but more dramatically in the later stage of the assembly process, leading to polydisperse branched colloidal chains (**Figure 17b**).[157] In another case where a strong anisotropic driving force prevents any unfavorable side attachment, the self-assembly occurs through single-particle addition and thus follows a chain-growth pathway (right panel in **Figure 17a**). This consideration partially explains why linear chains are produced through the chain-growth pathway (**Figure 17c**).[158] The chain branching is possible in step growth, and one may expect highly cross-linked short chains in the final products instead of perfect linear chains. Although the electrostatic repulsion is also anisotropic in step-growth self-assembly, its weak strength probably explains why the kinetically favored branching effect can occur.

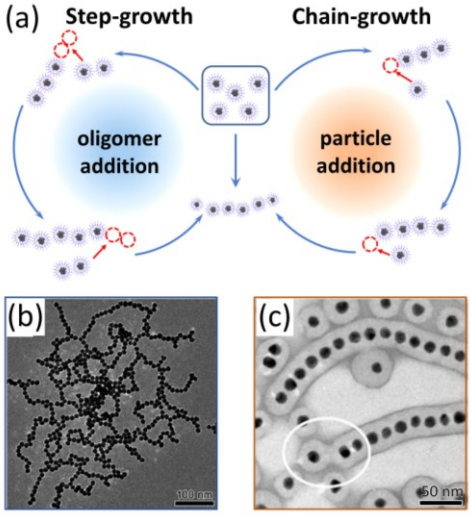

Figure 17. Self-assembly pathway of plasmonic nanospheres mediated by surface ligand interactions and van der Waals forces. (a) Scheme of two representative pathways. Reproduced with permission from ref [74]. Copyright 2020 Elsevier. (b) TEM images of (b) branched chains from the step-growth pathway. Reproduced with permission from ref [157]. Copyright 2011 American Chemical Society. (c) TEM image of perfectly line chains from the chain-growth pathway. Reproduced with permission from ref [158]. Copyright 2012 John Wiley and Sons.

Electrostatic self-assembly of oppositely charged nanoparticles can produce superstructures of defined crystal symmetry, mainly due to the interplay between electrostatic repulsion and attraction of similar magnitudes in such binary systems. For binary metal nanoparticles of similar sizes (**Figure 18a**),[131] screening electrostatic interactions is significant due to the metallic cores and presence of counterions. The short screening length implies that electrostatic forces are effective only for nanoparticles with the closest proximity. Crystallizing such a binary system in proper solvent leads to a diamond lattice with each nanoparticle coordinated with four oppositely charged neighbors (**Figure 18b**). The particle arrangement in diamond lattices has larger interparticle separation than NaCl and CsCl lattices, with a value close to $2\kappa^{-1}$. This unique structure features negligible positive electrostatic potentials due to the week repulsion between like-charged nanoparticles, making it energetically favorable compared with the other two candidates. Notably, the stoichiometry of a diamond lattice is simple AB type despite its low structural symmetry. A few close studies demonstrate that it is possible to further extending the structural stoichiometry to AB_6 type using binary nanoparticles but with different sizes (**Figure 18c**).[159] One great benefit associated with large size difference is a high likelihood that smaller particles can self-assemble in free gaps between larger particles. The infilling ratio and the lattice stoichiometry are dependent on the particle size and screening length of each component. In the self-assembly of equally sized nanoparticles, the phase diagram is simple, only producing NaCl and CsCl lattices in the crystalline domains (**Figure 18d**). Simply increasing the size difference of the two components yields a surprisingly complex phase diagram (**Figure 18e**), with the crystal symmetry highly depending on particle charge ratio.

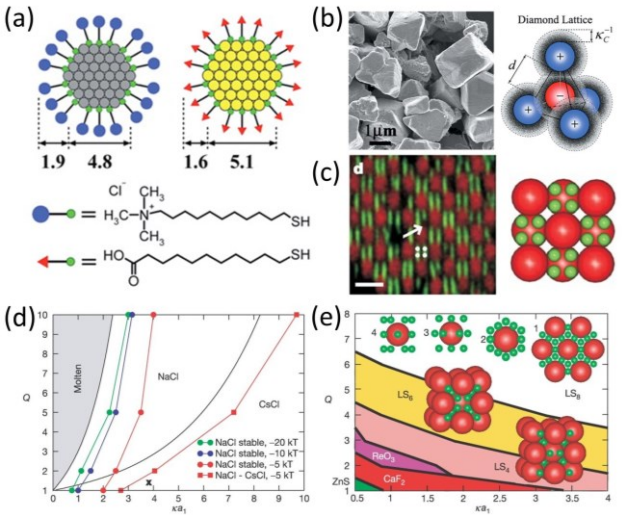

Figure 18. Self-assembly of oppositely charged nanoparticles through electrostatic interactions. (a) Scheme and size of oppositely charged Au and Ag nanoparticles. (b) SEM image of assembled colloidal crystals and particle arrangement in the lattice. Reproduced with permission from ref [131]. Copyright 2006 The American Association for the Advancement of Science. (c) Confocal image and the scheme of binary colloidal crystals. Scale bar: 4 μm. Self-assembly phase diagram of two types of nanospheres with a size ratio of (d) 1 and (e) 0.31. Positively and negatively charged polymethylmethacrylate (PMMA) particles are represented in red and green spheres, respectively. Reproduced with permission from ref [159]. Copyright 2005 Springer Nature.

To tune the particle separation more efficiently, other short- and long-range forces have been introduced to electrostatic self-assembly, including steric repulsion,[29] van der Waals force,[160-162] entropic force,[163] and surface patchy interaction.[164] These forces allow to precisely tune the attractive overlap and electrical double layers, direct the colloidal self-assembly into superlattices,

and, in some cases, fix the assembled crystals. For example, introducing polymer brushes can induce effective steric repulsion, which prevents interacting nanoparticles from falling into the van der Waals regime and regulates the overlap of the electrical double layers.[29] Its interplay with electrostatic attraction facilitates the tuning of interparticle separation and their electrostatic attraction, making the self-assembly susceptible to screening length. This consideration is confirmed by the pair potential profile, which demonstrates the convenient tuning of the local minimum by controlling screening length relative to polymer spacer. A comparable screening length to polymer thickness is important to establish a suitable ionic bond for the crystallization of oppositely charged particles. In experiments, this optimization can be readily reached by controlling NaCl concentration, leading to perfectly ordered ionic solids (**Figure 19a**). There only exists one narrow crystallization window for an established combination of screening length and polymer thickness. Such explicit dependence makes the superstructures stable through a self-locking mechanism. If a charged substrate is introduced to accommodate heterogeneous nucleation, oppositely charged particles are possible to crystallize along specific directions, effectively shaping the grown solids (**Figure 19b**). This strategy is based on the electrostatic attractions between charged substrates and particles, which is also used in templated self-assembly on charge-patterned substrates[165] and electrical assembly of tunable photonic crystals in electric cells.[166,167]

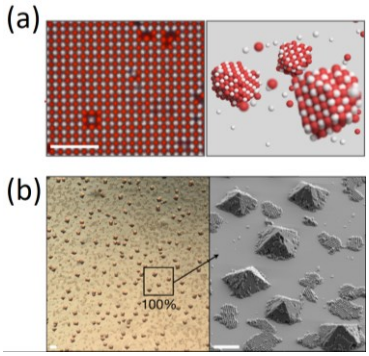

Figure 19. Self-assembly of oppositely charged colloids into ionic solids. (a) Confocal microscopy (left) and computer simulations (right) of the ionic solids. Scale bar: 4 μm. (b) Bright-field micrograph (left) and SEM image (right) of monodisperse pyramid-like crystals. Scale bars: 20 μm. Reproduced with permission from ref [29]. Copyright 2020 Springer Nature.

2.3.2. Hydrogen Bonding

A hydrogen bond refers to a universal electrostatic force between a hydrogen atom and a neighboring electronegative atom having a lone pair of electrons. Despite the associated complexity and chemical variability of hydrogen bonds, it is possible to propose a flexible and general definition, which covers the strongest and weakest species of the family and inter- and intramolecular interactions. In the strict sense as proposed by Steiner and illustrated in the inset of **Figure 20a**,[168] an *X-H···A* interaction is a "hydrogen bond" if it constitutes a local bond and *X-H* acts as a proton donor to *A*. Its dissociation energies span 0.2-40 kcal/mol depending on donor and acceptor atoms, bond geometry, and environment, giving rise to a bond strength between van der Waals attractions and covalent or ionic bonds.[168] A typical hydrogen bond potential is given in **Figure 20a**, and it suggests an optimal bond length at the global minimum of these interacting potentials. And a hydrogen bond diverging from this equilibrium length implies a force toward the geometry of the lowest energy, that is, by attraction and repulsion if the real bond length is larger and smaller than the optimal length, respectively. In practice, distortion from the optimal bond length is still possible, but only a small population has an energy differing by more than 1 kcal/mol from the lowest energy.[169,170]

Although its relatively weak bond strength compared with covalent or ionic bonds, its effect in the macromolecular and supramolecular systems is significant due to the high density in polymer networks.[171-174] It was later used as an effective driving force for the responsive self-assembly of colloidal particles, including nanospheres[175-177] and nanorods.[144,178,179] One straightforward strategy in this regard is to modify metal nanoparticle surfaces with functional groups that are possible to form hydrogen bonds (e.g., -OH, -COOH, -NH_2).[175] Depending on the bond strength, the order of the secondary structures and their degree of aggregation varies between different assembly conditions.[180] Similar hydrogen bonds can also form between colloidal particles and copolymers, leading to special particle arrangement on a soft copolymer template (**Figures 20b** and **20c**).[181] A few advanced strategies proposed controllable colloidal self-assembly using site-selective functionalization of particle surfaces[178,179] and by pH-responsive hydrogen bonds.[144,175] An interesting example in the first strategy is the end-to-end assembly of Au nanorods driven by hydrogen bonds. This unique directional self-assembly takes advantage of the inhomogeneous distribution of ligands on Au nanorods for selective functionalization of carboxylic groups. Because the dissociation constant of these functional groups is dependent on ionic strength, pH, temperature, etc., most of the secondary structures cross-linked by hydrogen bonds are responsive to these stimuli. This compelling characteristic makes hydrogen bonds very useful in developing smart colloidal assemblies in many solution processes and solid states.

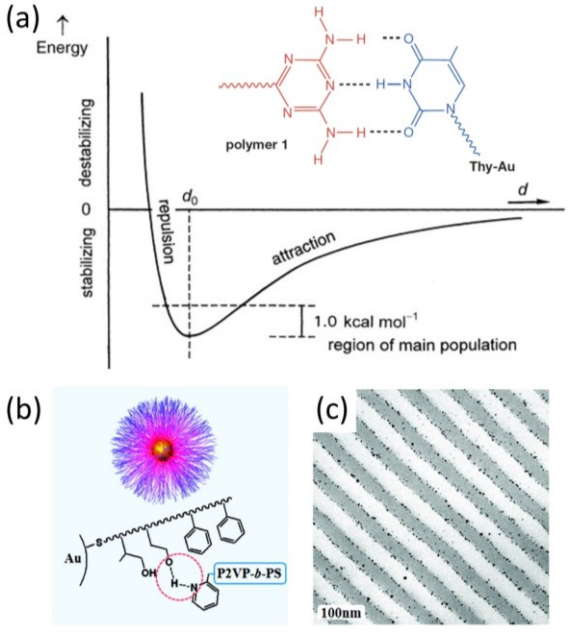

Figure 20. Self-assembly of colloidal superstructures driven by hydrogen bonding. (a) Schematic representation of a typical hydrogen bond potential. Reproduced with permission from ref [168]. Copyright 2002 John Wiley and Sons. Inset is representative interactions between polymers. Reproduced with permission from ref [177]. Copyright 2000 Springer Nature. (b) Scheme of hydrogen bonds between nanoparticles and polymers. (c)TME image of self-assembled nanoparticles on polymer substrates. Reproduced with permission from ref [181]. Copyright 2011 American Chemical Society.

2.3.3. Molecular Dipole-Dipole Interaction

Molecular dipole-dipole interactions are attractive forces between the permanent dipoles of molecules. Under such electrostatic attractions, polar molecules will align such that the positive end of one molecule interacts with the negative end of another molecule. Therefore, the force strength is usually stronger than the London forces and weaker than ion-ion interactions. The potential energy in terms of k_BT of an interaction between two permanent dipoles with moments of m_1 and m_2 can be simply calculated by $V_{dd}(r)=-m_1m_2/2\pi\varepsilon_0\varepsilon_r r^3$, where r is the minimal distance between the dipoles. Notably, the dependence of dipole-dipole potential on distance is different from that of Keesom force due to electrostatic interactions between rotating permanent dipoles. In fact, the electrostatic potential of different rotational orientations of these dipoles needs to be averaged to calculate the Keesom interaction potential. Azobenzene is a photoactive molecule that can transform from its nonpolar trans configuration (m=0 debye) to polar cis (m=4.4 debye) configuration (**Figure 21a**) under ultraviolet (UV) light excitation.[182] The molecular dipole-dipole interaction is much weaker in a polar solvent than a nonpolar solvent. If the molecular rotation freedom is considered, the Keesom interaction potential is reduced to -0.9 k_BT in toluene (see **section 2.3** for Keesom interaction).

If colloids are modified with polar molecules, the dipole-dipole interaction on the particle surface is strong enough to drive colloidal self-assembly. In this case, the total dipole-dipole interaction potential between two nanoparticles of radius a can be estimated by $A_{eff}V_{dd}(r)N$ where N is the surface density of polar molecules and $A_{eff}=2\pi ar$ is the effective contact areas. This calculation leads to total interaction energy of approximately 40 k_BT for two 3-nm Au nanoparticles bearing azobenzene on their surfaces, which is much stronger than the van der Waals forces. This consideration leads to the self-assembly of Au nanoparticles into a dense cluster (**Figure 21b**).[183] And the photoactive reversible isomerization enables the assembly and disassembly of the colloidal crystals in response to light irradiation (**Figure 21c**), leading to dynamic color switching and potential applications in color printing and anticounterfeiting. A practical strategy has incorporated the photoactive assembly of plasmonic nanoparticles into polymer matrix for rewritable plasmonic papers along this line.[184]

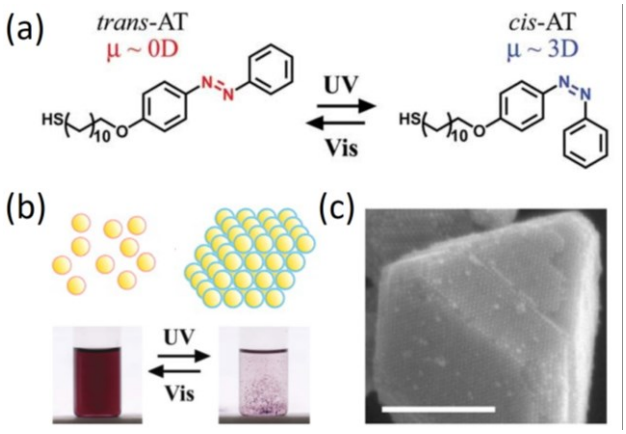

Figure 21. Self-assembly of colloidal superstructures driven by molecular dipole interactions. (a) Scheme of azobenzene thiol isomerizes from the trans- to the cis-conformation upon UV light exposure. The cis-isomer has a strong molecular dipole. Reproduced with permission from ref [118]. Copyright 2009 John Wiley and Sons. (b) Scheme (top) and digital pictures (bottom) showing the self-assembly of Au nanoparticles driven by the dipole interactions between azobenzene derivatives. (c) SEM image of the self-assembled colloidal crystals. Scale bar: 200 nm. Reproduced with permission from ref [183]. Copyright 2007 National Academy of Sciences.

2.3.4. DNA Base-Pair Interaction

Deoxyribonucleic acid (DNA) is a biomolecule made of two polynucleotide helical chains, which encodes genetic information into its four nucleobases, adenine (A), guanine (G), cytosine (C), and thymine (T).[185] To realize biological functions, molecular machinery needs to translate a sequence of the four nucleobases into personalized materials using the twenty-one proteinogenic α-amino acids. The assembly of DNA double-helical chains relies on the Watson-Crick base pair interactions, which are the preferential interactions between two base pairs, namely A with T and G with C, through hydrogen bonding (**Figure 22a**).[185,186] There are a few unique features that make DNA base pair interactions particularly useful in developing smart materials and structures. Firstly, the base pair interactions are highly specific so that one DNA strand only reacts strongly with its complementary strand.[187] Secondly, since the base pair recognition is based on hydrogen bonds, the dissociation constant of base pairs is dependent on temperature and ionic strength,[188-190] with the bond strength and population responsive to external stimuli.[191] To this end, a critical temperature is introduced where dissociation of hydrogen bonds occurs in DNA base pair to describe such thermoresponsive DNA recognition, which is between 40ºC to 80ºC for oligomers with ~20 bases.[192] While the high specificity allows the programmable design of functional materials, the temperature-dependent properties make DNA reconfigurable and responsive to surrounding changes, both of which are highly desirable in developing smart materials. Thirdly, the helical DNA chains are ideal templates for assembling chiral superstructures with tunable pitch and chirality (See **section 3.3.4.**).[193-195] These unique features have promoted extensive studies of the self-assembly of DNA into functional nanoscale structures. As a result, many concepts and principles for controlling the size, shape, and di-

mension of the soft materials have been developed for these materials composed of DNA (purely DNA-based structural materials, like DNA origami).[196-198] However, a unified set of self-assembly protocols and concepts is simultaneously applied to composite materials containing DNA components, such as the nanoparticle-DNA hybrid nanostructures.[20,193,199,200] These materials are expected to extend the application of DNA in colloidal self-assembly, representing an emerging approach to smart materials.

As a leading technique in colloidal self-assembly, colloidal crystals engineered with DNA have manifested the unique advantages of using DNA base pair interaction in controlling nanoparticle connection. In current literature, the first evidence is the astonishing structural diversity of colloidal crystals involving DNA as a crosslinker, which varies from the most common unary *fcc* crystals (**Figure 22b**) to emerging isostructural crystals with alkali-fullerene complex Cs_6C_{60} (**Figure 22c**).[201,202] In developing these high-quality crystals, three empirical strategies have been recognized for driving colloidal self-assembly, with differences in DNA number and length. In the first scheme, double-stranded DNA serving as crosslinker is modified on particle surface through anchor DNA; the linker DNA has a single, unpaired flexor base so that this adhesive end can connect to particles. In a simpler protocol, nanoparticles are modified with self-complementary, single-stranded DNA, whose sticky ends at the terminus assemble nanoparticles into superlattices. The third scheme modifies the nanoparticles using single-stranded DNA but most frequently without self-complementary capability. Colloidal connection requires an additional DNA crosslinker (**Figure 22d**).[203]

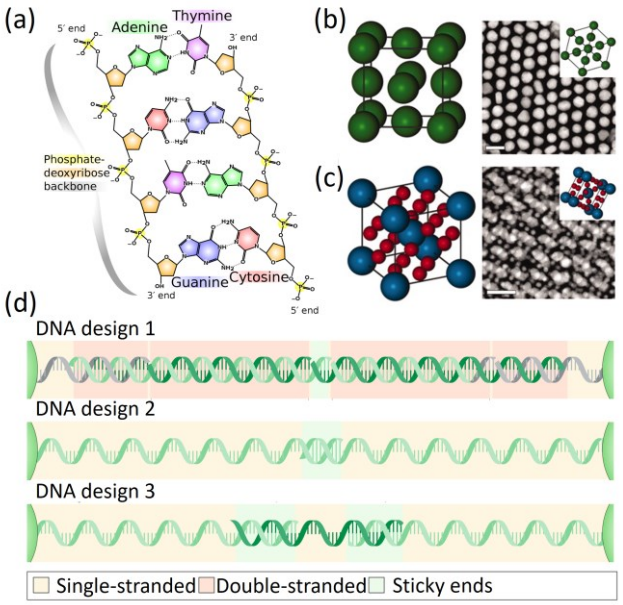

Figure 22. Colloidal self-assembly driven by DNA base pair interactions. (a) Scheme showing the two base-pair interactions between DNA chains (credit to Madeleine Price Ball). Scheme (left) and TEM images (right) of (b) fcc and (c) Cs_6C_{60} superlattices from Au nanoparticles. Scale bars: 50 nm. Reproduced with permission from ref [201]. Copyright 2011 The American Association for the Advancement of Science. (d) Three practical strategies for DNA-directed self-assembly. Reproduced with permission from ref [203]. Copyright 2019 Springer Nature.

Previous studies have recognized a few critical parameters in determining the self-assembly dynamics and kinetics, including DNA chain length, the sequence of the nucleobases, and the structural ratio of single-stranded DNA segments. A systematic study of the assembly phase and structures is beneficial to outline a set of concepts and predict the DNA-directed colloidal self-assembly. That is, nanoparticles with the same hydrodynamic radii tend to form as many numbers of DNA bonds as possible; this simple rule is first proposed by the complementary contact model and has been confirmed in the self-assembly of isotropic nanoparticles (**Figure 23a**).[201] For example, single-component systems with self-complementary DNA strands self-assemble into *fcc* supercrystals with close packing and maximum DNA bonds.[22,204-206] While in binary systems functionalized with two or more different but complementary DNA strands, body-centered cubic (*bcc*) crystals are the thermodynamic products because nanoparticles in a *bcc* superlattice possess the most DNA bonds with their complementary counterparts.[22,201,204,206] An advanced strategy further extends the structural diversity using building blocks with multiple sticky ends such that a programmable connection is possible between nanoparticles (**Figure 23b**). Specifically, a binary lattice can be further used as templates to assemble their building blocks into predictable positions if the particles have the suitable size to accommodate such intercalation.[201,207,208] In addition to the base pair interactions, there are other interactions between DNA chains, particularly the steric and electrostatic repulsion between the polyanionic phosphate backbones. These enthalpic and entropic forces react with the base pair attraction, change the interaction potential profile, and yield emerging lattices with crystal symmetry difficult to predict by the complementary contact model (**Figure 23c**). The role of repulsion in colloidal crystals engineered with DNA is quantitatively described in a self-assembly system coupled with DNA base pair attraction and excluded volume repulsion.[209] One direct result of introducing repulsion is to increase the interparticle separation, which derives the crystal symmetry from the predicted CsCl phase to the Th_3P_4 phase for a binary system. This simple change in interparticle separation implies subtle evolution in lattice symmetry, underpinning the important role of repulsion in producing superlattices with reduced symmetry.[208-211] These assembly protocols and concepts can also be applied to prepare superstructures from anisotropic building blocks (**Figures 23d, 23e**) or colloids with anisotropic surface properties (**Figure 23f**). Readers may refer to a recent critical review on colloidal crystals engineered with DNA for a complete library of lattice symmetry.[203]

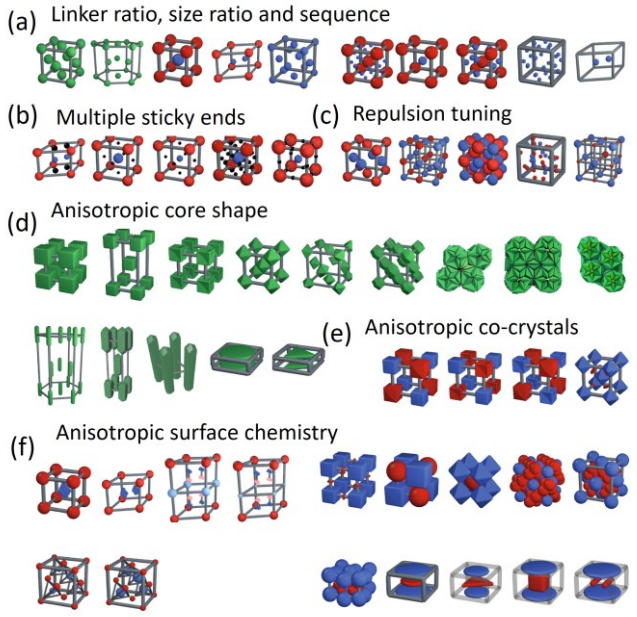

Figure 23. A summary of superlattices that have been achieved based on DNA-directed self-assembly. Reproduced with permission from ref [203]. Copyright 2019 Springer Nature.

2.3.5. Nonadditivity of Nanoscale Force

The interactions between nanoparticles are normally estimated based on many assumptions to approximate the ligand distribution and to simplify the calculation.[212] For example, the classic DLVO theory is being extensively cited to quantitatively describe the colloidal interactions, which uses distinct energy terms to compute individual force.[213] In its classic equation, the total interaction potential is the sum of electrostatic (V_{el}), vdW (V_{vdW}), and other contributing potentials (V').[214] In approaching each interaction potential, DLVO theory uses a few assumptions to deal with these dynamic forces acting on nanoparticles, which, however, sets limitations to its uses. Colloidal particles are simulated as regularly shaped objects with smooth surface curvature, homogeneous ligands on their surfaces, and negligibly small ligands and solvation layers (**Figure 24a**).[215] These assumptions provide a reasonably accurate description of assembly behaviors of large particles but are facing increasing challenges to deal with the self-assembly of nanoparticles smaller than ~50 nm. Such essential distinction mainly originates from the size difference of a few orders of magnitude between microparticles and nanoparticles. Thence, the high specific surface areas of nanoparticles facilitate the morphology control during nanocrystal synthesis, which is most frequently achieved by choosing proper capping ligands to limit crystal growth on specific facets and yield nanoparticles of diverse shapes (e.g., cube, polyhedron, rod, dumbbells, plate, and star).[216-218] While the nanocrystals with defined shapes are of both fundamental and practical importance to understand the unique properties associated with their nanometer sizes, the above facts pose additional challenges to predict their phase behavior during self-assembly because of the anisotropy in both ligand distribution and orientation (**Figure 24b**).[215,219] Even the as-claimed spherical nanocrystals are, in fact, highly faceted such that the spontaneous unevenness of their accurate shapes, ligands, and solvation layers need to be taken into consideration.[220] A particular example in this regard is the collective behaviors of capping ligands on nanocrystal surfaces, exhibiting multibody phenomena at the molecular level, such as the spontaneous bunching of organic molecules (**Figure 24c**).[221,222] One consequence of these events is the reconfigurable solvation layers in response to various physical parameters, like temperature, ionic strength, pH, solvent, and particle aggregation state,[223-225] calling for additional efforts to understand their dynamic properties. These considerations, in combination with the dynamic organic-inorganic interfaces of individual nanoparticles,[1] underpins the importance of developing new molecular dynamics to address such nonadditivity barriers spanning from molecular to nanometer scales.

At the current stage, a new set of analyzing tools has been proposed to solve the highly correlated forces and the interaction nonadditivity, such as atomistic simulations.[215] The discreteness of capping ligands and quantum effect caused by the reduced size and large specific surface area of nanocrystals make it difficult to reach a reasonable correlation with experiments by simply adding smooth potentials contributed from the individual force. Molecular simulation methods, instead, avoid such complexity and determine the net interparticle potential of mean force directly from the atomistic level. This strategy provides adequate accuracy in describing the self-assembly and phase behavior of nanoparticles that have been observed in current characterization techniques. It also allows considering additional underlying forces (e.g., hydrogen bonding, capillary force, hydrophobic interactions) in understanding the self-assembly of nanoparticles, which are difficult to be incorporated individually in the classic DLVO theory.[226-228] On the other hand, the fast advances in liquid cell electron microscopy and in situ spectroscopy have enabled accurate description and direct observation of nanoparticle structures and defects, fine structures of ligands, interaction potential of nanoparticles in response to external stimuli.[229-231] In some cases of anisotropic nanoparticles, the *in situ* liquid cell electron microscopy serves as an experimental approach to the interaction potential of nanoparticles mediated by their capping ligands. Through mapping the total number of nanorods and their distribution around reference Au nanorods (**Figure 24d**), it is possible to derive the site-dependent interaction potential.[232] This interesting result confirms the uneven distribution of ligands on anisotropic nanocrystals and explains some preferential bonding that has been observed in colloidal self-assembly. It also enables the selective functionalization of other ligands on the less capped particle surfaces, which is responsible for the achievements in site-selective crystal growth and specific arrangement in nanoparticle self-assembly (**Figure 24e**).[233,234] Therefore, this important technical progress is reliable to verify the results of molecular simulations, which together provide new opportunities in modulating the ligand interactions during colloidal self-assembly and further produce emerging superstructures. In fact, we are approaching an exciting era when the capability of computer simulation, the precision of nanoparticle synthesis, and the resolution of characterizing techniques join at the nanoscale, setting the stage ready for exploiting the self-organization of nanoparticles within the nonadditivity regime.

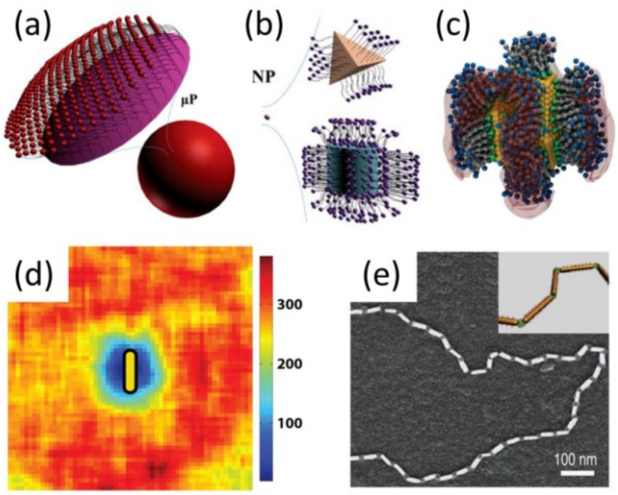

Figure 24. Nonadditivity of nanoparticle interactions. Scheme showing the ligand distribution on (a) microparticles and (b) nanoparticles. Reproduced with permission from ref [215]. Copyright 2015 The American Association for the Advancement of Science. (c) Snapshot of MD simulation of charged icosahedral nanoparticles. Reproduced with permission from ref [221]. Copyright 2011 American Chemical Society. (d) The color-coded counts of a total number of rods in the 2D plane of 5 nm by 5 nm pixels. Interacting rods become oriented with respect to each other before they assemble tip-to-tip. Reproduced with permission from ref [232]. Copyright 2015 American Chemical Society. (e) SEM image and scheme (inset) of the end-to-end self-assembly of gold nanorods. Reproduced with permission from ref [233]. Copyright 2015 Springer Nature.

2.4. Depletion Force

A depletion force is an attractive force between suspended large colloids in a dilute solution of depletants, which are normally small solutes (e.g., polymers, small nanoparticles, micelles, salts). It was first recognized by Bondy back in 1938 that rubber latex aggregated upon the addition of polymer depletants.[235] This interesting phenomenon was later explained by the established Asakura–Oosawa model. The attractive force to cause the latex aggregation is regarded as entropic force,[236] which becomes effective because of the tendency of a system to increase its entropy rather than a particular physical interaction between atoms. Consider the large colloids and the small depletants as dissimilarly sized hard spheres and imagine a hard-sphere potential between them. An excluded volume exists (highlighted in dashed lines in **Figure 25a**) surrounding the large colloids, which is unavailable to the center of small depletants and has the same thickness as the depletant radius. When two large colloids approach close enough with surface-to-surface distance smaller than the depletant diameter, the excluded volume starts to overlap, and thus the vicinity between large colloids is not accessible to depletants. This sequence of events will cause an osmotic pressure to the colloids and assemble them into dense clusters. From the entropy point of view, the volume overlap will offer more accessible free spaces to accommodate the depletants and increase their translational degree of freedom so that the system entropy will increase. The ensuing decrease in the Helmholtz free energy makes the system stable, yielding a thermodynamic equilibrium in the assembled state.

The depletion force and potential can be derived from the osmotic pressure using the model shown in the inset of **Figure 25b**. Notably, the depletants in this model are approximated as penetrable hard spheres; the osmotic pressure (P_0) on two large nanospheres can be calculated by the Van't Hoff law: $P_0=n_bk_BT$, where n_b is the bulk number density of the depletant particles. For two interacting nanoparticles with a given volume overlap, their depletion force is derived by integrating the osmotic pressure over the overlapping surface.[237]

$$F = -\pi n_b k_B T R_d^2 [1 - (\frac{r}{2R_d})^2] \quad (9)$$

In this equation, r is the center-to-center distance of the large colloids, and R_d is the sum of the large colloid radius (R) and the excluded volume thickness (σ/2). The depletion force potential can thus be obtained by integrating the force over the working distance.

$$V = -\frac{4}{3}\pi n_b k_B T R_d^3 [1 - \frac{3r}{4R_d} + \frac{1}{16}(\frac{r}{R_d})^3] \quad (10)$$

The force and potential decay gradually with the interparticle separation (r) in the range of [2R, $2R_d$] and vanish when the separation is larger than $2R_d$ (**Figure 25b**). The depletion force equation and its derivation are different between different large colloidal particles and types of depletants (e.g., penetrable hard spheres, ideal polymers, colloidal hard spheres, and thin colloidal disks).[237] It is therefore important to use the right equation for an accurate description of the force. In experiments, diverse superstructures have been observed by regulating the depletion in colloidal dispersions, including face-to-face stacking of nanoplates,[238] side-on attachment of nanorods,[109] block-copolymer micelles,[239] and chains of cylindrical particles and plates.[240,241] A recent study describes the self-assembly of semiconductor nanorods into vertical bundles (**Figure 25c**), multilayer stacking, and smectic monolayers depending on the relative magnitude of depletion forces between nanorods and between nanorods and a substrate.[242]

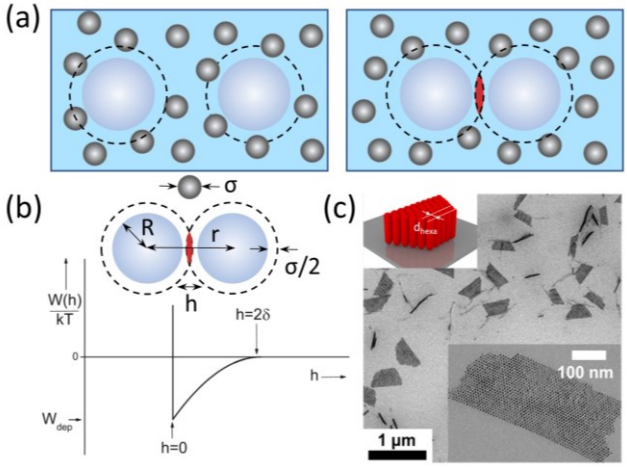

Figure 25. Depletion force between colloidal particles. (a) Schematic illustration of the depletion between two nanospheres. (b) Depletion interaction potential between nanospheres as illustrated in the scheme. Reproduced with permission from ref [237]. Copyright 2011 Springer Nature. (c) TEM images and scheme of the bundle

of standing semiconductor nanorods on solid substrates. Reproduced with permission from ref [242]. Copyright 2019 American Chemical Society.

2.5. Gravity Force

Gravity is a universal force for particles at all scales. Its effect is, however, relatively weak compared with other driven forces (e.g., capillary force). But for large nanoparticles, it is still a plausible driving force that causes them to sediment from colloidal dispersions. This common physical process can be used to assemble colloidal crystals if it can be carefully controlled in experiments. For example, uniform Ag polyhedral nanocrystals self-assemble into densely packed colloidal crystals driven by gravity.[30] The gravity of 300-nm Ag octahedra is equivalent to 0.23 k_BT per micrometer, and steadily seating a dilute solution of Ag nanoparticles causes them to self-assemble into colloidal crystals. The resulting crystals exhibit both translational and orientational orders in a large length scale (**Figure 26**). Specifically, Ag nanocubes self-assemble into simple cubic crystals, such that the densest lattice packing can propagate up to 10 μm (**Figure 26a**). The dense tessellation of highly faceted nanocrystals is also observed in truncated octahedra and octahedra but with different crystal symmetries. In the same precipitation condition, Ag truncated octahedra and octahedra nanocrystals self-assemble into space-filling Kelvin structure (body-centered cubic lattice) and perfect Minkowski lattice (**Figure 26b**), respectively. The deterministic effect of gravity can be well understood in Monte Carlo simulation by mimicking the experimental process. At the initial stage, the nanocrystals in a low-density dispersion begin to sediment, causing a density gradient along the vertical direction. The resulting pressure that the nanocrystals at the bottom are experiencing is sufficient to drive the spontaneous crystallization into colloidal crystals. This consideration also explains why the self-assembly normally occurs within at least a few hours. The slow precipitation of nanocrystals is purely driven by gravity, which has high resistance in aqueous dispersions. However, this slow process allows bottom particles to rearrange their position and orientation such that a thermodynamic equilibrium state can be reached before the dense fluid further condenses into solid aggregates. Because of the weak connection between precipitated nanocrystals, the stability of such superlattices needs to be addressed before their further advances to practical applications.

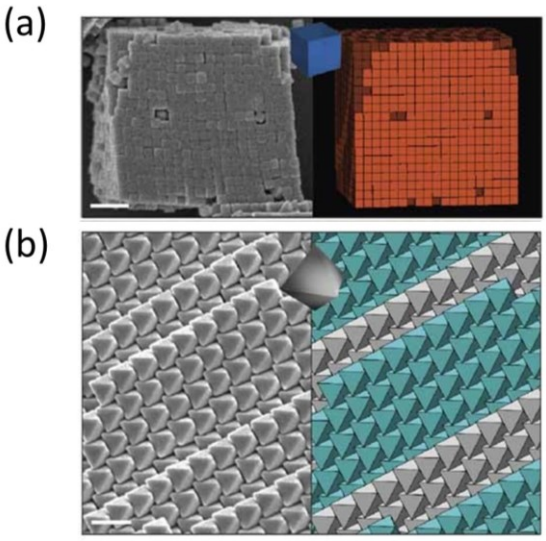

Figure 26. Self-assembly of uniform polyhedral silver nanocrystals driven by gravity force. SEM images (left) and corresponding diagrams (right) of the dense packing of (a) Ag nanocube and (b) octahedra. Scale bar: 500 nm. Reproduced with permission from ref [30]. Copyright 2012 Springer Nature.

2.6. Capillary Force

The cohesive forces between molecules of the same type cause the surface of a liquid to contract to a minimum possible surface area, which is generally called surface tension and explains copious interesting phenomena in daily life. Molecules at the liquid surface experience higher cohesive forces with inner liquid molecules than the adhesive forces with molecules in the gas phase so that the liquid contracts into droplet shapes to minimize their surface energy. In fact, the competition between the cohesive forces among liquid molecules and the adhesive forces between liquid-gas and liquid-solid plays an important role in manipulating diverse interfacial effects and transportations in both microscopic and macroscopic length scales. In bulk materials, this competing interaction can be readily characterized by the contact angle where a liquid-vapor interface meets a bulk solid surface.[243] In capillary tubes, interestingly, this competing interaction causes the liquid to be raised or to be suppressed depending on its wettability to the solid surface; the driven force for such capillary action is called capillary force, which is determined by the cohesive forces among liquid molecules and their adhesive forces with the solid and gas molecules. Similar phenomena have also been observed in diverse narrow slits around the meniscus between colloidal particles in considerable proximity, which normally occurs in drying a dense colloidal dispersion or in floating colloids at a liquid-air interface. For lyophilic colloids, their adhesive attraction with water molecules is stronger than the cohesive forces among water molecules themselves, causing an effective capillary force that drives the self-assembly of colloidal particles into close packing.

The capillary force-driven self-assembly occurs among colloids well-dispersed in a water-air interface or during various drying processes. Because the water-air interface serves as a soft template to confine and regulate the colloidal self-assembly, this

method will be introduced as a template-assisted colloidal assembly in **section 2.7.2**. In the second scenario, nanoparticles self-assemble into colloidal crystal arrays featuring the so-called close packing. In fact, this method has been extensively used in assembling monodisperse nanospheres into opals and in creating inverse opals, which represent a well-established approach to smart nanostructures in response to an extended set of stimuli from temperature changes to external fields. In a typical preparation scheme, colloidal dispersion is first deposited on a proper solid surface to form a thin liquid film or small droplets. Upon solvent evaporation, colloidal particles are pulled together as the concentration increases to a critical volume fraction where the capillary force becomes effective and drives the self-assembly of the dense fluid into close-packed photonic films (**Figure 27a**).[244] Treating colloidal building blocks as reactive atoms, it is possible to understand the dynamic and complex drying assembly within the classic nucleation-growth regime, which involves a two-step physical event. In the nucleation step, the attractive capillary force, mediated by the liquid meniscus between adjacent colloidal particles at the drying front, causes colloids to nucleate into small cluster oligomers, which will initiate colloidal crystallization. In the growth step, solvent evaporation from the solvent front generates a convective colloid flux from a bulk suspension to the liquid film edge so that evenly crystal growth occurs at the dynamic water-solid-air interfaces.

During experimental implementation, depositing colloidal dispersions on solid substrates is important to prepare stimuli-responsive photonic films with desirable sizes, shapes, and patterns. From the application point of view, there are a few prerequisites for a good deposition method, such as large-scale production, uniform film deposition, controllable solvent evaporation, and the ability to pattern film formation. To this end, several standard procedures have been established or simply borrowed from conventional coating methods to transfer bulk colloidal dispersions to solid substrates, including spin coating,[245-248] spray coating,[249-251] doctor blade coating,[252-255] dip coating (or vertical deposition),[256-259] inkjet printing,[244,260-265] and capillary bridge technique.[266] Spin coating, as a conventional coating method in microfabrication of functional films (e.g., photoresist layers in photolithography), has been extensively studied in depositing polymeric and colloidal materials on substrates.[267-269] It therefore allows a flexible choice of preparatory solutions for wafer-scale film processing, during which the film thickness can be readily tuned from monolayer to hundreds of layers by controlling spinning conditions.[270] Its compatibility with conventional micro-/nanofabrication techniques also facilitates further film processing to diverse functional materials and optical devices in data storage, sensing, and anticounterfeiting.[271] Spray coating produces large-scale colloidal crystals within a few seconds regardless of the particle size, shape, component, and surface property.[249,272-274] Both the spray coating and doctor blade coating are capable of roll-to-roll production of photonic films of the colloidal dispersion, and depositing substrate can be engineered in a continuous manner. One apparent difference between these two techniques is using a blade in the latter, which involves shear forces to control the film thickness and colloidal order.[252,254,275] Dip coating or vertical deposition method has a significantly different film formation process, in which colloids self-assemble on a vertical substrate in convective flows. It was firstly developed in the Nagayama group to fabricate 2D colloidal crystals and was later extended to prepare 3D colloidal films by other researchers.[276-278] In a typical assembly process, a solid substrate is vertically dipped into a colloidal dispersion, and the capillary force at the meniscus drives the self-assembly of colloidal particles on the substrate.[279] Notably, during the drying process, simultaneous sedimentation is possible for large colloids, which is highly undesirable because it changes the colloid concentration, deposition kinetics, and film thickness. Previous studies have reached an empirical agreement that this method is operational to colloids smaller than 400 nm in diameter. One way to break such a size limit is to create controllable convective flow in colloidal dispersion to prevent particle sedimentation, making this method feasible to sub-micrometer particles.[280] Compared with the extremely fast drying process in liquid films or droplets, dip coating occurs slowly in a bulk solution, allowing precise control over the assembly kinetics and deposition uniformity, and enabling large-scale production of high-quality colloidal crystals.[281] The inkjet printing is unique in producing patterned photonic crystals because of its easy control over the deposition position using commercial printers, which combines colloidal self-assembly with direct printing.[264,282,283] After its first introduction in assembling latex spheres using single-orifice inkjet printing,[260,262,263,284] its potentials have been extensively exploited with a specific focus on creating patterned photonic crystals.[71] Song et al. developed a colloidal ink by mixing latex colloidal particles with a high-boiling-point solvent (ethylene glycol), which is printed on an optimized substrate for the effective spreading of the colloidal ink.[244] In addition to ink, the quality of the colloidal crystals is also affected by the wettability of the printing substrates and evaporation kinetics. In an optimal condition, inkjet printing is advantageous for customizable photonic patterns, adjustable ink components, continuous crystal production, and recyclable printing setups.[285-287]

These fabrication methods produce colloidal crystals with single- or polycrystalline domains, normally with their (111) planes parallel to crystal surfaces (**Figure 27b**). It is possible to fabricate colloidal crystals with different exposed crystal planes using templates with unique surface features to control the nucleation. For example, assembling polystyrene beads on 2D regular arrays of square pyramidal pits etched into Si wafers yields colloidal crystals with their (100) planes exposed on the film surfaces, which will be discussed in detail in **section 2.7.1**.[288] Another characteristic of colloidal assemblies driven by capillary forces is their size-dependent optical diffraction and structural colors due to the periodicity of 3D lattices (**Figure 27c**).[244] Therefore, the particle size and uniformity should be carefully chosen before assembly for desirable structural colors. Colloidal assemblies driven by capillary force are associated with crack defects because of significant volume shrinkage and tensile stress during solvent evaporation, which unfortunately deteriorates the color uniformity and intensity. A few advanced strategies have been developed to overcome this challenge and prepare crack-free colloidal crystals, focusing on how to eliminate uneven volume shrinkage during the drying process. Substituting "hard" building blocks with "soft" microgels or polymer colloids is one possible way considering that these deformable particles interact with each other through soft interaction potentials and can dissipate tensile stress over a long distance.[289,290] Using polymeric building blocks also facilitates the

introduction of reactive groups on particle surfaces, which joints neighboring colloids with covalent bonds. Such a soft connection can counteract the inner tensile stress and stabilize the colloidal crystals.[291-294] Another practical strategy is to form a hard connection between assembled colloids to strengthen the crystal mechanical properties.[295,296] In this regard, adding sol-gel precursor is a reliable method. Upon hydrolysis, a 3D hard matrix of SiO_2 forms to fix the colloid position in the crystal lattice. For example, crack-free colloidal crystals of SiO_2 and PS nanospheres have been reported by introducing SiO_2 precursors to assembly solutions.[281,297,298]

Manipulating the capillary bridge formed by confining colloidal dispersions between templates is an emerging technique to assemble colloids into patterned superstructures.[266] This general method is realized by sandwiching colloidal dispersions between a target substrate and a micropillar-structured template (**Figure 27d**). During the dewetting process, the colloidal dispersion will be trapped in the confined spaces between the bottom micropillars and the top substrates, which produces superstructures with identical shape and symmetry as the pre-designed template after solvent evaporation (**Figure 27e**). For example, self-assembly of $BaTiO_3$ nanocubes using a linear array yields long-stripe superstructures, with the nanocubes arranged into simple cubic crystals driven by the capillary force during drying.[266] In another study, solvent viscosity is recognized as an important property to tune the assembled superstructures, which determines particle rearrangement in the confined spaces.[299] While solvents of high viscosity limit particle rearrangement during the self-assembly, leading to zigzag colloidal chains, low-viscosity solvents allows particles to rearrange into linear or zipper chains if proper templates are used. It is also possible to assemble particles of different sizes into binary superstructures with size-sorted patterns by a similar templated dewetting approach.[300,301] For example, co-assembly of polystyrene nanoparticles of two different sizes produces asymmetric 1D binary superstructures (**Figure 27f**).[300]

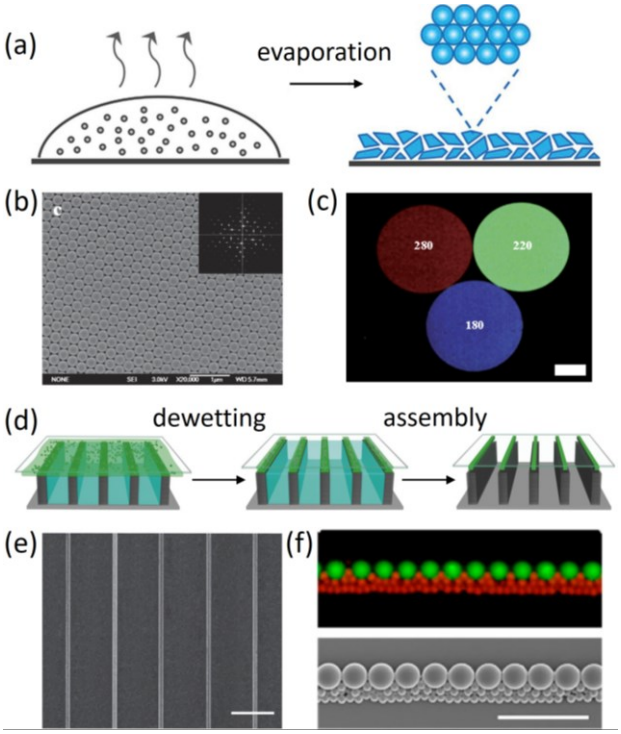

Figure 27. Self-assembly of colloidal crystal array driven by capillary force. (a) Schematic illustration of colloidal crystal formation upon solvent evaporation. Reproduced with permission from ref [251]. Copyright 2021 John Wiley and Sons. (b) SEM image of the colloidal crystal array made of latex spheres. Scale bar: 1 μm. (c) The structural colors of the colloidal crystal array on nanosphere size. Scale bar: 1 cm. Reproduced with permission from ref [244]. Copyright 2009 Royal Society of Chemistry. (d) Schematic illustration of the formation of capillary bridge and self-assembly of the patterned superstructures in the confined spaces. (e) SEM image of superstructure array from self-assembly of $BaTiO_3$ nanocubes. Scale bar: 5 μm. Reproduced with permission from ref [266]. Copyright 2017 John Wiley and Sons. (f) Bottom-view confocal micrograph (upper panel) and top-view SEM image (bottom panel) showing the asymmetric 1D binary superstructures assembled from 3.00-μm (green) and 0.34-μm (red) polystyrene particles. Scale bar: 10 μm. Reproduced with permission from ref [300]. Copyright 2017 American Chemical Society.

2.7. Template-assisted Colloidal Self-assembly

In contrast to colloidal self-assembly in bulk solutions, template-assisted assembly confines colloidal particles in pre-designed spaces or interfaces so that their self-assembly occurs locally. Based on their deformability, commonly used templates can be divided into hard and soft templates. The hard templates are solid substrates with pre-designed surface cavities, defined sizes, and shapes, most frequently made by lithography. In most circumstances, the colloidal assemblies will adopt the specific shapes and sizes of the templates. Some hard templates may serve as microscopic containers to confine the assembly into uniform and regular superstructures. However, in soft templates, their volumes, sizes, or interfaces where the self-assembly occurs change across the assembly process, during which colloidal particles can adjust their positions and orientations to minimize the system energy. In both cases, templates are used

to assemble colloidal particles into nano-, micro-sized superstructures or thin films with controllable shapes, sizes, and crystal orientation. These templating techniques produce several emerging superstructures or lattices that are otherwise not attainable, such as regular homo- or hetero-clusters, uniform plasmonic hybrid oligomers, 2D complex colloidal tessellations, and colloidal crystals with high-energy facets.

2.7.1. Hard Templates

Self-assembly involving hard templates most often occurs in a dewetting process, in which colloidal particles are trapped into periodic templates on 2D arrays and organize locally into colloidal aggregates with well-defined sizes, shapes, and structures.[302] Typical 2D array templates are made by lithography techniques through anisotropic chemical etching in either photoresist films or silicon wafer surfaces. During the following dewetting process, the designated 2D templates provide confined spaces and limit the assembly from some directions.[303] In patterning single particles, for example, only when colloidal particles fit the hole size may they be trapped into the individual template at the meniscus of the dewetting front. Being first demonstrated in 2001, the early effort of this technique was focused on assembling monodisperse colloidal particles, both silica and polymer nanospheres, into uniform clusters with different sizes, shapes, and symmetries. With cylindrical holes in a 2D square array as a simple template, uniform colloidal clusters were assembled inside the holes (**Figure 28a**). Tuning the composing particle number is possible by simply changing the particle size. Sequentially decreasing particle size from a value close to the hole diameter leads to the formation of colloidal monomers, dimers, trimers, and complex polygonal clusters on the same template.[304] A representative example of hexagonal clusters in the left panel of **Figure 28b** demonstrates the high cluster uniformity and the precise position of colloids within each cluster.[305] During the solvent evaporation, the nanospheres confined in each hole could adjust their positions to allow a size-maximized packing, whose symmetry is mainly determined by the geometric confinement. This templating principle is readily extended to assembling 3D clusters comprising multilayered units of colloids if the hole depth is reasonably larger than the colloidal diameter.[304] Introducing templates of other shapes in place of cylinder holes yields colloidal clusters with copious dimensions and symmetries. In this regard, a few compelling structures include linear or zigzag chains (right panel of **Figure 28b**),[304] helical chains with well-controlled handedness.[306] To create hetero-clusters with asymmetric shapes, a template containing a 2D array of the first component is used in another step of self-assembly to add a different colloid into the remaining spaces of each template.[307] Another interesting effect of templates is that they can direct colloidal assembly to begin at particular facets. For example, templating assembly of monodisperse colloids against a regular array of square pyramidal pits produces (100)-oriented *fcc* crystals.[288,308] Because the template-assisted self-assembly is driven by capillary force, it is possible to extend this strategy to a number of colloidal particles, leading to plentiful smart superstructures that are valuable to new applications.[139,309]

With twenty years' development, a few advanced techniques have being innovated in template-assisted self-assembly. While the use of capillary force is beneficial for the wide application of this method, its low selectivity limits the degree of precision within which the secondary structures can achieve. To this end, a derived technique introduces the specific interaction between DNA, in place of capillary force, as the driving force to assemble plasmonic nanoparticles inside a hard template.[310] **Figure 28c** illustrates a 2D array of cylindrical holes on the Au surface, whose exposed areas at the cylinder bottom are modified with DNA. The self-assembly of plasmonic nanoparticles in the confined spaces occurs in a layer-by-layer manner by designing each layer of particles to have a terminal DNA sequence complementary to the previous layer. The DNA-functionalized template is directly submerged in a particle solution to enable specific recognition of DNA strands. With plasmonic nanoparticles with different shapes and sizes, it is possible to assemble plasmonic superstructures with controllable configurations and particle numbers. Two exquisite architectures are shown in **Figure 28d**, with three-layer superstructures made of different plasmonic particles. The erect superstructures imply the vertical deposition of one particle in the cylindrical holes, as limited by the templates. Albeit driven by a different force, the high-yield production of these plasmonic superstructures still needs to fulfill the size-matching role, an empirical practice that delineates the proper particle size range for a given template. However, in a recent study, this strict requirement is found to be not necessary, thus extending the template-assisted self-assembly to a situation where the colloidal particles can be much smaller than the templates.[311] This strategy uses a similar 2D array of cylinder holes but with a large size (**Figure 28e**). One significant benefit of this new advance is the high flexibility in choosing building blocks, making it a universal assembly strategy at all scales. Instead of individual colloids, this strategy confines a constant volume of solution that contains nanoparticles, molecules, or mixtures. The following solvent evaporation drives the assembly of the solute in each template into colloidal or molecular crystals. Accompanied by significant volume shrinkage, this approach yields clusters or crystals with their shape independent of the template (left panel in **Figure 28f**). In practice, various molecules and particles have been assembled with one template, including salts, polymers, cells, nanostructures (e.g., Au nanospheres, polydopamine nanoparticles, FeOOH nanorods, and Fe_2O_3 nanodiscs in **Figure 28f**).

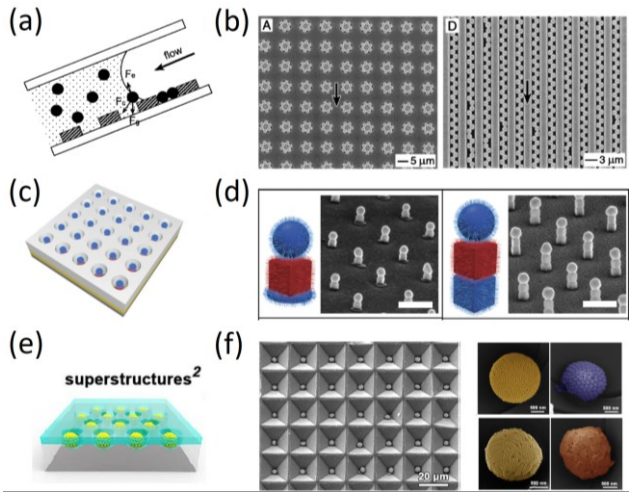

Figure 28. Hard template-assisted colloidal self-assembly. (a) Schematic illustration of the hard template that was used to assemble colloidal particles into defined aggregates. (b) SEM images of the assembled colloidal aggregates (left) and zigzag chains (right) of polystyrene beads. Reproduced with permission from ref [305]. Copyright 2001 American Chemical Society. (c) Schematic illustration of the hard template that was used to assemble Au nanoparticles into defined chains. (d) SEM images of the assembled colloidal chains. Scale bars: 300 nm. Reproduced with permission from ref [310]. Copyright 2018 The American Association for the Advancement of Science. (e) Schematic illustration of the hard template that was used to assemble silica colloidal particles into spherical clusters. (f) SEM images of the assembled colloidal clusters. The building blocks are Au nanospheres (top left), polydopamine nanoparticles (top right), FeOOH nanorods (bottom left), and Fe_2O_3 nanodiscs (bottom right). Scale bars in the right panels: 500 nm. Reproduced with permission from ref [311]. Copyright 2020 Elsevier.

2.7.2. Soft Templates

Soft templates allow colloids to adjust their positional and orientational orders in confined spaces and generally lead to forming large clusters or 2D colloidal crystals. One merit associated with this structural feature is the active response of colloidal assemblies under external stimuli, making them promising and attractive in developing smart materials. The Langmuir-Blodgett technique using the liquid-air interface as a soft template is a famous example.[312] Upon its introduction, this technique was a powerful tool to assemble amphiphilic compounds at the air-water interface into molecular monolayers.[313] Its later extension to colloidal particles has attracted lots of attention, particularly in producing 2D colloidal crystals. In 1992, the behavior of hydrophobic colloids at the air/water interface and the energy to transfer them upward from the interface were quantitatively described, setting the stage ready for fully exploiting new possibilities.[314] It is the theoretical basis behind many interesting interfacial phenomena and suggests a few practical routes to manipulate the 2D superstructures. Shortly, a few careful studies pointed out that the deliberate surface functionalization on hydrophilic particles was not always necessary to form a stable colloidal film.[315] Specifically, silica particles prepared in ethanol with diameters between 180 and 360 nm do not require the surface modification largely because the CH_2 units of ethanol contribute to the surface hydrophobicity. Continuous production of high-quality photonic crystals is possible in a modern technique, which simply uses a roll-to-roll device to transfer the photonic layer (**Figure 29a**).[316] This procedure yields hexagonal-packed 2D photonic crystals with monodisperse silica nanospheres as building blocks (**Figure 29b**). Such close packing is the most common configuration among the superstructures that have been developed in the Langmuir-Blodgett assembly. While the interface confines the assembly within the 2D plane, the soft surface allows colloids to move under a driving force to adopt the close packing. Compared with self-assembly occurring on a hard surface, the free movement of colloids within the soft interface is important to anneal out any defects, leading to the formation of the most energy-favorable superstructures. The significance of this unique property is further manifested by a few emerging superlattices from the interface-confined self-assembly.[96,317] For example, small magnetite nanocubes self-assembled into nanobelts, single- or double-stranded helices at a liquid interface under a uniform magnetic field.[96] These attractive superstructures were attributed to the delicate balance between the dipole-dipole interactions and Zeeman coupling, during which the nanocubes can easily adjust their orientational and translational orders to minimize the global energy without being interfered with by undesirable forces from hard templates. In addition, the soft interface can afford any chape changes of the complex superstructures so that these elegant structures are measurable in carefully designed assembly processes. Later, this strategy was extended to preparing tunable porous Au nanoallotropes from binary nanoparticle superlattices assembled at the same interface.[317] The observation of copious binary superlattices, with some of them being first prepared, underpins the important role of soft templates in colloidal self-assembly, which is not attainable through self-assembly in bulk solutions or on hard templates. The easy transfer of the superstructures from the soft interfaces is also advantageous to assemble complicated superstructures by a self-templating strategy.[318] This modified Langmuir-Blodgett technique employs a water-oil interface to confine the self-assembly of microgels into a common hexagonal lattice (**Figure 29c**), which is carefully transferred to a solid substrate. Simply depositing another monolayer on the same substrate interestingly elicits many 2D complex lattices that cannot be produced in a single assembly step, with interlocking-S structures and hexagonal superlattices shown in the left and right panels of **Figure 29d**, respectively. This complicated phase transition is due to the reconfiguration of the second layer mediated by the fixed monolayer template through repulsive short-range interactions. This self-templating strategy demonstrates the likelihood that colloidal particles can re-configure inside the interface to reach the thermodynamic equilibrium that is determined by both the driving force and the surface property of a template.

Colloidal templates are another widely used soft template, which can be produced by emulsification via microfluidics or simply mechanical stirring.[319] Due to the flexibility in producing monodisperse microdroplets, microfluidics have been extensively used to assemble mono-component, multi-component, and Janus superstructures. The size, component, surface property, and structures of the colloidal templates can be readily controlled by engineering the emulsification, adjusting flow rate, and choosing functional materials. A typical setup to produce core/shell colloidal templates is illustrated in **Figure 29e**.[320] This double emulsion system produces highly uniform micro-sized templates, where the self-assembly of nanospheres happens. Its versability is manifested by facial production of multi-core emulsions if the flow rate of the core and shell stream reaches optimal values (**Figure 29f**). One exciting advance in microfluidics is the great diversity in engineering the capillary chips, which have been created for producing simple, core/shell, multi-core, multi-component, Janus, spindle-knotted particles or fibers.[321,322] Readers may refer to a comprehensive review for understanding up-to-date research activities in engineering droplet microfluidics.[323]

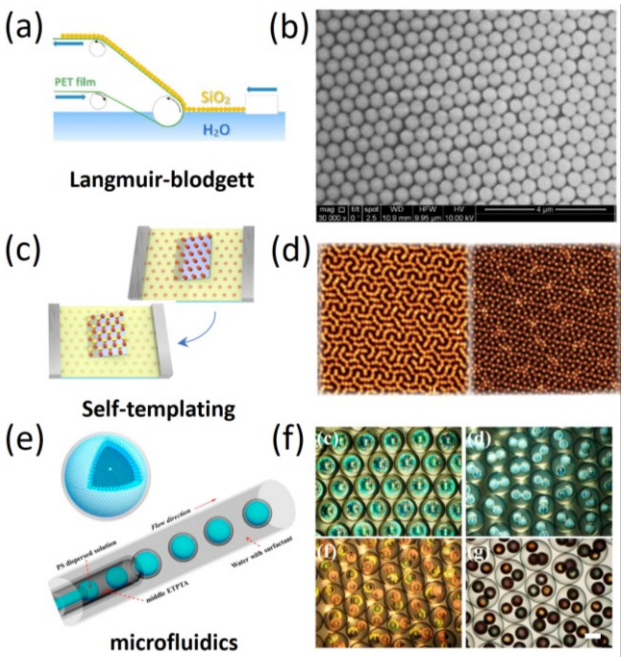

Figure 29. Soft template-assisted colloidal self-assembly. (a) Schematic illustration of the roll-to-roll Langmuir–Blodgett technique. (b) SEM image of the assembled silica colloidal crystal arrays. Scale bar: 4 μm. Reproduced with permission from ref [316]. Copyright 2016 American Chemical Society. (c) Schematic illustration of the self-templating assembly of soft microparticles. (d) Atomic force microscopy (AFM) image of the experimental superstructures assembled from monodisperse poly(N-isopropylacrylamide) (PNIPAM) microgels. Reproduced with permission from ref [318]. Copyright 2020 Springer Nature. (e) Schematic illustration of colloidal self-assembly using microfluidic emulsification process. (f) Microscope photographs of polystyrene photonic bubbles with different numbers of blue cores (top) and with two (bottom left) and three (bottom right) different cores. Scale bar: 300 μm. Reproduced with permission from ref [320]. Copyright 2015 American Chemical Society.

2.8. Self-assembly of Janus Particles

Janus colloidal particles are attractive building blocks for assembling complex superstructures.[324-326] These emerging superlattices and networks at multiscale are expected to provide a set of systems whose structures and properties can respond to external stimuli if designed properly. Their contributions to developing smart materials are of both fundamental and practical importance. Their unique structures are expected to offer new phase transition under external stimuli, which is responsible for emerging materials and properties. The precise control over the binding direction and particle valence is an ideal measurable system to understand the kinetics and dynamics of chemical reactions by mimicking the reactions in colloidal systems under properly designed stimuli. In 1991, the Nobel Laureate P. G. de Gennes brought this unique class of particles to the public attention in his Nobel lecture entitled "Soft Matter".[327] Just like the meaning of the name, Janus colloidal particles are famous for their customizable surfaces having distinct chemical and physical properties.[328,329] The past two decades have witnessed great advances in the synthesis of diverse Janus particles and their assembly into superstructures at different scales. A comprehensive review by Walther and Muller summarized progress in synthesis, assembly, and emerging applications of Janus particles in the first decade of the 21st century.[330] While chemists have developed various synthetic approaches to Janus particles of different shapes, the binary or multiple compartmentalizations of physicochemical properties may occur at different scales within individual colloids.[331] It can occur through the solid colloidal cores with heterogeneous interfaces, through surface capping layers with different functional patches, or both with multilevel Janus structures. One compelling feature of these heterogeneous patches or material domains is their highly directed interactions between individual Janus colloids, which is of profound fundamental and practical interest in colloidal self-assembly. As summarized in **Figure 30**, there are a few key parameters that determine the dimension, size, symmetry, and shape of the superstructures from Janus particles, including both structural characteristics (e.g., patch size, number, and shape) and component aspects (including surface capping ligands, interaction motif, chemical components of cores, etc.).

Spherical Janus particles have been most extensively exploited largely because of their relatively easy synthesis and selective surface functionalization, representing an ideal and open platform to address the fundamental aspects of Janus particle self-assembly. Tuning the patch size and number is the first step to study the assembly phase behavior. A close investigation performed by Pine et al. recognized that the interaction strength of the attractive patch and the Janus balance, defined as the fractional area of the attractive patch, played an important role in determining the equilibrium states of superstructures. Although the Janus balance is related to the structural details of the assemblies, it resembles the hydrophilic-lipophilic balance (HLB) that determines the amphiphilicity of macromolecules.[332] To prepare Janus particles with precisely and widely tunable Janus balance, a cosolvent emulsion droplet was introduced, and varying monomer amounts yielded Janus particles with different surface properties. These colloids were used as model systems after selective DNA surface modification. Colloids with small patch ratios are self-assembled into colloidal oligomers because such a small attractive domain only allows the attachment of a few particles. Simply increasing the pitch ratio diversifies the observed superstructures from low-dimension oligomers to high-dimension colloidal chains, rings, and bilayers (**Figure 30a**). These results imply that it is possible to create colloidal molecules with pre-designed valence and specific bonding directions if one can accurately control the patch of Janus particles. To this end, a DNA patch with programmable coordination numbers is developed based on the bioconjugation technique.[333] The specific binding between DNA strands leads to supracolloidal molecules with intrinsic hybridized atomic orbitals depending on patch numbers (**Figure 30b**). In addition, the patch shape also plays an important role in determining the superstructure symmetry. Using a cluster encapsulation method,[334] a recent study could produce monodisperse biphasic triblock particles, in which the patch size and shape can be simultaneously tuned to achieve regioselective bonding.[335] Adding a proper surfactant drives the self-assembly of the Janus ellipsoids into emerging superstructures through depletion forces, with 1D cross-chains, ladder chains, and tilted ladder chains being observed for micelle depletant. Interestingly, modifying the middle patch from a concave shape to a convex shape with a simultaneous change of aspect ratio leads to 2D colloidal poly-

morphs, whose representative structures are presented in **Figure 30c**. These herringbone (left panels) and brick-wall (right panels) monolayers co-exist in colloidal dispersions, with the latter dominating the observed phases. These unique structures underpin the critical roles of pitch shape in determining the final superstructures; using Janus particles of low-symmetry patches in place of spherical ones as building blocks produces new spatial configurations through regioselective depletion.

Through surface and colloidal chemistry, it is possible to carefully tune the physicochemical properties of Janus particles, which can self-assemble into superstructures unique to their intrinsic driving forces. Several well-established driving forces in this regard include specific binding between biological molecules, electrostatic interaction, hydrophobic attraction, depletion force, hydrodynamic force, and magnetic force.[331,336-338] Selective surface modification of self-complementary DNA strands has been used as a delicate approach to emerging colloidal crystals, with diamond and clathrate crystals being the two most attractive examples.[339,340] A few additional advantages include high binding efficiency, superior specificity, and the capability of responding to external stimuli (e.g., temperature), allowing both directional interactions and crystal reconfiguration.[341] In several functionalization techniques, bioconjugation (e.g., biotin-avidin) or chemical addition reaction are typical.[156,342] For example, tetrahedral clusters of four polystyrene colloids bound to a center DNA patch are synthesized through selectively functionalizing the center domain of colloidal tetramers by azide-alkyne cycloaddition.[340] The self-complementary DNA strands are carefully designed so that their radial extent is retracted from the plane formed by the spherical lobes. This structure allows DNA to bind only if the lobes on different tetramers are orientated in a staggered conformation (inset in **Figure 30d**), avoiding other isomers. If occurring on a large scale, such a unique arrangement leads to perfect diamond colloidal crystals (**Figure 30d**), which have been theoretically proposed to generate complete photonic bandgaps for two decades.[343,344] Hydrophobic attraction is another broadly used driving force in Janus particle assembly. While it is less specific than DNA binding, it is still possible to produce complex lattices by cooperating with other forces. Electrostatic repulsion, for example, is an ideal candidate, which occurs between the hydrophilic domains and helps regulate the Janus particle assembly into ordered structures. Triblock Janus spheres with hydrophobic poles and hydrophilic equator are a simple model system to fulfill these requirements.[345] Under the presence of salt to screen the electrostatic repulsion, the Janus particles self-assemble into kagome structure, an open 2D lattice presented in **Figure 30e**. The weak repulsion between the middle patches and hydrophobic attraction between the pole patches are responsible for such a unique network. The intricate control of the two forces is likely the main reason why a 2D lattice is favored in place of 3D superstructures, which again demonstrates the critical roles of driving forces in assembling Janus particles. A similar dependence is also observed in Janus particles with heterogeneous solid cores instead of a "soft" surface patch. Introducing functional domains in Janus particles also allows remote control of their self-assembly, providing possible ways to manipulating the collective behavior of the assemblies. A few promising driving stimuli include magnetic fields[346] and electric fields.[347] To prepare such Janus particles, a seeded polymerization was introduced, during which polymer domains are partially coated on various colloidal seeds.[348] If magnetic nanocubes are used, this process yield Janus spheres with well-defined magnetic patches (red domains in **Figure 30f**).[349] In colloidal dispersions, the strong magnetic interactions between nanocubes tend to assemble in a close proximity while the polymer domains limits the further growth of the assemblies along other directions. This sequence of events creates colloidal oligomers depending on particle sizes or chains if a magnetic field is applied (**Figure 30f**). The directional magnetic interactions between magnetic dipoles or external fields with dipoles are the main reason for such interesting phase behaviors.

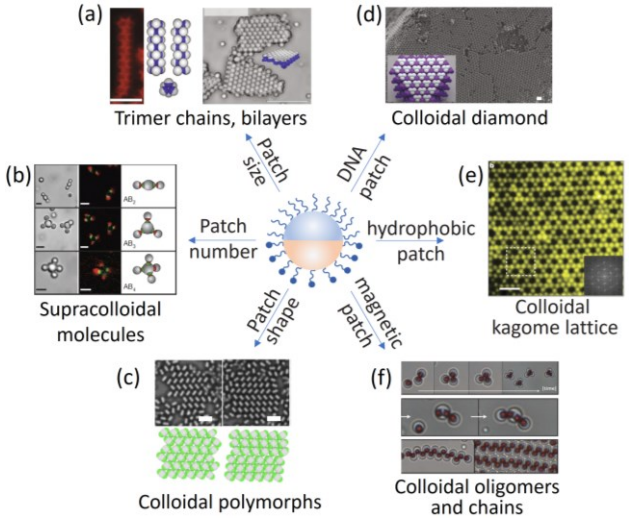

Figure 30. Self-assembly of Janus colloids with (a) different patch sizes, (b) different patch numbers, (c) different patch shapes, (d) DNA patch, (e) hydrophobic patch, and (f) magnetic patch. Scale bars are (b) 2 μm; (c) 5 μm; (d) 5 μm; (e) 4 μm. (a) Reproduced with permission from ref [332]. Copyright 2019 The Author(s). (b) Reproduced with permission from ref [333]. Copyright 2012 Springer Nature. (c) Reproduced with permission from ref [335]. Copyright 2020 Springer Nature. (d) Reproduced with permission from ref [340]. Copyright 2020 Springer Nature. (e) Reproduced with permission from ref [345]. Copyright 2011 Springer Nature. (f) Reproduced with permission from ref [349]. Copyright 2012 American Chemical Society.

3. ENGINEERING SMARTNESS in COLLOIDAL ASSEMBLIES

Based on the detailed interpretation of nanoscale interactions between colloidal particles and the diverse secondary structures driven by these forces, this section comprehensively introduces working principles for and practical strategies of creating smart colloidal assemblies, whose collective optical, mechanical, and electric properties are responsive to local environmental changes (temperature, pH, ionic strength, depletant, humidity, solvent, etc.) and remote perturbation (electric field, magnetic field, mechanical force, gravity force, light, etc.). Both interparticle connectivity and separation play important roles in designing stimuli-responsive colloidal assemblies. The regular and tunable particle separation in a secondary structure provides readily accessible spaces and interfaces, which allows for tuning surrounding physical properties of the superstructures and

leads to fast and impressive color changes. Inverse opal is a typical example in this regard, and its preparation strategies are summarized at the beginning of this section, followed by the introduction of these remarkable porous frameworks in developing smart materials. The weak particle connectivity within the superstructures and dynamic interplays between constituent colloids with external stimuli enable many advanced strategies to precisely tune colloidal crystal order and orientation. These dynamic processes are most frequently enabled by using responsive building blocks, surface functionalization of colloids with reactive molecules, or embedding colloidal crystals in stimuli-responsive matrix. Many interesting color and shape changes of these smart materials in response to an extended set of stimuli are presented based on the category of the external stimuli in each subsection.

3.1. Tuning Surrounding Physical Properties

The fact that there is a volume fraction of 26% even in closed packing structures provides plenty of room to incorporate smart or responsive features into the space contained within the colloidal assemblies. The refractive index and dielectric constant of the chemical environment of colloidal assemblies are important parameters that have been carefully manipulated to tune the optical, electric, chemical properties. This subsection outlines a set of existing strategies for preparing smart colloidal assemblies by controlling their surrounding physical properties in response to temperature, electric field, chemical, and light.

3.1.1. Preparation of Inverse Opals

Inverse opals consist of a solid material framework and interconnected, highly ordered air pores, which are fabricated by templating against opals. Because opals are 3D colloidal crystals assembled from close-packing of monodisperse nanospheres, inverse opals share the same crystal symmetry but with their structures complementary to opals.[350] These 3D-ordered macroporous materials have unique physicochemical properties, making them extremely useful in various importation applications, including photonics and catalysis.[351] Particularly, these materials exhibit brilliant structural colors due to their ordered pores, leading to size-dependent coloration for colorimetric sensing and anticounterfeiting. In addition, the highly porous structures have extremely large surfaces and interfaces, which facilitates the mass transportation of chemicals and their absorption/desorption to these interfaces. The widely accessible perfusion materials make it an open-ended approach to smart materials of desirable properties. In a general sense, their preparation principle is simple by forming solid materials between interspaces of opal structures and then etching away the initial templates. But its experimental implementation can be quite flexible and complicated, leading to hierarchical materials with structures spanning different length scales and pores varying from microporous to mesoporous and macroporous sizes.

In literature, three typical methods have been established to prepare inverse opals (**Figure 31**), involving self-assembly and then etching of opal crystals.[40] In the first scheme (**Figure 31a**), the fabrication follows sequential self-assembly, precursor infiltration, and template removal. The most used colloidal particles in this method are monodisperse SiO_2 and polystyrene nanospheres largely because of their widely accessible sizes, high particle uniformity, low cost, and easy in situ chemical etching.[47] The quality of opal templates is important to prepare perfect inverse opals since any crystal defects will be transferred to the inverse opals after etching. Since the first introduction back in the 1990s,[352,353] this method has been greatly modified to prepare diverse inverse opals by approaches of wet chemical process,[354-357] chemical vapor deposition (CVD),[356,358,359] and atom layer deposition (ALD).[360-362] In the last etching step, SiO_2 can be readily removed by HF etching, while PS nanospheres can be etched by a few different methods, including dissolution in proper solvents and high-temperature calcination. It opens the ordered air pores and exposes interspace walls so that the skeletal materials are accessible. Another interesting result is the interconnected macropore through twelve windows to its neighbours, which originates from the close packing and hard contact of the colloidal templates and facilitates mass transfer in inverse opals. In the second approach to inverse opals, co-self-assembly of nanoparticles with different sizes occurs (**Figure 31b**), where larger particles self-assemble into an opal template, and smaller ones infill it to form an inverse opal skeleton.[363-366] Simply etching the primary template yields inverse opals made of small particle aggregates. This approach is advantageous to produce hierarchical structures considering the widely accessible nanoparticles of different sizes and components. But the size of the small particles relative to the large ones should be carefully chosen so that the inverse opal structures are stable after removal of the particle template. The third method is to directly assemble core-shell nanoparticles into opals, and the following selective etching of core materials leads to inverse opals made of contacted nanoshells (**Figure 31c**).[367-369] One unique benefit associated with this method is the easy control over the volume ratio of the air pores, which can be achieved by changing the shell thickness of the colloidal templates. Because of this property, the air pores are closed and separated by the shells, decreasing the porosity and connectivity of the resulting inverse opals.

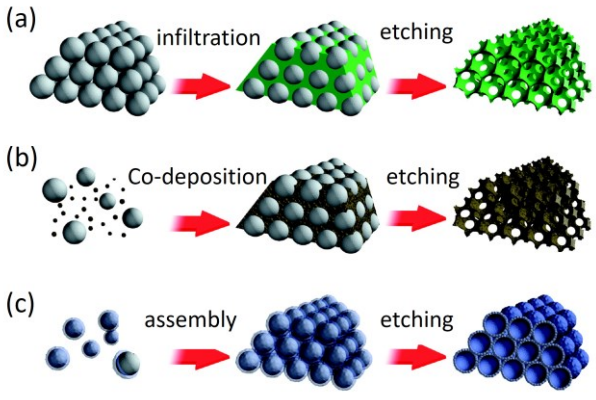

Figure 31. Inver opals by templating against opals. (a) The assembly-infiltration process. (b) The co-self-assembly process. (c) The assembly-etching process. Reproduced with permission from ref [40]. Copyright 2008 American Chemical Society.

Considering the 74% volume fraction of opals, one may expect an equal or higher air space in inverse opals due to possible incomplete material infiltration.[40] This consideration is confirmed by the presence of high-density pores connecting adjacent air holes in inverse opals prepared by the first two methods. The

skeletal wall thickness is within tens of nanometers if submicrometer particles are used as templates, making inverse opals a bulk material but with similar properties of nanoparticles, like high specific surface areas and confinement effect. Their prime material architectures are beautiful and elegant under an electron microscope due to the periodic arrangement of air pores, producing many compelling images that have been documented in the literature (**Figure 32**).[279] Although opals and inverse opals normally have their (111) planes on their crystal surfaces, it is possible to visualize other planes by etching the crystals through reactive ion etching. For *fcc* crystals, their (111) planes have hexagonal symmetry (**Figure 32a**), and (100) planes have square symmetry (**Figure 32b**).

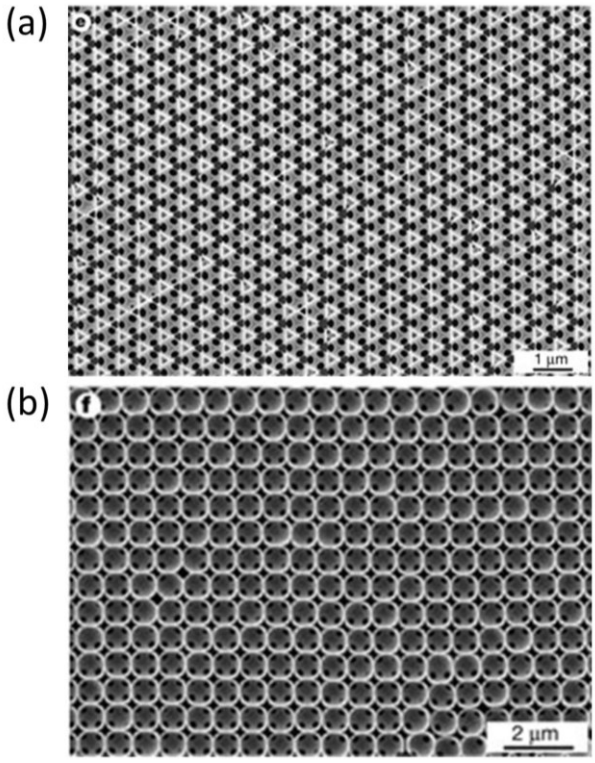

Figure 32. Structures of inverse opals. SEM images of silicon inverse opals (a) with a planar (111) surface and with (b) with a planar (100) surface. Reproduced with permission from ref [279]. Copyright 2001 Springer Nature.

3.1.2. Thermoresponsive Assemblies

Some functional materials can change their phases upon heating or cooling, which alters their physical properties, like permittivity and refractive index. These thermoresponsive materials are good candidates for designing smart colloidal assemblies that are controlled by temperature. Typical materials in this regard include liquid crystals, polymers, and metal oxides. One attractive advantage of using metal oxides is their extremely fast phase transitions, with less than 10^{-12} s for VO_2 under pulsed laser irradiation.[370] When being heated above its phase transition temperature (~68 ºC), VO_2 transits from semiconductor phase to metallic phase with a simultaneous decrease in its refractive index from 2.9 to 2.3.[371] Using this unique property, a temperature-responsive photonic crystal was prepared by impregnating SiO_2 opals with VO_2 through chemical bath deposition, which exhibited 21-nm blueshift under 800-nm laser irradiation.[372] Other promising inorganic materials are Se and β-Ag_2Se, with an amorphous to trigonal phase transition at 31ºC and β to α phase transition at 133ºC, respectively. A polyol process was used to prepare monodisperse Se@Ag_2Se nanospheres, which self-assembled into opal crystals; increasing the crystal temperature above 150ºC led to a blueshift of their diffraction peaks due to the increase of Se@Ag_2Se refractive index.[373] Using diverse thermochromic molecules and liquid crystals, it is also possible to prepare thermoresponsive colloidal crystals via incorporating them into ordered structures. **Figure 33a** shows a reversible thermochromic reaction that has been employed in preparing color-switching materials.[374] These thermochromic molecules are infiltrated into the porous inverse opals, and changing the temperature produces dynamic color changes. The color switching is achieved by the phase transition of the thermochromic molecules from a red crystalline state to a transparent molten state when temperature increases. At a low temperature, the thermochromic molecule is in a crystalline state and exhibits pigmentary red color. When temperature increases over a critical phase transition temperature, it is in its molten state and becomes transparent. At this stage, a composite responsive film comprising the molecules in an inverse opal scaffold (**Figure 33b**) exhibits brilliant structural colors, which is determined by initial particle size (inset in **Figure 33b**). This responsive color-switching is beneficial for developing high-performance thermochromic probes and highly desirable in information encryption and anticounterfeiting.

3.1.3. Electroresponsive Assemblies

Liquid crystals have anisotropic physical properties due to the crystallization of rod-like molecules, including elastic, electric, magnetic, and optical properties. Among these, optical birefringence is attractive in developing smart optical devices because it provides a simple and efficient way to modulate light intensity, color, and polarization. Such interesting birefringence is due to the varying refractive index along different crystal directions. Therefore, it is possible to modulate the refractive index for a constant light incidence by simply applying electric fields to change the phase of liquid crystals (**Figure 33c**). To this end, early studies demonstrated a few electroresponsive inverse opals via infiltrating nematic liquid crystals into the porous structures.[375-377] Applying voltages to this composite material alters the effective surrounding refractive index of the inverse opals, thus creating responsive optical signals. Although this method is effective, it provides weak optical responses under a high voltage largely because the change in refractive index is small during the isotropic-nematic phase transition. Another approach to voltage-driven smart colloidal assemblies is through electrochemical reactions, which use electrochromic materials for reversible color-switching (e.g., WO_3 and NiO).[378,379] While WO_3 changes from the bleached state to the color state upon electrochemical reduction, NiO has opposite appearance changes. If these two materials are assembled layer-by-layer on an electrode, their diffraction intensity can be modulated by applying voltages.[380]

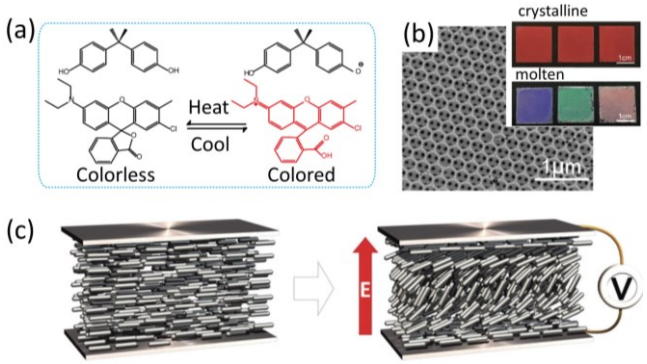

Figure 33. Thermo- and electroresponsive colloidal assemblies. (a) Thermoresponsive color changes of organic molecules. (b) SEM image of the SnO_2 inverse opals. Inset pictures show the color changes in different states. Reproduced with permission from ref [374]. Copyright 2019 American Chemical Society. (c) Liquid crystal alignment changes in response to the applied voltage. Reproduced with permission from ref [167]. Copyright 2015 Royal Society of Chemistry.

3.1.4. Chemoresponsive Assemblies

Colorimetric refractive index sensor is a famous example of chemoresponsive smart materials based on changes of surrounding physical properties. Compared with single-particle sensing platforms, colloidal assemblies provide much better sensitivity due to their collective optical properties, which can enhance the optical response through different physical processes. The LSPR of plasmonic nanostructures has been extensively used in detecting refractive index relying on its optical response to surrounding physical properties. Under light excitation, free electrons in plasmonic nanostructures form resonant oscillation with the electric field, and the induced surface plasmon changes the polarization of the surrounding medium. Specifically, permittivity (ε) is a measure of the electric polarizability of a dielectric, and a material with high permittivity is expected to be more significantly polarized than a low-permittivity material. Therefore, the charge density in a high-ε medium surrounding a plasmonic nanostructure is higher than that in a low-ε medium under light excitation. This simple dependence implies that the electrostatic potential in an excited plasmonic nanostructure will be reduced if its surrounding permittivity increases, making the resonant frequency shifting to low-energy regions. This consideration further explains the LSPR peak shift of plasmonic nanostructures in response to changes in the surrounding refractive index. In fact, plasmonic superstructures are advantageous in developing high-performance refractive index sensors due to the plasmon coupling between two plasmonic particles in proximity. It generates a remarkably enhanced localized electric field within a few nanometers, which is normally several orders of magnitude higher than the field enhancement of a single plasmonic particle. For example, an Au mushroom array demonstrates a 1050-nm shift per refractive index unit (RIU),[381] which is much higher than the optimal value of single nanoparticles (e.g., 700 nm for Au nanobranches[382,383]). A relevant comparison of sensing performances between superstructures and single particles is manifested in core-satellite Au assemblies.[384] A few Au nanospheres of small size are assembled around a large nanosphere through a so-called "hydroxylamine mediated assembly method" (**Figure 34a**). Such satellite superstructure shows significantly higher sensitivity than single Au nanospheres of different sizes (**Figure 34b**), which demonstrates the superior sensing performances of plasmonic assemblies over single particles. Notably, based on the capability of responding to refractive index changes, plasmonic superstructures are further processed for detecting various chemicals and chemical reactions, such as electrochemical process, humidity, pH, ionic strength, biomolecules, and metal redox reactions.[385-388]

Because the effective light pathway is proportional to the surrounding refractive index, any changes in chemical environments make photonic crystals responsive through peak shifts and color changes. There exist a few prerequisites in developing high-performance photonic chemical sensors, including fast response, large peak shift, and reversible color change. Inverse opals in this regard are a natural choice because of their high porosity, largely accessible interfaces, and durable mechanical properties. Following a similar templating approach (**Figure 34c**), inverse opals of different materials have been developed for chemical sensors, such as metals,[389,390] oxides,[391] semiconductors,[392] polymers,[393,394] salts,[395] carbon materials,[396] etc. Their diffraction peak shifts have a linear dependence on the refractive index changes when different solvents are diffused into the porous frameworks, with ~370-nm shift per refractive index. Since the kinetics of such diffusion are highly dependent on inverse opal surface property, it is possible to control the optical responses through surface modification, allowing the creation of optical patterns in response to solvent diffusion.[397,398] Notably, this sensing platform is universal as the refractive index change is driven by physical diffusion. Specific detection of chemicals using inverse opals can be achieved by introducing materials that can react with the analyte to their skeletons, pore walls, or interconnected pores. For example, backfilling the TiO_2 inverse opals with polyaniline leads to reversible blueshift and redshift of structural colors in exposure to HCl and NH_3 vapors.[399] This opposite color change is due to the phase transition of polyaniline from emeraldine salt under the acidic condition to emeraldine base under basic conditions, which is associated with a refractive index increase. Detection of biomolecules is often enabled using a hydrogel inverse opal with a considerably high detection limit, which was reported down to 1×10^{-9} M for DNA[400] and 1 ng/mL for protein[401] with opposite peak shifts.[70] In detecting vapors or gas, semiconducting oxides or metal-organic frameworks are more often used as these materials have excellent adsorption capability toward gas molecules. A ZnO inverse opal can exhibit a 40% change in transmittance in response to UV irradiation-induced O_2 dissociation from its surface.[402] Metal-organic frameworks are famous porous materials nowadays and have specific interactions with guest molecules due to the presence of highly accessible organic ligands in their 3D networks. Their skeletons provide plenty of active sites to the guest molecules that are diffused in through the inverse opal pores. Therefore, inverse opals of metal-organic frameworks are uniquely attractive in developing smart colloidal assemblies. An elegant example uses inverse opal made by $Cu_3(BTC)_2$ (BTC = benzenetricarboxylate) to detect various solvent vapors with optimal detection limit of 10 ppm.[403] Their reversible optical responses can occur within 30 s with opposite peak shift though depending highly on the physicochemical properties of guest molecules: redshift for cyclohexane and toluene (**Figure 34d**) while blueshift for ethanol and acetone.

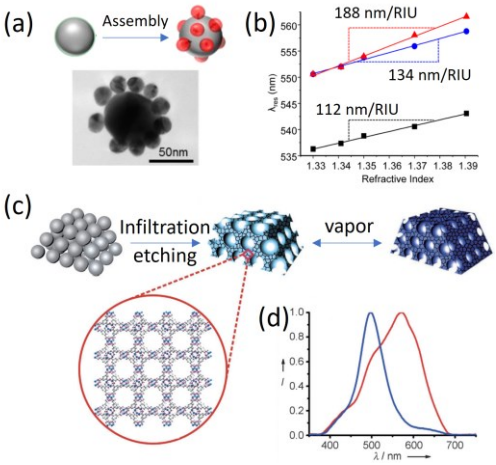

Figure 34. Chemo-responsive colloidal assemblies. (a) Self-assembly of binary Au nanospheres into core-satellite superstructures. Inset shows a typical TEM image. (b) Dependence of plasmonic peak position on the refractive index of solvents. Reproduced with permission from ref [384]. Copyright 2015 American Chemical Society. (c) Preparation of inverse opals of metal-organic frameworks. (d) The diffraction peak shift in response to methanol vapor exposure. Reproduced with permission from ref [403]. Copyright 2011 John Wiley and Sons.

3.1.5. Light-responsive Assemblies

Light-responsive colloidal assemblies are driven by light irradiation and therefore are advantageous for energy conversion and soft robotics if one considers its remote control, fast response, and renewable feature. To induce measurable changes in surrounding physical properties, photochromic molecules are integrated into colloidal assemblies so that their reversible switch between two thermodynamically stable states causes smart responses. In current literature, commonly used photochemical reactions include cis-trans isomerization,[404] photocyclizations,[405,406] and intramolecular mass transfer. In an early effort to create such structures in the 1990s, the plasmonic film was coated with polymers doped with photochromic molecules so that the film reflectance could be regulated by the color switching of the doped molecules under UV light irradiation.[407,408] This strategy was further employed to modify Au nanostructures with azobenzene, a model photochromic molecule, through thiol chemistry.[404] Under blue light (450 nm), azobenzene has *cis*-to-*trans* transition, whose reverse reaction occurs under VU light irradiation. Such *cis*-to-*trans* transition increases molecule height by ~0.5 nm, changes the surrounding dielectric properties, and redshifts the absorption of Au nanostructures. Notably, these established approaches use individual plasmonic structures, and developing optically responsive colloidal assemblies is rarely reported largely because of the existing challenges to incorporate photoactive molecules into colloidal assemblies.

3.2. Tuning the Order of Secondary Structures

3.2.1. Magnetically Responsive Assemblies

The concept of nanoscale magnetic assembly has provided a unique set of colloidal crystals, whose potential in many important applications lies in not only the instant colloidal assembly but also the rapid tuning of the colloidal crystal periodicity, orientation, and therefore their physical properties. Among a few exciting properties associated with the highly ordered structures, structural color is most attractive and thus has been extensively studied. For a perfect linear chain made of nanospheres, the diffraction of incident light is predicted by Bragg's law, $\lambda=2nd\sin\Theta$. This simple equation provides a considerably precise prediction of the diffraction wavelength (λ), given the diffraction order (n), structural periodicity (d), and incident angle (Θ). It also suggests that tuning the crystal periodicity and orientation can lead to corresponding diffraction peak shifts. In experiments, the key to the successful tuning of the crystal periodicity is the dynamic balance between the magnetic attraction and electrostatic repulsion from surface charges. Simply decreasing the external field strength will change the color of a colloidal dispersion of photonic chains (TEM shown in **Figure 4b**) across the whole visible range from purple to red (**Figure 35a**).[85,87] Within the 1D chains, the interparticle separation is determined by the two interplaying forces, and to explain the field-dependent diffraction needs first analysis of the magnetic interactions between adjacent nanoparticles. As shown in **Figure 35b**, the magnetic attraction between two adjacent nanospheres will decrease with the external field strength; the strong electrostatic repulsion will thus increase the interparticle separation until reaching a new equilibrium state. This sequence of events causes an associated redshift of the diffraction peaks and simultaneous color changes in the colloidal dispersion (**Figure 35c**). Such magnetic periodicity control is rapid, fully reversible, and contactless, providing predictable color changes in response to a magnetic field. This unique smart material has been used in a wide range of practical applications, including color printing, rewritable photonic papers, anticounterfeiting, and color display (See **chapter 4** for a detailed introduction). If this remarkable photonic chain is fixed by a silica layer, it enables active tuning of the collective physical properties of the fixed 1D chain of Fe_3O_4 nanospheres through another important concept of magnetic orientation control, which will be systematically discussed in **section 3.3**.

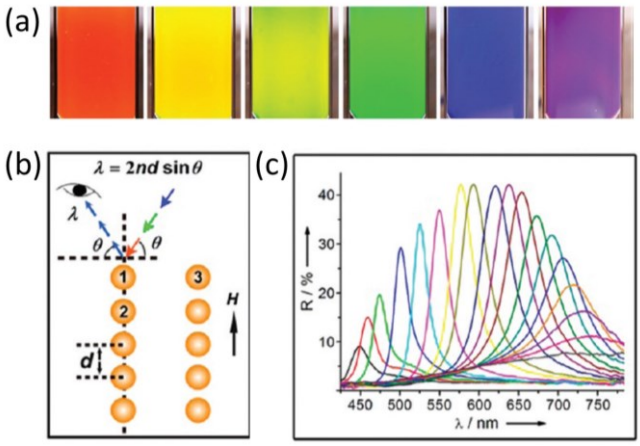

Figure 35. Magnetically responsive and highly tunable 1D photonic crystals from the magnetic assembly of superparamagnetic Fe_3O_4 colloidal nanocrystal clusters. (a) Digital images of a colloidal dispersion of the Fe_3O_4 nanoparticles under gradually increasing field strength from left to right image. (b) Schematic illustration of the 1D chains and their diffraction under light illumination. Reproduced with permission from ref [85]. Copyright 2012 American Chemical Society. (c) Dependence of diffraction peak position on

the magnetic field strength. Reproduced with permission from ref [88]. Copyright 2007 Wiley-VCH Verlag GmbH & Co. KGaA, Weinheim.

3.2.2. Thermoresponsive Assemblies

Thermoresponsive materials that have been used for designing smart colloidal assemblies include polymers capable of phase transition or common thermal expansion, thermochromic molecules, liquid crystals, etc. The spontaneous changes of their physicochemical properties allow colloidal assemblies to respond to temperature changes, leading to dramatic color or/and shape changes of the composite materials. Such attractive responses are usually associated with a critical temperature where the phase transition or molecular stereoisomerism occurs. Conversely, the thermal expansion of polymers is more often characterized by continuous shape changes in response to temperature increases. Temperature-responsive polymers are an attractive category of functional materials and have been extensively studied in creating smart colloidal assemblies. Most polymer films experience thermal volume expansion with an intrinsic coefficient of linear thermal expansion depending on chemical components and crosslinking ratio. In the solution phase, some weakly cross-linked polymers can swell in water to form hydrogels, which undergo phase transition upon temperature changes. This physical transition induces simultaneous changes in polymer configuration, volume, and hydrophilicity.[409]

Among synthetic polymers, poly(N-isopropylacrylamide) (PNIPAM) is the most popular thermoresponsive polymer, which reversibly transits from a swollen, hydrophilic state to a collapsed, hydrophobic state above its lower critical solution temperature (LCST) at 32°C (**Figure 36a**).[410] Notably, this critical temperature is often modified by forming copolymers between N-isopropylacrylamide and other monomers.[411] Contrary to the polymers with LCST, some polymers have thermosensitive phase transitions with an upper critical solution temperature (UCST), below which the dispersed polymers become less soluble. As predicted by the Flory-Huggins theory,[412] the UCST polymers perform a temperature-dependent "entropy-favored mixing" in solutions. At a temperature higher than its UCST, the polymer is soluble as favored by the entropy term $-T\Delta S_m$ while the polymer loses its solubility because the entropy term becomes less negative at a low temperature. Therefore, the self-assembly of colloidal particles that are modified by a UCST polymer is expected to occur upon cooling the solution, which is likely a converse process to the self-assembly involving LCST polymers. A few typical UCST polymers that have been used in thermoresponsive colloidal self-assembly include polystyrene,[413,414] poly(N-acryloyl glycinamide),[415] and poly(3-dimethyl- (methacryloyloxyethyl)ammonium propanesulfonate).[416] Among those, poly(N-acryloyl glycinamide) is a long known thermoresponsive gel in concentrated solutions, which was first synthesized back in 1964.[417] A careful study recognized that such temperature-sensitive cross-linking was attributed to randomly distributed hydrogen bonds as evidenced by the facts that the gel formation could be prevented by lowing the polymer concentration or adding hydrogen bond interrupting agents.[418] As shown in **Figure 36b**, at a temperature lower than its UCST, the polymer is a gel due to the crosslinking of hydrogen bonds, which can fully dissolve in a solvent by increasing the solution temperature.[415,419] To take advantage of this unique property, two relevant strategies have been proposed to assemble thermoresponsive colloidal superstructures. In the first scheme, microgels made of thermoresponsive polymers or colloidal particles functionalized with these polymers are directly assembled into colloidal superstructures (top panel in **Figure 36c**).[420,421] In an alternative approach, colloidal crystals are first assembled from monodisperse particles, followed by infiltration and polymerization of monomers (bottom panel in **Figure 36c**). The volume shrinkage of PNIPAM above the LCST induces a sharp lattice and volume contraction while the solution of UCST gels disassembles colloidal clusters at a high temperature. This sequence of events has been extensively employed for preparing thermoresponsive second structures. For example, an opal structure of PNIPAM microgels manifests a continuous blueshift in its diffraction peaks in response to temperature increase (**Figure 36d**).[422] These two approaches can be applied to colloidal crystals with different dimensions, symmetries, and sizes. A few examples are colloidal crystal arrays with close packing of nanoparticles.[292,423-425] It is later extended to developing thermoresponsive 1D photonic crystals prepared by the magnetic assembly.[426,427]

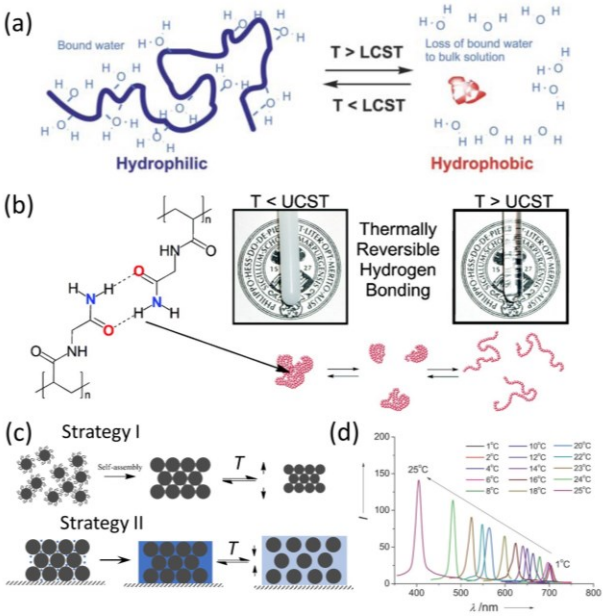

Figure 36. Thermo-responsive phasing-changing polymers for smart photonic crystals. Schematic illustration of thermo-responsive polymers with (a) a lower critical solution temperature and (b) an upper critical solution temperature. (a) Reproduced with permission from ref [410]. Copyright 2005 American Chemical Society. (b) Reproduced with permission from ref [415]. Copyright 2011 American Chemical Society. (c) Schematic illustration of two strategies to prepare thermo-responsive colloidal crystal arrays. (d) Peak shift of the structural colors in response to temperature changes. Reproduced with permission from ref [420]. Copyright 2013 John Wiley and Sons.

Liquid crystals normally exert smart responses via their controllable thermoresponsive volume expansion and shrinkage.[428] In a case that involves photonic crystals, the shape is normally accompanied by observable color changes because of the deformation-induced periodicity changes. For example, nematic liq-

uid crystals can be readily integrated into colloidal crystal arrays through the infiltration-polymerization process.[429] At a low temperature, the nematic state has parallel liquid crystal moieties to the film surface (**Figure 37a**). When the film is heated to close to the nematic−isotropic transition temperature, the moiety re-orientation causes shape changes in the films, with simultaneous periodicity changes and diffraction peak shift (**Figure 37b**). Notably, the orientation of liquid crystal molecules can be controlled so that achieving volume expansion or shrinkage is optional using the same liquid crystal. In addition, the infiltration-polymerization strategy is not limited to the component of the colloidal crystals, thus representing a general approach to smart materials.[430]

Thermoresponsive colloidal assemblies are also possible in solution-processed self-assembly by controlling solution temperature to modulate particle interactions. This strategy is operational for charged nanoparticles because their electrostatic interaction is dependent on temperature.[122,431] In a carefully prepared reaction, negatively charged Au nanoparticles are dispersed in a mixture of salt and polymer solution at high temperature, which forms a gel upon lowing the solution temperature.[123] By sweeping the temperature between a suitable range, the Au nanoparticles can be assembled and disassembled, as evidenced by a remarkable red-blue color change in the dispersion (**Figure 37c**). A simple Zeta potential measurement indicates a dramatic, simultaneous decrease in surface charges with solution temperature. Therefore, it is expected that the Au nanoparticles self-assemble into chain-like secondary structures, which is manifested by the regular redshift of plasmon coupling peaks (**Figure 37d**). One advantage associated with using temperature as a physical stimulus is its higher reversibility to regulate nanoparticle interactions compared with adding chemicals.

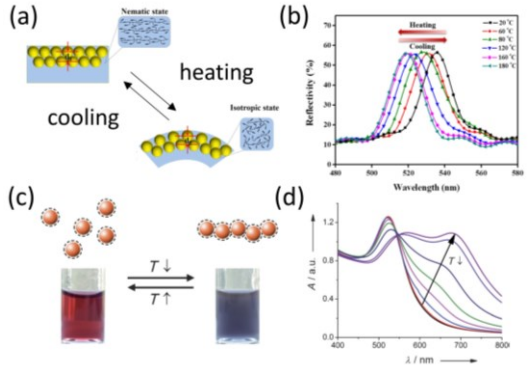

Figure 37. Thermo-responsive colloidal assemblies. (a) Schematic illustration of the thermo-responsive actuation and lattice constant changes. (b) The corresponding reflectivity changes. Reproduced with permission from ref [429]. Copyright 2016 American Chemical Society. (c) Schematic illustration of reversible assembly-disassembly of Au nanoparticles in response to temperature changes. (d) The corresponding plasmonic peak shifts. Reproduced with permission from ref [123]. Copyright 2012 John Wiley and Sons.

3.2.3. Light-responsive Assemblies

The use of light as external stimuli has many merits, such as precise control over the excitation wavelength and light intensity, remote manipulation, and fast response. Light-responsive colloidal assemblies normally occur through two types of reactions, the photochemical reaction and the photothermal effect. The photothermal effect is an energy conversion process where light energy is converted to heat by light-absorbing materials. The local high temperature is expected to drive phase transition in liquid crystal elastomers and photochromic molecules as well as volume changes in polymer films, leading to pre-designed responses in colloidal assemblies. Depending on the working mechanism, light irradiation can induce volume shrinkage or expansion of soft materials, although thermal expansion is more often observed. The performance of photothermal expansion is dependent on the physical properties of the polymer, with their expansion degree being determined by the coefficient of thermal expansion, which can be found in previous publications.[432] Polydimethylsiloxane (PDMS with the molecular structure shown in **Figure 38a**), for example, is a polymeric organosilicon compound that has a higher expansion coefficient compared with other common polymers. It has been widely used for designing shape-changing smart materials that consist of another passive layer with less thermal expansion. In this design, colloidal assemblies may play different roles. As shown in the bottom panel in **Figure 38a**, a co-assembled layer of plasmonic nanoparticles and graphene oxide nanosheets on the PDMS surface serves as both the passive layer and the photothermal converter, which induces local heating and bending on this bilayer film upon light irradiation.[433] Photothermal volume shrinkage is also possible if polymers have a negative thermal expansion coefficient.[434-436] In designing smart materials, however, it is more frequently achieved through a different mechanism, which involves the desorption of water molecules from the polymer matrix.[437,438] To this end, highly absorbent polymers, particularly hydrogels and celluloses, are natural choices for creating these opposite volume changes. As a polysaccharide, cellulose has abundant hydroxyl groups that can absorb water molecules through hydrogen bonds (**Figure 38b**). By assembling MXene into multilayered structures under the presence of cellulose, it is possible to develop light-responsive actuators.[439] Under light irradiation, MXene can efficiently convert light energy into heat via the photothermal effect, and the high temperature causes water desorption from the assemblies, leading to volume shrinkage of this domain (bottom panel in **Figure 38b**). In addition to light, the water absorption-desorption is also very sensitive to humidity changes, making this actuator a multi-responsive smart device.

An advanced technique is developed by taking advantage of the phase transition of liquid crystal elastomers and photochromic molecular crystals.[440,441] Incorporation of photochromic moieties into soft polymer allows colloidal crystals to respond to light irradiation, during which the crystal order, orientation, and volume may change accordingly. In liquid crystal elastomers, nematic and smectic phases are the two most common ordered structures. Generally, there exist two types of phase transitions at a critical temperature, the order-disorder transition and the order-order transition. The first transition involves the light-driven transition of crystal moieties to an isotropic state featuring random molecular orientation.[442] Albeit less common, the order-order transition contains minor changes of liquid crystal orientation, which normally occurs during photopolarization and photochemical process and, in practice, can be described as homeotropic (perpendicular to the substrate), homogeneous

(parallel to the substrate), and tilted alignment (titled with respect to the substrate normal).[443-445] In the case of order-disorder phase transition, controlling the initial alignment of mesogens is important because their initial collective orientation determines the shape deformation of their host macroscopic films. Such flexibly accessible molecule alignment leads to copious shape deformation and therefore is one compelling feature of liquid crystal elastomers over other photomechanical systems. In existing strategies, there are two approaches to controlled alignment of liquid crystal mesogens, including two-step crosslinking[446] and in situ polymerization.[447-449] During two-step crosslinking, a linear polymer is slightly crosslinked to form a solid film, which is subsequently stretched for uniaxial alignment of the mesogens. The stretched film is further crosslinked to fix such alignment and also the shape of the elastomers.[450] The in situ polymerization involves simultaneous polymerization and crosslinking in glass cells that have been modified by alignment layers (e.g., rubbed polyimides).[451] The alignment of mesogens in this process is temporarily fixed by the crosslinked polymer matrix. One advantage associated with photopolymerization is the adjustable reaction temperature to facilitate the crystal phase formation.[452] **Figure 38c** is a molecular formula of a liquid crystal monomer, which can be made into elastomer through the in situ polymerization strategy.[453] The alignment of mesogens is performed in polyvinyl alcohol-coated glass slides that have been rubbed in antiparallel directions. Meanwhile, Au nanorods that preferentially align along the same direction induced by capillary infiltration into the glass cell is uniformly dispersed in the mixture. Such host-guest system is polymerized through UV exposure, leading to a liquid crystal elastomer doped with well-aligned Au nanorods. At this carefully prepared condition, the alignment of nematic liquid crystal molecules are parallel to elastomer surface. The constituent Au nanorods can generate local heat under light irradiation at their resonant wavelength, which further drives the nematic-isotropic phase transition of the elastomers. The re-alignment of mesogens from homogeneous state to isotropic state cause the elastomer to shrink along the initial alignment direction and expand in the other direction. In an elastomer film with a proper thickness, the light intensity decays gradually along the thickness direction, producing a temperature gradient. Therefore, elastomer surface that is exposed to strong light contracts more along the shrinking direction than does the elastomer bottom. This asymmetric volume change cause the liquid crystal elastomer to bend toward the light source (bottom panel in **Figure 38c**).

Molecular crystals of chromophores with both positional and translational order are another important category of light-responsive organic materials.[454] Their photoisomerization in response to light exposure can drive various interesting physical transitions, such as dissolution, bending, twisting, and rotation. Their use and performance in developing photoactuators will be discussed in detail in **section 4**. Here, an example of photochromic diarylethene crystal is introduced with its chemical structure shown in the top panel in **Figure 38d**.[455] Upon UV light irradiation, the molecule undergoes a photocyclization reaction from its open-ring isomer to close-ring isomer. A crystal film simultaneously twists with an apparent colorless-to-blue change in its appearance (**Figure 38d**). This process is reversible by simple visible-light irradiation. Notably, the manifested shape morphing is dependent on the crystal orientation and symmetry, which is, however, more difficult to control during crystallization compared with the mesogen alignment in the polymerization of liquid crystal elastomers.[456]

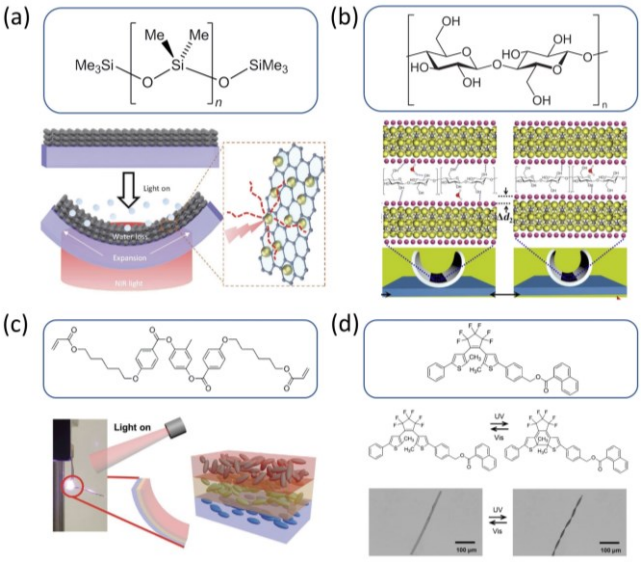

Figure 38. Photo-responsive colloidal assemblies. (a) The use of thermal expansion of PDMS for developing photothermal actuators. Reproduced with permission from ref [433]. Copyright 2020 John Wiley and Sons. (b) The water desorption from cellulose matrix upon photothermal heating of MXene. Reproduced with permission from ref [439]. Copyright 2019 The Authors, some rights reserved, exclusive licensee American Association for the Advancement of Science. (c) The nematic to the isotropic phase transition of liquid crystal elastomers for photothermal actuators. Reproduced with permission from ref [453]. Copyright 2020 John Wiley and Sons. (d) Photochromic crystal twisting. Reproduced with permission from ref [455]. Copyright 2013 John Wiley and Sons.

Azobenzene is another attractive example of photochromic organic compounds, which have been used in developing photomechanical materials. Under 380-nm light excitation, azobenzene changes from its trans to cis configuration with a subtle molecular size decrease (**Figure 39a**), whose reverse reaction occurs under visible light irradiation.[457] To further understand this interesting photoisomerization and its developments in creating smart materials, readers are referred to a few comprehensive reviews.[458-462] In a recent study, it is modified on plasmonic Au nanoparticles for reversible assembly of colloidal crystals in response to light.[463] This strategy incorporates azobenzene into DNA sticky end to actively regulate the reversible recognition between DNA strands (**Figure 39b**). Under visible light, azobenzene is in the *trans* configuration so that DNA sticky ends remain hybridized, leading to the assembly of cubic crystals. Under visible light, azobenzene *cis* form induces the dehybridization of DNA strands so that the Au superstructures disassemble. By selectively disassembling surface-grown crystal film using light, this technique allows the creation of plasmonic patterns (**Figure 39c**).

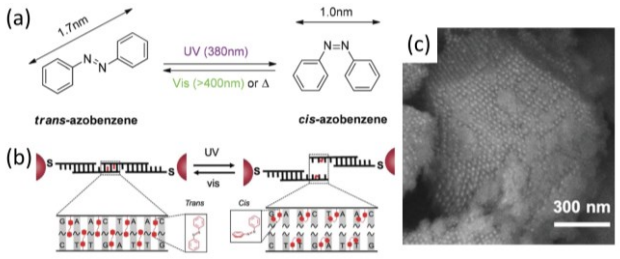

Figure 39. Photo-responsive colloidal self-assembly. (a) The responsive trans-cis transition of azobenzene. Reproduced with permission from ref [457]. Copyright 2018 Royal Society of Chemistry. (b) The reversible DNA base pair interactions mediated by the photo-responsive trans-cis transition. (c) SEM image of the bcc crystals. Reproduced with permission from ref [463]. Copyright 2020 John Wiley and Sons.

3.2.4. Electroresponsive Polymers

Electroresponsive colloidal assemblies are a class of superstructures with tunable physicochemical properties responsive to an applied voltage. Depending on working principles, they can be engineered through electrophysical processes or electrochemical reactions. Electrophoretic force is a common driving force to assemble charged colloids or polymers in solutions. Polyelectrolytes, for example, are charged polymers with their repeating units bearing electrolyte groups. In a proper solvent, the charges on the polymer matrix make it susceptible to electric fields so that the matrix contracts unidirectionally (**Figure 40a**).[464] This mechanism is an established approach to smart inverse opals via polymerization of electrolytes against colloidal crystal templates.[465-467] An alternative approach to electronically tunable crystals employs an electric field-induced straining effect, which is based on the electrostatic interaction between water-dispersed colloidal particles.[468] To stabilize the colloidal dispersion, the particles are fixed in a hydrogel matrix, whose soft property allows reversible volume changes.[469] Once a working voltage is applied, the colloidal crystal contract along the vertical direction and expand in lateral directions, leading to a decrease in periodicity along the light incidence (**Figure 40b**). This early study produces a peak shift of tens of nanometers in response to a direct-current voltage of a few kilovolts. The other two electrophysical processes involve liquid crystals or liquid crystal elastomers, which renders superstructures responsive to electric fields via changing structural refractive index or crystal volume. Solid elastomers containing liquid crystal mesogens can change the order of colloidal assemblies in response to electric fields. This working mechanism regulates the superstructure lattice constants to enhance their optical responses to a voltage (**Figure 40c**). Inverse opals of liquid crystal elastomers can be readily prepared by the infiltration-polymerization method with unidirectionally aligned mesogens.[470] Through introducing an electrothermal layer (e.g., graphite), the applied voltage heats the electric cell to a critical temperature where the nematic-isotropic phase transition occurs. It produces remarkable vertical volume expansion as determined by the initial horizontal mesogen alignment. This physical process creates a color-switching smart device with its structural color being tunable over the whole visible range, demonstrating much broader color changes under a lower voltage compared with the previous orientational control strategy.

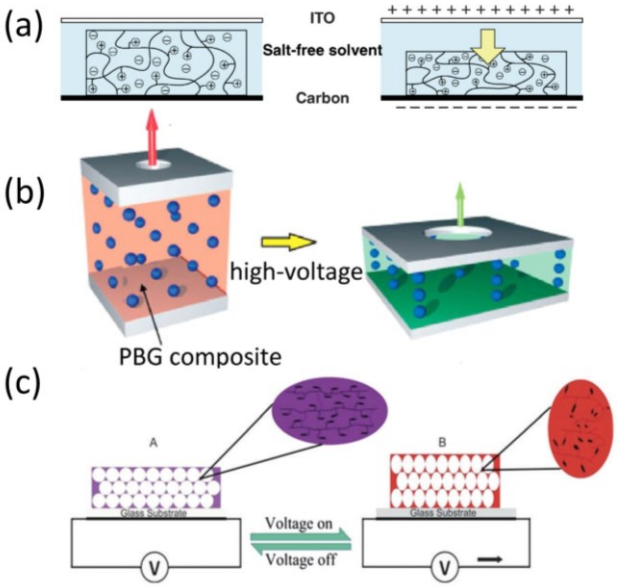

Figure 40. Electroresponsive colloidal self-assembly. (a) Schematic illustration of the voltage-driven structural color changes of inverse opals. Reproduced with permission from ref [464]. Copyright 2009 Royal Society of Chemistry. (b) Schematic illustration of electric-field-induced structural color tuning of photonic crystals. Reproduced with permission from ref [468]. Copyright 2005 John Wiley and Sons. (c) Schematic illustration of the lattice constant changes of inverse opals in response to the applied voltage. Reproduced with permission from ref [470]. Copyright 2012 Royal Society of Chemistry.

With similar electronic cells, electrochemical reactions can be carefully designed so that they can produce desirable smart responses. These chemical reactions involve charge transfer processes to enable responses, with the redox reaction and the acid-base exchange being most promising. After the reactions, the charged products associated with polymer backbones produce electrostatic interaction between each soft domain, which is responsible for a simultaneous volume expansion driven by the repulsive forces. Notably, the design of reactive groups is flexible since they can present as side functional groups or as cross-linkers. The underlying forces and subtle changes in polymer electrical property cause colloidal crystals to re-organize to minimize their free energy, which is manifested by color and/or volume changes (**Figure 41a**). Such a charge-transfer reaction requires a proper conductive solvent to facilitate the migration of solvent molecules and charge carriers, including ions and electrons. The conductive solvent in which reactants covalently bonded to polymer chains react with electrons is one of the most important parameters influencing the response rate. Another critical parameter to access the performance of the smart device is switching time, which is more often related to the polymer matrix porosity and polymer affinity with the chosen solvent. There exist two challenges in designing the electrochemical cell for achieving a fast response. The first one is to find a proper reversible chemical reaction that can be powered by a considerably low voltage. The second challenge is how to realize the physical responses utilizing the electrochemical reaction. To overcome the first one, chemists have recognized a set of molecules that can react to an applied voltage to yield charged products with full reversibility. At a few early studies in this regard,

ferrocene-containing polymers are first introduced into responsive photonic crystals because of their redox-mediated optoelectronic and catalytic switching properties.[471-473] **Figure 41b** presents an electrochemical reaction of polyferrocenylsilane (PFS) under applied voltage. Its neutral reactant is oxidized to positively charged products in electrochemical cells, which is reversible through reduction. Other examples that have been used in developing electroresponsive assemblies include poly(methacrylic acid),[424] polypyrrole,[474-477] poly(2-vinyl pyridine), and poly(3.4-ethylenedioxythiophene),[478,479] with their molecular structures and working voltages summarized in **Figure 41c**.

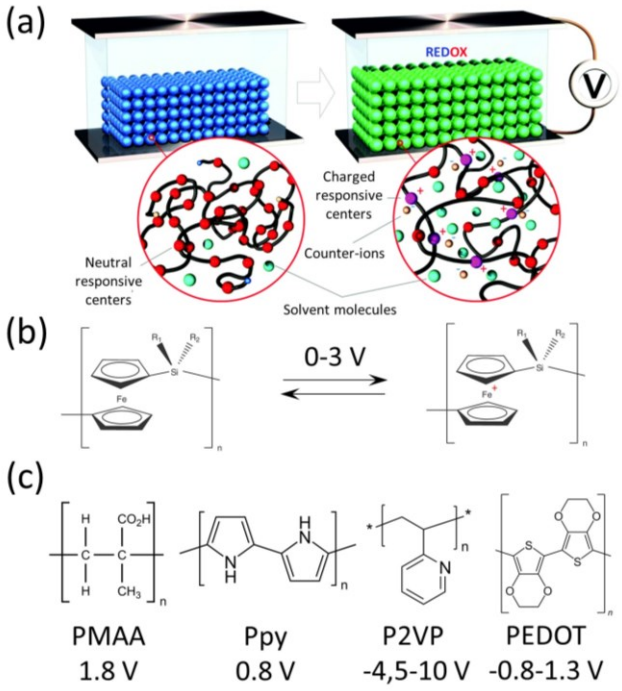

Figure 41. Electrochemical polymers for smart colloidal assembly. (a) Schematic illustration of responsive photonic crystals based on electrochemical cells. Reproduced with permission from ref [167]. Copyright 2015 Royal Society of Chemistry. (b) The electrochemical reaction of polyferrocenylsilane. (c) The molecular structures of commonly used electrochemical polymers for preparing electroresponsive colloidal crystals. PMAA: poly (methacrylic acid); Ppy: polypyrrole; P2VP: poly-2-vinylpyridine; PEDOT: poly(3,4-ethylenedioxythiophene).

3.2.5. Chemoresponsive Assemblies

Chemical species, like protons, metal cations, anions, and many biomolecules, are important to various biological functions in living organisms and to chemical reactions in developing smart systems. Understanding their deterministic roles requires advanced detection techniques to analyze their concentrations in the liquid phase and their reactions with other reactants.[480] Therefore, developing smart materials with sensitive responses to chemicals is of both fundamental and practical importance. Albeit their diverse structures and responses, colloidal assemblies responsive to chemicals are feasible through three empirical strategies, including using responsive building blocks, incorporating colloidal assemblies in a functional matrix, and employing porous superstructures like inverse opals. Their smart responses, dominantly in color or spectrum changes, in contact with analytes, occur based on changes of surrounding refractive index (**section 3.1.4**) or alteration of structural orders. Their working principles to alter the secondary structure orders are diverse, with some involving chemical reactions and others containing only physical processes. For the developments of chemical sensors in the early 2000s, one may find a few comprehensive reviews that focus on different responsive materials, e.g., photonic crystals[481] and plasmonic assemblies.[482,483]

The driving forces altering the structural order of the assembled entities depend on the types of analytes. Organic solvents or vapors are neutral molecules, which can swell or de-swell polymers having a similar polarity or high affinity through altering polymer chain conformation. Such solvent-induced mechanical deformation allows the embedded colloidal crystals to adjust their periodicity, thus inducing apparent color changes in response to solvent exposure (**Figure 42a**). To this end, a quick screening of polymer monomers, for which the analyte is a good solvent, is a feasible starting place to find the right polymetric materials. PDMS is the most commonly used polymer for detecting both polar and nonpolar solvents if colloidal crystal arrays, particularly silica or polystyrene nanospheres, are embedded.[484-486] A few systematic studies on detecting a series of organic solvents recognize an interesting fact that such composite photonic film has superior sensitivity in detecting non-polar solvents over polar solvents. Particularly, in early research,[487] the same PDMS photonic film made of PS colloidal crystal arrays experienced ~400-nm peak shift in detecting non-polar solvents (benzene, toluene, xylene, etc.), whose sensitivity was much higher than that in detecting polar solvents, like alcohols and water. This observation underpins the importance of the "affinity rule" in developing high-performance chemical sensors for organic solvents. That is, polymers with highly polar functional groups are good candidates for detecting organic solvents with strong polarity. For example, a copolymer was used with a significant peak shift in detecting acetonitrile, tetrahydrofuran, dimethylformamide, or dimethyl sulfoxide.[488,489] Similarly, these sensors are also responsive to organic vapors if proper materials are used.[490,491] One apparent limitation associated with this detection mechanism is the low specificity of the physical diffusion-swelling processes, making it difficult to selectively detect certain organic molecules. Another minor disadvantage is the sluggish diffusion of organic molecules inside the polymer matrix, which may reduce the response rate.

Detecting ions is possible using similar photonic films, whose constituent polymers need to be replaced based on the "affinity rule" for optimal sensitivity. Because ions are charged substances, polyelectrolytes with charged or ionizable functional groups are a natural choice for pH and ionic strength sensors. Such ionic gels exhibit interesting volume-phase transitions in response to pH or ionic strength changes, which causes the guest crystal lattice to contract or expand.[492-494] The randomly distributed charged functional groups in the hydrolyzed gels allow the polymer segments to interact with each other through electrostatic interactions or hydrogen bonding, the combination of which drives the phase transitions.[495] This conclusion explains why the ionic gels shrink when the solution ionic strength increases (**Figure 42b**). The high-concentration counter ions presented in detection solutions reduce the net charge repulsion between the polymer segments, thus leading to gel volume

shrinkage. Such phase transition has been observed on various polymer-colloidal crystal composites since its first use in ionic detection,[496] such as PS nanospheres in polyacrylamide,[496,497] poly-(2-vinyl pyridine),[498] poly(acrylamide-co-acrylic acid),[499] poly(vinyl alcohol)/3-aminophenol,[500] silica nanospheres in poly(hydroxyethyl methacrylate-co-methacrylic acid),[501] and morpho butterfly wing scales in polymethacrylic acid.[502] Although the performances of these sensors vary, a few detailed studies suggest a quasilinear response to the log scale value of salt concentrations in a certain concentration or pH range.[497] Again, these sensing platforms suffer from low sensing selectivity because they are based on non-specific electrostatic interactions. A few advanced techniques have instead been developed to overcome this lasting challenge and improve ion sensitivity. One chemical approach uses the specific interactions between ions and organic compounds for ion-selective sensing. Among cation detections, crown ethers were introduced as molecular receptors into hydrogels for selective detection of potassium[503] or lead (II) ions.[504-506] Selective detection of anions is also possible using a photonic ionic-liquid polymer or a hydrogel opal structure.[507,508] Another powerful derivative combines molecular imprinting technique with the polymer-colloidal crystal sensing platform, which commonly uses inverse opals as sensing scaffolds. In a typical preparation process, inverse opals are made by following the classic infiltration-polymerization recipe, during which an analyte is added to serve as molecular imprints. The initial opal template is later removed to create defined spaces, into which the analyte from a sample can diffuse only if it fits. This emerging sensing method has been extensively used in detecting biomolecules, including egg albumin and lysozymes,[509] cholesterol,[510] L-pyroglutamic acid,[511] or in detecting organic compounds (e.g., Bisphenol A,[509,512] vanillin[513]).

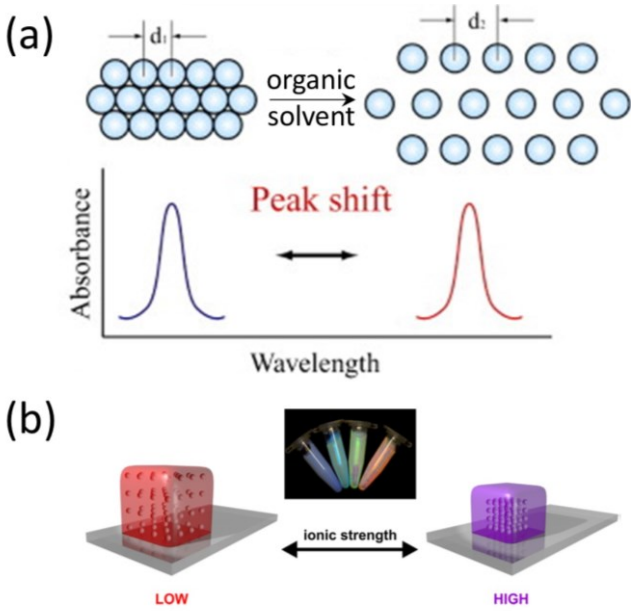

Figure 42. Chemo-responsive photonic crystals. (a) Peak position shifts in response to lattice changes of photonic crystals. Reproduced with permission from ref [487]. Copyright 2007 Elsevier. (b) Schematic illustration of photonic crystal response to ionic strength changes. Inset pictures show the color of colloidal dispersions with various ionic strengths. Reproduced with permission from ref [497]. Copyright 2012 American Chemical Society.

In developing biosensors, the selectivity of the photonic crystals can be further improved by taking advantage of specific recognition of biomolecules or certain chemical interactions. These strategies have been fully manifested by detecting glucose through various chemical routes, exhibiting complex dependence of diffraction peak shift on glucose concentration. Asher et al. developed a set of glucose sensors by engineering the functional groups associated with a polyacrylamide hydrogel matrix that incorporates colloidal crystal arrays. These different sensors are designed based on glucose-boronic acid complexation, whose optical performance depends on both glucose concentration and ionic strength. At low ionic strength, the binding of glucose causes the formation of anionic boronate groups in the polymer matrix, which increases the electrostatic repulsion between hydrogel segments.[514] This sequence of events also creates significant ionic strength differences inside and outside the hydrogel, which generates a Donnan potential.[496,504,515] Both these two inferences explain the hydrogel volume expansion and diffraction peak redshift of the colloidal crystal arrays.[516,517] Under high ionic strength or the presence of PEG, however, the boronate charges generated during glucose binding are neutralized by PEG-capped sodium cations, which increases the association constant of the bidentate complex. This complex further condenses the hydrogel through crosslinking, leading to its volume shrinkage and diffraction peak blueshift.[518,519] Similar strategies can be developed using biological molecule probes (gene, antibody, aptamer, enzyme, etc.) to recognize a specific target. Common molecular recognition in developing biosensors include creatinine-enzyme creatinine deiminase,[520] cholesterol-cholesterol oxidase,[521] avidin-biotin,[522] and nucleotide oligomer-DNA,[523-525] which have been used in compound screening, ligand-receptor screening, label-free optical detection, and cell morphology studies.

Another sensing scheme uses plasmonic assemblies for colorimetric and spectroscopic detection, which works based on tuning the interparticle separation and thus their plasmon coupling. It benefits from diverse plasmonic superstructures that are assembled in the solution phase, whose further process to durable chemical sensors needs additional efforts of preparing solid-state color-switching systems. One strategy to overcome this barrier is to incorporate plasmonic assemblies into chemoresponsive polymers[526,527] or to modify the constituent nanoparticles with responsive polymer brushes.[528,529] The reversible colorimetric sensing can be achieved by polymer structure changes upon introducing chemical stimuli, like pH,[530] humidity,[531,532] biomolecules.[533] These plasmonic polymer nanocomposites have been extensively studied because of their sharp absorption peaks and widely tunable colors, whose further development is, however, limited by slow color switching, small peak shift, poor reversibility, and duration. A recent study reports a new plasmonic chemical sensor by coupling reversible humidity-sensitive salt hydrolysis with the deprotonation/protonation of surface-capped PAA.[534] This advanced technique assembles PAA-capped Ag nanoparticles into a solid film on a sodium borate-coated substrate. Upon humidity exposure, sodium borate hydrolyzes into H_3BO_3, releasing OH^- ions (**Figure 43a**),[535] which subsequently deprotonates the carboxyl groups

of PAA on the particle surface.[536] This sequence of events increases particle surface charges and interparticle separation such that the coupling peak of the Ag assemblies blueshifts. This plasmonic film demonstrates fast responses within 200 ms (**Figure 43b**) upon breathing. Through simple UV irradiation, Ag nanoparticles can easily ripen into large particles, which limits their disassembly under vapor exposure. This additional treatment creates patterns on the Ag plasmonic film in response to humidity. Its sensitive response allows color-switching even under the humidity from a touchless fingertip (**Figure 43c**).

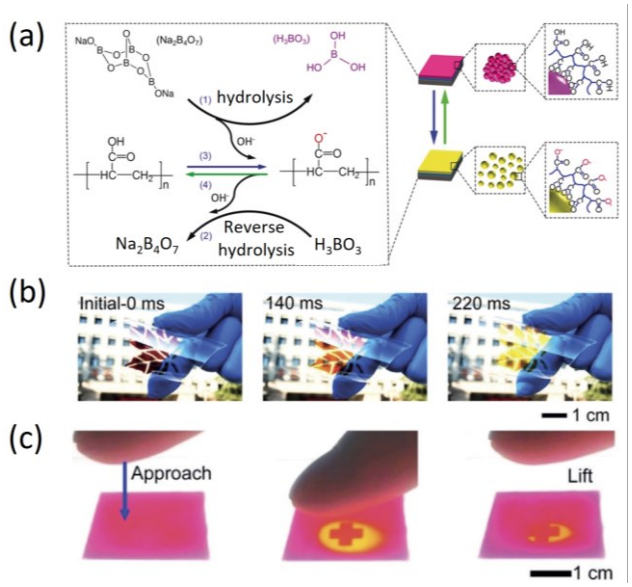

Figure 43. Chemo-responsive plasmonic superstructures. (a) Peak position shifts in response to lattice changes of photonic crystals. Working principle of color-switching plasmonic films. (b) The fast color switching of the plasmonic Ag film upon humidity changes. (c) Touchless plasmonic color-switching of the plasmonic film of Ag nanoparticles. Reproduced with permission from ref [534]. Copyright 2019 John Wiley and Sons.

3.2.6. Mechanically Responsive Polymers

The order of secondary structures can be efficiently tuned by mechanical forces if they are incorporated into a soft polymer matrix. This method is simple and effective in regulating structural orders with a widely accessible response rate and sensitivity. Compared with electronic or fluorescent mechanical sensors, mechanoresponsive colloidal assemblies are advantageous in detecting various mechanical deformations and locomotion. Firstly, their multi-color responses allow strain mapping with high spatial resolution. Depending on the soft matrix and working mechanism, colloidal assemblies provide widely accessible sensing platforms with tunable detection limits and sensitivity. Besides, their colorimetric responses enable fast, on-site estimation of local stresses, and the degree of precision within which they can achieve is not attainable in monochromatic or grayscale sensors. In most cases, the mechanochromic responses are reversible thanks to the elastic deformation of the polymer matrix, enabling the multiple uses of such sensors in practical applications.[537] In developing robust mechanical sensors, self-assembly of block copolymers into lamellar structures is a typical approach to mechanochromic elastomers, where the copolymers serve as deformable matrices and meanwhile maintain photonic bandgaps due to their 1D periodic structures.[538-541] A few representative examples in this regard include PS/P2VP,[539] PSS/PMMA,[542] PDMS/PSPI,[543] and PDGI/PAAm.[544]

Incorporating colloidal crystals into the soft polymer matrix is an alternative approach to mechanochromic superstructures. Upon mechanical stresses, the host polymer substrate deforms and induces concomitant order change in the guest colloidal assemblies. This indirect mechanism is feasible for both photonic crystals and plasmonic assemblies, which exhibit similar color changes. Ge et al. systematically studied the mechanochromic performances of a silica opal embedded in poly(ethylene glycol) methacrylate in response to various mechanical deformations (**Figure 44a**).[545] Their results demonstrate a deformation-dependent color change on a similar mechanochromic film. That is, the diffraction peak of the silica opal redshifts only when such composite gel expands its volume in the vertical direction. Pushing, for example, is a typical unidirectional force that makes the photonic film shrink along the force directions while expanding along the other direction. In this regard, ~22% horizontal shrinkage yields a 100-nm peak redshift (**Figure 44b**). Conversely, pressing the photonic film leads to a blueshift of its diffraction peaks due to the reduced periodicity along the vertical direction (**Figure 44c**). Compared with conventional photonic gels, this silica opal gel has improved mechanochromic sensitivity, extended color tuning range, and fully reversible responses in milliseconds. For early developments of such mechanochromic photonic gels, readers may refer to a review article for a quick overview.[546]

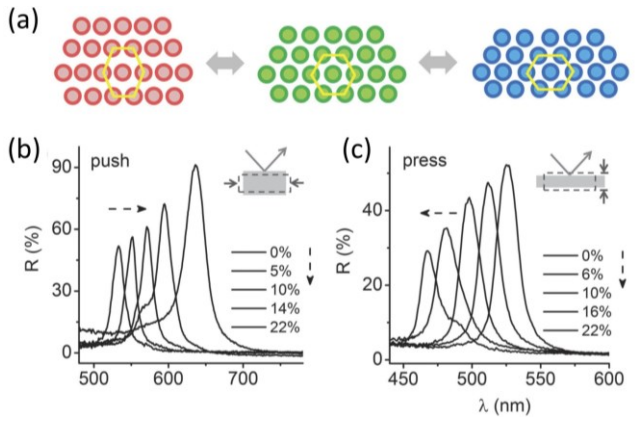

Figure 44. Mechanoresponsive photonic crystals. (a) Schematic illustration of the lattice changes of a photonic crystal in response to mechanical stress. (b) The continuous redshift of colloidal crystal array in response to pushing. (c) The continuous blueshift of colloidal crystal array in response to pressing. Reproduced with permission from ref [545]. Copyright 2014 John Wiley and Sons.

Through this similar material design, plasmonic pressure sensors have also been developed, whose colorimetric responses are determined by the plasmon coupling between adjacent particles.[547] For example, a plasmonic film sensor comprises Au nanoparticle chains in plastic polymer substrates, which self-assemble in colloidal dispersions (**Figure 45a**). At the initial state, the proximity between assembled Au nanoparticles gen-

erates strong plasmon coupling and has a characteristic coupling peak at a long wavelength, which explains the complementary blue color in the plasmonic film. Under uniform mechanical pressing, the plastic deformation of PVP drives the disassembly of the Au nanoparticle chains, leading to a continuous blueshift of the absorption of the plasmonic film (**Figure 45b**). Meanwhile, the perceptible film color changes from blue to red as the pressure increases. Tuning the mechanochromic sensitivity is possible in this strategy by modifying the polymer plasticity using a mixture of two polymers.

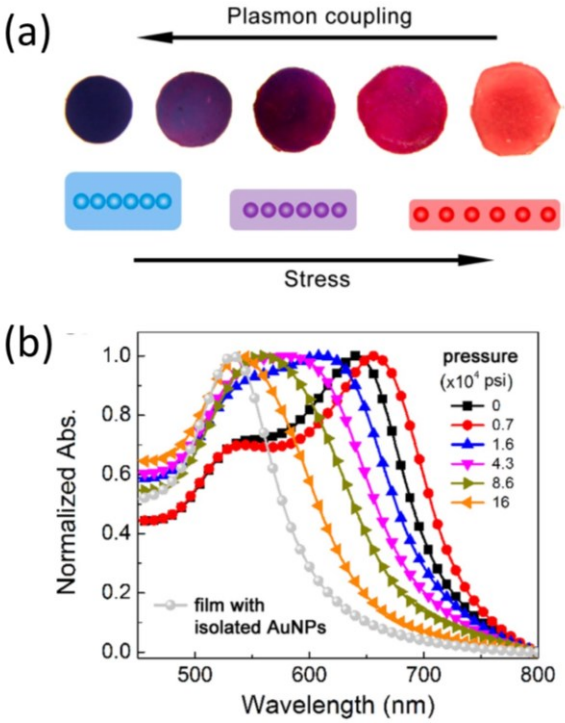

Figure 45. Mechanoresponsive plasmonic chains. (a) The colorimetric responses of the plasmonic film under different pressures. (b) The continuous blueshift of the plasmonic peak in response to mechanical pressure. Reproduced with permission from ref [547]. Copyright 2014 American Chemical Society.

3.2.7. Biohybrid Smart Assemblies

Many biomolecules or cells are natural responsive entities, which play important and unique roles in performing bodily functions. Integrating these living materials into synthetic colloidal assemblies represents an emerging approach to biohybrid smart materials. Before its experimental implementation, one challenge to be addressed is the biocompatibility of the assembled entities, which determines the normal responses and functions of these living materials. To this end, Zhao et al. established a few strategies to integrate synthetic materials with responsive biological systems by carefully engineering the biocompatible organic-inorganic interfaces. One simple route to the proposed biohybrid materials is to introduce biocompatible materials while preparing the colloidal assemblies. Methacrylate gelatin hydrogel is such a natural candidate because of its high compatibility to biological systems,[548,549] which is introduced as scaffold materials of an inverse opal prepared by templating against silica colloidal crystals.[550] Using this inverse opal as substrates, cardiomyocyte has been cultured on the porous materials, and the cell elongation and contraction in the beating processes create a synchronous shift of the inverse opal diffraction peaks. This strategy is later extended to Janus microparticles with the same inverse opal structures (**Figure 46a**).[551] With enough cardiomyocytes attached to the particle surface, an autonomous color change can be observed on the Janus structures because the cell contraction deforms the hydrogel inverse opals and changes the structural orders during each beat (**Figure 46b**). This biohybrid living material that integrates natural responsive biomaterials with synthetic structures is expected to open a new platform to improve life healthcare.[552] One advantage of these biohybrid structures is their ready accessibility to various clinical medicine and bioengineering, like tissue repair and regeneration. Bioinspired structural color patch, for example, is a recent advance among these exciting applications, which is prepared by infiltrating adhesive polydopamine layer into an inverse opal of anti-adhesive poly(ethylene glycol) diacrylate (PEGDA) hydrogel.[553] Such an established method yields a colorimetric Janus tissue patch, with excellent adhesion properties and anti-adhesion property on the other surface (**Figure 46c**). The superior adhesion allows this patch to be applied to biological tissues in vitro, and the synchronous color changes of the photonic patch with the mechanical contraction of the heart demonstrate the good reliability of the biological-synthetic interfaces. With these unique properties and biomimetic smart responses, one may expect a growing interest in this emerging approach in designing smart colloidal structures.

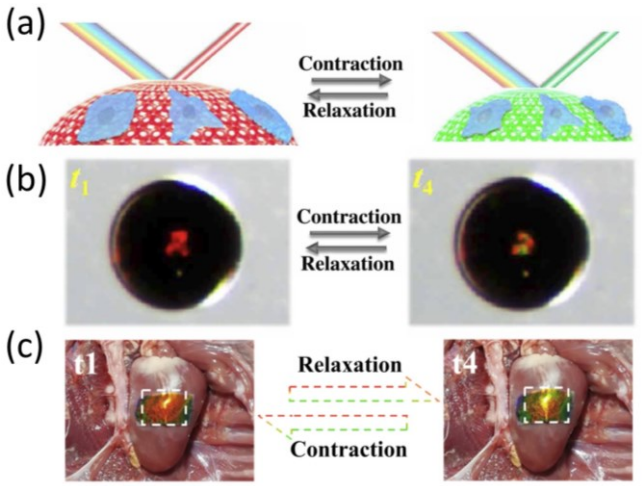

Figure 46. Living photonic crystals enabled by active biological materials. (a) Schematic illustration of living hydrogel inverse opals using cardiomyocyte. (b) Optical microscope images of the structural color changes during half myocardial cycles. Reproduced with permission from ref [551]. Copyright 2020 The Authors, some rights reserved; exclusive licensee American Association for the Advancement of Science. (c) Optical images of the structural color changes of a fixed patch actuated by a duck cardiac. Reproduced with permission from ref [553]. Copyright 2020 The Authors, some rights reserved, exclusive licensee American Association for the Advancement of Science.

3.2.8. Colloidal assemblies with other tunable properties

In addition to the optical properties, strategies to tune the electronic, mechanical, and magnetic properties have also been established by controlling the orders and symmetry of colloidal assemblies.[554] These extended techniques demonstrate the widely accessible phases of colloidal assemblies and the associated diverse solid-state properties by controlling the assembly conditions and magnitude of forces involved. Controlling the surface ligand coverage has been demonstrated as an effective method to tune the interactions in colloidal assembly as well as the physical properties of the superstructures. In assembling oil-phase small nanocrystals, this principle has been employed to create superstructures with different crystal symmetry and electronic properties by choosing different solvents. For example, the coverage of oleic acid on PbS nanocrystals can be tuned if methanol (MeOH), dimethyl sulfoxide (DMSO), and acetonitrile (MeCN) with decreasing solubility to dissolve the oleic acid are used as the bottom liquid during a liquid/air interface assembly.[555] The considerably low coverage in the case of MeOH produces random aggregates while the medium and full coverage using DMSO and MeCN as solvents produce square lattices featuring oriented attachment (**Figure 47a**) and quasi-honeycomb lattices comprising two-layer hexagonal lattices (**Figure 47b**), respectively. Such different assembly manners are due to the different stripping capability of these three solvents. Since MeCN has lowest solubility to oleic acid, the high-density capping ligands on PbS nanocrystals form isotropic solvation layers and thus produce hexagonal lattices. In the case of DMSO with mild oleic acid solubility, the ligand stripping occurs on all the [100] facets because oleic acid has a much weaker binding strength on the [100] facets than the [111] facets in PbS nanocrystals.[556] These selectively exposed [100] facets lead to the orientated attachment between interacting nanocrystals at the interfaces.[557] When MeOH is used as the bottom liquid to completely remove the oleic acid ligands, the nanocrystals assemble into random aggregates driven by the strong coulombic forces between nanocrystals. An ionic-liquid-gated field-effect transistor is later introduced to study the electronic properties of the prepared superstructures (**Figure 47c**). Among all the three samples, the quasi-honeycomb lattice shows no obvious modulated electrical conductivity due to the entirely oleic acid-capped nanocrystals. The square lattices demonstrate prominent electron mobility compared with the random aggregates largely due to the highly ordered lattices with oriented attachment (**Figure 47d**).

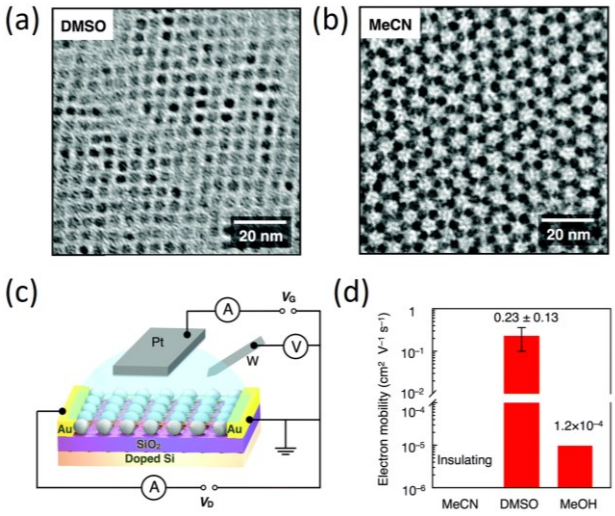

Figure 47. Tunable electronic properties of PbS nanocrystal assemblies. (a, b) TEM images of PbS superlattices with (a) dimethyl sulfoxide and (b) acetonitrile as the bottom liquids during the assembly at the air/liquid interfaces. (c) Schematic illustration of the prepared ionic-liquid-gated field-effect transistor. (d) Mobility values of the PbS NC films prepared using various bottom liquids. Reproduced with permission from ref [555]. Copyright 2019, Royal Society of Chemistry.

Another important property associated with superlattice structures is mechanical properties. The widely accessible crystal symmetry and lattice constants of colloidal assemblies make it possible to link the mechanical properties to the superlattice order and symmetry and to elaborate superstructures with defined strength, stiffness, and toughness by controlling the particle separation and connectivity. Polymer-capped nanocrystals are ideal for studying the dependence of mechanical strength of superstructures on crystal architectures and dimensions due to the highly tunable polymer length, type, and grafting density on particle surfaces. Through a similar evaporation-induced interfacial assembly process, polystyrene-capped Au nanoparticles can be assembled into hexagonal lattices, with millimeter to centimeter lateral dimensions and up to hundreds of nanometers thickness.[558] The superlattice periodicity can be carefully tuned by changing the polystyrene molecular weight while maintaining the Au nanoparticle size. Increasing the molecule weight leads to hexagonal superlattices with increasing particle separation (**Figures 48a** and **48b**). The structural conformation of capped polystyrene can be described by the polymer brush model, which deals with polymers with their one end connected to an interface.[559,560] This model supports two physical interactions between capped polymers, including entanglement between long chains and physically interlocked segments between interdigitated polymer strands, which in combination with the Van der Waals forces between the inorganic cores contribute to the different elastic moduli of the superstructures. Specifically, the elastic modulus of Au superstructures increases as with the molecular weight and the crystal periodicity, which are all higher than that of pure polystyrene films (**Figure 48c**). This observation confirms the critical role of superlattice structures and the contribution of surface capping ligands on the mechanical properties of colloidal assemblies. If colloidal particles are

assembled into superstructures featuring hard surface contact and interlocked junction, it is possible to greatly enhance the mechanical properties of the assemblies. To this end, europium oxide nanosheets are assembled into superstructure films with controllable nanosheet configurations, including face-to-face and interlocked manners (**Figure 48d**), using a similar interfacial assembly method.[561] The formation of the interesting, interlocked phase is due to selective exfoliation of oleic acid ligands from the nanosheet edge and the ensuing anisotropic atomic packing factor on the nanosheets. One direct consequence of this event is the greater solvophobicity on the nanosheet edges than that of the top and bottom surfaces, making nanosheets reconfigure into the interlocked phase to reduce the surface potential. Such a unique phase leads to a greatly enhanced Young's modulus of the interlocked phase than that of random and face-to-face assemblies (**Figure 48e**). Further theoretical analysis and experimental results demonstrate the superior mechanical properties of the interlocked phase with enhanced transverse compression and slipping resistance.

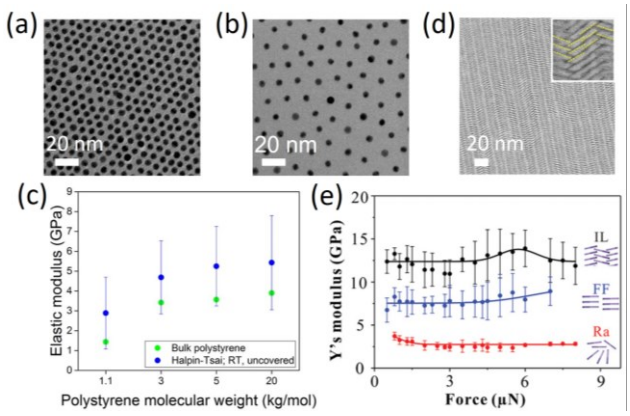

Figure 48. Mechanical properties of superstructures assembled from polystyrene-grafted Au nanocrystals with different polystyrene molecular weights. TEM images of Au superlattices with polystyrene molecular weight of (a) 1.1-kg/mol and (b) 20-kg/mol. (c) The elastic modulus of bulk polystyrene (green dots) and superlattice (blue dots) calculated using the Halpin–Tsai model. Reproduced with permission from ref [558]. Copyright 2017 The Authors. (d) TEM image of the europium oxide nanosheet superstructures. (e) Young's modulus as a function of loading force for different superstructures. The IL, FF, and Ra represent interlocked, face-to-face, and random assemblies, respectively. Reproduced with permission from ref [561]. Copyright 2020 John Wiley and Sons.

Tuning the magnetic properties of materials is also possible by controlling the assembly of colloidal particles. It has been long recognized that the magnetic properties of nanostructures are dependent on particle size, morphology, and surface properties. When nanostructures are assembled in proximity, their induced magnetic dipoles interact, with strength and direction highly dependent on particle arrangement within the assemblies. For example, superstructures of nickel nanoparticles, including nanochains, nanowires, fabrics, and foils, demonstrate tunable coercivity depending on the superstructure morphologies and sizes.[562] In a close study, a reversible transformation between paramagnetic and ferromagnetic properties is achieved by assembling and jamming a monolayer of magnetic nanoparticles at the water-oil interfaces.[563] An aqueous dispersion of carboxylated, 22-nm Fe_3O_4 nanoparticles are firstly immersed into amine-modified polyhedral oligomeric silsesquioxane (POSS-NH2) in toluene. The surfactant POSS-NH_2 self-assembles at the interfaces and interacts with the magnetic nanoparticles due to the electrostatic attraction, leading to the formation of a monolayer of the magnetic nanoparticles at the interfaces (insets in **Figure 49a**). The saturated magnetization, coercive field, and remanent magnetization of the ferrofluid droplets depend on the total number of nanoparticles in the droplets. Adding more surfactants or decreasing pH will cause more particles to assemble at the interfaces, and more interfaces will be covered by the magnetic particles with reduced surface tension. With sufficient surface coverage, the particle will jam at the liquid-liquid interfaces, leading to a transition from paramagnetic to ferromagnetic droplets (**Figure 49a**). If the nanoparticles are not jammed, there is no hysteresis in the magnetization measurement, but yielding different saturated magnetization under different pH values and particle concentrations (**Figure 49b**), which underpins the importance of particle jamming in the ferromagnetic transition. Another remarkable feature of the ferromagnetic droplets is that their shapes can be reconfigured using a template. As demonstrated in **Figure 49c**, a spherical droplet is drawn into a glass capillary and transformed to a rod shape while retaining the ferromagnetic properties after being released. This interesting shape change is driven by the decrease of interfacial energy caused by a 2.5-fold increase in interface areas and more particles jammed at the interfaces. The formation of ferromagnetic droplets is reversible. By controlling the monolayer assemblies at the interfaces, the magnetic properties and the shapes of the droplets can be tuned in response to external stimuli, opening the door to reconfigurable materials through the colloidal assembly.

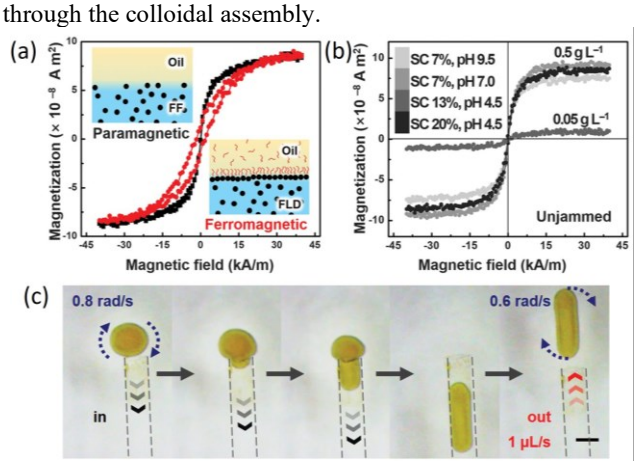

Figure 49. Reconfigurable magnetic properties of liquid droplet superstructures. (a) Magnetic hysteresis loops of droplets with and without an interfacial layer of 22-nm Fe_3O_4 nanoparticles. Insets show the ferrofluid (FF) and ferromagnetic liquid droplet (FLD). (b) Hysteresis loops of individual 5-mL aqueous droplets with an interfacial layer of Fe_3O_4 nanoparticles in response to pH changes. (c) Reconfigurable shape changes of the droplets using a glass capillary as a mechanical mold. Scale bar: 1 mm. Reproduced with permission from ref [563]. Copyright 2019 The American Association for the Advancement of Science.

3.3. Tuning the Assembly Orientation

3.3.1. Magnetic Orientation Control

Magnetic anisotropy describes the direction-dependent magnetization properties of magnetic materials, which allows remote, reversible, and rapid orientational control over many physical and chemical properties (see the nanoscale magnetic assembly in **section 2.1**).[564] This unique property can be easily developed to control the collective orientation of magnetic nanorods for magnetically actuated liquid crystals.[63] It allows instant and reversible manipulation of rod orientation in a dispersion using a considerably weak magnetic field, which exhibits orientation-dependent light transmittance between two polarizers (**Figure 50a**). A close measurement demonstrates their extremely fast optical responses to a magnetic field (within a few milliseconds in **Figure 50b**). This technique can be combined with magnetic field-assisted lithography to create pre-designed patterns, which may be further processed for displays or anticounterfeiting (**Figure 50c**). The combination of orientation-dependent physical properties and the widely accessible monodisperse nanostructures make this strategy promising for creating smart responses through regulating orientations.

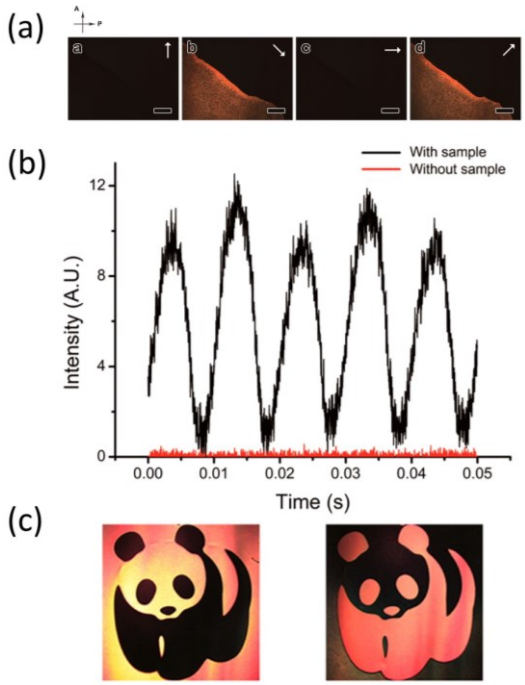

Figure 50. Magnetically actuated liquid crystals. (a) Polarized optical microscopy images of liquid crystals under different magnetic field directions (white arrows). Scale bars: 500 μm. (b) Fast and reversible transmittance changes in response to an alternating magnetic field. (c) Polarization-modulated patterns under cross polarizers. Reproduced with permission from ref [63]. Copyright 2014 American Chemical Society.

But the ability to control the structure orientation is not only of practical interest: easy and repeatable access to colloidal crystal orientational control is the key to understanding and exploiting their unique collective properties. Paramagnetic nanoparticles are a natural choice because of their easy fabrication and processing under external magnetic fields. One challenge associated with this implementation is that some monodisperse superparamagnetic colloids are spherical and lack magnetic anisotropy.[565] Assembling them into anisotropic superstructures is an empirical approach to overcome this barrier by either fixing the superstructures or embedding them into a polymer matrix.[426,566-568] In the case of photonic microspheres made of 1D magnetic chains, their magnetic shape anisotropy aligns the chains along the external magnetic field so that the microsphere orientation and photonic crystal diffraction can be tuned using a permanent magnet (**Figure 51a**).[569] This photonic microsphere is prepared by polymerizing emulsion droplets under the presence of a magnetic field to assemble 1D chains and uniformly align them, and the diffraction of the products can be tuned over 100 nm by changing the field direction (**Figure 51a**). By combining the field strength and orientational control, it is possible to prepare multicolor photonic balls with their on-off states highly tunable by changing the field direction (**Figure 51b**). The potential of magnetic shape anisotropy is not only to practically control assembly orientation and properties but also to fundamentally determine the crystal symmetry and structures during the self-assembly process. In fact, a few recent studies have underpinned this important role, providing emerging photonic structures and optical tunability. Ellipsoidal nanoparticles are unique in this regard due to their tunable aspect ratios and easy magnetization along their geometrical long-axis.[570] They self-assembled into face-centered orthorhombic photonic crystals driven by the interplay between electrostatic repulsion and magnetic attraction, whose optical properties are highly tunable by changing magnet directions (**Figure 51c**). Considering a constant incident light, changing the field direction from parallel to perpendicular to light incidence induces a continuous diffraction blueshift (**Figure 51d**). Under a linear Halbach array, the photonic crystals exhibit defined monochromatic stripes in accordance with the periodic field changes (**Figure 51e**).

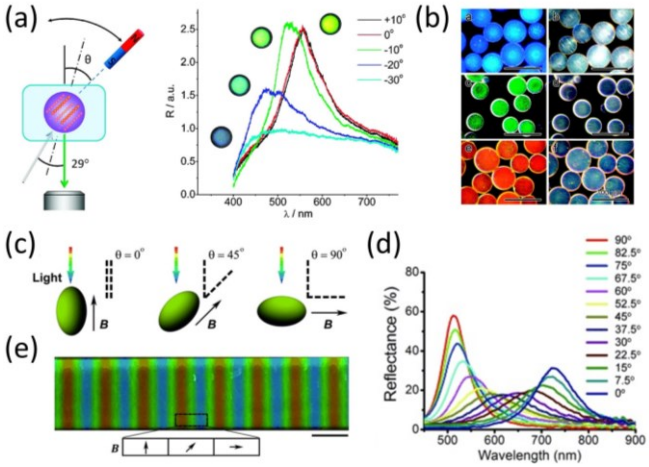

Figure 51. Responsive photonic crystals by tuning magnetic field directions. (a) Schematic illustration (left) and reflection spectra (right) of orientation-dependent photonic balls in response to different magnetic field directions. (b) Optical microscopy images of the photonic balls, whose structural colors can be switched on (left panels) and off (right panels) by changing the field direction. Scale bars: 100 μm. Reproduced with permission from ref [569]. Copyright 2009 American Chemical Society. (c) Schematic outline of the magnetic assembly and field-tuning of photonic crystals from ellipsoidal nanoparticles. (d) The reflection spectra under different

magnetic fields. (e) Digital pictures of the photonic crystals under a non-ideal linear Halbach array. Scale bar: 5 mm. Reproduced with permission from ref [570]. Copyright 2015 John Wiley and Sons.

Similarly, highly tunable structural colors are also observed in the magnetic assembly of large nanorods into body-centered tetragonal crystals (crystals shown in **Figure 11**), which are directly driven by magnetic forces (**Figure 52a**). In the case of large nanorods, one apparent distinction from the small ones is the much stronger magnetic force in an external magnetic field than the electrostatic repulsion; the magnetic interaction will thus dominate their assembly process, leading to better lattice periodicity and more bright colors (**Figure 52b**). Another interesting phenomenon unique to the large nanorods is that the tetragonal colloidal crystals have a needle-like microscopic morphology and a reduced crystal transverse symmetry. Switching the external field will cause the colloidal crystals to rotate along their long axes if they are confined in two glass slides, which is largely because of the Zeeman coupling between the large crystal and the external field. This sequence of events creates simultaneous color changes since different facets will be exposed with a corresponding periodicity change during the rotation of a small piece of colloidal crystal (**Figure 52c**).

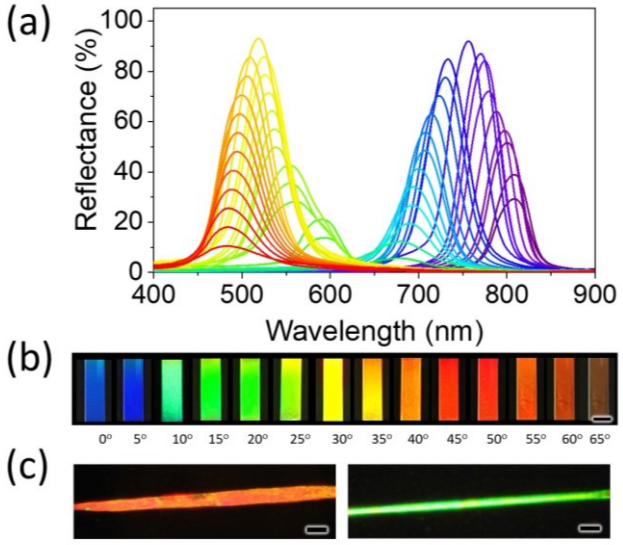

Figure 52. Magnetically responsive and highly tunable 3D photonic crystals from the magnetic assembly of Fe_3O_4 nanorods. (a) Reflection spectra of the photonic crystals under different magnetic field directions. (b) Digital images demonstrating the bright structural colors in a colloidal dispersion of the photonic crystals. Scale bar: 5 mm. (c) Optical microscopy images of one photonic crystal under different orientations by switching the applied field direction. Scale bar: 20 μm.

If the magnetic shape anisotropy of colloids is coupled with their dipole-dipole interactions, it is possible to prepare new types of photonic structures, which, however, require comparable Zeeman coupling strength and dipole-dipole coupling strength. To this end, a recent study using magnetic nanocubes as building blocks explains how this particular condition can be fulfilled.[97] Specifically, the easy axis of paramagnetic nanocubes is their body diagonals. Driven by the Zeeman coupling, nanocubes tend to tilt themselves such that the diagonals are parallel to the external field. The dipole-dipole coupling between nanocubes, however, favors close face-to-face packing to minimize the magnetic potential energy, which is apparently different from their easy axes. In a colloidal dispersion of magnetic nanocubes, such competing interplay between Zeeman coupling and dipole-dipole coupling interestingly leads to 1D chains of nanocubes in an edge-by-edge manner (**Figure 53a**). The [110] chains diffract light to a direction that is different from the incident light, whose structural colors are dependent on both viewing angles and magnetic field directions (highlighted in the bottom panel in **Figure 53a**). One of their main difference with 1D photonic chains of nanospheres is the highly orientation-dependent photonic responses, which can be reversibly, continuously tuned from UV to visible, and near-infrared (NIR) regions by simply changing the field direction (**Figure 53b**). A low-concentration nanocube dispersion can efficiently diffract brilliant structural colors upon applying a magnetic field, whose intensity is qualitatively higher than that of nanosphere photonic chains (**Figure 53c**). This new photonic structure and its unique optical properties, in combination with our unpublished results that magnetic nanorods can magnetically assemble into tetragonal or orthorhombic lattices depending on assembly conditions, further underpin the importance and great potentials of magnetic shape anisotropy in assembling novel smart superstructures.

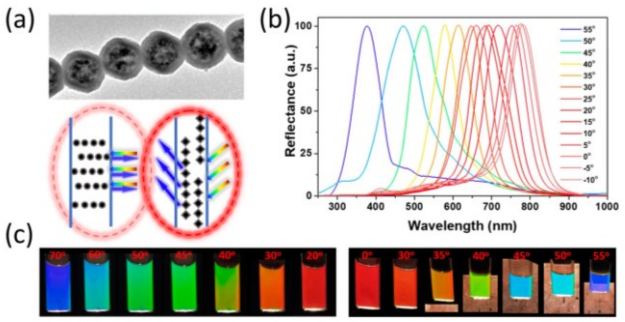

Figure 53. Magnetic assembly of nanocubes for orientation-dependent photonic responses. (a) TEM image of a photonic chain assembled from Fe_3O_4 nanocubes with edge-to-edge manner. The bottom inset demonstrates the different diffraction performances between photonic chains made of nanospheres and nanocubes. (b) Reflection spectra of photonic crystals measured under different magnetic field directions. (c) Structural colors of a colloidal dispersion of nanocubes in response to different viewing angles (left panels) and magnetic field directions (right panels). Reproduced with permission from ref [97]. Copyright 2019 American Chemical Society.

Thanks to its high effectiveness, magnetic orientational control offers many opportunities, especially when it is coupled with other physical properties, such as surface plasmon resonance. Au nanorods have been extensively used in this regard largely because of their high stability, widely accessible synthesis, highly tunable sizes, and plasmonic properties. The resonant oscillation of free electrons under light excitation is dependent on the excitation geometry, which has been illustrated in **Figure 54a**. Consider a z-polarized light and imagine the rotation of a single Au nanorod in the y-z plane. Its free electrons can form resonant oscillation within rod short or long axes, causing a transverse and longitudinal plasmon mode, respectively. In

principle, selective excitation of these two modes is possible by controlling the collective orientation of Au nanorods, which is practically difficult due to the lack of an efficient driving force. Magnetic forces are the right candidate for overcoming this long-term challenge if one considers their efficient orientation control and long-range effectiveness, whose implementation is then determined by how to integrate magnetic anisotropy into plasmonic nanostructures. Back in 2013, our group reported direct attachment of Au nanorods to the surfaces of magnetic nanorods through electrostatic interactions; this method yields magnetic-plasmonic hybrid nanorods with coupled magnetic and plasmonic anisotropy (**Figure 54b**).[571] By using the orientation control shown in **Figure 54a**, the transverse (at ~515 nm) and longitudinal (at ~725 nm) modes can be selectively excited by simply applying magnetic fields to assemble the dispersed hybrid nanorods (**Figure 54c**). A different but advanced approach uses templating strategy to directly grow Au nanorods alongside magnetic nanorods,[572] which employs highly permeable polymer shells to confine the seeded growth in a gap.[573] This seed-mediated space-confined growth is universal to prepare Janus nanorods with different chemical components and plasmonic properties. The polymer shells not only confine the anisotropic growth of Au into a shape complementary to the gap but also allows parallel alignment of the two rods, as demonstrated in **Figure 54d**. A joint experimental and theoretical study suggests a trigonometric dependence of the two plasmon modes on orientational angles (**Figure 54e**).

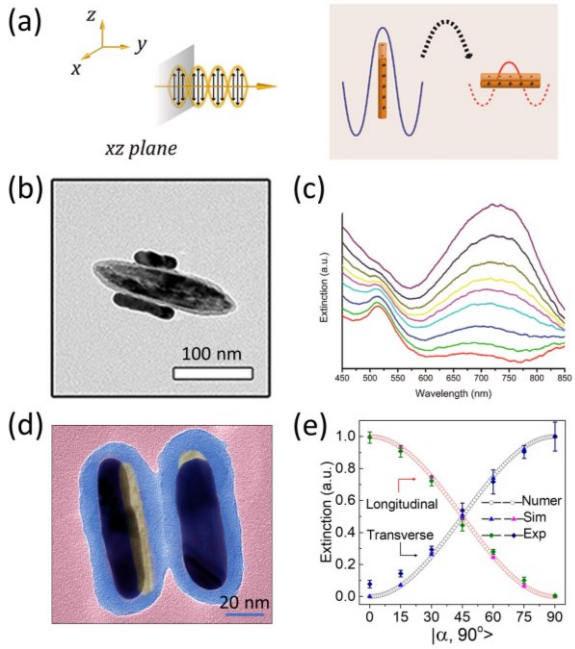

Figure 54. Magnetically tunable plasmonic excitation of hybrid nanorods. (a) Schematic illustration of the orientation-dependent excitation of longitudinal and transverse resonant modes of plasmonic nanorods. (b) TEM image of hybrid Fe_3O_4/Au nanorods assembled by surface attachment. (c) Extinction spectra of hybrid nanorods under different magnetic fields. Reproduced with permission from ref [571]. Copyright 2013 American Chemical Society. (d) TEM image of hybrid Fe_3O_4/Au nanorods prepared from space-confined seeded growth. (e) The dependence of plasmonic excitation and longitudinal plasmon mode of Au nanorods relative to light polarization. Reproduced with permission from ref [572]. Copyright 2020 The Author(s).

This strategy has recently been successfully extended to prepare Fe_3O_4/Cu and Fe_3O_4/Ag hybrid nanorods with a similar size and morphology; their unique coupled plasmonic-magnetic anisotropy is useful in fabricating polarization-sensitive optical devices and robots.[574] Two other alternative approaches produce nanorods with different fine structures but similar coupled magnetic-plasmonic anisotropy. Templated self-assembly of superparamagnetic and Au nanocrystals in nanoscale rod-like templates produces magnetically switchable plasmonic nanorods. The rods comprise a mixture of binary nanocrystals, with their size being determined by the used templates (**Figure 55a**).[575] Notably, the self-assembly process allows flexible changes of building blocks so that one may expect to produce many colloidal superparticles of desirable components. Because of the large size of the products, their optical modulation mainly occurs in NIR regions, which is achieved by changing the direction of a magnet (**Figure 55b**). Another templating strategy is extensively reported by electrochemical deposition of magnetic and plasmonic segments in anodized aluminum oxide (AAO) channels.[576-578] Controlling the chemical components of each block is important to optimize the magnetic and plasmonic properties, which can be achieved by tuning the sequence and amount of metal plating solution during the electrochemical deposition. Currently available components for magnetic and plasmonic blocks include Fe, Ni, and Au, respectively (triblock Au-Fe-Au nanorods shown in **Figure 55c**).[577-580] These multi-block nanorods are more often used for dynamic modulation of plasmonic scattering or absorption under a rotating magnetic field for biodetection (**Figure 55d**).[576,581]

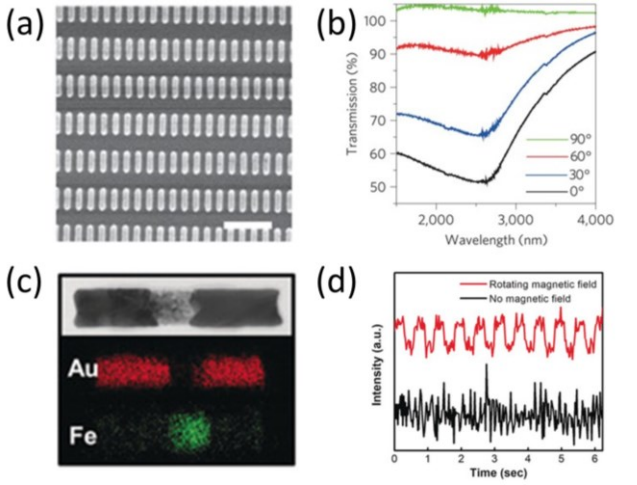

Figure 55. Magnetically tunable plasmonic excitation of hybrid nanorods. (a) SEM image of hybrid nanorod arrays assembled from a binary nanocrystal mixture. Scale bar: 1 μm. (b) Transmission changes of the binary hybrid nanorods response to different magnetic fields. Reproduced with permission from ref [575]. Copyright 2017 Springer Nature. (c) TEM image and elemental mapping of triblock nanorods. (d) The dynamic optical response of the nanorods under an alternating magnetic field. Reproduced with permission from ref [576]. Copyright 2018 John Wiley and Sons.

Magnetic orientation control is also applicable to colloidal assemblies with tunable metasurfaces. This technique takes advantage of remote, rapid, and reversible magnetic responses to tune the surface properties of solid films. To make the soft materials magnetically responsive, ferromagnetic particles are commonly mixed with polymer precursors, which are polymerized against a template to generate designed surface features, like the 2D arrays of pillars shown in **Figure 56a**.[582] An external magnetic field is applied simultaneously to magnetize the employed magnetic particles so that each pillar act as a micrometer permanent magnet, whose orientation can be actively tuned by a magnetic field. One sequence of this magnetic orientation control is the anisotropic transportation properties, leading to the fast movement of liquid droplets along the tilt-angle direction (**Figure 56b**). Based on the same strategy, another study reports a metasurface with tunable surface adhesion in response to magnetic field changes.[583] The T-shaped surface patterns (**Figure 56c**) show similar responses to an external magnetic field, leading to dynamic switching between an adhesive and non-adhesive state (**Figure 56d**).

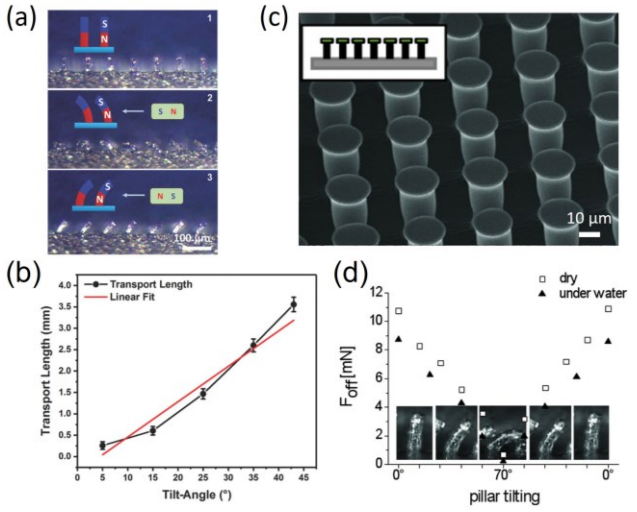

Figure 56. Tunable surface properties of magnetic micropillar arrays in response to a magnetic field. (a) Optical images showing the micropillar arrays in response to different magnetic fields. Scale bar: 100 μm. (b) The dependence of transport length on tilting angle. Reproduced with permission from ref [582]. Copyright 2013, John Wiley and Sons. (c) SEM image of magnetic polymer patterns. (d) Change of the adhesion force with the bending of the pillars caused by changing the magnetic fields. Inset: the corresponding microscopic images of the tilted pillars. Reproduced with permission from ref 381[583]. Copyright 2013, John Wiley and Sons.

3.3.2. Mechanical Force

When a secondary structure of nanoparticles adheres to or is embedded in a polymer matrix, their positional and orientational orders are subject to mechanical forces that are acting on the film. In a simple case where a polymer film is unidirectionally stretched or compressed, its deformation features simultaneous expansion and contraction depending on the strains and directions. In the case of being compressed, it has axial contraction and transverse expansion, which is contrary to a film being stretched. These processes can be precisely described by Poisson's ratio, which is between -1.0 and 0.5 for elastic polymer films because of the requirement for Young's modulus, the shear modulus, and the bulk modulus to have positive values. Such mechanical strains modify the structures of associated colloidal assemblies via changing their positions, orientations, or both, with the first one having been introduced in **section 3.2**. The fact that the Poisson's ratio is smaller than 0.5 in most cases implies the presence of shear forces under the uniaxial strains, which is responsible for the ensuing alignment of anisotropic structures. Such a deformation mode featuring a small Poisson's ratio has been used to assemble various anisotropic nanostructures, such as Au nanorods,[572,584] carbon nanotubes,[585,586] cells,[587] liquid crystal mesogens.[588] An impressive consequence of uniaxial stretch is the unidirectional alignment of the long axis of randomly distributed anisotropic structures relative to the mechanical forces, whose orientational orders have been demonstrated by spectroscopy and electron microscopy. If the nanostructures have been assembled into a liquid crystal phase in the polymer film prior to mechanical strains, they can provide a precise assessment of how these mechanical forces change the collective orientation through deformation and enable the design of highly sensitive mechanical sensors by monitoring such reorientation.[572]

Compared with stretching and pressing, twisting is more complex but promising to enable new superstructures that are not attainable by other means. Because twisting a polymer film induces chiral deformation, it is a natural platform to create chiral colloidal assemblies. Its potential in this regard has been demonstrated in a recent study that uses the hybrid magnetic-plasmonic nanorods shown in **Figure 54d** as building blocks, in which the assembled chiral superstructures exhibit compelling optical properties in response to linear and circular polarized light (**Figure 57a**).[572] During preparation, the hybrid nanorods are firstly assembled into a nematic phase with perfect orientational order using a magnet, followed by polymerization to fix such phase in a polymer film (**Figure 57b**). Their orientation is deliberately fixed at 45° relative to film edges so that the following structure reorientation can be conveniently observed using a linear polarizer. Interestingly, twisting the plasmonic film causes site-dependent orientation changes of the hybrid nanorods and helical films, which drive the transition of the associated superstructures from a nematic phase to a chiral phase (left panel in **Figure 57b**). In addition to the generation of remarkable circular dichroism signals in the twisted film, an alternative color switching is observed under a linear polarized light because of the reorientation of hybrid nanorods (right panel in **Figure 57b**). This consideration is further confirmed by a simple model during a finite-element analysis, in which the local orientation of individual nanorods can be precisely calculated based on the twisting angle and the rod position. This simple model predicts a linear increase in the rotation angle of each nanorod and a nonlinear change of their azimuth orientation in response to twisting deformation, leading to a chiral configuration of the hybrid nanorods (**Figure 57c**).

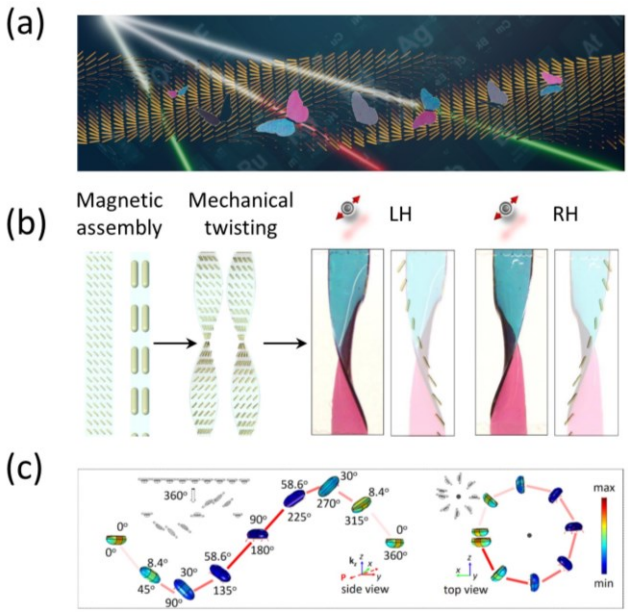

Figure 57. Twisting chirality enabled by the nanoscale magnetic assembly and mechanical deformation. (a) Schematic illustration of the chiral configuration of plasmonic nanorods. (b) Schematic illustration (left panels) and digital pictures (right panels) of the twisted plasmonic film. (c) Simulation snapshot of chiral plasmonic nanorods under linearly polarized light excitation. Reproduced with permission from ref [572]. Copyright 2020 The Author(s).

Another relevant but simple strategy assembles nanospheres into chiral superstructures.[589] This inverse procedure starts with twisted polymer films, on which nanospheres are deposited through layer-by-layer assembly (**Figure 58a**). Simply releasing the twisted films leads to a transfer of the macroscale chirality to the underlying nanostructures in a top-down manner (**Figure 58b**). One significant advantage associated with the macroscale mechanical manipulation is the easy control over the nanoscale superstructure handedness and CD single intensity (**Figure 58c**). Because the chirality is determined by the macroscopic twisting deformation, repeated stretch-release cycles cause reversible chiroptical responses in the composite film. Such a strategy is operational for various nanostructures, which represents a general approach to mechanoresponsive smart materials with tunable chirality and unique optical properties.

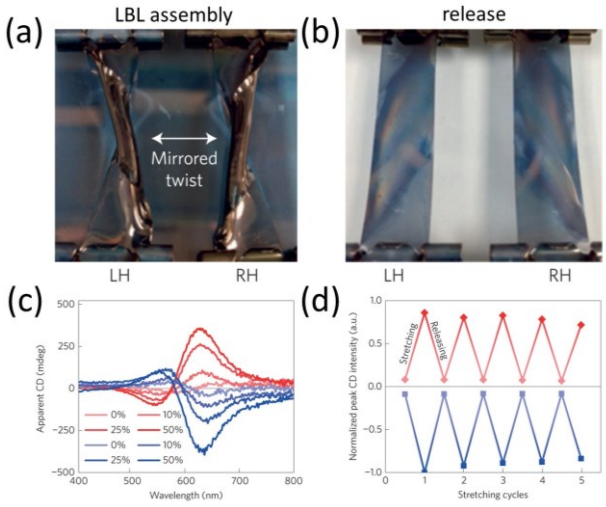

Figure 58. Reconfigurable chiroptical nanocomposites. (a) Polymer substrate after deposition of plasmonic nanoparticles in left-handed and right-handed configurations. (b) Relaxed polymer substrate coated with Au nanoparticle multilayers. (c) Apparent CD spectra of samples under different mechanical stretching. (d) The highly tunable and reversible tuning of CD intensity in response to mechanical stretching and releasing. Reproduced with permission from ref [589]. Copyright 2016 Springer Nature.

3.3.3. Liquid Crystals

The phase transition of liquid crystals is associated with distinctive collective reorientation of molecules under external stimuli, which can be used as host systems to control the orientation of a guest colloidal crystal.[590-592] Albeit full of challenges, the design of such composite materials that combine the fluidity of liquid crystals and the ordering of colloids is of both fundamental importance and technical interest.[593] In fact, several pioneering studies have confirmed the possibility of using liquid crystals to control colloidal orientation by coupling them in a model host-guest system with controllable boundary conditions. The host-guest system comprises a dispersion of colloidal particles with proper surface properties in a liquid crystal; the mixture is infiltrated into glass cells, rectangular capillaries, or microfabricated containers of various dimensions, with their inner surfaces having been modified to impart molecule alignment. Although these studies use colloids of different shapes (e.g., nanorods,[594,595] nanoplates,[593,596-599] dumpling-shaped particles,[136] helices[600]), this new understanding has allowed one to appreciate that the interfacial interaction in the boundary conditions is determined by the surface property of the guest colloids. In experiments, the boundary conditions can be precisely controlled by the density of polymer brushes (e.g., PEG) on the colloid surface; the degree of sensitivity with which the orientation and symmetry of the guest colloid crystal are affected is so high that simply increasing the PEG density on ferromagnetic nanoplates leads to perpendicular to nearly tangential alignment relative to the host molecules.[593,596,597] These consideration explains why the emergency of new orientational order in the coupled colloids-liquid crystals system is possible, which is different from the symmetry properties of their own.[598] The stimuli-responsive boundary conditions on the colloidal surfaces interplay with the competing electrostatic and elastic interactions between each constituent, allowing colloids to rotate relative to the liquid

crystal host in response to external stimuli. This sequence of events first assembles colloids into a thermodynamically favorable phase, which in turn transforms its symmetry to and changes the phase of the host liquid crystal via ensuing molecule reconfiguration.

Other deterministic properties that influence crystal symmetry include solution temperature, constituent concentration, and colloid surface charge. In a few close studies of these important parameters, charged colloidal disks (**Figure 59a**) in a nematic host could self-assemble into the nematic, smectic, columnar organization with symmetries varying from uniaxial[601,602] to orthorhombic[595,603-606] and monoclinic.[607-609] To ensure their good colloidal stability and optimize the boundary condition towards self-reconfigurability, upconversion nanodiscs are coated with silica and modified with polyethylene glycol.[598] When dispersed in a nematic liquid crystal in a unified container, nanodiscs locally distort the molecular nematic order, and the anisotropic interactions on their surfaces cause strong elasticity-mediated interactions, whose binding energy is thousands of times greater than thermal energy.[610,611] Therefore, the nanodiscs can self-assemble with unidirectional order in the dispersion, which is surprisingly dependent on solution temperature (**Figure 59b**). It is pointed out that increasing the temperature causes the nanodiscs to rotate from perpendicular to parallel orientation relative to liquid crystal molecule alignment. Such temperature-dependent orientation control is attributed to boundary condition changes mediated by the interplay between electrostatic[612] and temperature-dependent molecular interactions[613] at the colloid surfaces. It further perturbs the order and symmetry of the liquid crystals depending on their relative orientation, which preserves the initial $D_{\infty h}$ symmetry of nanodiscs and liquid crystals at parallel alignment but induces D_{2h} symmetry and C_{2h} symmetry at perpendicular and tilted alignment, respectively. In addition to temperature, voltages are also found to have profound impacts on colloid orientation and crystal symmetry because they can change the phase and alignment of the host liquid crystals.[614]

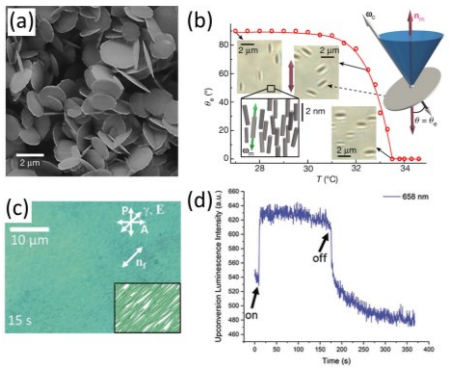

Figure 59. Thermo- and electro-responsive liquid colloidal crystals. (a) SEM image of disk building blocks. Scale bar: 2 μm. (b) The transition of orientational order of the liquid colloidal crystals in response to different temperatures. Reproduced with permission from ref [598]. Copyright 2021 Springer Nature. (c) Co-alignment of nanorods relative to an electric field. (d) The upconversion luminescence intensity of liquid colloidal crystals in response to application of an electric field. Reproduced with permission from ref [594]. Copyright 2019 John Wiley and Sons.

In other carefully prepared conditions, colloidal nanoparticles of highly anisotropic shapes can self-assemble into a lyotropic nematic liquid-crystalline phase without the need for an anisotropic liquid crystal host.[615-617] Under this scenario, the orientational order is driven by the interactions between nanorods in a high-concentration colloidal dispersion, whose orientation and properties show interesting dependence on electric fields.[618-621] For example, upconversion nanorods with large aspect ratios can transit from an isotropic phase to a nematic phase upon applying an electric field, with the rod orientation parallel to the field direction (**Figure 59c**). Such orientational order produces a field-induced birefringence and anisotropic upconversion emission, which is dependent on field strength and direction. In **Figure 59d**, the upconversion fluorescence intensity shows a sharp rise and fall in response to on-off switching of the electric field, demonstrating that the polarization dependence of the upconversion luminescence is determined by the nanorod orientation. These interesting observations, in combination with the diverse crystal structures presented in the guest-host systems, underpins both the fundamental importance and the practical potentials of liquid crystals in developing orientation-mediated smart superstructures.

3.3.4. DNA Templates

Assembling colloidal structures with chiral symmetry is an extreme case that requires precise control over particle position and orientation. One of the fundamental challenges is to design chiral superstructures in a high precision within which the chirality and circular dichroism can be tuned similarly in assembling colloidal lattices. To overcome this challenge, DNA techniques have been extensively introduced in many powerful bottom-up approaches to precisely control the relative orientation and position of colloidal particles, particularly plasmonic Ag and Au nanostructures, due to their unique optical properties and easy binding to functional groups in DNA strands.[67] Depending on the working mechanism, current strategies consist of the DNA templating method and DNA scaffold-directed self-assembly. In some self-assembly, colloidal particles are first modified with single-stranded DNA, which can react with other specifically functionalized particles, during which the specific DNA recognition directs colloids to self-assemble in a designated manner into configurational or constitutional chiral structures. In the templating strategy, DNA backbone or complex origami templates act as nanoscale rigid substrates for site-sensitive colloid deposition. The DNA origami templates, such as sheets or bundles, comprise long DNA strands that are assembled and folded into solid nanoscale templates in a programmable manner.[622-624] The various pre-designed binding sites containing single-stranded DNA on the templates capture colloids modified with complementary DNA strands via DNA hybridization, leading to chiral oligomers,[625,626] clusters,[627,628] and chains.[193,629]

The potential of DNA templates in controlling colloid orientation allows the design of a stepwise plasmonic clock, whose optical signals are highly sensitive to the relative orientation of rod dimers and specific DNA strands.[630] The plasmonic clock consists of an Au nanorod dimer (**Figure 60a**), with one nanorod assembled on a bottom DNA origami nanoplate and the other one attached on a top origami bundle.[196,631,632] Both the two tem-

plates contain 10 binding sites, allowing the assembly of Au nanorods with designated orientation to the template surfaces. Two 12-nt foot strands are extended from the two ends of the DNA origami bundle, which serve as a rotator to accurately control the orientation of the top nanorod. A ring-shaped DNA template is introduced to facilitate rod orientation with sixteen footholds evenly distributed on a circular track.[633] Each foothold is encoded with a binding block with an identical sequence and a toehold block with the specific binding information. Upon addition of carefully designed blocking and removal strands, the up nanorods can rotate to their neighboring binding sites with a step length of ~6.5 nm and step angle of ~π/8 (**Figure 60b**).[634] Depending on the sequence of adding these DNA fuels, the dimer can form clockwise or counterclockwise rotation with similar sensitivity and step size, allowing highly sensitive chirality responses (**Figure 60c**). Based on a similar "release and capture" mechanism, a so-called plasmonic walker is also developed, which drives the translational move of Au nanorods relative to another rod. The relative position changes between the two orthogonally aligned nanorods alter the chiral symmetry of the dimers and thus its circular dichroism signals.[634]

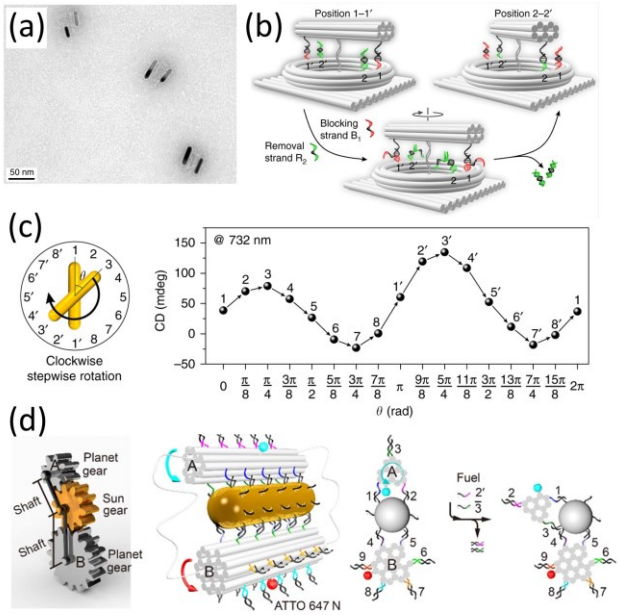

Figure 60. Rotary chiral plasmonics by templating against DNA origami. (a) TEM image of self-assembled plasmonic nanoclocks. (b) Working principle of the smart nanoclocks in response to the addition of DNA strands. (c) Schematic illustration (left) and measured CD intensity (right) of the smart assemblies during a full-turn clockwise rotation process. Reproduced with permission from ref [630]. Copyright 2019 The Authors. (d) The design principle (left) and working mechanism (right two panels) of epicyclic gearset. Reproduced with permission from ref [635]. Copyright 2019 The Authors, some rights reserved; exclusive licensee American Association for the Advancement of Science.

The DNA templating strategy is further extended to functional materials of different components, sizes, and shapes, such as fluorophores, which enables the design of smart nanomachinery with regulated and coordinated motion.[635] These highly integrated devices consist of responsive elements, which drive coordinated motion under external stimuli, and functional constituent materials, such as nanocrystals and fluorophores. They are assembled into hybrid machinery through DNA cross-linking, which can independently revolve around an Au nanorod driven by DNA fuels. As a representative design in **Figure 60d**, two DNA origami filaments of different diameters are crosslinked to a middle Au nanorod, the DNA binding between which can be regulated in response to the addition of blocking and removal strands.[636,637] It allows filament A to rotate with a step rotation angle of 120° around Au nanorod surface and changes its position relative to filament B. This sequence of events also alters the distance of two fluorophores attached on the two DNA filaments to the Au nanorod surface, and thus their fluorescent intensity due to the distance-dependent quenching effects. Tracking the fluorescent intensity also allows precisely monitoring the rotation of DNA filaments in response to the addition of DNA fuels. A similar design principle has been used to develop various nanomachinery to perform desirable functions, including independent rotation, synchronous rotation, and joint motion. These inspiring nanomachines take advantage of precise positional, orientational control of DNA techniques and sensitivity of functional materials in response to their configurational changes and is therefore promising in developing smart nanoscale robots.

4. APPLICATIONS OF SMART COLLOIDAL ASSEMBLIES

4.1. Color Displays and Filters

4.1.1. Liquid Crystal Displays

Liquid crystals have attracted long-lasting interest in both academic research and industrial developments.[638] They share the physical properties of crystalline materials and the unique features of fluids. The long-range order endows them with anisotropic optical properties, viscosity, and elasticity, while the fluidity provides controllable susceptibility to external stimuli, like electric fields, magnetic fields, mechanical forces, and light.[54] These properties make liquid crystals (LCs) one of the most promising materials for color displays.[55] In addition to the conventional liquid crystal displays (LCD) that are made of organic molecules, colloidal particles can self-assemble in solution phases and respond to external stimuli, representing another promising material for color displays.[55] A few well-known examples are graphene oxide nanosheets and cellulose LCs.[62,639,640] Due to their larger sizes and higher aspect ratios than organic LCs molecules, their optical properties can be easily regulated with lower energy consumption (e.g., lower voltages). Cellulose nanocrystals (CNCs) are rod-like crystalline materials with varying diameters between 3 and 20 nm and lengths ranging from 50 nm to a few micrometers.[641] In aqueous dispersions, some of them form chiral nematic phases and a pseudolayered helical structure, whose structures can be fixed by evaporating water.[642] Depending on the helical pitches, separated domains exhibit vivid structural colors, with blue color for a small pitch.

As predicted by Onsager's theory, carbon nanotubes and graphene oxide nanosheets in colloidal dispersions can transit from an isotropic to a nematic phase as their concentrations increase.[643,644] The optimal concentrations depend sensitively on structural aspect ratios. In experiments, their phase behaviors

have been extensively studied, promoting the research for exploiting their practical applications in colloidal LCDs.[645,646] If an electric field is applied, birefringence is observed in all three phases of graphene oxide (GO) nanosheets. However, to avoid chemical reduction and electrolysis, a high-frequency, low-magnitude electric field is preferred. In a typical measurement shown in **Figure 61a**, the application of an electric field yields obvious birefringence in the dispersion.[647] Notably, the field magnitude is three orders of magnitude weaker than the field for conventional molecular LC switching. After the field is switched off, the birefringence gradually disappears, demonstrating the transition from the nematic phase to the isotropic phase. As predicted, the electric field-induced phase transition of GO is dependent on concentration, with an optical concentration at ~0.11 vol% (**Figure 61b**). The optical response of GO is very sensitive to external fields, which is characterized by the Kerr coefficient and three orders higher than any other Kerr materials. The significance of such a large Kerr coefficient is the fast response to the electric field. In an electronic device, the optical signals can be readily switched on and off by simply applying a voltage of 20 V (**Figure 61c**). Its further optimization may lead to a comparable performance to commercial LCDs but requires additional efforts in synthesizing high-concentration GO dispersion for high saturated birefringence and in controlling ionic influence for long-term stability.[640,648]

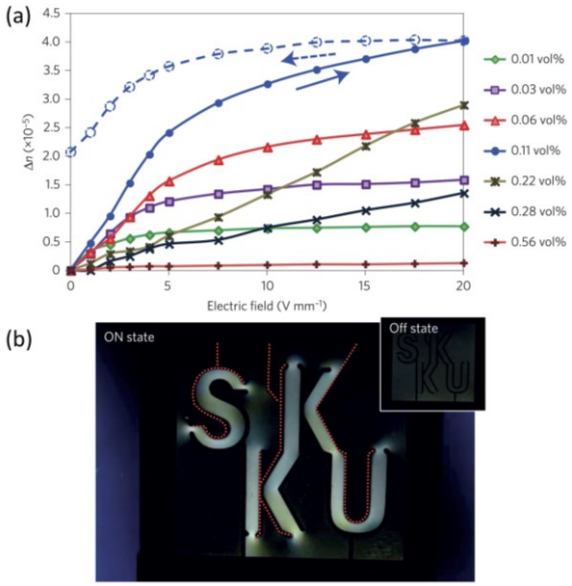

Figure 61. Electro-optical switching of colloidal liquid crystals for displays. (a) Optical responses of a graphene oxide dispersion under different electric fields. The vertical axis represents the induced birefringence obtained by subtracting the initial birefringence at 0 V mm^{-1} from the measured birefringence. (b) Field-induced birefringence curves by applying extremely low electric fields. (c) The on and off state of a liquid crystal display. Reproduced with permission from ref [647]. Copyright 2014 Springer Nature.

4.1.2. Plasmonic Color Displays and Filters

The LSPR of plasmonic nanostructures has many advantages in designing color displays and filters, particularly compared with conventional pigmentation-based display technologies.[649-651] Firstly, the LSPR peak position can be easily tuned by changing the structural sizes, morphologies, and assemblies. It provides widely accessible color ranges that cover the whole visible spectrum for displaying wide color gamut images. Secondly, the LSPR produces a sharp peak at the resonant wavelength, leading to high monochromaticity for color mixing.[652] Thirdly, the resonant absorption and scattering of plasmonic nanostructures offer optional display modes. Their structure-determined light scattering enables the design of transparent displays that can exhibit arbitrary monochromatic images.[653] Instead, plasmonic nanostructures with absorption-dominated optical properties are promising in designing high-performance color filters and in displaying pre-designed pictures in a transmission mode.[654] Lastly, many well-established fabrication techniques (e.g., colloidal assembly and lithography) enable large-scale production of high-resolution plasmonic pixels.[655] In this regard, the LSPR of plasmonic nanostructures has inimitable merits because their highly localized electric fields can regulate light propagation below the diffraction limits.[656] The use of these advanced techniques also allows for integrating plasmonic pixels into conventional electronic devices (e.g., LCDs); it represents an open platform for designing active plasmonic displays for consumer electro-optical devices.

Two challenges in developing these inspiring displays are to synthesize monodisperse plasmonic nanostructures with well-defined optical properties and to manipulate their large-scale assemblies with nanometer precision. In existing techniques, templating synthesis and assembly are promising. For example, high-quality Fe_3O_4@Au nanoparticles can be made on a large scale using an advanced templating method.[657] It yields Au nanoshells with controllable inner diameters, thicknesses, and optical properties. The hollow nanostructures have hybridized plasmon modes, which offer widely accessible resonant wavelength and predominant scattering of light. Therefore, a transparent display has been developed using the Fe_3O_4@Au nanoparticles as building blocks (**Figure 62a**). This display is highly transparent due to the use of non-absorbing polymers in the visible spectrum (**Figure 62b**). By choosing Au nanoshells with proper inner diameters, the transparent display can scatter light at the nanoshell resonant wavelength while remaining high transparency elsewhere in the visible spectrum (**Figures 62c** and **62d**). Templates with pre-created features can also regulate the assembly of plasmonic nanoparticles into complex structures.[310] This technique is a directed assembly process and guides plasmonic nanoparticles of different chemical components, shapes, and sizes to assemble in pre-designed geometries and locations.[658] A 2D template with defined gaps is created using electron-beam lithography. The generated patterns are further modified by polylysine for positively charged surfaces, which serve as binding sites for assembling negatively charged particles. As shown in **Figure 62d**, colloidal linear chains of 35-nm silver nanoparticles can be produced with controllable length and particle number. These assemblies act as plasmonic pixels that have two unique properties. One is the length-dependent plasmon coupling, in which the resonant peak positions can be tuned across the whole visible spectrum (the spectra in **Figure 62d**). The second character is their polarization-dependent color switching (**Figure 62e**).

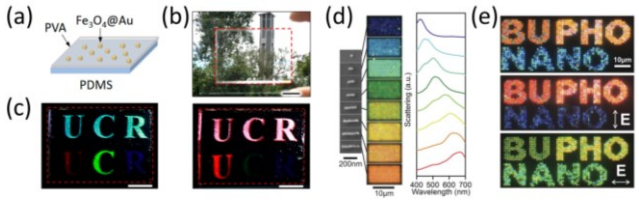

Figure 62. Plasmonic color displays. (a) Fabrication of the plasmonic color display based on resonant scattering of Au nanoshells. (b) Digital image of the highly transparent plasmonic display. (c) Digital images of the display made of small (left) and large (right) Au nanoshells, which exhibit different colors. Scale bars: 1 cm. Reproduced with permission from ref [657]. Copyright 2020 American Chemical Society. (d) SEM images (left), optical images (middle), and scattering spectra (right) of the longitudinal mode of linear plasmonic chains. (e) Polarization-dependent color switching of the plasmonic color display. Reproduced with permission from ref [658]. Copyright 2016 John Wiley and Sons.

To develop actively addressable plasmonic displays, the optical properties of plasmonic structures need to be responsive to external stimuli. Electric fields are a promising and useful stimulus in this regard, considering their easy fabrication and promising applications in various electronic devices. There exist two approaches to active displays with plasmonic assemblies as back reflectors and liquid crystals for color switching. Using the established nanofabrication techniques, including electron beam lithography,[659-661] photolithography,[662] and colloidal self-assembly,[229,663] it is possible to create plasmonic nanostructures on desirable substrates with sub-10-nm precision. The tiny small sizes lead to ultra-fine color pixels and high-resolution images beyond the conventional diffraction limits.[655] Franklin and Chanda established a mature method to fabricate actively tunable color displays by integrating imprinted or self-assembled plasmonic surfaces into LC cells.[649,663,664] In their early studies, a plasmonic-liquid crystal cell was developed with impinging white light. Transmitted light through the LC layers interacts with the plasmonic layers while reflecting complementary colors. The wavelength of absorbed light is determined by the LC orientation near the interfaces so that the plasmonic coloration can be actively tuned by voltages.[649] Simply adding a polarizer to the integrated electronic cells leads to actively addressed full-color plasmonic displays that can exhibit polarization-dependent images.[664] The use of lithography techniques to prepare large-scale 2D plasmonic arrays has several limitations in further commercialization. The coloration in these ordered plasmonic structures is dependent on light incident angles. A self-assembled plasmonic reflector was recently developed to better suit practical applications.[663] A physical vapor deposition method was employed to grow plasmonic nanostructures with random plasmon coupling. This simple modification provides randomly dispersed plasmonic particles and therefore overcomes the challenges of viewing-angle dependence and the absence of black/gray states. The working principle of this new electronic device uses dispersed LCs as the color modulator. In the off state, the chiral configuration of LCs allows for the reflected light to penetrate the cell, thus displaying pixel-wise colors. When voltage is applied, the pixels turn black because the vertical aligned LCs do not change the polarization of incident light, and the reflected light will be absorbed by a surface polarizer. One promise of this technique is its ease of integration into commercial displays so that a prototype device is demonstrated to display arbitrary motion pictures. Another approach to active plasmonic coloration assembles plasmonic nanostructures in electronic cells. This technique relies on the anisotropic electric susceptibility of plasmonic nanorods or on the interactions between LC molecules and the guest plasmonic nanostructures.[64,665,666] Taking the plasmonic guest-host LCs for example, Au nanorods are first modified by poly(ethylene glycol) to induce weak interactions with the host LC molecules.[614] The significance of this surface modification is nanorod co-alignment with the molecules under an applied electric field (**Figure 63a**). It, therefore, leads to long-range order in colloidal dispersions and allows for electrically switching the rod optical properties (**Figure 63b**). Notably, this strategy relies on the interactions between surface ligands and LC molecules for assembling anisotropic plasmonic nanostructures, which is not limited to particle shapes, sizes, and chemical components. Its highly compatible fabrication with conventional LC cells sets the stage ready for exploiting its practical uses (e.g., plasmonic displays, smart windows, and color filters).

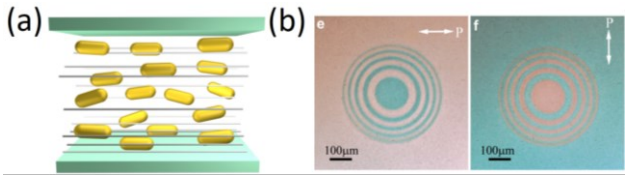

Figure 63. Self-assembly of plasmonic nanoparticles for color displays. (a) Schematic illustration of the orientational orders of Au nanorods in liquid crystals. (b) Optical microscopy images of the plasmonic displays in response to different polarization. Reproduced with permission from ref [614]. Copyright 2014 American Chemical Society.

4.1.3. Photonic Crystal Display

Photonic crystals are famous for their intrinsic photonic bandgaps and unique optical properties. Their coloration has dramatic merits in place of conventional pigments in developing optical devices.[667] The structural colors are determined by structural periodicity and therefore do not photobleach. An ideal photonic display is expected to reflect light in the whole visible range in response to external stimuli. The application of physical or chemical stimuli alters the photonic bandgaps and structural colors so that desirable patterns can display on photonic materials. In some advanced strategies, a few microfabrication techniques are involved for actively addressable, pixel-wise display. The existing external stimuli evoking color changes include chemicals,[668,669] electric fields,[472,476,477,667,670-673] heat,[674] magnetic fields,[569] and mechanical forces.[545,675,676] In some photonic displays, they can exhibit designated patterns in reaction to multiple stimuli.[677,678]

Electrically driven photonic crystal displays consist of photonic crystals, transparent electrodes, and electrolytes. In electrochemical cells, reactive or phase-changing polymers are needed to impose tunability on structural periodicity and colors. Self-assembly of copolymers into layered photonic films is one approach to responsive coloration via film swelling under applied voltages. A noticeable copolymer is polystyrene-b-poly(2-vinyl pyridine) (PS-b-P2VP).[476,477] Under anodic bias voltage, the pyridine groups in the P2VP block are protonated so that anion

electrolytes will migrate toward the photonic films, which increases the periodicity of the photonic films. Colloidal crystal arrays are another promising example in developing photonic crystal displays, which involves the colloidal self-assembly of photonic crystals and the infiltration of reactive polymers in the crystal networks. Ozin et al. introduced a crosslinked network of polyferrocenylsilane into the crystal matrix of silica nanoparticles that are prepared by convective self-assembly.[472] The polyferrocenylsilane has electrochemical oxidation and reduction under applied voltages, leading to partial electronic delocalization in the polymer backbone. This process electrochemically drives swelling and shrinking of the polymer matrix and actively regulates the lattice spacing of the photonic crystals (**Figure 64a**), demonstrating whole spectral tunability, high brightness, and color saturation.[671] If ITO arrays are used as patterned electrodes, the optical device can display well-defined images by controlling the voltages on each electrode. **Figure 64b** demonstrates alternating green and red stripes by applying voltages to every other electrode line. Increasing the applied voltage will redshift the structural colors to near-infrared regions so that the display becomes transparent. The power consumption of this electrochemical cells is compatible with some portable electronics, which is promising in developing active camouflage and full-color photonic crystal displays.

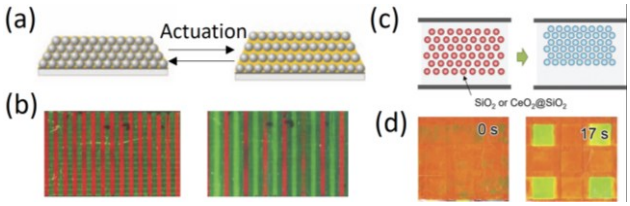

Figure 64. Self-assembly of colloidal particles for photonic full-color displays. (a) Schematic illustration and working principle of electric actuation of photonic crystal lattice for dynamic full-color displays. (b) Images of a photonic ink film under different applied voltages. Reproduced with permission from ref [472]. Copyright 2007 Springer Nature. (c) Working principle of the electrically driven photonic display. (d) Digital photos of the photonic crystal display. Reproduced with permission from ref [672]. Copyright 2018 John Wiley and Sons.

Using electrophoresis of charged colloidal particles in uniform electric fields, it is possible to directly assemble colloidal particles and tune lattice spacing in electronic cells (**Figure 64c**). A few monodisperse particles or core/shell nanostructures (e.g., SiO_2, CeO_2, Fe_3O_4@SiO_2) are good suitable building blocks largely because of their high uniformity, simple synthesis, and high mobility in an electric field.[670,672,679] A 3D photonic crystal is assembled between two transparent ITO electrodes using a spontaneous precipitation method.[672] When an electric field with a proper magnitude is applied, positively and negatively charged particles would migrate to the cathode and anode, respectively, driven by electrophoretic forces. In both cases, the colloidal particles will be packed more densely towards the electrodes, leading to a dramatic decrease in lattice spacing and blueshifts in structural colors. A prototype of reflective displays is demonstrated by employing patterned electrodes as pixels. Each electronic cell is powered separately so that the color of an individual pixel can be conveniently tuned (**Figure 64d**). A simple extension of this working principle to assemble amorphous photonic crystals leads to a viewing angle-independent color display,[670] which is more desirable in inventing commercial color displays.

Photonic crystals that are responsive to magnetic fields or mechanical forces can also be properly designed to display images. One advantage is their high response rate, which is normally within 1s. By dispersing magnetic nanoparticles in emulsion droplets, Ge et al. developed an effective approach to magnetochromatic microspheres.[569] It is achieved by first dispersing magnetic particles in PEGDA monomers, followed by emulsion formation and UV polymerization (**Figure 65a**). This process yields magnetochromatic microspheres with well-aligned 1D photonic chains. While their structural colors are determined by the interparticle separation and chain orientation, the coloration can be switched on and off by controlling the magnetic field direction. To prepare solid optical devices, temperature-sensitive PEG is introduced as a phase-changing matrix so that the chain orientation and the display color can be reversibly controlled by a magnetic field ("on" and "off" states shown in the left and right panels, respectively in **Figure 65b**). Different from the remote magnetic control, mechanical forces exert contact impact on deformable photonic elastomers for mechanochromic responses. The optical performances are highly dependent on the way that the mechanical forces are applied. For example, stretching or pressing induce blueshift of the structural colors while pushing the elastomer lateral leads to redshifts.[545] In creating patterns, the imprinting technique has been established to display pre-designed images on monochromatic photonic crystal display.[675,676]

Developing multi-responsive photonic crystal displays are attractive because of their potential broad applications. Using functional polymers to enclose photonic crystals is a simple way. While their functional groups make the displayed color susceptible to chemicals, like pH and water, the polymer elasticity offers mechanochromic responses.[677] Pixel-wise display is also possible by using the microfluidic technique to assemble multi-responsive Janus microspheres.[204,680] An elegant example is presented in **Figure 65c**, with triple optical responses to magnetic fields, light, and temperature changes.[678] While the optical performance is promising in these established methods, how to manage or take advantage of the multiple optical responses for more advanced optical devices remains a challenge.

4.2. Color Printing and Rewritable Papers

The active optical responses of colloidal assemblies can be utilized to develop color printing processes and create rewritable papers.[52] Their working principles are similar to those established in color displays but are more focused on reproducing pre-designed images and printing letters. In responsive photonic crystals, active tuning of the periodicity of photonic crystals and orientational control represent two typical approaches to color printing. Plasmonic assemblies generate shape- and structure-dependent coloration so that color printing is also possible by modulating their collective optical properties. Depending on the color-changing mechanism, they can be categorized into permanent color printing and rewritable papers.[166,485,681] Some techniques themselves or combined with other physical pro-

cesses provide irreversible color changes in colloidal assemblies and are therefore developed for printing permanent images. A few established techniques in this regard include magnetic field- or electric field-assisted photolithography, mechanical imprinting, and some irreversible chemical reactions. Meanwhile, some optical devices have been developed with reversible color changes so that they can be used multiple times as rewritable papers. In this regard, magnetic orientational control and the chemical-induced swelling-deswelling of polymers are two noticeable examples, which are either made into rigid optical devices or flexible paper-like films.

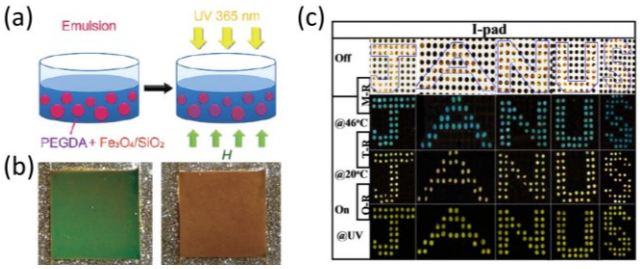

Figure 65. Responsive color displays to multiple stimuli. (a) Schematic illustration of preparing magnetic photonic microspheres. (b) Digital images of the on (left) and off (right) states of photonic display regulated by a magnetic field. Reproduced with permission from ref [569]. Copyright 2009 American Chemical Society. (c) The on-off switching and dynamic color changes of a photonic display in response to multiple stimuli. Reproduced with permission from ref [678]. Copyright 2015 American Chemical Society.

4.2.1. Magnetic Color Printing

Magnetic color printing utilizes the interactions between colloidal particles and external magnetic fields for color generation. For colloidal particles with a simple spherical shape, they self-assemble into 1D chain-like structures under magnetic fields, which diffract light only when light is incident along or at a small angle to the chain. Based on this orientation-dependent coloration, a magnetically rewritable ink is created.[682] This technique uses the fixed 1D chains as color units (**Figure 66a**), which can be rapidly and reversibly switched on and off by applying vertical and horizontal magnetic fields, respectively. One challenge for using this ink for magnetic printing is how to stabilize the chain orientation in a considerably long time to present the printed images. In this regard, highly viscous solvents are introduced as a dispersant, which suppresses the chain rotation at ambient conditions. Notably, the coloration state can be elongated from a few seconds to several minutes by simply increasing the viscosity of the dispersant. A digital image in **Figure 66b** shows well-defined patterns right after removing a stripe-patterned magnet. The printed image can be erased by applying a horizontal magnetic field. And letters can be directly written on the same optical device using a small permanent magnet as a pen (**Figure 66c**). An alternative strategy employs photolithography to selectively fix the magnetic nanostructures in a polymer matrix, leaving other areas still responsive to a magnetic field.[683,684] To prepare a solid film, superparamagnetic nanoparticles are first dispersed in a prepolymer of PEGDA, which is then thoroughly mixed with a PDMS precursor to form an emulsion. After thermally curing the PDMS, the magnetic particles in PEGDA droplets can still move freely until UV irradiation is applied under a photomask to polymerize some droplets. Notably, the droplets that are covered by the photomask contain well-dispersed magnetic particles. They can still self-assemble under a magnetic field, and the device displays an image that is determined by the photomask. If the magnetically tunable structural color is coupled with a maskless lithography system, it is possible to directly print arbitrary images using magnetic ink.[685] This composite ink comprises superparamagnetic nanoparticles, PEGDA prepolymers, and ethanol as solvent. In an integrated printing system, a digital micromirror array modulator can reflect patterned UV light to polymerize the magnetic ink while a magnetic field with proper strength is applied to produce desirable structural colors (**Figure 66d**). This technique allows for instantaneous modulation of the structural colors so that high-resolution, structural-color images can be printed (**Figure 66e**). The digital modulator produces pixels of 16.7 μm×16.7 μm with a resolution of ~1500 dpi. Such a small size of the printed dost also enables reflection intensity modulation and spatial color mixing, thereby broadening the capability of color expression.

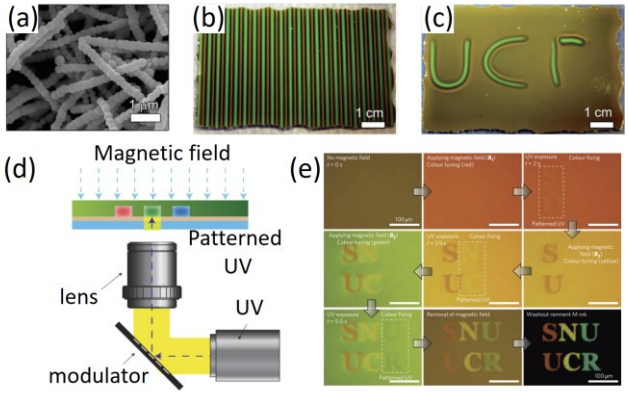

Figure 66. Magnetically responsive photonic nanostructures for color printing. (a) SEM image of photonic chains from the magnetic assembly of nanospheres. (b) Multicolor photonic display showing color pattern under a stripe-patterned magnet. (c) Magnetic writing letters on the photonic display. Reproduced with permission from ref [682]. Copyright 2013 Royal Society of Chemistry. (d) Schematic illustration of magnetic field-assisted photonic lithography. (e) Digital pictures demonstrating the rapid printing of high-resolution photonic images. Scale bars: 100 μm. Reproduced with permission from ref [685]. Copyright 2009 Springer Nature.

4.2.2. Mechanical Imprinting

Mechanical imprinting is a replication process capable of nanomanufacturing and reproduces pre-created patterns on soft or thermoplastic substrates. Generally, nanoimprint lithography (NIL) is a famous mechanical imprinting process, which can be divided into thermoplastic nanoimprint lithography, photo nanoimprint lithography, and direct nanoimprint lithography. In these established techniques, direct mechanical imprinting is resist-free, simple, and therefore has been extensively used in color printing. Photonic crystals or plasmonic assemblies demonstrating vivid colors are ideal materials for mechanical imprinting. It relies on mechanical forces-induced deformations and evolves corresponding color changes.[686] This approach offers an alternative method to print images with improved throughput and yields.[687]

Ge and his colleagues developed a strategy to prepare mechanochromic photonic prints by fixing photonic crystals in transparent polymers (e.g., photo-curable PEGDA and thermal curable PDMS).[688,689] A metastable colloidal crystal array is used as responsive photonic crystals and is first fixed in the matrix of ethylene glycol and poly(ethylene glycol) methacrylate. The invisible patterns are printed on the photonic film by soaking the film with PEGDA, followed by crosslinking the unshielded region through a photomask. Because the second step causes negligible changes in the film's optical properties, the printed patterns are invisible under a relaxed state. However, the second photopolymerization during the second light exposure leads to highly cross-linked domains in the photonic films, whose Young's modulus is much higher than that of the shielded domains. Upon mechanical forces, including stretching, squeezing, the different elasticity in the two domains induces non-uniform mechanical deformation and thus distinct color changes (**Figure 67a**).[689] The resolution of the printed images is mainly determined by the surface features of the imprint. For example, a linear resolution of ~10 μm is possible on 2D images that are imprinted from a properly prepared PDMS staple (**Figures 67b** and **67c**). The mechanical imprinting technique has advantages of large-scale production and high-resolution printing, leading to many promising applications in both consumer and professional devices.

Because mechanical imprinting changes the interparticle separation in colloidal assemblies, it is possible to print colors on plasmonic nanostructures whose absorption and complementary colors are determined by interparticle separation. Ag nanoparticles are an ideal material for dynamic color tuning because of the low price, strong, and widely tunable LSPR in the visible range. A limited-ligand-protection strategy is reported to enable reversible assembly of Ag nanoparticles with precisely controlled surface passivation of poly(acrylic acid) ligands.[690] By adding a limited amount of PAA, assemblies of Ag nanoparticles can be directly formed in the reaction solution (scheme shown in **Figure 67d**). The self-assembly is evidenced by the obvious redshift of the absorption peaks of the products, whose complementary colors simultaneously change from yellow to red and blue (**Figure 67e**). Since the self-assembly of Ag nanoparticles is determined by their surface charges, it is possible to reversibly assemble and disassemble the particles by adding H_3PO_4 and NaOH, respectively. Incorporating the Ag superstructures in solid films is a reliable method for colorimetric sensing or mechanical imprinting. When the film is subjected to mechanical pressures, its deformation causes Ag nanoparticles to disassemble so that the film color changes accordingly. If a stamp is used, it is possible to print images on the plasmonic film with pronounced contrasts (**Figure 67f**).

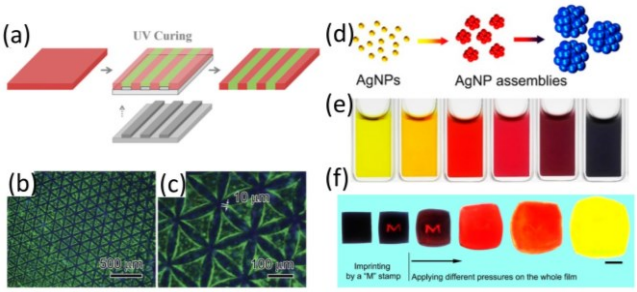

Figure 67. Responsive photonic and plasmonic films under mechanical pressure. (a) Working principle of the mechanochromic photonic crystal films. (b-c) Optical microscope images of a hexagonal array of micro triangles printed on the paper. Reproduced with permission from ref [689]. Copyright 2015 Royal Society of Chemistry. (d) Self-assembly of Ag nanospheres for mechanochromic plasmonic film. (e) Digital pictures of the dynamic color changes during the self-assembly of Ag nanospheres. (f) Mechanochromic film under different mechanical pressure. Reproduced with permission from ref [690]. Copyright 2018 American Chemical Society.

4.2.3. Electronic Color Printing

Electronic color printing uses an electric field to actively tune the structural color of photonic crystals. One typical strategy is to integrate electroactive photonic crystals in electronic cells. These optical devices can display permanent or bistable color printing without the use of inks or stamps. Electrophoresis describes the motion of dispersed, charged particles in colloidal solutions under an electric field.[691,692] If the colloidal particles have self-assembled into colloidal crystal arrays, it leads to lattice contraction and expansion. One merit of this working principle is that the structural colors can be tuned continuously over a broad spectrum by simply changing the field magnitude (**Figure 68a**).[166] Multicolor printing is possible by fixing the equilibrium structures in the electronic cells using lithography. **Figure 68b** demonstrates a multicolor printing process by combining electric field tuning and UV curing. In addition to particle electrophoresis, electroactive polymers have also been used for electronic color printing. In some established strategies, photonic polymer matrices are reversibly swelled through redox reaction or hydrogel hysteresis.[475,477,693,694] Dielectric elastomers are another type of electroactive polymers, which induce mechanical compression or stretch of photonic crystal lattices under an electric field.[468,695,696] To induce bistable color printing, the modified photonic film needs to be temporarily fixed so that writing can maintain for a considerably long time and be erased on demand. To this end, a shape-memory electroactive copolymer is used, whose phase-changing is dependent on temperature.[697] Above the phase-changing temperature, an applied electric field can locally actuate the composite photonic film and print images on the optical devices. The writing is enduring by decreasing the film temperature, while any written patterns can be erased by heating the film above the phase-changing temperature.

4.2.4. Photonic Papers with Chemical inks

Photonic papers comprise photonic crystals in a polymer matrix, exhibiting obvious color changes in exposure to solvents or ions. In a few cases, the polymer matrix self-assembles into 1D photonic crystals and serves as both the coloration elements and responsive materials.[698,699] In other cases, the preparation of photonic papers involves the assembly of photonic crystals (e.g., 1D chains or 3D colloidal crystal arrays), followed by fixing the formed structures in a responsive polymer matrix. When the solvents or ions are in contact with the photonic papers, their diffusion swells the polymer matrix so that the periodicity of the photonic crystals increases. This sequence of events leads to vivid color changes in the drawn areas and creates images on the photonic papers. Several reported chemical inks include water,[699-704] salt solution,[705] carbon disulfide,[706] ethanol,[698] tetrahydrofuran,[707] propanol,[484] and silicone fluid.[485] The macroscopic

increase in polymer volume induced by solvent diffusion is ascribed to both pore geometry changes and reconfiguration of polymer chains.[708] Solvents having strong interactions with chemical groups in the polymer have the potential to swell the matrix so that they can be used as chemical inks. A quick search of good solvent to the monomer of a target polymer is a good starting place to screen a proper writing solvent. As shown in **Figure 68c**, a photonic paper is prepared by magnetically assembling magnetite nanoparticles into 1D nanochains and further fixing the chains in the PEGDA matrix.[705] A water-ethanol solution of chloride salts is used to write on this photonic paper directly. The PEGDA swelling increases the interparticle separation and induces a redshift of the perceived colors (**Figure 68d**). Simply rinsing the used paper in distilled water removes salt inks and allows the polymer to recover its initial volume. Therefore, the ink marks can be easily erased because of the blueshift of structural colors in the swelling areas. The use of the salt solution in place of pure water is to create stable writing on the photonic papers, the key challenge of which is to maintain the swelling state of the marked areas. The hygroscopic salts can absorb water from the surroundings, which results in an equilibrium wetting and swelling state in the polymer matrix. This chemical ink produces stable writing for a few months with improved durability. Based on the same working principle, many photonic crystals have been used for photonic papers, whose writing performances highly depend on the transport properties and phase behavior of polymers and the used chemical inks. In addition to conventional writing, photonic papers with invisible color print are also reported.[398,700,702] This technique modifies the transport properties of the polymer matrix, with selective surface treatment being the commonly used method. For example, if the surface of the photonic paper is partially treated by hydrophobic agents (e.g., fluoroalkylsilane), an invisible photonic print with different wetting ability and swelling performances is prepared.[702] Immersing the "blank" photonic papers in water will visualize the encrypted prints due to the water diffusion difference in the hydrophobic and hydrophilic regions. Another strategy modifies the crosslinking ratio of the polymeric photonic paper by light irradiation.[700] This method is compatible with the fabrication process of light-curable photonic papers and leads to polymer matrix with different mechanical properties.

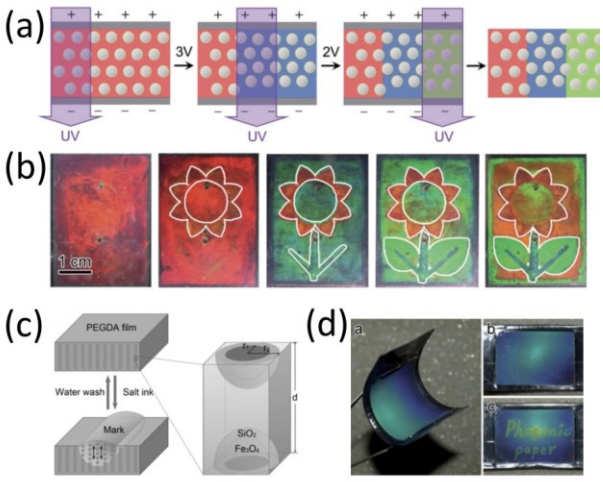

Figure 68. Multicolor printing and writing via repeated electric tuning and chemical inks. (a) Schematic illustration of multicolor printing on photonic film. (b) Printing multicolor patterns on the photonic film via photolithography. Reproduced with permission from ref [166]. Copyright 2017 John Wiley and Sons. (c) Rewritable photonic papers using a salt solution as chemical ink. (d) Digital pictures of the writing arbitrary letters on the flexible photonic paper. Reproduced with permission from ref [705]. Copyright 2017 John Wiley and Sons.

4.2.5. Laser Printing

Laser printing uses light as environmentally friendly stimuli and produces high-quality text and images. Compared with mechanical imprinting and writing with chemical inks, it is much faster in reproducing images with higher resolution. Different from conventional electrostatic digital printing, the emerging laser printing based on smart materials relies on the photothermal effects when light interacts with nanostructures.[709] It modulates the collective optical properties of colloidal assemblies for generating color contrast and forming images. Recent advances in this regard have demonstrated that both plasmonic nanostructures and photonic crystals can be used as "papers" in laser printing. In a recent report, an inverse opal photonic film was prepared by templating against a colloidal crystal array of silica.[710] To prepare photonic paper, inverse opals are mechanically compressed at ambient temperature to a deformed state (lower than the glass transition temperature of the copolymer). During this mechanical deformation, the inverse opals collapse, and the disordered structure becomes translucent. This deformed state is stable unless the temperature of the deformed inverse opal is heated above the critical glass transition temperature by either direct heating or photothermal heating. The relaxation of the compressed inverse opal produces a few metastable states, whose final periodicity and structural colors are determined by the working temperature and heating duration. If a laser is used to induce local photothermal heating, it is possible to directly print images or to copy existing images from a conventional paper. As illustrated in **Figure 69a**, the NIR laser-programmable multi-color photocopy uses a black image printed on paper as a template. Upon light irradiation, the black inks can locally heat the bottom photonic paper such that the printed information can be transferred downwards. This printing technique can reproduce complex images with high resolution and contrast (**Figure 69b**).

Another laser printing strategy involves the photothermal effects of plasmonic nanostructures and their shape-dependent coloration.[709] Plasmonic color generation has many advantages compared with the coloration of dyes or pigments, including smaller pixel size, higher resolution, and higher stability for ambient use.[656] A printable plasmonic metasurface is prepared by nanoimprinting technique,[711] with metal disks on top of dielectric pillars (**Figure 69c**). Pulsed laser irradiation induces intensive local heat generation that melts and reshapes the plasmonic nanostructures (**Figure 69d**). Depending on the laser intensity, intermediate shapes can be obtained, leading to different plasmonic resonances and colors. This plasmonic color printing yields all primary colors and high-resolution images (up to 127000 DPI in **Figure 69e**).

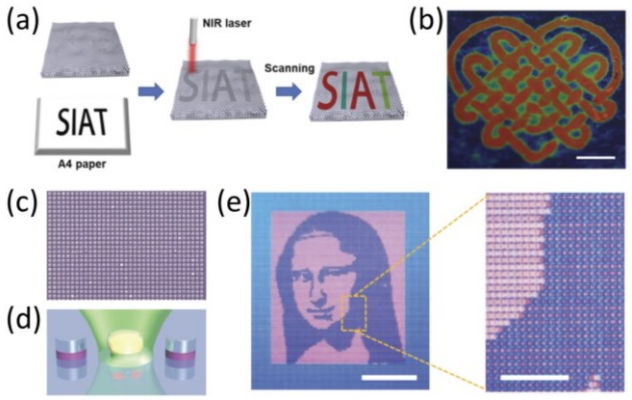

Figure 69. Laser printing on colloidal crystals and arrays. (a) Schematic illustration of laser printing on photonic paper. (b) A printed image on photonic paper. Scale bar: 1 cm. Reproduced with permission from ref [710]. Copyright 2020 The Royal Society of Chemistry. (c) SEM image of a plasmonic metasurface. (d) Laser photothermal printing and the associated shape change of plasmonic pixels. (e) A printed high-resolution image (left) and the underlying deformed color pixels. Scale bars at the left and right panels are 2 mm and 500 μm, respectively. Reproduced with permission from ref [712]. Copyright 2016 Springer Nature.

4.3. Colorimetric Sensing and Spectroscopic Detections

Nowadays, human beings are facing internal and external uncertainties. While evolution has allowed living organisms to adopt astonishing complexity, our understanding of biological progress and their subtle evolution has been greatly limited by the available detection and sensing techniques. Meanwhile, the environmental and energy crisis is the most rigorous external challenge that we are facing. Unraveling these requires powerful tools to probe the molecular reactions and provide useful feedback on the origin and development of these uncertainties. Colorimetric sensing and spectroscopic detection provide such a powerful methodology and lay the foundation for biomedical, environmental, and energy research and practices. Because their advances will significantly enrich our understanding of important biological processes and functions and provide sensitive approaches to monitor environmental deterioration, diverse molecular probes and detection devices have been developed. Among these striking developments, colorimetric sensors involving colloidal superstructures represent an emerging category. Nanoparticles themselves or their superstructures have many unparalleled merits compared with bulk materials and reactive molecules. Nanostructured materials have large specific surface areas, which provide sufficient binding sites for detecting molecular analytes with a low detection limit. The widely accessible nanoparticles and superstructures have distinct physical and chemical properties that are unique to their low-dimension sizes and structures. A few famous examples include LSPR of plasmonic nanostructures, emission of quantum dots, and diffraction in photonic crystals. Another advantage associated with these properties is the diversity of the sensor readouts; they provide qualitative signals (e.g., colorimetric responses) for quick assessment of the targets, while some platforms produce a quantitative analysis of the analytes (e.g., spectroscopic detection technique). Lastly, compared with conventional labeling techniques, smart nanosensors can screen and concentrate target analytes so that no additional purification steps are required to remove any byproducts or impurities. The main significance of this merit is the in-situ detection of important biological molecules, such as an antibody, antigen, and various biomarkers. To this end, chemists and biologists have derived several key concepts from this technique advances, including single-molecule detection and molecular imaging. This subsection outlines a set of basic concepts in colorimetric sensing and spectroscopic detection using smart colloidal assemblies. It delineates crucial developments in designing high-performance nanosensors based on responsive colloidal assemblies, with a specific focus on fluorescence, surface-enhanced Raman scattering (SERS), LSPR, and diffraction from colloidal assemblies.

4.3.1. Fluorescence Sensing Enhanced by Colloidal Self-assembly

Fluorescence occurs in many colloidal particles and involves various physical processes.[713,714] A striking example is quantum dots that emit long-wavelength light within nanoseconds after absorbing short-wavelength light. In this process, the electronic transition from a high-energy state to a low-energy state produces the famous Stokes shift in fluorescence spectroscopy. In other cases, the emitted photons have high energy than the absorbed photons, leading to anti-Stokes shifts. Upconversion nanoparticles are a typical example in this regard. One astonishing benefit of using fluorescent nanoparticles for detection is the high signal-to-noise ratio. Therefore, fluorescence sensors have been extensively used in biological imaging, DNA sequences, medical theranostics, and chemical detection.[715-717] The invention of high-performance sensors requires advanced techniques, which are expected to reduce the detection limits and improve the sensing specificity. Assembling fluorescent colloids into superstructures with long-range orders or incorporating fluorescent probes in colloidal assemblies are two approaches in colloidal chemistry. Developing strategies to enrich the fluorescence of covalently or physically attached fluorophores and to modulate the fluorescence resonance energy transfer (FRET) processes is the key to high-performance detection, bioimaging, advanced labeling techniques, optoelectronic devices.[718,719]

The driving forces to assemble fluorescent particles (e.g., supermolecule particles and inorganic crystals) include depletion attraction,[109,242] valency interactions,[720] mechanical forces,[721,722] van der Waals, and dipole interactions.[110,111,723] The self-assembly of fluorophores into superstructures produces additional fascinating properties that are unique to the ordered structures. For example, supramolecule and polymeric assemblies are ideal platforms to achieve stimuli-responsive fluorescence emission, with aggregation-induced emission (AIE) being the most compelling example.[724-726] The ease of changing chemical components and moiety functions through physical interactions and chemical reactions has greatly diversified the types of responsive fluorescence materials. Noncovalently incorporating fluorescent moieties into stimuli-responsive polymeric assemblies is a simple strategy.[727-729] For applications requiring high structural stability, covalent labeling through copolymerization or fluorophore functionalization is a better choice.[345,730-733] Nowadays, diverse supramolecular and macromolecular probes have been developed, whose photoluminescence responds to light,[728,734,735] salts,[736-738] biological molecules (e.g., enzyme, DNA, RNA, proteins),[739] temperature,[740,741] pH,[733] and ions.[742]

Some carefully designed probes are responsive to multiple stimuli.[743,744] Anisotropic photoluminescence is another attractive phenomenon, which has been observed in a few well-defined superstructures from anisotropic luminescent colloids.[110,722] It is well-known that anisotropic fluorophores (e.g., semiconductor nanowires,[745] quantum dots,[746] and organic dyes[747]) have polarized emissions largely due to the quantum size effect and the electric field confinement effect on both excitation and emission.[748-750] An early close study demonstrated that the photoluminescence anisotropy of semiconductor nanorods could be significantly enhanced if they were self-assembled into mesoscopic superstructures.[110] Such enhanced emission anisotropy is likely caused by a synergistic dielectric effect and collective electric dipole coupling effects among the assembled nanorods. In addition to fluorophores, rare-earth phosphors have a similar polarized emission but with distinct mechanisms and longer luminescence timescales. The multiple transition levels and degenerate sublevels of lanthanide ions in a crystalline host produce many sharp peaks in their photoluminescence spectrum.[751] The emission from each sublevel is polarized along a pre-defined direction by the crystallographic symmetry. This phenomenon is independent of crystal size, shape, and excitation polarization; it produces different line shapes if the crystal's orientation changes.[752,753] Using the orientation-dependent emission, it is possible to sensitively probe dynamic parameters in fluids,[722] whose working mechanism is shown in **Figure 70a**. Poiseuille flow of a nanorod dispersion experiences different shear forces along the transverse direction so that the rods will self-assemble into a liquid phase. Its orientational order is sensitive to both the flow velocity (**Figure 70b**) and the rods' transverse position. Carefully monitoring the polarized emission using a confocal microscope produces flow shear tomography with high spatial resolution and accuracy (**Figure 70c**).

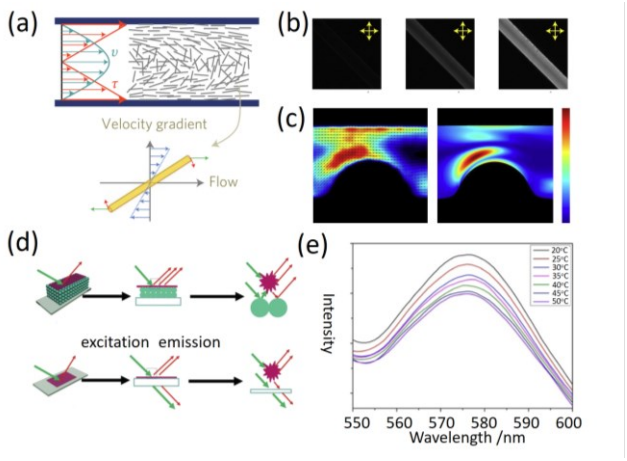

Figure 70. Responsive colloidal assembly for fluorescent sensing. (a) Schematic illustration of self-assembly of nanorods into liquid crystals under shearing low. (b) Optical transmission microscopy images of the liquid crystal flowing through a microfluidic channel for three different average shear rates, which increase from 0.45 s^{-1} (left panel) to 4.5 s^{-1} (middle panel), and 45 s^{-1} (right panel). (c) Experimental and simulated results of flow shear tomography based on the fluorescent sensors. Reproduced with permission from ref [722]. Copyright 2017 Springer Nature. (d) Schematic illustration of fluorescence enhancement using photonic films. (e) Thermo-responsive fluorescent intensity. Reproduced with permission from ref [754]. Copyright 2016 Springer Nature.

Many research results have joined in appreciating that co-assembly of fluorophores and colloidal particles into hybrid or crystal structures may lead to fluorescence enhancement. As first proposed by Purcell in 1964, fluorescence can be modified by resonant coupling to the external electromagnetic environment.[755] A number of fundamental studies have recognized this coupling effect, with photonic crystals and plasmonic structures (both single particles and superstructures) being extensively studied.[756] Plasmon-enhanced fluorescence is a surface-enhanced spectroscopy technique, which involves the co-assembly of fluorophores and plasmonic structures in suitable proximity.[757-759] In extreme cases where fluorophores are directly attached to metal particles, an opposite fluorescence quenching occurs through several possible non-radiative energy transfer processes (e.g., Förster resonance energy transfer, Dexter electron transfer, and static quenching).[760,761] Upon light excitation, the LSPR of plasmonic structures will generate strong, localized electric fields. The enhanced dipole field will excite the nearby fluorophores, leading to a field enhancement factor of E^2, where E is the near field enhancement.[762-764] These theoretical considerations underpin the important roles of plasmonic assemblies in preparing advanced fluorescent: their response to external stimuli leads to detectable intensity changes for high-performance sensing.

Through a distinct physical process and mechanism, photonic crystals also demonstrate enhanced fluorescence. When the excitation or emission of fluorophores matches the stop bands of photonic crystals, the angle-dependent diffraction will promote the absorption of incident photons or reflect more emitted photons to a detector, both of which increase the fluorescence intensity (**Figure 70d**).[754,765,766] This unique property allows the development of multiangle fluorescent chips for the efficient detection of saccharides.[767] Another interesting optical effect is the shift of fluorescence emission with detection angles, which has been observed on 1D photonic crystals.[768,769] These observations suggest that incorporating fluorophores into responsive photonic crystals is a feasible approach to smart fluorescent sensors, whose photoluminescence can be actively switched by changing crystal structures and material properties. A related example is the use of responsive building blocks, such as PS@PNIPAM, with a tunable lattice constant in response to external stimuli.[754] Depending on the shift of diffraction peaks relative to the fluorophore emission, a monotonic periodicity increase can lead to either an increase or decrease in the fluorescence intensity (**Figure 70e**). This fluorescence switching is reversible; the response rate and tunability depend on the stimulation mechanism and diffraction peak shifts.[718,770]

4.3.2. Active Plasmonic Assemblies for Sensing

The unique electron-photon interactions in plasmonic materials provide surface plasmon resonance (SPR), which has been demonstrated with great potentials in developing high-performance sensors. Generally, two types of plasmon resonance are employed, propagating surface plasmon polaritons (SPPs, the propagating mode of SPR normally occurring in thin metal films) and the LSPR in nanostructured metals.[53,771,772] Compared with SPPs, LSPR is more attractive because of its higher flexibility in tuning the localized electric field directions and magnitudes, benefiting from diverse synthetic and lithographic approaches to plasmonic nanostructures. Previous studies have

underpinned the importance of coupling gap and superstructure orientation in determining LSPR properties. These dependencies have also been broadly used as practical guidelines to create responsive plasmonic sensors. For example, in response to existing physical or chemical stimuli, plasmonic assemblies can alter surrounding dielectrics, interparticle separation, or orientation so that their LSPR peaks will shift accordingly. Observing these colorimetric responses or precisely measuring the spectroscopic shifts provides diverse ways to estimate the stimuli with widely accessible accuracy.[482] Smart plasmonic superstructures are also ideal platforms for enhanced fluorescence detection and SERS analysis if they are coupled with fluorophores and Raman molecules, which will be introduced individually in separated sections. Because the charge distribution of LSPR is very sensitive to surrounding dielectrics, plasmonic nanostructures have been extensively used for sensing surrounding refractive index. Generally, increases in refractive index induce redshifts of LSPR peaks. In this regard, many techniques have been developed to monitor such peak shifts, including angular interrogation, wavelength interrogation, or intensity measurements. Their sensing performances are usually estimated by the wavelength shift per refractive index unit. In single-particle sensors, ideal nanostructures have sharp features for highly localized electric field enhancement (e.g., Au nanostars[382] and bipyramids[773]). These highly sensitive plasmonic probes enable the analysis of important parameters in the physical process and the detection of reactive species in chemical reactions. For example, optically or thermally responsive plasmonic structures are important branches because they can provide kinetic and thermodynamic data during various physicochemical events. They employ photochromic molecules, photochemical reactions, or temperature-dependent phase-changing materials for colorimetric responses. Another important branch is responsive plasmonic nanostructures to chemicals. Plasmonic chemical sensors and biosensors are famous tools for probing diverse molecular binding events, including electrochemical reactions, hydration, protonation, coordination, and particularly the specific interactions between biological molecules.[385,387,388,774]

Compared with individual plasmonic colloids, the LSPR of their superstructures has much higher electric field enhancement due to the unique plasmon coupling effect. Therefore, the assembly of metal particles into responsive entities is predominant in developing smart plasmonic sensors. Many plasmonic assemblies, in the cases of Au, Ag, and Al, have demonstrated this unique property.[775-777] The advances in this regard have derived several important concepts in sensing, with plasmon ruler and plasmonic metamolecules as two compelling examples.[79,778-783] The first approach to tunable plasmon coupling is the surface functionalization of plasmonic nanoparticles. A noticeable plasmonic sensing system, particularly for biological molecules and ions, uses solution-processed assembly-disassembly of plasmonic particles.[784,785] This working principle leverages the easy surface functionalization of plasmonic nanostructures for selective recognition of analytes, which commonly accomplishes the assembly of these structures in colloidal solutions and redshifts of LSPR peaks. Depending on the dimension and shape of the superstructures, the assembly kinetics, thermodynamics, driving forces, and optical performances may vary significantly in the reported literature. Regarding plasmonic superstructures geometry, the current sensing units can be divided into dimers, oligomers, 1D chains, branched chains, 2D monolayers, 3D aggregates, and crystals.[786] They are of particular importance in real-time biosensing with single-molecule resolution. In this regard, typical applications include RNAse cleavage,[787] telomerase activity,[779] DNA hairpin folding,[788] membrane receptor separation,[789] mRNA quantification,[790] DNA screening,[791] protein detection,[792] living cell tracking,[793] isomerization monitoring,[794] aptamer analysis,[795] and single-chain measurement.[796] The working mechanism of a plasmonic ruler made of Au dimers is presented in **Figure 71a**. The coupled Au nanoparticles in the scheme are capped by a single aptamer, which is capable of binding individual target molecules. This specific recognition triggers reconfiguration of the aptamer crosslinker so that the decreased Au-Au separation leads to measurable redshifts with single-molecule sensitivity (**Figure 71b**).[795] The second approach is to incorporate plasmonic assemblies into a responsive matrix (e.g., colloids or thin films). While many superstructures can be directly embedded into functional materials, plasmonic particles can be co-assembled with responsive polymers into hybrid structures, both of which share smart responses in sensing and detection. Plasmonic nanoparticles are conductive organic particles stabilized by capping ligands that are neutral or charged organic molecules.[112,797] It is, therefore, possible to assemble plasmonic colloids by regulating these interparticle forces.[6] One may refer to a recently published review for a quick overview of colloidal assembly and active tuning of coupled plasmonic particles. In solution-processed self-assembly, the driving forces include van der Waals force and entropic force and a counterforce is necessary for exquisite control over the superstructures and optical properties, which typically include long-range electrostatic repulsion and short-range steric repulsion.[122,798,799] In several carefully prepared reactions, branched chains are observed by manipulating these interacting force pairs, which have optimal optical performances in place of random plasmonic aggregates. Typical examples include pH-, salt-, and temperature-driven assembly of plasmonic nanoparticles of different chemical components and sizes.[143-146,148,800] They can be used for sensing different types of solutes in solution or surrounding temperatures. Besides, these superstructures can further act as responsive units to probe solid-state physical processes and chemical reactions. Because of the strong plasmon coupling, a film containing Au chains appears blue that is the complementary color to the LSPR peak at the long wavelength. Pressing the film increases the interparticle separation and decreases the coupling strength so that the film gradually turns red. This colorimetric pressure sensor also provide progressive spectroscopic shifts for accurately evaluating mechanical strains.[547]

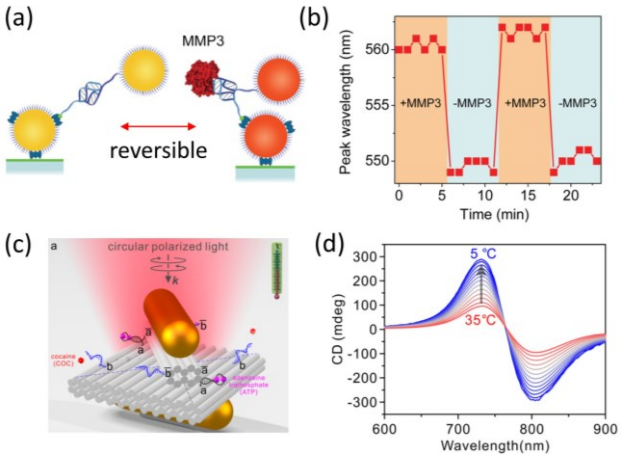

Figure 71. Active plasmonic assemblies for colorimetric sensing and spectroscopic detection. (a) Working principle of plasmonic dimer ruler for detection of biomolecules. (b) Reversible plasmonic peak shift in response to biomolecules. Reproduced with permission from ref [795]. Copyright 2015 American Chemical Society. (c) Schematic illustration of the dual-responsive plasmonic assemblies to thermal and aptamer-target regulations. (d) Reversible circular dichroism signal changes in response to temperature. Reproduced with permission from ref [801]. Copyright 2018 American Chemical Society.

Anisotropic plasmonic nanostructures have apparent benefits in colorimetric sensing, including enhanced sensitivity and multiplexed detection capability. To this end, self-assembly of anisotropic plasmonic colloids with precise orientational control has been developed using electric fields,[802] magnetic fields,[68,572] mechanical forces,[584] electrospinning,[803] and DNA templates.[634,804] Generally, the first four techniques yield plasmonic assemblies with collective orientational orders on a large scale, and the DNA templating technique is famous for producing small-size superstructures (typical of a few particles) with exclusively positional and orientational accuracy.[805] DNA templates with customizable sizes and reactivities can be prepared by the DNA origami technique. **Figure 71c** exemplifies such a complex structure, with a rotary bundle connected to a bilayer rectangular plate via a scaffold DNA strand. Two Au nanorods can be assembled to the top rotary bundle and the back surface of the origami plate. The as-prepared 3D plasmonic chiral dimers feature asymmetric coupling that is sensitive to circularly polarized light, leading to strong circular dichroism. Decreasing the solution temperature stabilizes the dimers and leads to a sensitive increase in circular dichroism (**Figure 71d**). This system can also be actively regulated by ATP molecules and demonstrates a dual-responsive plasmonic sensor.[801] One advantage associated with circular dichroism spectroscopy is the high signal-to-noise ratio, allowing for solution-processed detection of biological molecules. The highly orientational order of plasmonic assemblies makes individual LSPR very sensitive to any structural reconfiguration that is imposed by external stimuli. This property is based on the selective LSPR excitation in anisotropic plasmonic structures. Plasmonic nanorods, particularly of Au and Ag, have transverse and longitudinal plasmon modes because of the resonant oscillation of free electrons along short and long geometrical axes, respectively. In a superstructure with liquid crystal phases, it is possible to detect any small, local changes in structural orientation by measuring the intensities of the two plasmon modes. To this end, we performed systematic studies on the orientation-dependent plasmonic excitation using magnetic-plasmonic hybrid nanorods as building blocks.[572] This unique Janus structure allows for precisely controlling the rod orientation by external magnetic fields. A numerical model predicts that the plasmonic sensitivity in response to a small orientational variation is dependent on initial alignment, with an optimal performance around 45° to surface normal (**Figure 72a**). An experimental prototype is fabricated by applying a magnetic field along the pre-designed direction. For example, a film with an initial 30° alignment demonstrates very sensitive changes in LSPR peak intensity in response to mechanical pressures (**Figure 72b**). This sensing platform is universal to mechanical deformation, rotation, bending, and twisting but with interestingly different optical performances. The perceived color changes are uniform in rotation as the well-aligned nanorods have identical, linear changes in their collective orientations (left panels in **Figures 72c** and **72d**). In bending deformation, different colors are observed in the film two ends, indicating an opposite change in the plasmon excitation in the two regions (right panels in **Figures 72c** and **72d**). In a complex twisting process, the unidirectionally aligned nanorods reconfigure their assemblies into a chiral arrangement. Under linear polarization, the twisted films demonstrate alternative red-green segments due to the selective excitation of the transverse-longitudinal modes, respectively. These fundamental studies reveal the great potentials of anisotropic plasmonic structures in developing emerging colorimetric sensors if they can be properly assembled. A further extension of this strategy leads to complex colorimetric responses with high contrast and sensitivity (**Figure 72e**).

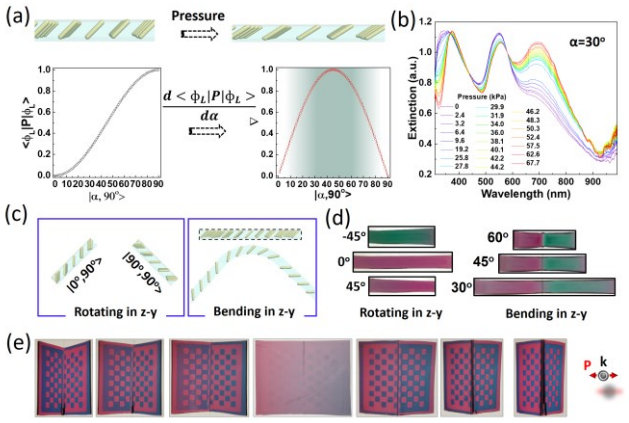

Figure 72. Mechanochromic plasmonic film enabled by the nanoscale magnetic assembly. (a) Theoretical prediction of the pressure-dependent orientation changes of plasmonic nanorods. (b) Extinction spectra of plasmonic films with unidirectional nanorod alignment under different mechanical pressure. (c) Schematic illustration and (d) colorimetric plasmonic films in response to rotation and bending. (e) Programmable mechanochromic responses of a plasmonic film. Reproduced with permission from ref [572]. Copyright 2020 The Authors.

4.3.3. Responsive Photonic Crystals for Sensing

Colorimetric sensing and detection is a well-established research field among many interesting applications of photonic crystals.[806] Several compelling examples are 1D photonic chains, 2D photonic films, and 3D opals or inverse opals with diverse optical responses to external stimuli (e.g., mechanical forces, chemicals, and heat). The large-scale fabrication of opals and inverse opals has been extensively exploited because of their low cost and easy fabrication. A typical sensing scheme is developed in **Figure 73a** through sequential assembly, infiltration, and etching.[807] In practice, the assembled opals, opals in a functional matrix, and inverse opals constitute a great proportion of photonic crystal sensors, with optical responses that are unique to their structures. For example, opals themselves have been extensively used for preparing chemical sensors based on the refractive index changes. They have apparent advantages of easy fabrication but have slower responses and smaller peak shifts compared with inverse opals. Embedding the opals into functional polymers can greatly extend their sensing capability because a great number of responsive polymers can be used to enhance their optical responses. For conventional sensors based on static reflection spectrum in an equilibrium state, many research results have reached an agreement that the dependence of peak shifts on refractive index or deformation is linear so that screening target analytes or analyzing mechanical strains is convenient. This implementation, in turn, limits the detection performances of photonic crystals. Instead, an advanced detecting technique measures the dynamic reflection spectrum to probe the diffusion kinetics and thus differentiate molecules with similar refractive index (**Figure 73b**).[808] When liquid analytes were added to a photonic crystal gel, the interdiffusion between the analytes and gel solvent is determined by the analyte polarity and its affinity to the gel. Therefore, molecules with high affinity led to fast analyte diffusion and significant swelling of the photonic gels so that a continuous redshift dominates the dynamic spectrum. In the case of non-polar and viscous solvents, gel extraction produced blueshifts. By carefully monitoring the dynamic peak shifts, it is possible to analyze molecules with similar physical properties, such as homologs (**Figure 73c**) and isomers.

2D and 1D photonic crystals can also be used for colorimetric detection. 2D array photonic crystals are usually made by assembling colloidal particles of a proper size at liquid-air interfaces or on flat substrates to limit the crystal growth along other directions.[499] Fixing the 2D structures in a polymer matrix is still necessary to enhance their mechanical properties and to allow reversible color changes in response to chemical or physical stimuli.[498] The process for polymer infiltration and their functions in colorimetric sensing are similar to what has been established in opals. 1D photonic chains are another attractive structure for sensing. In addition to being incorporated into the polymer matrix, the chains can serve as individual sensing pixels, allowing high-contrast, high-resolution colorimetric detection. Experimentally, this design can be achieved by magnetically aligning photonic chains so that vivid color changes can be observed during sensing. A recent study developed soft photonic chains made of magnetic nanoparticles using a pH-sensitive hydrogel to crosslink neighboring magnetic nanoparticles (**Figure 73d**).[809] Under a vertical magnetic field, the photonic chains can be aligned in the same direction, exhibiting bright structural colors determined by the interparticle separation. Increasing the pH alters the chain length and interparticle separation so that uniform color changes can be observed on individual chains (**Figure 73e**). This technique allows solution-processed colorimetric detection with greatly enhanced resolution and response rate.

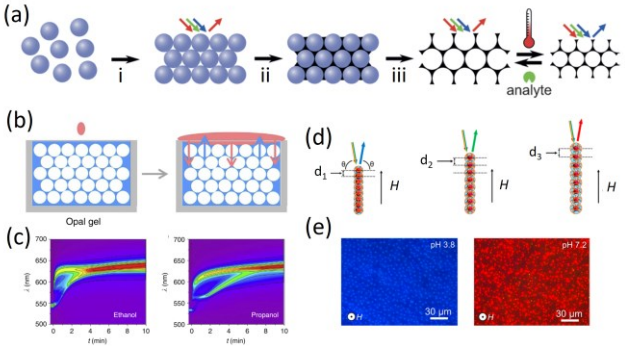

Figure 73. Smart photonic structures for sensing and detection. (a) Inverse opals for macromolecule sensing. Reproduced with permission from ref [807]. Copyright 2015 John Wiley and Sons. (b) Inverse opals for dynamic spectroscopic detection of solvents. (c) Dynamic reflection patterns in the detection of ethanol (left) and propanol (right). Reproduced with permission from ref [808]. Copyright 2015 The Authors. (d) Schematic illustration of the pH-induced color changing process of photonic chains. (e) Dark-field optical microscopy images showing the colorimetric response for different pH values. Reproduced with permission from ref [809]. Copyright 2020 American Chemical Society.

4.4. Anticounterfeiting and Information Encryption

4.4.1. Fluorescent Colloidal Assemblies

Fluorescent colloidal particles are ideal candidates for anticounterfeiting and information encryption because their emission can only be excited by light with a proper wavelength. Several compelling fluorescent colloids include quantum dots,[810,811] polymer nanoparticles,[812,813] carbon dots,[814] upconversion nanoparticles,[815-817] supramolecular particles.[818] In practical applications, a UV light is commonly used to read the encoded information or to access the authentication. This has been seen in several commercialized techniques in easy-to-use labels integrated into products or banknotes. For encoding information into customizable optical signals, many assembly or lithography techniques have been developed, such as nanoimprinting,[819] inkjet printing,[820-823] template-assisted assembly,[824-826] and simply handwriting.[827] Instead of forming highly ordered structures, these methods focus on creating arbitrary images and patterns that can communicate useful messages. Inkjet printing, for example, produces fluorescent images and letters with considerable resolution in cm^2-sized areas. It provides multilevel, high throughput production of customizable light-emitting tags and labels.

4.4.2. Plasmonic Colloidal Assemblies in Encryption

The LSPR of plasmonic colloidal particles features many attractive optical phenomena. They provide not only visible readouts

but also IR and SERS signals for high-level information encoding. Early attempts use their shape- and size-dependent LSPR for producing unique, high-density encoding.[828-830] The ability to manipulate light beyond the diffraction limits leads to high-resolution visible images that are difficult to be reproduced by other materials.[831] If the fabricated nanostructures are made with anisotropic shapes, the encrypted information can only be interpreted by applying a proper polarizer.[832-835] Assembling these metallic nanostructures in crystal phases (with both transitional and orientational orders) or mesophases (with either transitional or orientational orders) provides an open platform to pattern informative images in numerous optical devices. Along these lines, one challenge in the experiment is to assemble plasmonic colloids into desirable superstructures. Interface assembly provides such an elegant control, which regulates the self-assembly of plasmonic nanoparticles into 2D monolayers.[822,836] In representative work, Au nanoparticles are modified by a pH- and thermo-responsive dendronized copolymer.[837] It points out that an increase in temperature or pH alters surrounding copolymer configuration such that the interparticle separation decreases and the LSPR peaks redshift (**Figure 74a**). Interestingly, increasing the film humidity induces a reverse peak shift because the swollen polymer chains enlarge the interparticle separation. This sequence of events can be used to design a multi-panel anticounterfeiting film, which can exhibit visible color changes in response to humidity, pH, and temperature (**Figure 74b**). This approach to multi-responsive safety labels enhances the security and creditability of plasmonic anticounterfeiting devices.

Besides the perceptible colors, there also exist other intriguing physical processes that can be used, with photothermal effect and SERS being two compelling examples.[838] In photothermal conversion, the energy of absorbed light by the plasmonic nanostructures is converted into heat, leading to drastic temperature increases and infrared light emission. Some research efforts have been made to develop photothermal encryption-decryption techniques in which the encoded information is readable only using an IR camera.[839,840] SERS is a spectroscopic technique that takes advantage of the significant electric field enhancement on plasmonic particle surfaces or within the nanogaps of plasmonic assemblies.[828,841-843] The enhanced scattering from Raman molecules can be mapped from the pre-designed images so that reading the encrypted information is possible using a Raman spectrometer.[844-846] Monitoring the orientation-dependent LSPR is an alternative approach whose implementation and performance depend on the optical properties of the plasmonic building blocks. For example, short Ag or Au nanorods have their longitudinal LSPR peaks in the visible spectrum so that naked-eye encryption is possible. In other cases, an advanced electronic terminal is required to interpret the invisible information. In a recent development, a photoelectric sensor (photodiode) is introduced to decrypt information from mesophase plasmonic assemblies.[847] Magnetic/plasmonic nanocomposites are magnetically aligned in a polymer matrix with a pre-designed orientation. The larger nanorods have a longitudinal LSPR peak in the NIR region, and the absorbance change in the visible spectrum is relatively small. This explanation indicates that the assembled plasmonic films have similar colors, although the nanorods have different orientations (**Figure 74c**). Instead, the encrypted information in the rod orientation can be decoded by using a properly polarized light and a photodiode. As demonstrated in **Figure 74d**, the different rod orientations can regulate the transmittance of NIR light through the plasmonic films so that corresponding electric signals can be recorded precisely (**Figure 74e**). This system allows for high throughput information encryption-decryption by miniaturizing the plasmonic films.

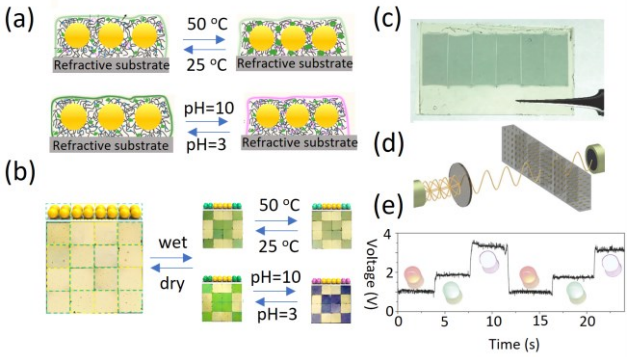

Figure 74. Smart colloidal assembly for anticounterfeiting and information encryption. (a) Schematic illustration of the crystal lattice changes in response to temperature and pH changes. (b) Multiple-coded anticounterfeit labels. Reproduced with permission from ref [837]. Copyright 2018 American Chemical Society. (c) Digital pictures of the plasmonic films for anticounterfeiting. (d) Schematic illustration of the decryption process. (e) Optoelectrical response of the plasmonic films. Reproduced with permission from ref [847]. Copyright 2018 The Authors.

4.4.3. Smart Photonic Crystals in Anticounterfeiting

The unique structural colors of photonic crystals have been extensively exploited for creating anticounterfeiting photonic films. For example, the structural colors of crystalline photonic structures are dependent on viewing angles or, in some cases, rotation angles. This special optical performance is not attainable by conventional pigments or dyes and has been widely used in consumer products in global markets due to the low cost and mass production. While industrialists favor a few well-established techniques for creating such structures (e.g., lithography and laser printing), several state-of-the-art approaches have been created to diversify the small anticounterfeiting films, with a focus on creating customizable patterns.[71,848] It includes several coating techniques (spray coating,[849] dipping coating,[850,851] and spin coating[246,247]), directed colloidal assembly,[852] nanoimprinting,[853] and printing.[848,854] Some advanced strategies use responsive photonic crystals for high-level anti-counterfeiting and information encryption. One distinct feature is their highly sensitive optical signals in response to external physical and chemical stimuli, enabling flexible information encryption-decryption. For practical applications, there are several criteria on the stimuli, including easy access in daily use, low cost, and high security. To this end, some biological stimuli (e.g., body temperature and humidity) are ideal. Shape memory or other thermal responsive photonic crystals offer such options for mechanochromic and thermochromic optical encryption.[855-857] Their color changes in response to mechanical forces and temperate allow potential authentication or information decryption using body temperature as a heat source if their phase transition temperature can be properly designed between ambient temperature and body temperature. In practice, combining responsive

materials with photonic crystals is a mature encryption strategy for information security.[858-860] Several previous reports come to appreciate that integrating photonic crystals with optically responsive layers (namely hidden layers) into heterolayers is simple yet effective approach.[858,860,861] The useful information is concealed in the encrypted layer of the hieratical structures, which can only be revealed by transparency changes of the top or surrounding hidden layers. Materials having been used for the hidden layer should have large transparency changes in a broad spectrum, including random colloidal aggregates[861] and amorphous opal array with a different structural colors.[858,862] A noticeable example is shown in **Figure 75a**, which contains top amorphous opal array and bottom crystalline inverse opals in the heterolayers.[862] At its dry state, the information is encrypted by the noniridescent structural color from the top layer. Interestingly, wiping ethanol discloses the information in the encrypted layer (bottom panel in **Figure 75a**). That is because ethanol has a similar refractive index with the top hidden layer so that this layer becomes transparent.

4.4.4. Hybrid Assemblies for Encryption

Colloidal particles may exhibit different physical and chemical properties depending on their organic/inorganic cores and the passivating ligands. Assembling them into binary or plural structures with tunable interparticle separation, hierarchy, and stoichiometry integrates these diverse functionalities and provides many compelling optical phenomena for information encryption and anticounterfeiting. Typical dual-mode encryption includes diffraction-emission[863] and absorption-emission.[864-866] The energy transfer between these physical processes has been used for highly secure encryption. When light-emitting materials (e.g., fluorescent molecules and upconversion nanoparticles) are in close contact with plasmonic nanostructures, their fluorescence is generally quenched due to a nonradiative process. On the contrary, when an intermediate graphene layer is introduced, the fluorescence is significantly enhanced largely because of the excitation of the gap plasmon polaritons. With this synergistic effect, a hybrid structure is developed (top panel in **Figure 75b**).[864] It comprises a top code pattern of plasmonic nanoparticles and a bottom code pattern of upconversion nanoparticles. The important information is encrypted into the hybrid structures and can only be interpreted correctly by NIR light irradiation (bottom panel in **Figure 75b**).

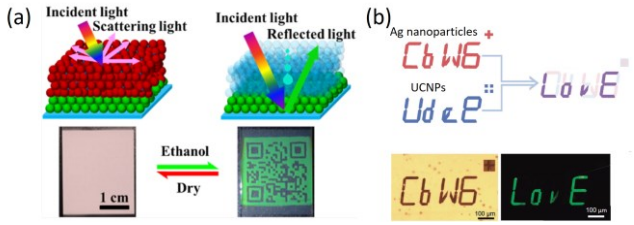

Figure 75. Smart colloidal assembly for anticounterfeiting and information encryption. (a) Working principle of photonic crystals for information encryption (top) and decryption in response to ethanol vapor (bottom). Reproduced with permission from ref [862]. Copyright 2020 American Chemical Society. (b) Working principle of hybrid superstructures for information encryption (top panel) and decryption under near-infrared light (bottom panel). Scale bars: 100 μm. Reproduced with permission from ref [864]. Copyright 2018 John Wiley and Sons.

4.5. Soft Actuators and Robots

Soft actuators and robots are made of composite materials for controllable mechanical deformation and locomotion.[867,868] One of their most attractive features is pre-designed shape morphing and locomotion powered by external stimuli, including light, chemicals, mechanical forces, electric fields, magnetic fields, electricity, and heat.[48,869] Compared with conventional mechanical robots made of rigid, high-density materials and skeletal structures, soft actuators have many advantages in performing mechanical work in place of their rigid counterparts. For example, they are usually made of low-density, soft materials, which can use the input energy more efficiently. Their soft bodies enable more flexible and more complex shape morphing and locomotion. This property also enables the design of smart adaptive robots that can perform untethered mechanical work in response to changing environments. While majority of the rigid robots use electricity, soft actuators and robots have more optional energy inputs, with some of them being renewable (e.g., light, wind).[870] In addition, relying on many advanced lithography and assembly techniques, the fabrication of soft robots is scalable and easy to be miniaturized. Therefore, soft actuators have been extensively exploited in many research fields, ranging from targeted drug delivery to bioimaging, man-made robots, artificial muscles, and bionic devices.[871,872] The key to creating desirable mechanical deformation or locomotion is to induce volume or shape changes in the composite structures. In this section, we summarize the existing colloidal assembly approaches to soft actuators and robots.

4.5.1. Magnetic Actuators

The magnetic interaction between external magnetic fields and particles embedded in actuators is one common driving force for magnetic actuation. This nanoscale magnetic assembly offers fine control over the orientational and/or positional orders of magnetic building blocks in soft materials.[66] The magnetic interactions are reversible, instant, and remote, setting the stage ready for designing multifunctional actuators and robots. For example, if the assembled magnetic nanostructures are patterned in specific domains, it is possible to develop magnetic actuators with complex and programmable shape morphing.[873] In addition, many functional soft materials can be introduced to design actuators that are responsive to multiple stimuli or perform reconfigurable shape changes in phase-changing polymers.

Aligning and pattering ferromagnetic particles in soft matrice is a simple yet promising method to prepare magnetic actuators. This approach uses the parallel alignment of ferromagnetic particles with the external magnetic fields for assembling each dipole into uniform orientational order and actuating individual domains into a collective, complex shape morphing. A noticeable example is NdFeB magnetic particles that are a few micrometers and ferromagnetic with high remanent magnetization and high coercivity. There exist several advanced techniques for assembling and patterning the magnetic particles inside the soft matrix. For example, applying a considerably strong magnetic field is able to magnetize the embedded particles, leading to an actuator configuration-dependent magnetization profile.[874] That is, the dipolar orientation and strength of magnetic particles in the soft actuator are determined by the spatial configuration of the soft body upon magnetization. Wrapping the soft structures

in a cylinder during magnetization yields soft actuators with periodic, harmonic magnetization profiles. This unique feature enables the soft actuators to adjust their deformations under different field strengths and directions. If an alternating magnetic field is used, an actuator prepared by the same design can perform multimodal locomotion, such as rolling, walking, jumping, crawling, and swimming. Given its high flexibility in deformation and locomotion, this adaptive magnetic actuator is expected to perform work in biological tissues and other unstructured environments. An alternative, more frequently used approach magnetizes the magnetic particles before polymerization of the soft actuators. This technique is combined with conventional printing or molding processes to produce pre-designed magnetization profiles and programmable deformations. Zhao et al. developed a continuum magnetic robot by firstly magnetizing the NdFeB microparticles in elastomer precursor and then printing the component ink into a 1D continuum robot.[875] In the first step, a strong impulse of a magnetic field is used to magnetically saturate the microparticles, and the following printing yields a uniform magnetic domain in the cured elastomers. Since the continuum robot has a circular cross-section, active steering is possible under magnetic field actuation. Although it can also perform work in complex biological tissues, it is tethered, which may limit its use to steerable delivery and navigation. An untethered fast-transforming soft robot can be created by printing ferromagnetic domains with controllable shapes and domain distribution. In a modified printing step (**Figure 76a**), an electromagnet is integrated into a dispensing nozzle so that the NdFeB microparticles will be magnetized and aligned with tunable orientational orders in each domain during printing. One advantage of using an electromagnet is the easy switching of the field direction, which is important for actuating complex deformations. Controlling the shape and dimensions of the soft body is also possible by the printing process. For example, annulus, hollow cross, quadrupedal and hexapedal (**Figure 76b**) structures can be easily printed, and applying a vertical magnetic field generates 3D shape changes determined by the encoded magnetic patterns. This process can be used to capture a fast-moving object using a permanent magnet (top panel in **Figure 76b**). More interestingly, the soft actuator can perform rolling-based locomotion under a rotating magnetic field and release the object on demand (bottom panel in **Figure 76b**). The magnetization of assembled structures can be programmed in sequence based on the different magnetic properties of the building blocks.[876] This material design enables reconfigurable and reprogrammable functions for a single actuator. **Figure 76c** shows a four-panel micromachine with 2D arrays of nanomagnets. Notably, the size of the nanomagnets is different, so that their magnetization profile is tunable. Under a carefully chosen magnetic switching field, the direction of the 2D arrays can be selectively reversed. The combined rigid magnetic panels and elastic joints induce complex 3D shape changes in response to static or changing magnetic fields (**Figure 76d**). This assembly-magnetization strategy is expected to provide smarter micromachines if a radio-frequency magnetic field is employed.

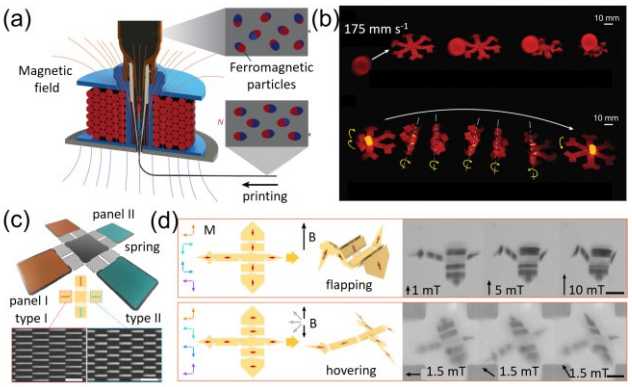

Figure 76. Colloidal superstructures for magnetic actuators. (a) Working principle of designing magnetic actuators by combining nanoscale magnetic assembly and printing. (b) A hexapedal robot capturing a fast-moving object (top) and shipping cargo using rolling-based locomotion under a rotating magnetic field. Scale bars: 10 mm. Reproduced with permission from ref [877]. Copyright 2018 Springer Nature. (c) Four-panel micromachine with an array of nanomagnets with different orientations (top) and SEM images of the nanomagnet 2D array (bottom). (d) Programmable microscale bird with multiple shape-morphing modes. Scale bars: 30 μm. Reproduced with permission from ref [876]. Copyright 2019 Springer Nature.

Assembling magnetic nanoparticles into 1D superstructures is another approach to magnetic soft actuators. This working principle relies on the magnetic anisotropy of the assembled superstructures for actuating soft materials. Magnetic field-assisted lithography is a common method because its flexibility allows for controlling the superstructure orientations by applying a magnetic field followed by curing the elastic precursors. In early research, Kim et al. used a digital micromirror modulator to pattern the assembled structures. This printing process provides accurate, high-resolution patterning of magnetic assemblies.[685] The well-defined magnetic anisotropy in the polymer matrix allows for predesigned, complex 2D and 3D motion.[878] In more common practice, a photomask is used to fix and pattern the assembled magnetic structures in elastomers.[879] **Figure 77a** shows a typical lithography process, during which magnetic fields are changed on demand so that the alignment of the superstructures in each soft domain is well-defined. One additional advantage of the aligned 1D assemblies is the anisotropic swelling property of the elastomers. Specifically, the swelling of polymer matrix along the perpendicular direction of 1D chains is much higher than the parallel direction because of the local reinforcement of the assembled 1D structures. In the example of **Figure 77a**, the structural tail is an elastomer monolayer with uniformly aligned chains. Its folding axis in water is perpendicular to the alignment of magnetic 1D chains, leading to a twisted shape. With the preferential parallel alignment of the assembled 1D structures in the curved actuator with magnetic fields, this unique swollen actuator can be propelled in water by applying a rotating magnetic field (**Figure 77b**). Realignment of the assembled magnetic structures is possible if they are embedded in phase-changing materials, such as oligomeric-PEG (**Figure 77c**).[880] The PEG oligomer used in this work has a melting temperature of 58 ºC so that the embedded magnetic chains can be re-aligned along any arbitrary directions by simply heating the elastomer and applying a magnetic field

(**Figure 77d**). Therefore, a single magnetic actuator can perform several complex shape changes (**Figure 77e**).

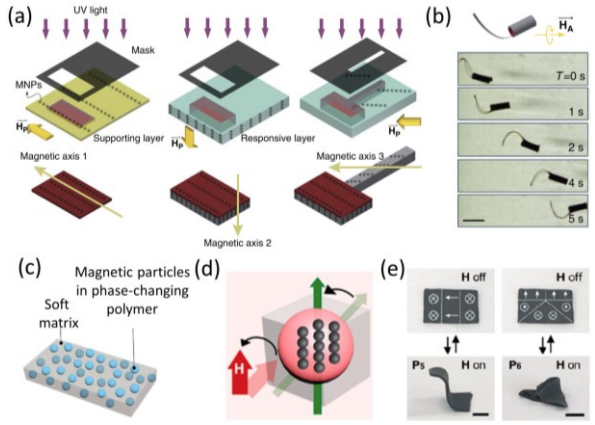

Figure 77. Preparation of magnetic actuators by lithography and nanoscale magnetic assembly. (a) Schematic illustration of the fabrication of biomimetic soft micromachines. (b) Optical images of a biomimetic robot driven by a rotating magnetic field. Scale bar: 2 mm. Reproduced with permission from ref [879]. Copyright 2016 The Authors. (c) Schematic illustration of structures of the reprogrammable magnetic actuators. (d) Schematic illustration of reprogramming the orientation of magnetic chains. (e) Digital pictures of the shape-morphing of the magnetic actuator. Scale bars: 10 mm. Reproduced with permission from ref [880]. Copyright 2020 American Chemical Society.

4.5.2. Photoactuators

Light-driven actuators and robots use light as renewable energy for actuating soft materials. They can convert light energy into mechanical deformations or locomotion at multiscale. Based on the working mechanism, light-driven soft actuators can be categorized into photochemical actuators and photothermal actuators.[881] Photoisomerization and photodimerization are two typical photochemical reactions to drive mechanical motions. To exploit the unique photochromic properties, chemists have synthesized many photosensitive chromophores with tunable response rate and wavelength, controllable conformal changes or chemical reactions, high sensitivity, and good stability. A few noticeable examples include diarylethene,[882,883] azobenzene,[458,884-886] anthracene derivatives,[454,887,888] salicylideneaniline family,[889-891] spiropyran derivatives,[892-894] phenylbutadiene derivatives,[895] and other alkenes.[896] Depending on the structural order of these photosensitive molecules, commonly used materials for photochemical actuators include liquid crystal elastomers (LCEs) and molecular crystals, with the former of purely orientational orders. LCEs have a polymer network that is functionalized with active photochromic dyes, with mesogens attached either in the polymer chains (main-chain LCEs) or via an alkyl spacer (sidechain LCEs). Therefore, dye photoisomerization, e.g., E/Z isomerization, valence isomerization, cycloaddition, and tautomerization, can be used for actuating the soft polymer matrix with designable deformations. In many carefully prepared reactions, some photochromic molecules will crystalize into photomechanical molecular crystals.[441] In solid-state, large changes in the molecular geometry lead to a dramatic photomechanical response in the bulky crystals. Several established photomechanical responses include bending,[897-899] twisting,[888,900] rotation,[901] crawling,[902] peeling,[903] expansion,[454] spreading,[895] and hopping.[904]

Photothermal actuators take advantage of the photothermal effect of light-absorbing materials for actuating soft materials. Under light irradiation, these materials can efficiently absorb light at a particular wavelength or over a broad spectrum and convert the light energy into heat. The temperature-induced phase changes of surrounding polymer networks or small molecules will lead to predesigned mechanical work, which is highly dependent on actuator designs, the assembled structures inside, and the phase-changing materials. A typical photothermal actuator comprises three components, the light-absorbing materials, a passive layer, and thermally responsive layers for volume expansion, phase changes, or molecule absorption/desorption. Commonly used light-absorbing materials include carbon nanostructures, plasmonic nanomaterials, and photochromic molecules. In some actuators, the light-absorbing materials also serve as responsive or passive layers. This simple design of materials represents an open platform to prepare diverse photothermal actuation.

Combining the photochemical and photothermal effects of LCEs has been demonstrated as a promising approach to reconfigurable photoactuators.[905] One attractive feature is their adaptive shape morphing in response to an identical stimulus. The dual responses of azobenzene photoisomerization are illustrated in **Figure 78a**. Its configuration changes lead to a simultaneous transition from the liquid-crystal phase to a disordered phase in the irradiated domain of LCEs and thus a slight shape change of the soft actuator. Because of this phase transition, the actuator shrinks along the initial alignment direction of the LC molecules and expands along the perpendicular direction. The ability to control the molecular orders in LCEs is the key to reconfiguration. As shown in **Figure 78b**, an LCEs film is first irradiated by UV light to generate photochemical patterns, with different molecular orders in each domain, leading to one type of shape-morphing under red-light irradiation. The original liquid phase can be recovered by blue-light irradiation so that the actuator shape-morphing can be reprogrammed. Photochemical patterning is a useful strategy for designing functional actuators, for example, photonic actuators. This scheme shown in **Figure 78c** incorporates inverse opals with LCEs for simultaneous shape-morphing and color changes.[906]

Carbon nanomaterials have many categories with distinct physical, chemical, and mechanical properties.[907-909] And, the majority of them (except diamond) have broad-band absorption in the visible range.[910] This unique property makes carbon materials extensively exploited in developing photothermal actuators.[432] Among these materials, carbon nanotubes, with their attractive 1D features, are a promising candidate. Many research works have demonstrated that aligned carbon nanotubes in a soft matter can significantly enhance and modulate the mechanical property of the substrate.[911] This effect can be used to prepare tunable photothermal actuators whose deformations (e.g., phototropic/apheliotropic bending, three-dimensional twisting) depends on the nanotube alignment.[912] The assembled carbon nanotubes were spun from spinnable arrays that were prepared by chemical vapor deposition.[913,914] A polyimide/paraffin bilayer film was used as a soft matrix, with carbon nanotube uni-

formly aligned inside. Cutting the film along different directions produced actuators with different nanotube orientations (**Figure 78d**) so that the soft actuator has anisotropic mechanical properties. This effect constraints longitudinal volume expansion of the actuator, only allowing expansion perpendicular to the orientation of aligned CNTs. Therefore, apheliotropic (top panel in **Figure 78d**) and phototropic bending (bottom panel in **Figure 78d**) can be achieved by aligning the carbon nanotubes along the transverse and longitudinal directions, respectively. Graphene oxide nanosheets are another attractive carbon material for photothermal actuators.[433,915,916] Their black color implies the broad-band absorption in the visible range, while their ability to absorb water molecules leads to unique swelling behavior. Co-assembly of CO nanosheets and polymer nanospheres with a composition gradient leads to photothermal actuators that are responsive to both moisture and light.[917] Upon light irradiation, the photothermal effect of GO nanosheets caused the volume expansion of polymer spheres and the bending toward the GO-rich side. When the actuator was exposed to moisture, however, the GO-rich side swelled, leading to an opposite bending.

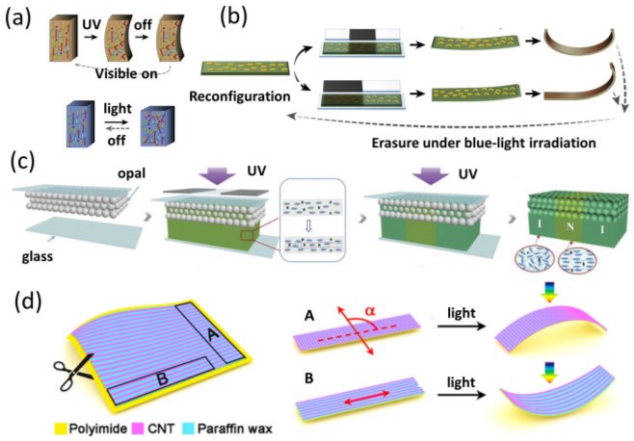

Figure 78. Preparation of magnetic actuators by lithography and nanoscale magnetic assembly. (a) Schematic illustration of the photochemical (top) and photothermal (bottom) actuation. (b) Schematic illustration of reconfigurable shape morphing. Reproduced with permission from ref [905]. Copyright 2018 The Authors. (c) Preparation of photothermal actuators using liquid crystal elastomer. Reproduced with permission from ref [906]. Copyright 2018 John Wiley and Sons. (d) Scheme of tunable photothermal actuators based on carbon nanotubes with pre-programmed alignment. Reproduced with permission from ref [912]. Copyright 2015 American Chemical Society.

In contrast to the broad-band absorption of carbon materials, nanostructured plasmonic materials have well-defined absorption at the resonant wavelength. One interesting effect of the LSPR is the local heating that is induced by electron-phonon relaxation.[918] By embedding or directly printing plasmonic nanostructures in phase-changing materials, a plain film can engage in designed deformations powered by light.[919-921] Printing plasmonic nanostructures requires first impregnating the polymer networks with metal precursors and reducing them to metal nanostructures by photochemical reactions.[922] This process yields printed features as small as a few micrometers and has precise control over the particle location in the soft matrices. Its high patterning performance has been used for designing emerging shape-morphing and complex collective motion of nanocomposite actuators.[921] Controlling the positional and/or orientational orders of plasmonic nanostructures by the colloidal assembly is an alternative approach to advanced photothermal actuators. However, assembling the plasmonic nanostructures in polymer networks is a challenge. Among the many established techniques, magnetic assembly is the most effective method largely because of its remote control, good reversibility, and fast response. A free-standing, multidirectional photothermal actuator is created by the nanoscale magnetic assembly of Janus Fe_3O_4/Ag nanorods.[574] A space-confined seeded-mediated growth of Ag is employed by templating against silica shells, which yields Janus Ag and Fe_3O_4 nanorods with parallel alignment (**Figure 79a**). If a magnetic field was applied during light-initiated polymerization of a polyacrylamide network, the Janus nanorods are assembled into liquid-crystal phases by the nanoscale magnetic assembly. The defined orientational order of the co-aligned Ag nanorods enables the selective excitation of the LSPR modes and on-demand bending of the PAM matrix under polarized light irradiation. For converting this unique bending into continuous locomotion, the Janus nanorods are aligned in horizontal and vertical directions in a bipedal robot's legs (**Figure 79b**). Switching the light polarization between the two directions leads to a continuous walking of the free-standing robot. Turning the robot to a desirable direction is also possible if the laser polarization is fixed for constant actuation of one leg. In another design, magnetic assembly is employed to cofacially align diamagnetic titanate nanosheets in a PNIPAM network (**Figure 79c**).[923] This soft actuator contains Au nanoparticles for photothermal conversion, which raises the network temperature and drives its phase transition under light irradiation. One interesting effect of the dehydration-rehydration transition of PNIPAM is the synchronous changes of its apparent electrostatic permittivity.[924] It leads to simultaneous modulation of the electrostatic interactions between the well-aligned titanate nanosheets so that a reversible expansion and contraction of the hydrogel occurs isovolumetrically along the nanosheet orthogonal direction (the scheme in **Figure 79d**).[925] A cylindrical soft actuator can therefore perform earthworm-like locomotion in a confined space (optical pictures in **Figure 79d**). These elegant designs of photothermal actuators come to appreciate the important role of colloidal assembly in designing bionic robots and functional devices.

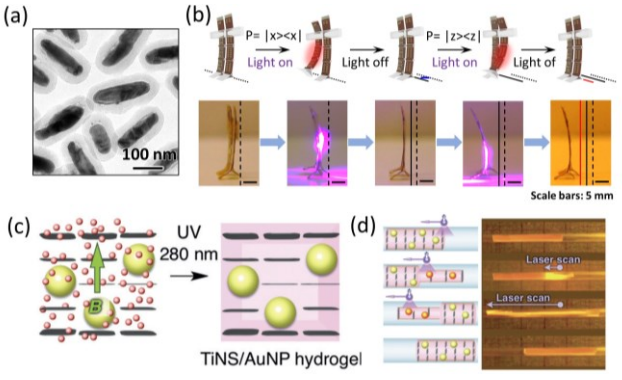

Figure 79. Advanced photothermal actuators enabled by the nanoscale magnetic assembly. (a) TEM image of magnetic-plasmonic hybrid nanorods. (b) Schematic illustration (top) and forward

movement (bottom) of the polarization-modulated soft robots. Reproduced with permission from ref [574]. Copyright 2020 John Wiley and Sons. (c) Schematic illustration of the anisotropic photothermal actuator enabled by the nanoscale magnetic assembly. (d) Working mechanism and digital pictures of the anisotropic hydrogel actuators driven by light irradiation. Reproduced with permission from ref [923]. Copyright 2018 John Wiley and Sons.

4.5.3. Thermal Actuators

Thermal actuators use heat as the input energy and have many similarities with photothermal actuators in structures and performances. Many phase-changing materials that have been used in photothermal actuators are also good candidates for thermal actuation, with bimorph being a common example.[926] The hierarchical structures have thermally responsive and passive layers/domains.[927] Creating gradient materials with changing mechanical properties or phase behaviors is another empirical approach to thermal actuators.[928] A few commonly used temperature-responsive materials include PNIPAM, LCEs, and PDMS.[929-931] One great benefit of employing colloidal assembly in this regard is to bring new functions in addition to shape morphing when the temperature changes. Color change takes advantage of the thermal deformations in soft matric for thermochromic responses. Because the elastomer deformation is associated with volume shrinkage or expansion, photonic crystals and plasmonic nanostructures whose color is dependent on the orders of colloidal particles are two promising materials.[429,430] They can be readily incorporated when polymerizing the elastomers, leading to color-changing thermal actuators. **Figure 80a** shows a working scheme for a plasmonic thermal actuator with a 2D Ag array on its surface.[430] The temperature-induced surface expansion of the LCEs leads to an increase in interparticle separations. The plasmon coupling between neighboring Ag nanoparticles becomes weak, and their LSPR peaks will blue shift with noticeable color changes. In a carefully designed system, colloidal assemblies can be crucial to driving the thermal actuation.[925] Its working mechanism is based on the electrostatic repulsion changes between assembled nanosheets, which is proposed in **Figure 79d**. An L-shaped, symmetric hydrogel actuator is created with cofacially oriented nanosheets to achieve unidirectional locomotion on a solid substrate (**Figure 80b**). At high temperatures, the strong electrostatic repulsion between the nanosheets drives the actuator to elongate perpendicularly to the sheet alignment. This sequence of events propels the hydrogel actuator to walk unidirectionally (**Figure 80c**). The mechanical response of thermal actuators is generally slower than that of photothermal actuators, largely because of heat diffusion in the bulk actuators.

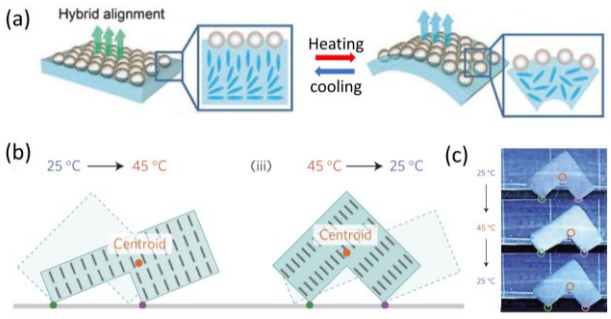

Figure 80. Thermal actuators. (a) Schematic illustration of the deformation behavior of plasmonic-liquid crystal hybrid actuators. Reproduced with permission from ref [430]. Copyright 2016 Royal Society of Chemistry and the Centre National de la Recherche Scientifique. (b) Working principle and (c) digital pictures of the anisotropic thermal actuators enabled by magnetic alignment. Reproduced with permission from ref [925]. Copyright 2015 Springer Nature.

4.5.4. Electric Actuators

Compared with other stimuli, the use of electricity as input energy has several advantages. For example, the easy modulation of the power, amperage, voltage, and current type enables flexible control over the actuation magnitude, phase, and vibration frequency. Besides, their designs are compatible with emerging soft electronics and conventional batteries. It is also possible to engineer them into self-powered electronic devices. Thirdly, the use of microcircuits or integrated circuits in designing electric actuators provides great opportunities in creating complex mechanical work and locomotion. It is therefore highly expected that integrating soft electronics with electric actuators has great potential in developing artificial muscles and organs, programmable microrobots, microfluidic devices, and wearable electronics.[932-934] To prepare electrically responsive actuators, there exist several empirical and fundamental criteria, including conductivity, deformability, fast response, and high efficiency. Several modern designs use tethered structures to power the soft actuators, while only a few examples introduce integrated batteries for self-sustained mechanical work.[935-937] No matter how they are powered, current studies have verified some important working principles for electric actuators, including electrothermal effects,[938-941] electro-hydraulic actuation,[942] electrophoresis,[943] and pseudocapacitance-based lattice contraction.[944]

Electrothermal actuators use Joule heating for actuating thermally responsive materials. Because of the resistance of conventional conductors (e.g., carbon materials, plasmonic nanostructures, and conductive polymers), the electric current passing through them will produce heat. Li et al. developed a printing assembly strategy to align GO sheets into laminar-structured patterns (**Figure 81a**).[938] The shear force during printing makes GO align along the flowing direction, and the close-packed structures after drying produce excellent conductivity. The printed patterns are uniform on a large scale, with an optical resolution of 200 μm (optical image in **Figure 81b**). One advantage of the printing assembly is the ease of its application on substrates or templates. For example, the patterns can be directly printed on soft PDMS films as electrodes. After applying a voltage, the Joule heating induces thermal expansion of the film surface, leading to reversible bending of the integrated film (**Figure 81c**). If printed domains are controlled by separate circuits, it is possible to create programmable actuators (**Figure 81d**). Their mechanical deformation and functions can be accurately controlled by the way to apply voltages. This invention is expected to produce miniature robots with integrated functionalities.

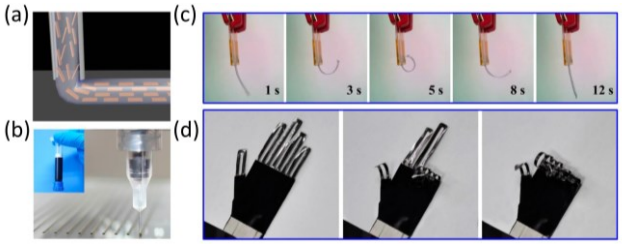

Figure 81. Electric actuators by printing assembly. (a) Scheme of the printing assembly. (b) Digital picture of the printing process. Inset is the picture of the ink. (c) Digital pictures of the bending under electrical stimulation. (d) Electrically tunable shape-morphing of a hand-shaped actuator. Reproduced with permission from ref [938]. Copyright 2016 American Chemical Society.

4.5.5. Chemically Responsive Actuators

A chemical stimulus can be in the liquid phase or gas phase, both of which need to experience the diffusion from the surroundings to the actuator body. Several typical examples include moisture, pH, salt, water, organic compounds, and biological molecules.[945] When in contact with the stimulus molecules, the soft networks may undergo chemical reactions, configuration changes, or phase transitions. One common feature of these changes is an apparent volume shrinkage or expansion so that mechanical actuation can occur. There exist a few challenges that are associated with the chemical reactions or physical transitions while choosing the soft matter and the working mechanism. For example, a structural or molecular design to facilitate massive mass transfer is highly desirable, which guarantees a fast response in exposure to chemicals. In some systems, it takes several minutes or even hours to reach the chemical and mechanical equilibrium. Therefore, it needs additional efforts in designing a soft actuator in fast response to target molecules. In this regard, the colloidal assembly approach plays a pivotal role in providing highly ordered and porous networks for fast chemical diffusion. The most famous example in this process is the use of inverse opals with 74% porosity to facilitate the mass transfer within photonic actuators. This implementation also provides additional color changes because of the well-defined 3D orders in the porous materials. Another challenge in chemically responsive actuators is to achieve complex shape morphing and desirable locomotion, largely because accurately controlling the diffusion direction of chemicals is difficult.

Natural species and living organisms have many fascinating shape changes in response to specific stimuli.[946-949] A few interesting examples are seed dispersal units, climbing plants, and carnivorous plants. A close investigation reveals that many natural plants use cellulose microfibers with well-defined alignment to anisotropically restrict the swelling/shrinkage of their organic matrices.[950,951] Inspired by this working mechanism, a self-shaping actuator with programmable microstructures is developed by magnetically assembling Al_2O_3 platelets in the soft network of a hydrogel.[950] Its significant restriction on the hydrogel swelling along the alignment direction leads to anisotropic mechanical properties. If the platelets were aligned orthogonally in the top and bottom of a bimorph, the soft actuator could bend on immersion in water. A simple extension to a 45° alignment to the film edge leads to a twisting deformation, whose pitch and charity can be readily controlled by changing the alignment angle. This magnetic assembly approach establishes a reliable approach to chemically responsive actuators with complex and programmable shape morphing. An advanced technique combines the reinforcement of assembled nanostructures with biomimetic 4D printing.[952] As shown in **Figure 82a**, stiff wood-derived cellulose fibrils are assembled into a liquid-crystal phase driven by shear forces when a composite ink flows through the deposition nozzle. It yields printed filaments with anisotropic stiffness and swelling behavior in the longitudinal direction compared to the transverse direction (**Figure 82b**), allowing accurate control over the bending curvature of bilayer structures with pre-designed, different fibril alignment.[953] Two interesting examples include logarithmic spiral and twisted bilayer strips when fibril alignment in the two layers is 90°/0° with inhomogeneous spaces and −45°/45° with uniform spaces, respectively. The programmable control over the ink paths can combine these simple curved surfaces so that biomimetic architectures can be produced. Specifically, to mimic flower opening and closing,[951,954] the bilayer was printed into a floral form with a 90°/0° configuration (left panel in **Figure 82c**). Simply changing the alignment to −45°/45° combination produces flower-like twisted deformations in water (right panel in **Figure 82c**). The actuator's network structures promote rapid diffusion and uptake of water through the filament radius so that the shape changes can occur in several minutes. This 4D printing technique combines the ease of a programmable printing pathway and the functionality of assembled microstructures, providing shape-changing architectures that can be controlled in space and time. Its easy extension to unlimited choices of functional materials and soft matrix represents an open platform to design bionic devices.

In addition to bilayer structures, colloidal assemblies in liquid-crystal phases are also used in producing gradient or composite materials. Bamboos are a famous natural composite material, which contains cellulose fibers embedded in a lignin−hemicellulose matrix. The gradient distribution of load-bearing fibers provides comprehensive hydrogen bonds among cellulose, lignin, and hemicellulose, providing strong mechanical strength.[955] Cao et al. developed a layer-by-layer assembly of MXene, fibers, and polymers into hierarchical gradient structures using a vacuum-assisted filtration process.[956] This method produces chemical actuators that have tensile strength, high Young's modulus, and fast hygroscopic response. Their unique mechanical properties lead to multimodal actuation powered by humidity exposure.

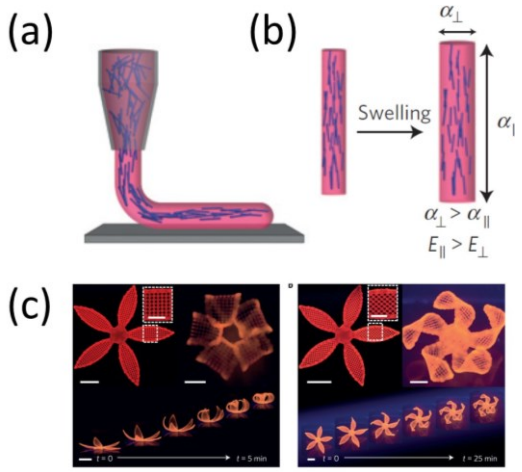

Figure 82. Chemical actuators by printing assembly. (a) Biomimetic 4D printing. (b) Anisotropic swelling of the hydrogel due to the alignment of cellulose fibrils. (c) Digital pictures of the predictable shape-morphing of soft actuators in response to immersion in water. Reproduced with permission from ref [952]. Copyright 2016 Springer Nature.

If colloidal assemblies have photonic bandgaps in the visible spectrum, it is possible to prepare colorimetric actuators by integrating self-assembly with actuator preparation.[47] Some representative photonic structures used for fabricating chemical actuators include opals,[957] inverse opals,[46,550,958] layered photonic gels,[959] and 1D cellulose photonic crystals.[960] Chameleons are inspiring natural creatures that can alter skin colors to communicate and create disguises during locomotion. To mimic their intriguing characteristics, wang et al. developed a structural-color actuator using inverse-opal soft networks.[46] Colloidal crystal arrays (CCAs) of silica nanoparticles are first assembled on a glass template using a conventional solvent evaporation method (**Figure 83a**). A trimethylolpropane triacrylate prepolymer solution was infiltrated into the CCAs, and the following polymerization and etching yielded an inverse opal film (**Figure 83b**). The highly ordered structures exhibit bright structural colors that are determined by their periodicity and surrounding refractive index. Meanwhile, the porous polymer network enables fast absorption and desorption of organic vapors. The diffusion of vapors leads to polymer network swelling, and thus the exposed surface expands, leading to bending deformation toward another film surface.[38,961] Therefore, a soft actuator with an anisotropic shape is created with simultaneous color changes and locomotion powered by acetone vapors (**Figure 83c**). A similar fabrication procedure was also used for preparing a living structural-color hydrogel actuator.[550] Instead of seeking external stimuli, the authors integrated cardiomyocyte tissues on synthetic inverse opal films (**Figure 83d**). This photonic structure contains bioactive hydrogels, whose extracellular matrix components facilitate the attachment, growth, alignment, and elongation of the cardiomyocyte.[962,963] Further introducing radial microgrooves by templating against microgroove patterns enables the cardiomyocytes to align anisotropically along the grooves. It provides corresponding anisotropic and synchronous contractions and relaxations to the substrate, which leads to simultaneous wing swinging and color shifts on a biomimetic butterfly (**Figure 83e**).

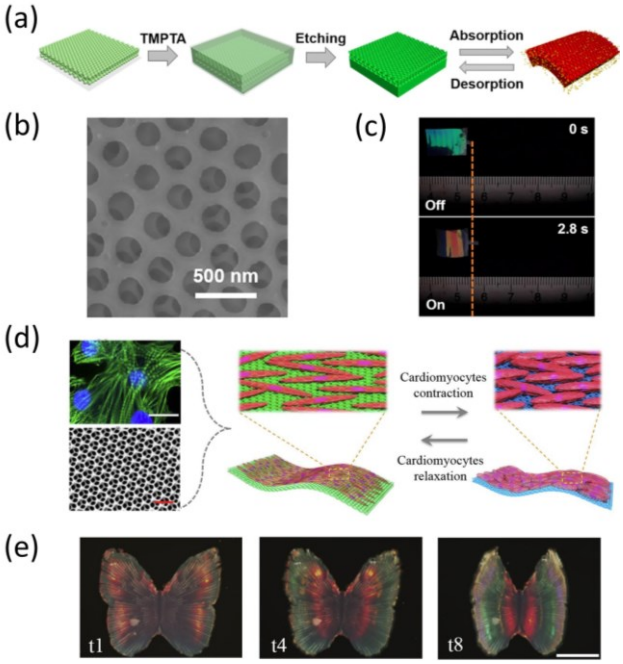

Figure 83. Inverse opal actuators. (a) Preparation of inverse opal soft actuator. (b) SEM image of the inverse opal. (c) The structural color actuator demonstrates simultaneous shape-morphing and color changes in response to vapor exposure. Reproduced with permission from ref [46]. Copyright 2019 Elsevier. (d) Design of bioinspired structural color actuators. (e) Optical microscope images of the structural color actuator driven by one myocardial cycle. Scale bar: 2 mm. Reproduced with permission from ref [550]. Copyright 2018 The American Association for the Advancement of Science.

4.6. Nanomedicine

The use of colloidal assemblies for biological applications requires additional efforts to solve the biocompatibility and colloidal stability issues.[508,964,965] In addition, there exists an optimal size range for in vivo biological imaging and cancer treatment.[82,83,966-969] To this end, plasmonic superstructures have been demonstrated as a promising theranostic platform for photoacoustic imaging and photothermal therapy, whose potential has also been extended to fluorescent and SERS imaging if light probes are used.[78,970,971] Within the scheme of colloidal assemblies, it is possible to develop smart imaging and therapy agents based on their unique property changes in response to either remote stimuli (light, electric fields, magnetic fields, etc.) or local stimuli in biological microenvironments (pH, H_2O_2, O_2, temperature, etc.). One great benefit of using plasmonic superstructures for nanomedicine is that their optical, photothermal, and photoacoustic properties are highly dependent on particle connection within the assemblies. By assembling plasmonic nanoparticles with therapeutic agents, it is possible to create a NIR-II light activatable nanomedicine (**Figure 84a**),[972] which comprises amphiphilic Au nanorods, polyprodrug, and NIR-II dyes (**Figure 84b**). The plasmon coupling of Au nanorods in the dense assemblies has high absorbance in the NIR region, which is used for in vivo photoacoustic imaging, while the close contact between Au nanorods and dyes quenches the fluorescence. Interestingly, the therapeutic vesicles disassemble upon laser irradiation, releasing the densely packed nanorods, polyprodrug, and dyes to the tumor microenvironment. This sequence of

events decreases the absorption of the Au nanorods in the NIR regions, and the fluorescence of dyes recovers from the quenched state. A simultaneous decrease in photoacoustic signals and a significant increase in fluorescence intensity occur due to the light-responsive agent disassembly (**Figure 84c**). A similar strategy uses the thermoresponsive PNIPAM microgel as the smart platform, and Au nanorods are grown on its matrix.[973] Increasing the temperature above the LCST of PNIPAM, the microgel shrinks due to its hydrophilic-to-hydrophobic phase transition. The associated change of plasmonic coupling between Au nanorods alters the extinction profiles and thus generates tunable photoacoustic signals. This process is reversible, leading to dynamic imaging signals in response to temperature changes, and the responsive photoacoustic agents have been used for background-free photoacoustic imaging. Zhou et al. developed an activatable theranostic agent, and its photoacoustic and photothermal conversion in the second biological tissue transparency window can be triggered by over-expressed H_2O_2 in tumor microenvironments.[974] Monodisperse Au nanoparticles are first assembled into plasmonic chains by mediating their electrostatic interactions. The proximity of Au nanoparticles enables their fusion in response to H_2O_2 exposure, which occurs through a redox reaction mechanism (**Figure 84d**) and leads to high absorbance in the NIR-II region. When the chains are targeted to the tumor, the over-expressed H_2O_2 will trigger such interesting property changes, giving rise to activatable *in vivo* imaging and photothermal treatment of cancer (**Figure 84e**).

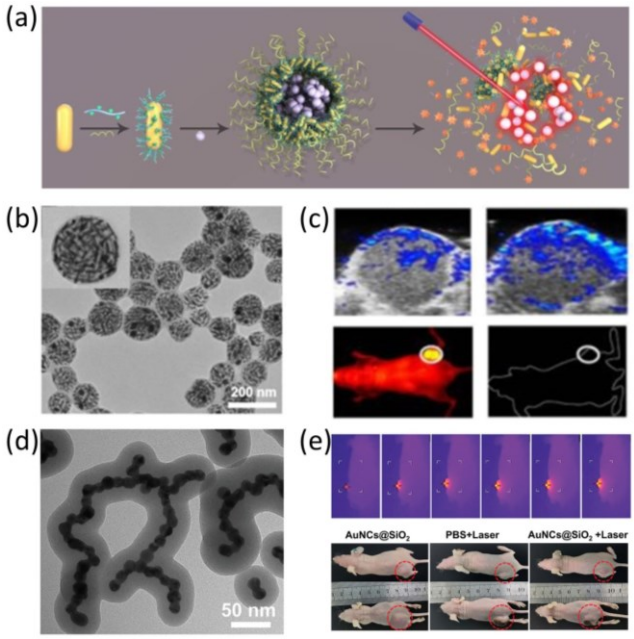

Figure 84. Responsive plasmonic superstructures for active biological imaging and therapy. (a) Schematic illustration of light-responsive therapeutic vesicles enabled by Au nanorod self-assembly. (b) TEM images of the plasmonic superstructure therapeutic vesicles. (c) Light-activable photoacoustic (top) and fluorescent (bottom) imaging. Reproduced with permission from ref [972]. Copyright 2020 The Authors. (d) TEM image of Au nanosphere chains. (e) Activable plasmonic chains for enhanced photothermal therapy of cancer. Top: infrared imaging upon laser irradiation; bottom: digital pictures of the mice after photothermal treatment. Reproduced with permission from ref [974]. Copyright 202 John Wiley and Sons.

4.7. Energy Storage and Conversion

The proximity of matter in colloidal assemblies provides many fascinating collective properties that are not attainable in individual nanoparticles.[975-977] The particle connectivity and separation in superstructures can regulate the nanoscale chemical transformation, mass transportation, and wave propagation in a predictable way, thus allowing precise control over their electronic, optical, chemical properties.[978-980] These structure-dependent collective properties are significantly important in regulating energy storage and conversion and in promoting energy conversion efficiency.[981] In electrochemical and electrophysical processes, colloidal superstructures are used as colloidal templates in nanoparticle lithography to produce highly porous and permeable 3D networks, like inverse opals.[982,983] These unique materials can serve as active electrodes and provide alternative methods to solve the existing challenge in batteries. For example, inverse opals have demonstrated improved stability, highly efficient electronic and ionic transportation, and greatly enhanced power capacity, charging-discharging rate, cycle performances in Li-ion batteries.[981] Specifically, they have been extensively used in anodes, cathodes, charge collectors, and separators in batteries depending on the type of the functional skeletal materials. Typical cathodic materials include $LiCoO_2$[984] and $LiFePO_4$,[45,985,986] which are prepared by infiltrating their precursors into an opal template followed by crystallization in high-temperature calcination. In developing anodic materials, carbon is a natural candidate due to its low cost and high conductivity.[396] A few studies in this regard have used inverse opals of carbon as anodes benefiting from the high mass transfer and easy electrolyte infiltration.[987,988] It is also possible to further enhance the rate performance and cycling stability by introducing more stable materials as the 3D network, such as TiO_2[989] and NiO.[990]

Patterned superstructures are also attractive candidates for enhancing catalytic performance in electrochemical reactions. In gas evolution reactions, there are two challenges caused by gas production. The gas bubble limits the mass transfer rate to the electrode surface and produces many inactive sites.[991,992] Besides, these gas bubbles will destroy the heterogeneous catalyst film due to the associated large stretch force when they detach from the film surface. To overcome these challenges in gas evolution reaction, Pt nanocrystals are assembled into 1D stripe patterns with defined sizes and separations using the capillary bridge technique introduced in section 2.6 (**Figure 85a**).[993] A TEM image in **Figure 85b** suggests the close-packed superlattices with an *fcc* crystal structure. Such superstructure catalysts are used for hydrogen evolution reaction (HER), which demonstrates a much lower overpotential compared with Pt nanocrystal film or Pt foil (**Figure 85c**). A close analysis attributes this enhanced catalytic performance to the higher mass transfer and the smaller stretch forces on the patterned superstructure catalyst than a flat Pt nanoparticle film (**Figure 85d**).

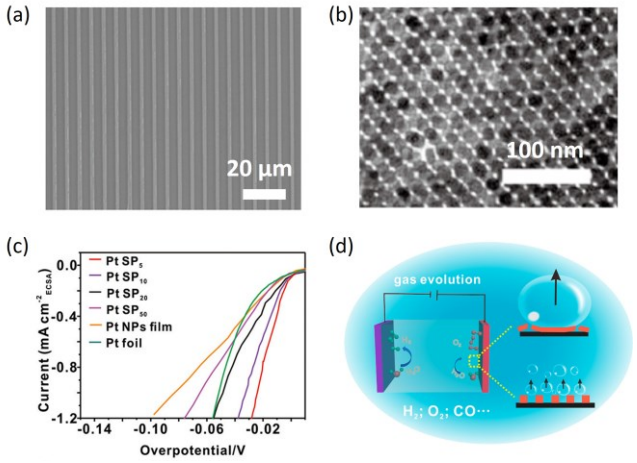

Figure 85. (a) SEM image of striped-pattern superstructures assembled of platinum nanocrystals. (b) TEM image of the nanocrystal superstructures. (c) Polarization curves of Pt superstructures with different gap widths (indicated as subscripts in μm), Pt nanoparticle film, Pt/C film, and Pt foil electrocatalysts normalized by electrochemically active surface areas. (d) Schematic illustration of the gas evolution on the electrodes. Reproduced with permission from ref [993]. Copyright 2019 American Chemical Society.

Another great benefit of periodic structures is their ability to modulate light propagation and to convert light energy into heat or electricity. The limiting steps in developing photovoltaic devices have been recognized as the photon-exciton conversion and the charge separation under light illumination.[994-996] Therefore, the incorporation of colloidal assemblies is expected to enhance the absorbance of light due to their unique collective properties and to promote charge separation based on their highly accessible interfaces. Because colloids have dimensions smaller than or comparable to the wavelength of visible light, they have high efficiency in tuning the scattering and absorption of visible light.[77] If they self-assemble into superstructures, the light can be trapped within the periodic structures, and therefore the photon-exciton conversion can be enhanced. This strategy can be practically achieved by light trapping using multiple scattering or photonic waveguides and coupled surface plasmon resonance in plasmonic superstructures. In addition to solar cells, light energy can also be converted to heat for solar steam generation. This emerging technique takes advantage of the plasmon coupling-induced broadband absorption in plasmonic superstructures for water purification and desalination.[997,998] Plasmonic nanoparticles usually have high absorption at a resonant wavelength due to the localized surface plasmon resonance.[999,1000] The absorbed light energy is converted to heat through the photothermal effect, which increases the surrounding temperature. To use the full-spectrum energy, they need to be assembled into superstructures with random coupling effects such that the resulting broadband absorption of the photothermal converters can absorb as much solar energy as possible.[1001-1003] Another great benefit associated with the dense assemblies is the heat localization with a small volume, which prevents the thermal dissipation to the surroundings and to the bulk water. Such heat localization produces extremely high temperatures to vaporize the nearby water. This concept has been unified for developing high-performance steam generators and is further extended to other light-absorbing materials and structures.[1004-1006]

5. Conclusion and Outlook

The past two decades have witnessed great advances in the synthesis of colloidal particles and their self-assembly into diverse secondary structures that have predictable responses to surrounding physicochemical changes.[1007,1008] Compared with other nanomanufacturing techniques, like top-down lithography, 3D printing, mechanical rubbing, and laser-based structuring, the colloidal assembly of nanostructured materials has many advantages in creating secondary structures. While the resolution of photolithography and laser-based structuring is restricted by the optical diffraction limit, colloidal self-assembly provides superstructures with nanometer precision. The periodicity of the superstructures is closely related to the building blocks, leading to highly tunable feature sizes and length scales of the secondary structures. Besides, as a printing technique, lithography uses multiple steps in manufacturing superstructures, in which the involved processes increase intensively in producing 3D microscale or nanoscale architectures. In contrast, the widely accessible assembly techniques provide high flexibility in creating superstructures with different dimensions, sizes, and symmetries. In addition to superstructures, colloidal assemblies provide many methods to precisely align anisotropic nanostructures, which is also achievable in the mechanical rubbing process but with much lower precision. 3D and 4D printing techniques are emerging in nanomanufacturing and provide programmable, highly customizable solutions to superstructures. Their developments, albeit rather quickly, are approaching the resolution limits of current existing printing techniques, making it still challenging in printing nanoscale objectives with defined superstructures and symmetry. Therefore, the colloidal assembly has superior superstructure resolution and compatibility with many conventional material processing methods. However, combining these fabrication methods may lead to new opportunities for smart materials. Particularly in developing responsive materials, 4D printing represents a promising direct printing technique, which produces architectures or composite materials with transformable properties or forms in response to external stimuli. Relying on the same technique of 3D printing, it adds the property changes or matter transformation over time to create responses in solid materials and can produce programmable configuration at a micrometer resolution. The combination of colloidal assembly and 3D printing is a good example of an advanced nanomanufacturing technique, which takes advantage of the intrinsic features of individual fabrication methods for creating smart materials with extended length scales, high resolution, programmable material properties, and defined responses to external stimuli over time.

The high degree of similarity in morphology and manufacturing between inorganic nanocrystals and colloidal crystals makes one realize the importance of a few key parameters in controlling the nanocrystal synthesis, colloidal self-assembly, and their dynamic responses. In fact, they are so relevant that colloidal self-assembly has been used as a model system to study the kinetics and dynamics of colloidal nanocrystal synthesis and the organic-inorganic interface formation. By the analogy of monodisperse nanoparticles to atoms, it is possible to directly observe the bond formation between colloidal building blocks and

to measure the bond strength by estimating the driving forces using either analytical equations or software simulation. To this end, the DNA-directed colloidal self-assembly and self-assembly of Janus colloids are two natural choices because of the high specificity of base-pair interactions and the defined directionality between designated surface patches, respectively.[20] These considerations have been manifested by the great diversity of the perfect Bravais lattices and superlattice symmetry that have been observed in colloidal crystals in DNA- and surface patch-directed self-assembly.[1009-1011] Particularly, the established colloidal syntheses and surface chemistry allow customizable and systematic modification of the surface patch number, size, and shape, making it possible to control the bond numbers, interparticle connectivity, and thus the symmetry of the colloidal cluster molecules in the self-assembly of Janus nanoparticles. In addition to these two interactions, other driving forces that can yield 3D superlattices with perfect crystallinity include depletion force, van der Waals force, gravity force, and capillary force. These packing forces work in different length scales. Thus one may expect to use a specific strategy to control the force strength and direction to fabricate desirable colloidal lattices. The short-range van der Waals force, for example, can occur between surface ligands and between the nanoparticle cores, leading to attractions with different magnitudes. In the self-assembly of anisotropic colloids, the van der Waals attraction between surface ligands is important as it determines the preferential binding direction and packing manner. Meanwhile, the capillary force has been extensively employed to produce colloidal crystal arrays with nanosphere close packing, which are further used as colloidal templates to prepare inverse opals. These dense colloidal crystals and highly porous 3D photonic frameworks represent a universal class of responsive photonic crystals, which have been extensively studied for smart optical devices. The electrostatic and van der Waals interactions are the two main contributions in DLVO theory, whose interplay in the self-assembly of plasmonic nanospheres is advantageous to yield active plasmonic superstructures. In reviewing these important driving forces and resulting secondary structures, it is reasonable to conclude that colloidal crystals can already be created with far more complex crystal structures and far greater control over their dimensions, sizes, connectivity, and symmetries than what has long been thought possible. But, at the time of writing, we are still facing critical challenges in describing these forces, particularly on self-assembly of small nanoparticles where additivity of individual interaction potential and many assumptions for large colloids are not operational. To move beyond the qualitative description of the colloidal assembly, developing analytical methodologies to simultaneously treat the atomic and entropic forces is essential. Obtaining this new knowledge will at least require accurate colloidal property measurements, detailed surrounding characterization, as well as quantum theoretical calculations.

Relying on empirical principles and theoretical predictions, chemists have achieved exquisite control over the colloidal crystal constant, orientation, and surrounding dielectrics. The high-density voids in colloidal crystals can be utilized to modulate the surrounding physical and chemical properties of the superstructures with constant interparticle connection and separation. This simple strategy allows direct use of superstructures or lattices for chemical and physical detection while remaining open to functional integration of other responsive materials. Inverse opals have great benefits in this regard due to their highly porous superstructures, brilliant structural colors, and sensitive colorimetric responses. Their 3D frameworks possess useful properties that are dependent on chemical composition and microstructure, and the interconnected pores ensure that these structures are highly accessible to guest molecules and are easy to process further to functional materials with more complex responses to external stimuli. This combination of features makes inverse opals compelling and promising for colorimetric sensors and smart optical devices. Compared with changing surrounding properties, actively regulating superlattice constant and orientation is more effective in developing smart colloidal assemblies. One great benefit associated with colloidal self-assembly is that chemists are achieving more elegant control over the composition, size, shape, and surface chemistry of colloidal building blocks, allowing widely accessible colloids for designed smart responses and functionalities. Some colloids themselves are reactive to external stimuli, like remote fields and local chemical surroundings, such that regulating their self-assemblies is possible by carefully taking advantage of these unique properties. This working principle produces responsive superstructures to magnetic fields, electric fields, temperature, ionic strength, humidity, etc. For non-responsive colloids, it is also possible to engineer smart responses by incorporating their superstructures into an active organic or inorganic matrix. Such guest-host strategy combines the unique collective properties of colloidal assemblies with plentiful functional materials, which represents an extended platform to smart colloidal assemblies. Compared with smart superstructures with constant particle separation, active colloidal assemblies with tunable superstructures are nimbler in performing optical responses or shape morphing under external stimuli, thus having been extensively used in practice. Their capability to react to ever-changing surroundings is not limited to the fixed spaces between colloidal separation, which more importantly releases these spaces for further material functionalization and device fabrication. Another associated advantage is the wider tunability in their optical, mechanical properties and higher sensitivity in response to external influences, which has been manifested in a few carefully designed responsive photonic crystals and active plasmonic superstructures with full visible spectrum tunability. Their compatible hierarchical structures also allow a widely accessible response rate from milliseconds to a few hours depending on the involved working mechanism, which provides a complete library of the functional materials to fulfill the complex requirements in practical applications.

Given these promising self-assembly strategies and associated exciting properties, scientists are leading their research to apply smart colloidal assemblies for solving existing challenges in a broad spectrum of applications. In early developments, colloidal assemblies, particularly photonic crystals and plasmonic superstructures, have served as superior systems for several key techniques in chemical sensing, including ultrafast spectroscopic detection and colorimetric sensing.[482,771,1012] Such dynamic color-switching is also highly desirable in anticounterfeiting and coloration, which uses responsive colloidal assemblies for security labels, multicolor displays, and rewritable papers. In addition to these conventional applications, the emerging soft actuators and robotics also significantly benefit from the flexible bottom-up approach to colloidal superstructures

that serve as responsive components. In developing high-performance soft actuators, colloidal assemblies can provide additional functionalities or enable new actuation modes in response to desirable stimuli. To this end, responsive colloidal assemblies have irreplaceable advantages over other material systems. Incorporating responsive colloidal assemblies into soft actuators offers simultaneous color changes in addition to shape morphing, which is very difficult to realize in conventional microfabrication methods. Besides, assembling anisotropic nanostructures in soft materials also enables the design of soft actuators with anisotropic mechanical properties. One great benefit is the successful creation of programmable and biomimetic soft actuators, which can mimic many interesting behaviors of nature creatures and enable a few fascinating manufacturing techniques, such as 4D printing. In fact, the fast development in precisely controlling and dynamically modulating the collective properties of colloidal superstructures has enabled new working principles in actuating soft robotics and has also provided integrated responses to external stimuli.[1013] This unique set of functional materials has great compatibility with many well-established nanomanufacturing techniques, offering copious choices of property changes to extended stimuli. In this regard, the assembly of anisotropic nanoparticles into liquid crystals with pure orientational order is a successful approach to biomimetic actuators, which can mimic many fascinating shape morphing of natural creatures. In addition, introducing responsive colloidal assemblies into soft materials allows additional control over their deformation through changing the light wavelength, light polarization, humidity, external fields, etc. For biological applications, responsive colloidal assemblies have been developed into smart theranostic platforms, which is highly desirable for drug delivery, background-free imaging, and specific treatment of cancer. They provide a general strategy to develop stimuli-responsive nanomedicines, whose physical properties or chemical reactivities can be modulated or can only be activated by target biomolecules, tumor microenvironments, or remote stimuli (such as X-ray, magnetic field, electronic field). Such on-demand responsiveness is the most attractive advantage of smart colloidal assemblies over conventional single-component or core/shell nanostructures. In energy storage and conversion, the accessible regular separation and the ordered nanomaterials can regulate the mass transportation and wave propagation in nanometer precision, making colloidal assemblies very promising in energy-related applications. For example, the proximity of noble metal nanoparticles in plasmonic assemblies produces extremely strong plasmon coupling, which has been extensively used for converting solar energy into heat or electricity. A great benefit of colloidal assemblies in this regard is that the coupling is highly tunable by changing the superlattice constant and symmetry, with a precision that is not attainable in conventional top-down lithography methods. It therefore allows optimization of the photothermal conversion efficiency for enhancing the performances of solar cells and solar steam generators. In electronic and electrochemical devices, colloidal assemblies have been demonstrated to overcome some challenges existing in conventional electrode materials. The regular separation and spaces can facilitate the electron and chemical transfer between the electrodes and electrolytes, while the highly ordered nanostructures serve as catalysts and solid supports to prevent deformation during use.

Despite these exciting achievements, smart nanostructured materials are still in the early stages of bringing real benefits to our daily lives and industrial production. Besides, we are still far away from quantitatively predicting the responses of many integrated systems that combine the collective properties of colloidal assemblies and other functional continuum materials. Progressing beyond many interesting phenomena and general qualitative descriptions of these responses requires detailed knowledge of the solid interfaces between the continuous and dispersed phases because, in most cases, these interfaces determine the overall performances. In some relatively mature applications, such as anti-counterfeiting and sensing, they are still facing critical challenges in large-scale production of defect-free superstructures at low cost, in stabilizing their fine structures for durable daily uses, and in providing biocompatible or environmentally friendly materials while maintaining their responsiveness and functionality. In developing color displays, it is still a challenge to create large-scale displays with a wide color gamut, low energy consumption, and a high response rate. Although some techniques provide active color displays based on photonic crystals or plasmonic superstructures, additional efforts are still required to improve the long-term stability, picture quality, and power efficiency and to tackle the viewing-angle dependent optical properties of many colloidal assemblies when competing with the conventional liquid crystal display (LCD) and emerging light-emitting techniques, like light-emitting diode (LED) and organic light-emitting diode (OLED). The introduction of colloidal assemblies in soft materials has established a few working mechanisms to develop soft actuators and robotics. The positional and orientational orders of nanostructured materials provide new functionalities or additional degrees of freedom to tune the shape morphing and movement of these soft actuators, demonstrating the unique advantages of responsive colloidal assemblies in creating integrated devices. Its further advance to the next generation requires the integration of colloidal assemblies with polymers for extending the fundamental shape morphing from bending to twisting, jumping. Also, developing mechanical oscillation under continuous external stimuli, such as light irradiation, is currently limited by a few working principles, although mechanical oscillation is highly desirable in biomimetic robotics. With the ability to produce materials with precise positional and/or orientational orders, colloidal assemblies are expected to overcome these existing challenges through a bottom-up approach. When designed for biological applications, colloidal assemblies have the same biocompatibility and safety concerns as with other nanostructured materials. Reducing the size of colloidal assemblies for meeting the requirements of biological microenvironments is an additional concern for developing smart colloidal assembles for in vivo applications. While in energy storage and conversion, the long-term chemical and physical stability of nanostructures take priority over other challenges due to the extreme working conditions, like high temperature, high ionic strength, strong redox potential in electronic and electrochemical devices. Because of the weak forces between the assembled colloids, superstructures are highly possible to dis-assemble and to transform to other phases under applied voltages or in aqueous solutions. It is therefore highly desirable to add further stabilization steps to improve the superstructure stability for practical applications.

In fact, it is inspiring that some responsive colloidal assemblies have been used in real-world applications, such as photonic

crystals for car painting and optical fibers, but their apparent advantages remain conceptual and have not been extensively used for replacing existing materials that are suffering high cost or environmental issues. In a few developing applications, smart superstructures by colloidal self-assembly serve as responsive elements in many fascinating "proof of concept" projects, such as rewritable papers, soft robotics, and biomedicine. In these emerging research fields, their blueprints need additional efforts in understanding the basic behaviors and assessing their performances in response to a target external stimuli. This will further extend the potential of many superstructures to other attractive fields. Clearly, inspiring opportunities remain in the self-assembly of responsive nanostructured materials. A better understanding of the driving forces between colloidal particles lays the foundation for preparing perfect colloidal crystal arrays and for exploiting new crystal structures and phases. The advances in these fundamental aspects hold the key to tuning the colloidal superstructures with nanometer precision, designing predictable responses to a set of external stimuli, and using these functional colloidal assemblies for a new generation of smart materials.

AUTHOR INFORMATION

Corresponding Author

Yadong Yin – Department of Chemistry, University of California, Riverside, California 92521, United States; orcid.org/0000- 0003-0218-3042; Email: yadong.yin@ucr.edu

Authors

Zhiwei Li – Department of Chemistry, University of California, Riverside, California 92521, United States; orcid.org/0000-0002-1489-4506

Qingsong Fan – Department of Chemistry, University of California, Riverside, California 92521, United States; orcid.org/0000-0001-8555-769X

Author Contributions

The manuscript was written through the contributions of all authors. All authors have given approval to the final version of the manuscript.

Notes

The authors declare no competing financial interest.

Biographies

Zhiwei Li obtained his Ph.D. in Physical Chemistry in 2019 from the University of California, Riverside. He currently continues his research as a postdoctoral fellow under the supervision of Prof. Yadong Yin there. His research interests include the synthesis of plasmonic nanostructures and the assembly of colloidal particles into smart nanostructured materials.

Qingsong Fan is currently pursuing his Ph.D. in Chemistry at the University of California, Riverside, under the supervision of Prof. Yadong Yin. He received his B.S. in Materials Science and Engineering at the Beijing University of Technology in 2017. His research interests include the synthesis of nanoparticles, assembly of responsive photonic crystals, and simulation of assembled structures.

Yadong Yin received his Ph.D. in Materials Science and Engineering from the University of Washington in 2002. In 2003, he worked as a postdoctoral fellow at the University of California, Berkeley, and the Lawrence Berkeley National Laboratory, and then a staff scientist at the LBNL. Since 2006, he has been a faculty member at the Department of Chemistry, University of California, Riverside. His research interests include synthesis, self-assembly, colloidal and interfacial properties, and various applications of nanostructured materials.

ACKNOWLEDGMENTS

We thank the support from the U.S. National Science Foundation (CHE-1808788 and DMR-1810485).

REFERENCES

(1) Yin, Y.; Alivisatos, A. P. Colloidal nanocrystal synthesis and the organic–inorganic interface. *Nature* **2005,** *437*, 664-670.

(2) Heuer-Jungemann, A.; Feliu, N.; Bakaimi, I.; Hamaly, M.; Alkilany, A.; Chakraborty, I.; Masood, A.; Casula, M. F.; Kostopoulou, A.; Oh, E. The role of ligands in the chemical synthesis and applications of inorganic nanoparticles. *Chem. Rev.* **2019,** *119*, 4819-4880.

(3) Green, M. The nature of quantum dot capping ligands. *J. Mater. Chem.* **2010,** *20*, 5797-5809.

(4) Lévy, R.; Thanh, N. T.; Doty, R. C.; Hussain, I.; Nichols, R. J.; Schiffrin, D. J.; Brust, M.; Fernig, D. G. Rational and combinatorial design of peptide capping ligands for gold nanoparticles. *J. Am. Chem. Soc.* **2004,** *126*, 10076-10084.

(5) Glotzer, S. C.; Solomon, M. J. Anisotropy of building blocks and their assembly into complex structures. *Nat. Mater.* **2007,** *6*, 557-562.

(6) Xu, W.; Li, Z.; Yin, Y. Colloidal assembly approaches to micro/nanostructures of complex morphologies. *Small* **2018,** *14*, 1801083.

(7) Li, F.; Josephson, D. P.; Stein, A. Colloidal assembly: the road from particles to colloidal molecules and crystals. *Angew. Chem. Int. Ed.* **2011,** *50*, 360-388.

(8) Smay, J. E.; Gratson, G. M.; Shepherd, R. F.; Cesarano III, J.; Lewis, J. A. Directed colloidal assembly of 3D periodic structures. *Adv. Mater.* **2002,** *14*, 1279-1283.

(9) Whitesides, G. M.; Grzybowski, B. Self-assembly at all scales. *Science* **2002,** *295*, 2418-2421.

(10) Liu, Q.; Campbell, M. G.; Evans, J. S.; Smalyukh, I. I. Orientationally ordered colloidal co‐dispersions of gold nanorods and cellulose

nanocrystals. *Adv. Mater.* **2014,** *26*, 7178-7184.

(11) Cai, Z.; Li, Z.; Ravaine, S.; He, M.; Song, Y.; Yin, Y.; Zheng, H.; Teng, J.; Zhang, A. From colloidal particles to photonic crystals: advances in self-assembly and their emerging applications. *Chem. Soc. Rev.* **2021,** *50*, 5898-5951.

(12) van Blaaderen, A. Chemistry: Colloidal molecules and beyond. *Science* **2003,** *301*, 470-471.

(13) Morphew, D.; Chakrabarti, D. Clusters of anisotropic colloidal particles: From colloidal molecules to supracolloidal structures. *Curr. Opin. Colloid Interface Sci.* **2017,** *30*, 70-80.

(14) Mirabello, G.; Ianiro, A.; Bomans, P. H.; Yoda, T.; Arakaki, A.; Friedrich, H.; de With, G.; Sommerdijk, N. A. Crystallization by particle attachment is a colloidal assembly process. *Nat. Mater.* **2020,** *19*, 391-396.

(15) Dushkin, C.; Yoshimura, H.; Nagayama, K. Nucleation and growth of two-dimensional colloidal crystals. *Chem. Phys. Lett.* **1993,** *204*, 455-460.

(16) Wang, Z.; Wang, F.; Peng, Y.; Zheng, Z.; Han, Y. Imaging the homogeneous nucleation during the melting of superheated colloidal crystals. *Science* **2012,** *338*, 87-90.

(17) Moradi, M.-A.; Eren, E. D.; Chiappini, M.; Rzadkiewicz, S.; Goudzwaard, M.; van Rijt, M. M.; Keizer, A. D.; Routh, A. F.; Dijkstra, M.; de With, G. Spontaneous organization of supracolloids into three-dimensional structured materials. *Nat. Mater.* **2021,** *20*, 541-547.

(18) Skelhon, T. S.; Chen, Y.; Bon, S. A. Hierarchical self-assembly of 'hard–soft'Janus particles into colloidal molecules and larger supracolloidal structures. *Soft Matter* **2014,** *10*, 7730-7735.

(19) Zhang, J.; Grzybowski, B. A.; Granick, S. Janus particle synthesis, assembly, and application. *Langmuir* **2017,** *33*, 6964-6977.

(20) Rogers, W. B.; Shih, W. M.; Manoharan, V. N. Using DNA to program the self-assembly of colloidal nanoparticles and microparticles. *Nat. Rev. Mater.* **2016,** *1*, 1-14.

(21) Zhang, J.; Luijten, E.; Granick, S. Toward design rules of directional Janus colloidal assembly. *Annu. Rev. Phys. Chem.* **2015,** *66*, 581-600.

(22) Nykypanchuk, D.; Maye, M. M.; Van Der Lelie, D.; Gang, O. DNA-guided crystallization of colloidal nanoparticles. *Nature* **2008,** *451*, 549-552.

(23) Woods, D.; Doty, D.; Myhrvold, C.; Hui, J.; Zhou, F.; Yin, P.; Winfree, E. Diverse and robust molecular algorithms using reprogrammable DNA self-assembly. *Nature* **2019,** *567*, 366-372.

(24) Lebovka, N. I.; Vygornitskii, N. V.; Gigiberiya, V. A.; Tarasevich, Y. Y. Monte Carlo simulation of evaporation-driven self-assembly in suspensions of colloidal rods. *Phys. Rev. E* **2016,** *94*, 062803.

(25) Damasceno, P. F.; Engel, M.; Glotzer, S. C. Predictive self-assembly of polyhedra into complex structures. *Science* **2012,** *337*, 453-457.

(26) Manoharan, V. N. Colloidal matter: Packing, geometry, and entropy. *Science* **2015,** *349*, 1253751.

(27) Robb, D. T.; Privman, V. Model of nanocrystal formation in solution by burst nucleation and diffusional growth. *Langmuir* **2008,** *24*, 26-35.

(28) Chu, D. B.; Owen, J. S.; Peters, B. Nucleation and growth kinetics from LaMer burst data. *J. Phys. Chem. A* **2017,** *121*, 7511-7517.

(29) Hueckel, T.; Hocky, G. M.; Palacci, J.; Sacanna, S. Ionic solids from common colloids. *Nature* **2020,** *580*, 487-490.

(30) Henzie, J.; Grünwald, M.; Widmer-Cooper, A.; Geissler, P. L.; Yang, P. Self-assembly of uniform polyhedral silver nanocrystals into densest packings and exotic superlattices. *Nat. Mater.* **2012,** *11*, 131-137.

(31) Fontecha, A. B.; Schöpe, H. J. Exotic crystal superstructures of colloidal crystals in confinement. *Phys. Rev. E* **2008,** *77*, 061401.

(32) Shevchenko, E. V.; Talapin, D. V.; Kotov, N. A.; O'Brien, S.; Murray, C. B. Structural diversity in binary nanoparticle superlattices. *Nature* **2006,** *439*, 55-59.

(33) Ye, X.; Chen, J.; Irrgang, M. E.; Engel, M.; Dong, A.; Glotzer, S. C.; Murray, C. B. Quasicrystalline nanocrystal superlattice with partial matching rules. *Nat. Mater.* **2017,** *16*, 214-219.

(34) Talapin, D. V.; Shevchenko, E. V.; Bodnarchuk, M. I.; Ye, X.; Chen, J.; Murray, C. B. Quasicrystalline order in self-assembled

binary nanoparticle superlattices. *Nature* **2009,** *461*, 964-967.

(35) Nagaoka, Y.; Zhu, H.; Eggert, D.; Chen, O. Single-component quasicrystalline nanocrystal superlattices through flexible polygon tiling rule. *Science* **2018,** *362*, 1396-1400.

(36) Galukhin, A.; Bolmatenkov, D.; Emelianova, A.; Zharov, I.; Gor, G. Y. Porous Structure of Silica Colloidal Crystals. *Langmuir* **2019,** *35*, 2230-2235.

(37) Avci, C.; Imaz, I.; Carné-Sánchez, A.; Pariente, J. A.; Tasios, N.; Pérez-Carvajal, J.; Alonso, M. I.; Blanco, A.; Dijkstra, M.; López, C. Self-assembly of polyhedral metal–organic framework particles into three-dimensional ordered superstructures. *Nat. Chem.* **2018,** *10*, 78-84.

(38) Diao, Y. Y.; Liu, X. Y.; Toh, G. W.; Shi, L.; Zi, J. Multiple structural coloring of silk‐fibroin photonic crystals and humidity‐responsive color sensing. *Adv. Funct. Mater.* **2013,** *23*, 5373-5380.

(39) Wu, X.; Hao, C.; Kumar, J.; Kuang, H.; Kotov, N. A.; Liz-Marzán, L. M.; Xu, C. Environmentally responsive plasmonic nanoassemblies for biosensing. *Chem. Soc. Rev.* **2018,** *47*, 4677-4696.

(40) Stein, A.; Li, F.; Denny, N. R. Morphological control in colloidal crystal templating of inverse opals, hierarchical structures, and shaped particles. *Chem. Mater.* **2008,** *20*, 649-666.

(41) Zhou, J.; Wang, J.; Huang, Y.; Liu, G.; Wang, L.; Chen, S.; Li, X.; Wang, D.; Song, Y.; Jiang, L. Large-area crack-free single-crystal photonic crystals via combined effects of polymerization-assisted assembly and flexible substrate. *NPG Asia Mater.* **2012,** *4*, e21-e21.

(42) Hou, J.; Li, M.; Song, Y. Recent advances in colloidal photonic crystal sensors: Materials, structures and analysis methods. *Nano Today* **2018,** *22*, 132-144.

(43) Parlett, C. M.; Wilson, K.; Lee, A. F. Hierarchical porous materials: catalytic applications. *Chem. Soc. Rev.* **2013,** *42*, 3876-3893.

(44) He, G.; Manthiram, A. Nanostructured Li2MnSiO4/C Cathodes with Hierarchical Macro‐/Mesoporosity for Lithium‐Ion Batteries. *Adv. Funct. Mater.* **2014,** *24*, 5277-5283.

(45) Doherty, C. M.; Caruso, R. A.; Smarsly, B. M.; Drummond, C. J. Colloidal crystal templating to produce hierarchically porous LiFePO4 electrode materials for high power lithium ion batteries. *Chem. Mater.* **2009,** *21*, 2895-2903.

(46) Wang, Y.; Cui, H.; Zhao, Q.; Du, X. Chameleon-inspired structural-color actuators. *Matter* **2019,** *1*, 626-638.

(47) Zeng, X.; Bai, Y.; Choi, S.; Tong, L.; Aleisa, R.; Li, Z.; Liu, X.; Yu, R.; Myung, N.; Yin, Y. Mesoporous TiO2 nanospheres loaded with highly dispersed Pd nanoparticles for pH-universal hydrogen evolution reaction. *Mater. Today Nano* **2019,** *6*, 100038.

(48) Hines, L.; Petersen, K.; Lum, G. Z.; Sitti, M. Soft actuators for small‐scale robotics. *Adv. Mater.* **2017,** *29*, 1603483.

(49) Li, Z.; Yin, Y. Stimuli‐responsive optical nanomaterials. *Adv. Mater.* **2019,** *31*, 1807061.

(50) Vernerey, F.; Benet, E.; Blue, L.; Fajrial, A.; Sridhar, S. L.; Lum, J.; Shakya, G.; Song, K.; Thomas, A.; Borden, M. Biological active matter aggregates: Inspiration for smart colloidal materials. *Adv. Colloid Interface Sci.* **2019,** *263*, 38-51.

(51) Brasse, Y.; Gupta, V.; Schollbach, H. T.; Karg, M.; König, T. A.; Fery, A. Mechanotunable plasmonic properties of colloidal assemblies. *Adv. Mater. Interfaces* **2020,** *7*, 1901678.

(52) Ge, J.; Yin, Y. Responsive photonic crystals. *Angew. Chem. Int. Ed.* **2011,** *50*, 1492-1522.

(53) Jiang, N.; Zhuo, X.; Wang, J. Active plasmonics: principles, structures, and applications. *Chem. Rev.* **2017,** *118*, 3054-3099.

(54) Gabriel, J. C.; Davidson, P. New trends in colloidal liquid crystals based on mineral moieties. *Adv. Mater.* **2000,** *12*, 9-20.

(55) Dierking, I. From colloids in liquid crystals to colloidal liquid crystals. *Liq. Cryst.* **2019,** *46*, 2057-2074.

(56) Khoo, I.-C. *Liquid crystals*; John Wiley & Sons, 2007, 1-365.

(57) Priestly, E. *Introduction to liquid crystals*; Springer Science & Business Media, 2012, 1-356.

(58) Binnemans, K. Ionic liquid crystals. *Chem. Rev.* **2005,** *105*, 4148-4204.

(59) Vertogen, G.; De Jeu, W. H. *Thermotropic liquid crystals, fundamentals*; Springer Science & Business Media, 2012, 1-324.
(60) Madsen, L. A.; Dingemans, T. J.; Nakata, M.; Samulski, E. T. Thermotropic biaxial nematic liquid crystals. *Phys. Rev. Lett.* **2004,** *92*, 145505.
(61) Xu, Z.; Gao, C. Graphene chiral liquid crystals and macroscopic assembled fibres. *Nat. Commun.* **2011,** *2*, 571.
(62) Kim, J. E.; Han, T. H.; Lee, S. H.; Kim, J. Y.; Ahn, C. W.; Yun, J. M.; Kim, S. O. Graphene Oxide Liquid Crystals. *Angew. Chem. Int. Ed.* **2011,** *50*, 3043-3047.
(63) Wang, M.; He, L.; Zorba, S.; Yin, Y. Magnetically actuated liquid crystals. *Nano Lett.* **2014,** *14*, 3966-3971.
(64) Liu, Q.; Cui, Y.; Gardner, D.; Li, X.; He, S.; Smalyukh, I. I. Self-alignment of plasmonic gold nanorods in reconfigurable anisotropic fluids for tunable bulk metamaterial applications. *Nano Lett.* **2010,** *10*, 1347-1353.
(65) Xin, G.; Zhu, W.; Deng, Y.; Cheng, J.; Zhang, L. T.; Chung, A. J.; De, S.; Lian, J. Microfluidics-enabled orientation and microstructure control of macroscopic graphene fibres. *Nat. Nanotechnol.* **2019,** *14*, 168-175.
(66) Li, Z.; Yang, F.; Yin, Y. Smart materials by nanoscale magnetic assembly. *Adv. Funct. Mater.* **2020,** *30*, 1903467.
(67) Hentschel, M.; Schäferling, M.; Duan, X.; Giessen, H.; Liu, N. Chiral plasmonics. *Sci. Adv.* **2017,** *3*, e1602735.
(68) Wang, M.; Yin, Y. Magnetically responsive nanostructures with tunable optical properties. *J. Am. Chem. Soc.* **2016,** *138*, 6315-6323.
(69) Joannopoulos, J. D.; Johnson, S. G.; Winn, J. N.; Meade, R. D. *Photonic crystals*; Princeton university press, 2011, 1-304.
(70) Zhao, Y.; Shang, L.; Cheng, Y.; Gu, Z. Spherical colloidal photonic crystals. *Acc. Chem. Res.* **2014,** *47*, 3632-3642.
(71) Hou, J.; Li, M.; Song, Y. Patterned colloidal photonic crystals. *Angew. Chem. Int. Ed.* **2018,** *57*, 2544-2553.
(72) Fu, Q.; Li, Z.; Fu, F.; Chen, X.; Song, J.; Yang, H. Stimuli-responsive plasmonic assemblies and their biomedical applications. *Nano Today* **2021,** *36*, 101014.
(73) Mayer, K. M.; Hafner, J. H. Localized surface plasmon resonance sensors. *Chem. Rev.* **2011,** *111*, 3828-3857.
(74) Li, Z.; Wang, W.; Yin, Y. Colloidal assembly and active tuning of coupled plasmonic nanospheres. *Trends Chem.* **2020,** *2*, 593-608.
(75) Lu, X.; Rycenga, M.; Skrabalak, S. E.; Wiley, B.; Xia, Y. Chemical synthesis of novel plasmonic nanoparticles. *Annu. Rev. Phys. Chem.* **2009,** *60*, 167-192.
(76) Olson, J.; Dominguez-Medina, S.; Hoggard, A.; Wang, L.-Y.; Chang, W.-S.; Link, S. Optical characterization of single plasmonic nanoparticles. *Chem. Soc. Rev.* **2015,** *44*, 40-57.
(77) Rycenga, M.; Cobley, C. M.; Zeng, J.; Li, W.; Moran, C. H.; Zhang, Q.; Qin, D.; Xia, Y. Controlling the synthesis and assembly of silver nanostructures for plasmonic applications. *Chem. Rev.* **2011,** *111*, 3669-3712.
(78) Hu, M.; Chen, J.; Li, Z.-Y.; Au, L.; Hartland, G. V.; Li, X.; Marquez, M.; Xia, Y. Gold nanostructures: engineering their plasmonic properties for biomedical applications. *Chem. Soc. Rev.* **2006,** *35*, 1084-1094.
(79) Sönnichsen, C.; Reinhard, B. M.; Liphardt, J.; Alivisatos, A. P. A molecular ruler based on plasmon coupling of single gold and silver nanoparticles. *Nat. Biotechnol.* **2005,** *23*, 741-745.
(80) Jain, P. K.; Huang, W.; El-Sayed, M. A. On the universal scaling behavior of the distance decay of plasmon coupling in metal nanoparticle pairs: a plasmon ruler equation. *Nano Lett.* **2007,** *7*, 2080-2088.
(81) Jain, P. K.; El-Sayed, M. A. Plasmonic coupling in noble metal nanostructures. *Chem. Phys. Lett.* **2010,** *487*, 153-164.
(82) Li, Z.; Yin, S.; Cheng, L.; Yang, K.; Li, Y.; Liu, Z. Magnetic targeting enhanced theranostic strategy based on multimodal imaging for selective ablation of cancer. *Adv. Funct. Mater.* **2014,** *24*, 2312-2321.
(83) Li, Z.; Wang, C.; Cheng, L.; Gong, H.; Yin, S.; Gong, Q.; Li, Y.; Liu, Z. PEG-functionalized iron oxide nanoclusters loaded with chlorin e6 for targeted, NIR light induced, photodynamic therapy. *Biomaterials* **2013,** *34*, 9160-9170.

(84) Xue, X.; Furlani, E. P. Analysis of the dynamics of magnetic core–shell nanoparticles and self-assembly of crystalline superstructures in gradient fields. *J. Phys. Chem. C* **2015,** *119*, 5714-5726.

(85) He, L.; Wang, M.; Ge, J.; Yin, Y. Magnetic assembly route to colloidal responsive photonic nanostructures. *Acc. Chem. Res.* **2012,** *45*, 1431-1440.

(86) Zhang, X.; Li, Z.; Feng, J.; Yang, F.; Wu, C.; Fan, Q.; Zhou, S.; Yin, Y. Dynamic Tuning of Optical Transmittance of 1D Colloidal Assemblies of Magnetic Nanostructures. *Adv. Intell. Syst.* **2019,** *1*, 1900099.

(87) Ge, J.; Hu, Y.; Biasini, M.; Beyermann, W. P.; Yin, Y. Superparamagnetic magnetite colloidal nanocrystal clusters. *Angew. Chem. Int. Ed.* **2007,** *46*, 4342-4345.

(88) Ge, J.; Hu, Y.; Yin, Y. Highly Tunable Superparamagnetic Colloidal Photonic Crystals. *Angew. Chem. Int. Ed.* **2007,** *46*, 7428-7431.

(89) Zhang, Q.; Janner, M.; He, L.; Wang, M.; Hu, Y.; Lu, Y.; Yin, Y. Photonic labyrinths: Two-dimensional dynamic magnetic assembly and in situ solidification. *Nano Lett.* **2013,** *13*, 1770-1775.

(90) Wang, M.; He, L.; Yin, Y. Magnetic field guided colloidal assembly. *Mater. Today* **2013,** *16*, 110-116.

(91) He, L.; Malik, V.; Wang, M.; Hu, Y.; Anson, F. E.; Yin, Y. Self-assembly and magnetically induced phase transition of three-dimensional colloidal photonic crystals. *Nanoscale* **2012,** *4*, 4438-4442.

(92) Skjeltorp, A. T. One-and two-dimensional crystallization of magnetic holes. *Phys. Rev. Lett.* **1983,** *51*, 2306.

(93) He, L.; Hu, Y.; Kim, H.; Ge, J.; Kwon, S.; Yin, Y. Magnetic assembly of nonmagnetic particles into photonic crystal structures. *Nano Lett.* **2010,** *10*, 4708-4714.

(94) He, L.; Wang, M.; Zhang, Q.; Lu, Y.; Yin, Y. Magnetic assembly and patterning of general nanoscale materials through nonmagnetic templates. *Nano Lett.* **2013,** *13*, 264-271.

(95) Erb, R. M.; Son, H. S.; Samanta, B.; Rotello, V. M.; Yellen, B. B. Magnetic assembly of colloidal superstructures with multipole symmetry. *Nature* **2009,** *457*, 999-1002.

(96) Singh, G.; Chan, H.; Baskin, A.; Gelman, E.; Repnin, N.; Král, P.; Klajn, R. Self-assembly of magnetite nanocubes into helical superstructures. *Science* **2014,** *345*, 1149-1153.

(97) Li, Z.; Wang, M.; Zhang, X.; Wang, D.; Xu, W.; Yin, Y. Magnetic assembly of nanocubes for orientation-dependent photonic responses. *Nano Lett.* **2019,** *19*, 6673-6680.

(98) Rance, G. A.; Marsh, D. H.; Bourne, S. J.; Reade, T. J.; Khlobystov, A. N. van der Waals interactions between nanotubes and nanoparticles for controlled assembly of composite nanostructures. *ACS nano* **2010,** *4*, 4920-4928.

(99) Klimov, V.; Lambrecht, A. Van der Waals forces between plasmonic nanoparticles. *Plasmonics* **2009,** *4*, 31-36.

(100) Boström, M.; Williams, D.; Ninham, B. Specific ion effects: why DLVO theory fails for biology and colloid systems. *Phys. Rev. Lett.* **2001,** *87*, 168103.

(101) London, F. The general theory of molecular forces. *Trans. Faraday Society* **1937,** *33*, 8b-26.

(102) Parsegian, V. A.; Weiss, G. H. Spectroscopic parameters for computation of van der Waals forces. *J. Colloid Interface Sci.* **1981,** *81*, 285-289.

(103) Ye, X.; Chen, J.; Engel, M.; Millan, J. A.; Li, W.; Qi, L.; Xing, G.; Collins, J. E.; Kagan, C. R.; Li, J. Competition of shape and interaction patchiness for self-assembling nanoplates. *Nat. Chem.* **2013,** *5*, 466-473.

(104) Mueggenburg, K. E.; Lin, X.-M.; Goldsmith, R. H.; Jaeger, H. M. Elastic membranes of close-packed nanoparticle arrays. *Nat. Mater.* **2007,** *6*, 656-660.

(105) Chen, Z.; Moore, J.; Radtke, G.; Sirringhaus, H.; O'Brien, S. Binary nanoparticle superlattices in the semiconductor− semiconductor system: CdTe and CdSe. *J. Am. Chem. Soc.* **2007,** *129*, 15702-15709.

(106) Landman, U.; Luedtke, W. Small is different: energetic, structural, thermal, and mechanical properties of passivated nanocluster assemblies. *Faraday Discuss.* **2004,** *125*, 1-22.

(107) Glotzer, S. C. Shape matters. *Nature* **2012,** *481*, 450-452.

(108) Talapin, D. V.; Shevchenko, E. V.; Murray, C. B.; Kornowski, A.; Förster, S.; Weller, H. CdSe and CdSe/CdS nanorod solids. *J. Am. Chem. Soc.* **2004,** *126*, 12984-12988.

(109) Baranov, D.; Fiore, A.; Van Huis, M.; Giannini, C.; Falqui, A.; Lafont, U.; Zandbergen, H.; Zanella, M.; Cingolani, R.; Manna, L. Assembly of colloidal semiconductor nanorods in solution by depletion attraction. *Nano Lett.* **2010,** *10*, 743-749.

(110) Wang, T.; Zhuang, J.; Lynch, J.; Chen, O.; Wang, Z.; Wang, X.; LaMontagne, D.; Wu, H.; Wang, Z.; Cao, Y. C. Self-assembled colloidal superparticles from nanorods. *Science* **2012,** *338*, 358-363.

(111) Zhuang, J.; Shaller, A. D.; Lynch, J.; Wu, H.; Chen, O.; Li, A. D.; Cao, Y. C. Cylindrical superparticles from semiconductor nanorods. *J. Am. Chem. Soc.* **2009,** *131*, 6084-6085.

(112) He, L.; Hu, Y.; Wang, M.; Yin, Y. Determination of solvation layer thickness by a magnetophotonic approach. *ACS nano* **2012,** *6*, 4196-4202.

(113) Wakeham, D.; Hayes, R.; Warr, G. G.; Atkin, R. Influence of temperature and molecular structure on ionic liquid solvation layers. *J. Phys. Chem. B* **2009,** *113*, 5961-5966.

(114) Boles, M. A.; Engel, M.; Talapin, D. V. Self-assembly of colloidal nanocrystals: From intricate structures to functional materials. *Chem. Rev.* **2016,** *116*, 11220-11289.

(115) Gebbie, M. A.; Smith, A. M.; Dobbs, H. A.; Warr, G. G.; Banquy, X.; Valtiner, M.; Rutland, M. W.; Israelachvili, J. N.; Perkin, S.; Atkin, R. Long range electrostatic forces in ionic liquids. *Chem. Commun.* **2017,** *53*, 1214-1224.

(116) Law, B.; Rieutord, F. Electrostatic forces in atomic force microscopy. *Phys. Rev. B* **2002,** *66*, 035402.

(117) Dianoux, R.; Martins, F.; Marchi, F.; Alandi, C.; Comin, F.; Chevrier, J. Detection of electrostatic forces with an atomic force microscope: Analytical and experimental dynamic force curves in the nonlinear regime. *Phys. Rev. B* **2003,** *68*, 045403.

(118) Bishop, K. J.; Wilmer, C. E.; Soh, S.; Grzybowski, B. A. Nanoscale forces and their uses in self‐assembly. *small* **2009,** *5*, 1600-1630.

(119) Moazzami-Gudarzi, M.; Kremer, T.; Valmacco, V.; Maroni, P.; Borkovec, M.; Trefalt, G. Interplay between depletion and double-layer forces acting between charged particles in solutions of like-charged polyelectrolytes. *Phys. Rev. Lett.* **2016,** *117*, 088001.

(120) Lopez-Garcia, J.; Aranda-Rascon, M.; Grosse, C.; Horno, J. Equilibrium Electric Double Layer of Charged Spherical Colloidal Particles: Effect of Different Distances of Minimum Ion Approach to The Particle Surface. *J. Phys. Chem. B* **2010,** *114*, 7548-7556.

(121) Smith, A. M.; Lee, A. A.; Perkin, S. The electrostatic screening length in concentrated electrolytes increases with concentration. *J. Phys. Chem. Lett.* **2016,** *7*, 2157-2163.

(122) Zhang, H.; Wang, D. Controlling the growth of charged‐nanoparticle chains through interparticle electrostatic repulsion. *Angew. Chem.* **2008,** *120*, 4048-4051.

(123) Liu, Y.; Han, X.; He, L.; Yin, Y. Thermoresponsive assembly of charged gold nanoparticles and their reversible tuning of plasmon coupling. *Angew. Chem. Int. Ed.* **2012,** *51*, 6373-6377.

(124) Behrens, S. H.; Christl, D. I.; Emmerzael, R.; Schurtenberger, P.; Borkovec, M. Charging and aggregation properties of carboxyl latex particles: Experiments versus DLVO theory. *Langmuir* **2000,** *16*, 2566-2575.

(125) Guldbrand, L.; Jönsson, B.; Wennerström, H.; Linse, P. Electrical double layer forces. A Monte Carlo study. *J. Chem. Phys.* **1984,** *80*, 2221-2228.

(126) Levin, Y. Electrostatic correlations: from plasma to biology. *Rep. Prog. Phys.* **2002,** *65*, 1577.

(127) Israelachvili, J. N. *Intermolecular and surface forces*; Academic press, 2011, 1-674.

(128) Verwey, E. J. W. Theory of the stability of lyophobic colloids. *The Journal of Physical Chemistry* **1947,** *51*, 631-636.

(129) Carnie, S. L.; Chan, D. Y.; Gunning, J. S. Electrical double layer interaction between dissimilar spherical colloidal particles and between a sphere and a plate: The linearized poisson-boltzmann theory. *Langmuir* **1994,** *10*, 2993-3009.

(130) Chan, D. Y.; Mitchell, D. J. The free energy of an electrical double layer. *J. Colloid Interface Sci.* **1983,** *95*, 193-197.

(131) Kalsin, A. M.; Fialkowski, M.; Paszewski, M.; Smoukov, S. K.; Bishop, K. J.; Grzybowski, B. A. Electrostatic self-assembly of binary nanoparticle crystals with a diamond-like lattice. *Science* **2006,** *312*, 420-424.

(132) Bishop, K. J.; Kowalczyk, B.; Grzybowski, B. A. Precipitation of oppositely charged nanoparticles by dilution and/or temperature increase. *J. Phys. Chem. B* **2009,** *113*, 1413-1417.

(133) Venermo, J.; Sihvola, A. Dielectric polarizability of circular cylinder. *J. Electrostatics* **2005,** *63*, 101-117.

(134) He, X.; Song, M.; Liang, H.; Pan, C. Self-assembly of the symmetric diblock copolymer in a confined state: Monte Carlo simulation. *J. Chem. Phys.* **2001,** *114*, 10510-10513.

(135) Sciortino, F.; Bianchi, E.; Douglas, J. F.; Tartaglia, P. Self-assembly of patchy particles into polymer chains: A parameter-free comparison between Wertheim theory and Monte Carlo simulation. *J. Chem. Phys.* **2007,** *126*, 194903.

(136) Everts, J. C.; Senyuk, B.; Mundoor, H.; Ravnik, M.; Smalyukh, I. I. Anisotropic electrostatic screening of charged colloids in nematic solvents. *Sci. Adv.* **2021,** *7*, eabd0662.

(137) Hapala, P.; Švec, M.; Stetsovych, O.; Van Der Heijden, N. J.; Ondráček, M.; Van Der Lit, J.; Mutombo, P.; Swart, I.; Jelínek, P. Mapping the electrostatic force field of single molecules from high-resolution scanning probe images. *Nat. Commun.* **2016,** *7*, 11560.

(138) Romo-Herrera, J. M.; Alvarez-Puebla, R. A.; Liz-Marzán, L. M. Controlled assembly of plasmonic colloidal nanoparticle clusters. *Nanoscale* **2011,** *3*, 1304-1315.

(139) Jones, M. R.; Osberg, K. D.; Macfarlane, R. J.; Langille, M. R.; Mirkin, C. A. Templated techniques for the synthesis and assembly of plasmonic nanostructures. *Chem. Rev.* **2011,** *111*, 3736-3827.

(140) Guerrini, L.; Graham, D. Molecularly-mediated assemblies of plasmonic nanoparticles for surface-enhanced Raman spectroscopy applications. *Chem. Soc. Rev.* **2012,** *41*, 7085-7107.

(141) Wang, J.-C.; Neogi, P.; Forciniti, D. On one-dimensional self-assembly of surfactant-coated nanoparticles. *J. Chem. Phys.* **2006,** *125*, 194717.

(142) Chen, Q.; Whitmer, J. K.; Jiang, S.; Bae, S. C.; Luijten, E.; Granick, S. Supracolloidal reaction kinetics of Janus spheres. *Science* **2011,** *331*, 199-202.

(143) Cheng, L.; Liu, A.; Peng, S.; Duan, H. Responsive plasmonic assemblies of amphiphilic nanocrystals at oil− water interfaces. *Acs Nano* **2010,** *4*, 6098-6104.

(144) Sun, Z.; Ni, W.; Yang, Z.; Kou, X.; Li, L.; Wang, J. pH‐controlled reversible assembly and disassembly of gold nanorods. *small* **2008,** *4*, 1287-1292.

(145) Song, J.; Cheng, L.; Liu, A.; Yin, J.; Kuang, M.; Duan, H. Plasmonic vesicles of amphiphilic gold nanocrystals: self-assembly and external-stimuli-triggered destruction. *J. Am. Chem. Soc.* **2011,** *133*, 10760-10763.

(146) Zhang, Z.; Maji, S.; Antunes, A. B. d. F.; De Rycke, R.; Zhang, Q.; Hoogenboom, R.; De Geest, B. G. Salt plays a pivotal role in the temperature-responsive aggregation and layer-by-layer assembly of polymer-decorated gold nanoparticles. *Chem. Mater.* **2013,** *25*, 4297-4303.

(147) Zhang, H.; Nayak, S.; Wang, W.; Mallapragada, S.; Vaknin, D. Interfacial self-assembly of polyelectrolyte-capped gold nanoparticles. *Langmuir* **2017,** *33*, 12227-12234.

(148) Shen, Y.; Kuang, M.; Shen, Z.; Nieberle, J.; Duan, H.; Frey, H. Gold nanoparticles coated with a thermosensitive hyperbranched polyelectrolyte: towards smart temperature and pH nanosensors. *Angew. Chem. Int. Ed.* **2008,** *47*, 2227-2230.

(149) Liu, K.; Nie, Z.; Zhao, N.; Li, W.; Rubinstein, M.; Kumacheva, E. Step-growth polymerization of inorganic nanoparticles. *Science* **2010,** *329*, 197-200.

(150) Wang, X.; Li, G.; Chen, T.; Yang, M.; Zhang, Z.; Wu, T.; Chen, H. Polymer-encapsulated gold-nanoparticle dimers: facile preparation and catalytical application in guided growth of dimeric ZnO-nanowires. *Nano Lett.* **2008,** *8*, 2643-2647.

(151) Liu, K.; Lukach, A.; Sugikawa, K.; Chung, S.; Vickery, J.; Therien‐Aubin, H.; Yang, B.; Rubinstein, M.; Kumacheva, E. Copolymerization of metal nanoparticles: a

route to colloidal plasmonic copolymers. *Angew. Chem. Int. Ed.* **2014,** *53*, 2648-2653.

(152) Yi, C.; Yang, Y.; Nie, Z. Alternating copolymerization of inorganic nanoparticles. *J. Am. Chem. Soc.* **2019,** *141*, 7917-7925.

(153) Shah, A. A.; Schultz, B.; Zhang, W.; Glotzer, S. C.; Solomon, M. J. Actuation of shape-memory colloidal fibres of Janus ellipsoids. *Nat. Mater.* **2015,** *14*, 117-124.

(154) Gröschel, A. H.; Walther, A.; Löbling, T. I.; Schacher, F. H.; Schmalz, H.; Müller, A. H. Guided hierarchical co-assembly of soft patchy nanoparticles. *Nature* **2013,** *503*, 247-251.

(155) Zhuang, Z.; Jiang, T.; Lin, J.; Gao, L.; Yang, C.; Wang, L.; Cai, C. Hierarchical nanowires synthesized by supramolecular stepwise polymerization. *Angew. Chem.* **2016,** *128*, 12710-12715.

(156) Cheng, X.; Zhao, G.; Lu, Y.; Yan, M.; Wang, H.; Chen, H. Controllable oligomerization: defying step-growth kinetics in the polymerization of gold nanoparticles. *Chem. Commun.* **2018,** *54*, 7746-7749.

(157) Han, X.; Goebl, J.; Lu, Z.; Yin, Y. Role of salt in the spontaneous assembly of charged gold nanoparticles in ethanol. *Langmuir* **2011,** *27*, 5282-5289.

(158) Wang, H.; Chen, L.; Shen, X.; Zhu, L.; He, J.; Chen, H. Unconventional Chain‐Growth Mode in the Assembly of Colloidal Gold Nanoparticles. *Angew. Chem.* **2012,** *124*, 8145-8149.

(159) Leunissen, M. E.; Christova, C. G.; Hynninen, A.-P.; Royall, C. P.; Campbell, A. I.; Imhof, A.; Dijkstra, M.; Van Roij, R.; Van Blaaderen, A. Ionic colloidal crystals of oppositely charged particles. *Nature* **2005,** *437*, 235-240.

(160) Salem, L. Attractive forces between long saturated chains at short distances. *J. Chem. Phys.* **1962,** *37*, 2100-2113.

(161) Bain, C. D.; Troughton, E. B.; Tao, Y. T.; Evall, J.; Whitesides, G. M.; Nuzzo, R. G. Formation of monolayer films by the spontaneous assembly of organic thiols from solution onto gold. *J. Am. Chem. Soc.* **1989,** *111*, 321-335.

(162) Ziherl, P.; Kamien, R. D. Soap froths and crystal structures. *Phys. Rev. Lett.* **2000,** *85*, 3528.

(163) Ziherl, P.; Kamien, R. Maximizing entropy by minimizing area: Towards a new principle of self-organization. *J. Phys. Chem. B* **2001,** *105*, 10147-10158.

(164) Kostiainen, M. A.; Hiekkataipale, P.; Laiho, A.; Lemieux, V.; Seitsonen, J.; Ruokolainen, J.; Ceci, P. Electrostatic assembly of binary nanoparticle superlattices using protein cages. *Nat. Nanotechnol.* **2013,** *8*, 52.

(165) Tzeng, S. D.; Lin, K. J.; Hu, J. C.; Chen, L. J.; Gwo, S. Templated Self‐Assembly of Colloidal Nanoparticles Controlled by Electrostatic Nanopatterning on a Si3N4/SiO2/Si Electret. *Adv. Mater.* **2006,** *18*, 1147-1151.

(166) Chen, K.; Fu, Q.; Ye, S.; Ge, J. Multicolor printing using electric‐field‐responsive and photocurable photonic crystals. *Adv. Funct. Mater.* **2017,** *27*, 1702825.

(167) Nucara, L.; Greco, F.; Mattoli, V. Electrically responsive photonic crystals: a review. *J. Mater. Chem. C* **2015,** *3*, 8449-8467.

(168) Steiner, T. The hydrogen bond in the solid state. *Angew. Chem. Int. Ed.* **2002,** *41*, 48-76.

(169) Kollman, P. A.; Allen, L. C. Theory of the hydrogen bond. *Chem. Rev.* **1972,** *72*, 283-303.

(170) Gilli, G.; Gilli, P. *The nature of the hydrogen bond: outline of a comprehensive hydrogen bond theory*; Oxford university press, 2009, 1-317.

(171) Desiraju, G. R. The C− H··· O hydrogen bond: structural implications and supramolecular design. *Acc. Chem. Res.* **1996,** *29*, 441-449.

(172) Aakeröy, C. B.; Beatty, A. M.; Helfrich, B. A. "Total synthesis" supramolecular style: Design and hydrogen‐bond‐directed assembly of ternary supermolecules. *Angew. Chem. Int. Ed.* **2001,** *40*, 3240-3242.

(173) Sherrington, D. C.; Taskinen, K. A. Self-assembly in synthetic macromolecular systems via multiple hydrogen bonding interactions. *Chem. Soc. Rev.* **2001,** *30*, 83-93.

(174) Keerl, M.; Smirnovas, V.; Winter, R.; Richtering, W. Interplay between hydrogen bonding and macromolecular architecture leading to unusual phase behavior in thermosensitive microgels. *Angew. Chem. Int. Ed.* **2008,** *47*, 338-341.

(175) Johnson, S.; Evans, S.; Brydson, R. Influence of a terminal functionality on the physical properties of surfactant-stabilized gold nanoparticles. *Langmuir* **1998,** *14*, 6639-6647.

(176) Cusack, L.; Rizza, R.; Gorelov, A.; Fitzmaurice, D. Self‐Assembly and Subsequent Self‐Organization of a Semiconductor Nanocrystallite Superlattice. *Angew. Chem., Int. Ed. Engl.* **1997,** *36*, 848-851.

(177) Boal, A. K.; Ilhan, F.; DeRouchey, J. E.; Thurn-Albrecht, T.; Russell, T. P.; Rotello, V. M. Self-assembly of nanoparticles into structured spherical and network aggregates. *Nature* **2000,** *404*, 746-748.

(178) Hu, X.; Cheng, W.; Wang, T.; Wang, E.; Dong, S. Well-ordered end-to-end linkage of gold nanorods. *Nanotechnology* **2005,** *16*, 2164.

(179) Thomas, K. G.; Barazzouk, S.; Ipe, B. I.; Joseph, S. S.; Kamat, P. V. Uniaxial plasmon coupling through longitudinal self-assembly of gold nanorods. *J. Phys. Chem. B* **2004,** *108*, 13066-13068.

(180) Kimura, M.; Kobayashi, S.; Kuroda, T.; Hanabusa, K.; Shirai, H. Assembly of Gold Nanoparticles into Fibrous Aggregates Using Thiol‐Terminated Gelators. *Adv. Mater.* **2004,** *16*, 335-338.

(181) Jang, S. G.; Kramer, E. J.; Hawker, C. J. Controlled supramolecular assembly of micelle-like gold nanoparticles in PS-b-P2VP diblock copolymers via hydrogen bonding. *J. Am. Chem. Soc.* **2011,** *133*, 16986-16996.

(182) Tong, X.; Wang, G.; Soldera, A.; Zhao, Y. How can azobenzene block copolymer vesicles be dissociated and reformed by light? *J. Phys. Chem. B* **2005,** *109*, 20281-20287.

(183) Klajn, R.; Bishop, K. J.; Grzybowski, B. A. Light-controlled self-assembly of reversible and irreversible nanoparticle suprastructures. *Proc. Natl. Acad. Sci. U.S.A.* **2007,** *104*, 10305-10309.

(184) Klajn, R.; Wesson, P. J.; Bishop, K. J.; Grzybowski, B. A. Writing self‐erasing images using metastable nanoparticle “inks”. *Angew. Chem. Int. Ed.* **2009,** *48*, 7035-7039.

(185) Watson, J. D.; Crick, F. H. Molecular structure of nucleic acids: a structure for deoxyribose nucleic acid. *Nature* **1953,** *171*, 737-738.

(186) Franklin, R. E.; Gosling, R. G. Molecular configuration in sodium thymonucleate. *Nature* **1953,** *171*, 740-741.

(187) Halford, S. E.; Marko, J. F. How do site‐specific DNA‐binding proteins find their targets? *Nucleic Acids Res.* **2004,** *32*, 3040-3052.

(188) Brunet, A.; Salomé, L.; Rousseau, P.; Destainville, N.; Manghi, M.; Tardin, C. How does temperature impact the conformation of single DNA molecules below melting temperature? *Nucleic Acids Res.* **2018,** *46*, 2074-2081.

(189) Panjkovich, A.; Melo, F. Comparison of different melting temperature calculation methods for short DNA sequences. *Bioinformatics* **2005,** *21*, 711-722.

(190) Gudnason, H.; Dufva, M.; Bang, D. D.; Wolff, A. Comparison of multiple DNA dyes for real-time PCR: effects of dye concentration and sequence composition on DNA amplification and melting temperature. *Nucleic Acids Res.* **2007,** *35*, e127.

(191) Lando, D. Y.; Fridman, A. S.; Chang, C.-L.; Grigoryan, I. E.; Galyuk, E. N.; Murashko, O. N.; Chen, C.-C.; Hu, C.-K. Determination of melting temperature and temperature melting range for DNA with multi-peak differential melting curves. *Anal. Biochem.* **2015,** *479*, 28-36.

(192) Rychlik, W.; Rhoads, R. E. A computer program for choosing optimal oligonudeotides for filter hybridization, sequencing and in vitro amplification of DNA. *Nucleic Acids Res.* **1989,** *17*, 8543-8551.

(193) Kuzyk, A.; Schreiber, R.; Fan, Z.; Pardatscher, G.; Roller, E.-M.; Högele, A.; Simmel, F. C.; Govorov, A. O.; Liedl, T. DNA-based self-assembly of chiral plasmonic nanostructures with tailored optical response. *Nature* **2012,** *483*, 311-314.

(194) Schreiber, R.; Luong, N.; Fan, Z.; Kuzyk, A.; Nickels, P. C.; Zhang, T.; Smith, D. M.; Yurke, B.; Kuang, W.; Govorov, A. O. Chiral plasmonic DNA nanostructures with switchable circular dichroism. *Nat. Commun.* **2013,** *4*, 2948.

(195) Mastroianni, A. J.; Claridge, S. A.; Alivisatos, A. P. Pyramidal and chiral groupings of gold nanocrystals assembled using DNA scaffolds. *J. Am. Chem. Soc.* **2009,** *131*, 8455-8459.

(196) Douglas, S. M.; Dietz, H.; Liedl, T.; Högberg, B.; Graf, F.; Shih, W. M. Self-assembly of DNA into nanoscale three-dimensional shapes. *Nature* **2009,** *459*, 414-418.

(197) Tørring, T.; Voigt, N. V.; Nangreave, J.; Yan, H.; Gothelf, K. V. DNA origami: a quantum leap for self-assembly of complex structures. *Chem. Soc. Rev.* **2011,** *40*, 5636-5646.

(198) Li, Z.; Liu, M.; Wang, L.; Nangreave, J.; Yan, H.; Liu, Y. Molecular behavior of DNA origami in higher-order self-assembly. *J. Am. Chem. Soc.* **2010,** *132*, 13545-13552.

(199) Maune, H. T.; Han, S.-p.; Barish, R. D.; Bockrath, M.; Goddard III, W. A.; Rothemund, P. W.; Winfree, E. Self-assembly of carbon nanotubes into two-dimensional geometries using DNA origami templates. *Nat. Nanotechnol.* **2010,** *5*, 61-66.

(200) Di Michele, L.; Varrato, F.; Kotar, J.; Nathan, S. H.; Foffi, G.; Eiser, E. Multistep kinetic self-assembly of DNA-coated colloids. *Nat. Commun.* **2013,** *4*, 2007.

(201) Macfarlane, R. J.; Lee, B.; Jones, M. R.; Harris, N.; Schatz, G. C.; Mirkin, C. A. Nanoparticle superlattice engineering with DNA. *Science* **2011,** *334*, 204-208.

(202) Zhou, O.; Fischer, J. E.; Coustel, N.; Kycia, S.; Zhu, Q.; McGhie, A. R.; Romanow, W. J.; McCauley, J. P.; Smith, A. B.; Cox, D. E. Structure and bonding in alkali-metal-doped C 60. *Nature* **1991,** *351*, 462-464.

(203) Laramy, C. R.; O'Brien, M. N.; Mirkin, C. A. Crystal engineering with DNA. *Nat. Rev. Mater.* **2019,** *4*, 201-224.

(204) Wang, Y.; Wang, Y.; Zheng, X.; Ducrot, É.; Yodh, J. S.; Weck, M.; Pine, D. J. Crystallization of DNA-coated colloids. *Nat. Commun.* **2015,** *6*, 7253.

(205) Boles, M. A.; Talapin, D. V. Many-body effects in nanocrystal superlattices: departure from sphere packing explains stability of binary phases. *J. Am. Chem. Soc.* **2015,** *137*, 4494-4502.

(206) Park, S. Y.; Lytton-Jean, A. K.; Lee, B.; Weigand, S.; Schatz, G. C.; Mirkin, C. A. DNA-programmable nanoparticle crystallization. *Nature* **2008,** *451*, 553-556.

(207) Macfarlane, R. J.; Jones, M. R.; Lee, B.; Auyeung, E.; Mirkin, C. A. Topotactic interconversion of nanoparticle superlattices. *Science* **2013,** *341*, 1222-1225.

(208) Zhang, Y.; Pal, S.; Srinivasan, B.; Vo, T.; Kumar, S.; Gang, O. Selective transformations between nanoparticle superlattices via the reprogramming of DNA-mediated interactions. *Nat. Mater.* **2015,** *14*, 840-847.

(209) Seo, S. E.; Li, T.; Senesi, A. J.; Mirkin, C. A.; Lee, B. The role of repulsion in colloidal crystal engineering with DNA. *J. Am. Chem. Soc.* **2017,** *139*, 16528-16535.

(210) Wang, M. X.; Brodin, J. D.; Millan, J. A.; Seo, S. E.; Girard, M.; Olvera de la Cruz, M.; Lee, B.; Mirkin, C. A. Altering DNA-programmable colloidal crystallization paths by modulating particle repulsion. *Nano Lett.* **2017,** *17*, 5126-5132.

(211) Thaner, R. V.; Eryazici, I.; Macfarlane, R. J.; Brown, K. A.; Lee, B.; Nguyen, S. T.; Mirkin, C. A. The significance of multivalent bonding motifs and "bond order" in DNA-directed nanoparticle crystallization. *J. Am. Chem. Soc.* **2016,** *138*, 6119-6122.

(212) Li, Q.; Jonas, U.; Zhao, X.; Kappl, M. The forces at work in colloidal self‐assembly: A review on fundamental interactions between colloidal particles. *Asia-Pac. J. Chem. Eng.* **2008,** *3*, 255-268.

(213) Bhattacharjee, S.; Elimelech, M.; Borkovec, M. DLVO interaction between colloidal particles: beyond Derjaguin's approximation. *Croat. Chem. Acta* **1998,** *71*, 883-903.

(214) Bhardwaj, R.; Fang, X.; Somasundaran, P.; Attinger, D. Self-assembly of colloidal particles from evaporating droplets: role of DLVO interactions and proposition of a phase diagram. *Langmuir* **2010,** *26*, 7833-7842.

(215) Batista, C. A. S.; Larson, R. G.; Kotov, N. A. Nonadditivity of nanoparticle interactions. *Science* **2015,** *350*, 1242477.

(216) O'Brien, M. N.; Jones, M. R.; Brown, K. A.; Mirkin, C. A. Universal noble metal nanoparticle seeds realized through iterative reductive growth and oxidative dissolution reactions. *J. Am. Chem. Soc.* **2014,** *136*, 7603-7606.

(217) Sun, Y.; Xia, Y. Shape-controlled synthesis of gold and silver nanoparticles. *Science* **2002,** *298*, 2176-2179.

(218) Xia, Y.; Xiong, Y.; Lim, B.; Skrabalak, S. E. Shape‐controlled synthesis of metal nanocrystals: simple chemistry meets complex physics? *Angew. Chem. Int. Ed.* **2009,** *48*, 60-103.

(219) Jones, M. R.; Macfarlane, R. J.; Prigodich, A. E.; Patel, P. C.; Mirkin, C. A. Nanoparticle shape anisotropy dictates the collective behavior of surface-bound ligands. *J. Am. Chem. Soc.* **2011,** *133*, 18865-18869.

(220) Wu, X.; Xu, L.; Liu, L.; Ma, W.; Yin, H.; Kuang, H.; Wang, L.; Xu, C.; Kotov, N. A. Unexpected chirality of nanoparticle dimers and ultrasensitive chiroplasmonic bioanalysis. *J. Am. Chem. Soc.* **2013,** *135*, 18629-18636.

(221) Guo, P.; Sknepnek, R.; Olvera de la Cruz, M. Electrostatic-driven ridge formation on nanoparticles coated with charged end-group ligands. *J. Phys. Chem. C* **2011,** *115*, 6484-6490.

(222) Ghorai, P. K.; Glotzer, S. C. Molecular dynamics simulation study of self-assembled monolayers of alkanethiol surfactants on spherical gold nanoparticles. *J. Phys. Chem. C* **2007,** *111*, 15857-15862.

(223) Qin, Y.; Fichthorn, K. A. Solvophobic solvation at large and intermediate length scales: Size, shape, and solvent effects. *Phys. Rev. E* **2006,** *74*, 020401.

(224) Qin, Y.; Fichthorn, K. A. Molecular dynamics simulation of the forces between colloidal nanoparticles in n-decane solvent. *J. Chem. Phys.* **2007,** *127*, 144911.

(225) Kim, H.-Y.; Sofo, J. O.; Velegol, D.; Cole, M. W.; Lucas, A. A. Van der Waals dispersion forces between dielectric nanoclusters. *Langmuir* **2007,** *23*, 1735-1740.

(226) Nie, Z.; Petukhova, A.; Kumacheva, E. Properties and emerging applications of self-assembled structures made from inorganic nanoparticles. *Nat. Nanotechnol.* **2010,** *5*, 15-25.

(227) Bishop, K.; Wilmer, C.; Soh, S. B. a. Grzybowski. *Small* **2009,** *5*, 1600-1630.

(228) Min, Y.; Akbulut, M.; Kristiansen, K.; Golan, Y.; Israelachvili, J. The role of interparticle and external forces in nanoparticle assembly. *Nat. Mater.* **2008,** *7*, 527-538.

(229) Wang, L.; Ng, R. J. H.; Safari Dinachali, S.; Jalali, M.; Yu, Y.; Yang, J. K. Large area plasmonic color palettes with expanded gamut using colloidal self-assembly. *ACS Photonics* **2016,** *3*, 627-633.

(230) Sun, Y.; Zuo, X.; Sankaranarayanan, S. K.; Peng, S.; Narayanan, B.; Kamath, G. Quantitative 3D evolution of colloidal nanoparticle oxidation in solution. *Science* **2017,** *356*, 303-307.

(231) Schaffer, M.; Pfeffer, S.; Mahamid, J.; Kleindiek, S.; Laugks, T.; Albert, S.; Engel, B. D.; Rummel, A.; Smith, A. J.; Baumeister, W. A cryo-FIB lift-out technique enables molecular-resolution cryo-ET within native Caenorhabditis elegans tissue. *Nat. Methods* **2019,** *16*, 757-762.

(232) Chen, Q.; Cho, H.; Manthiram, K.; Yoshida, M.; Ye, X.; Alivisatos, A. P. Interaction potentials of anisotropic nanocrystals from the trajectory sampling of particle motion using in situ liquid phase transmission electron microscopy. *ACS Cent. Sci.* **2015,** *1*, 33-39.

(233) Nie, Z.; Fava, D.; Kumacheva, E.; Zou, S.; Walker, G. C.; Rubinstein, M. Self-assembly of metal–polymer analogues of amphiphilic triblock copolymers. *Nat. Mater.* **2007,** *6*, 609-614.

(234) Li, Y.; Lin, H.; Zhou, W.; Sun, L.; Samanta, D.; Mirkin, C. A. Corner-, edge-, and facet-controlled growth of nanocrystals. *Sci. Adv.* **2021,** *7*, eabf1410.

(235) Bondy, C. The creaming of rubber latex. *Trans. Faraday Society* **1939,** *35*, 1093-1108.

(236) Asakura, S.; Oosawa, F. On interaction between two bodies immersed in a solution of macromolecules. *J. Chem. Phys.* **1954,** *22*, 1255-1256.

(237) Lekkerkerker, H. N.; Tuinier, R. In *Colloids and the depletion interaction*; Springer, 2011, 57-108.

(238) Zhang, J.; Lang, P. R.; Meyer, M.; Dhont, J. K. Synthesis and self-assembly of squarelike PbCrO4 nanoplatelets via micelle-mediated depletion attraction. *Langmuir* **2013,** *29*, 4679-4687.

(239) Abbas, S.; Lodge, T. P. Depletion interactions: a new control parameter for the self-assembly of diblock copolymer micelles. *Phys. Rev. Lett.* **2007,** *99*, 137802.

(240) Badaire, S.; Cottin-Bizonne, C.; Stroock, A. D. Experimental investigation of selective colloidal interactions controlled by shape, surface roughness, and steric layers. *Langmuir* **2008,** *24*, 11451-11463.

(241) Zhao, K.; Mason, T. G. Directing colloidal self-assembly through roughness-controlled

depletion attractions. *Phys. Rev. Lett.* **2007,** *99*, 268301.

(242) Kim, D.; Bae, W. K.; Kim, S.-H.; Lee, D. C. Depletion-Mediated Interfacial Assembly of Semiconductor Nanorods. *Nano Lett.* **2019,** *19*, 963-970.

(243) Kwok, D. Y.; Neumann, A. W. Contact angle measurement and contact angle interpretation. *Adv. Colloid Interface Sci.* **1999,** *81*, 167-249.

(244) Cui, L.; Li, Y.; Wang, J.; Tian, E.; Zhang, X.; Zhang, Y.; Song, Y.; Jiang, L. Fabrication of large-area patterned photonic crystals by ink-jet printing. *J. Mater. Chem.* **2009,** *19*, 5499-5502.

(245) Jiang, P.; McFarland, M. J. Large-scale fabrication of wafer-size colloidal crystals, macroporous polymers and nanocomposites by spin-coating. *J. Am. Chem. Soc.* **2004,** *126*, 13778-13786.

(246) Pozas, R.; Mihi, A.; Ocaña, M.; Míguez, H. Building Nanocrystalline Planar Defects within Self‐Assembled Photonic Crystals by Spin‐Coating. *Adv. Mater.* **2006,** *18*, 1183-1187.

(247) Wang, H.; Yan, K.; Xie, J.; Duan, M. Fabrication of ZnO colloidal photonic crystal by spin-coating method. *Mater. Sci. Semicond. Process.* **2008,** *11*, 44-47.

(248) Mihi, A.; Ocaña, M.; Míguez, H. Oriented colloidal‐crystal thin films by spin‐coating microspheres dispersed in volatile media. *Adv. Mater.* **2006,** *18*, 2244-2249.

(249) Cui, L.; Zhang, Y.; Wang, J.; Ren, Y.; Song, Y.; Jiang, L. Ultra‐fast fabrication of colloidal photonic crystals by spray coating. *Macromol. Rapid Commun.* **2009,** *30*, 598-603.

(250) Sprafke, A. N.; Schneevoigt, D.; Seidel, S.; Schweizer, S. L.; Wehrspohn, R. B. Automated spray coating process for the fabrication of large-area artificial opals on textured substrates. *Opt. Express* **2013,** *21*, A528-A538.

(251) Wang, C.; Lin, X.; Schäfer, C. G.; Hirsemann, S.; Ge, J. Spray Synthesis of Photonic Crystal Based Automotive Coatings with Bright and Angular‐Dependent Structural Colors. *Adv. Funct. Mater.* **2021,** *31*, 2008601.

(252) Yang, H.; Jiang, P. Large-scale colloidal self-assembly by doctor blade coating. *Langmuir* **2010,** *26*, 13173-13182.

(253) Hsieh, C.-H.; Lu, Y.-C.; Yang, H. Self-Assembled Mechanochromic Shape Memory Photonic Crystals by Doctor Blade Coating. *ACS Appl. Mater. Interfaces* **2020,** *12*, 36478-36484.

(254) Ko, Y.-L.; Tsai, H.-P.; Lin, K.-Y.; Chen, Y.-C.; Yang, H. Reusable macroporous photonic crystal-based ethanol vapor detectors by doctor blade coating. *J. Colloid Interface Sci.* **2017,** *487*, 360-369.

(255) Li, Y.; Fan, Q.; Wang, X.; Liu, G.; Chai, L.; Zhou, L.; Shao, J.; Yin, Y. Shear‐Induced Assembly of Liquid Colloidal Crystals for Large‐Scale Structural Coloration of Textiles. *Adv. Funct. Mater.* **2021**, 2010746.

(256) Zhou, Z.; Zhao, X. Flow-controlled vertical deposition method for the fabrication of photonic crystals. *Langmuir* **2004,** *20*, 1524-1526.

(257) García Núñez, C.; Navaraj, W. T.; Liu, F.; Shakthivel, D.; Dahiya, R. Large-area self-assembly of silica microspheres/nanospheres by temperature-assisted dip-coating. *ACS Appl. Mater. Interfaces* **2018,** *10*, 3058-3068.

(258) Zhou, Z.; Zhao, X. Opal and inverse opal fabricated with a flow-controlled vertical deposition method. *Langmuir* **2005,** *21*, 4717-4723.

(259) Meijer, J.-M.; Hagemans, F.; Rossi, L.; Byelov, D. V.; Castillo, S. I.; Snigirev, A.; Snigireva, I.; Philipse, A. P.; Petukhov, A. V. Self-assembly of colloidal cubes via vertical deposition. *Langmuir* **2012,** *28*, 7631-7638.

(260) Park, J.; Moon, J. Control of colloidal particle deposit patterns within picoliter droplets ejected by ink-jet printing. *Langmuir* **2006,** *22*, 3506-3513.

(261) Zhang, J.; Zhu, Z.; Yu, Z.; Ling, L.; Wang, C.-F.; Chen, S. Large-scale colloidal films with robust structural colors. *Mater. Horiz.* **2019,** *6*, 90-96.

(262) Wang, D.; Park, M.; Park, J.; Moon, J. Optical properties of single droplet of photonic crystal assembled by ink-jet printing. *Appl. Phys. Lett.* **2005,** *86*, 241114.

(263) Ko, H.-Y.; Park, J.; Shin, H.; Moon, J. Rapid self-assembly of monodisperse colloidal spheres in an ink-jet printed droplet. *Chem. Mater.* **2004,** *16*, 4212-4215.

(264) Wong, S.; Deubel, M.; Pérez‐Willard, F.; John, S.; Ozin, G. A.; Wegener, M.; von Freymann, G. Direct laser writing of three‐dimensional

photonic crystals with a complete photonic bandgap in chalcogenide glasses. *Adv. Mater.* **2006,** *18*, 265-269.

(265) Al-Milaji, K. N.; Radhakrishnan, V.; Kamerkar, P.; Zhao, H. pH-modulated self-assembly of colloidal nanoparticles in a dual-droplet inkjet printing process. *J. Colloid Interface Sci.* **2018,** *529*, 234-242.

(266) Feng, J.; Song, Q.; Zhang, B.; Wu, Y.; Wang, T.; Jiang, L. Large‐Scale, Long‐Range‐Ordered Patterning of Nanocrystals via Capillary‐Bridge Manipulation. *Adv. Mater.* **2017,** *29*, 1703143.

(267) Lawrence, C. The mechanics of spin coating of polymer films. *The Physics of fluids* **1988,** *31*, 2786-2795.

(268) Natsume, Y.; Sakata, H. Zinc oxide films prepared by sol-gel spin-coating. *Thin Solid Films* **2000,** *372*, 30-36.

(269) Flack, W. W.; Soong, D. S.; Bell, A. T.; Hess, D. W. A mathematical model for spin coating of polymer resists. *J. Appl. Phys.* **1984,** *56*, 1199-1206.

(270) Min, W.-L.; Jiang, P.; Jiang, B. Large-scale assembly of colloidal nanoparticles and fabrication of periodic subwavelength structures. *Nanotechnology* **2008,** *19*, 475604.

(271) Fang, Y.; Phillips, B. M.; Askar, K.; Choi, B.; Jiang, P.; Jiang, B. Scalable bottom-up fabrication of colloidal photonic crystals and periodic plasmonic nanostructures. *J. Mater. Chem. C* **2013,** *1*, 6031-6047.

(272) Moridi, A.; Hassani-Gangaraj, S. M.; Guagliano, M.; Dao, M. Cold spray coating: review of material systems and future perspectives. *Surf. Eng.* **2014,** *30*, 369-395.

(273) Pham, V. H.; Cuong, T. V.; Hur, S. H.; Shin, E. W.; Kim, J. S.; Chung, J. S.; Kim, E. J. Fast and simple fabrication of a large transparent chemically-converted graphene film by spray-coating. *Carbon* **2010,** *48*, 1945-1951.

(274) Paik, M. J.; Lee, Y.; Yun, H. S.; Lee, S. U.; Hong, S. T.; Seok, S. I. TiO2 Colloid‐Spray Coated Electron‐Transporting Layers for Efficient Perovskite Solar Cells. *Adv. Energy Mater.* **2020,** *10*, 2001799.

(275) Deng, Y.; Wang, Q.; Yuan, Y.; Huang, J. Vividly colorful hybrid perovskite solar cells by doctor-blade coating with perovskite photonic nanostructures. *Mater. Horiz.* **2015,** *2*, 578-583.

(276) Dimitrov, A. S.; Nagayama, K. Continuous convective assembling of fine particles into two-dimensional arrays on solid surfaces. *Langmuir* **1996,** *12*, 1303-1311.

(277) Jiang, P.; Bertone, J.; Hwang, K. S.; Colvin, V. Single-crystal colloidal multilayers of controlled thickness. *Chem. Mater.* **1999,** *11*, 2132-2140.

(278) Deleuze, C.; Sarrat, B.; Ehrenfeld, F.; Perquis, S.; Derail, C.; Billon, L. Photonic properties of hybrid colloidal crystals fabricated by a rapid dip-coating process. *Phys. Chem. Chem. Phys.* **2011,** *13*, 10681-10689.

(279) Vlasov, Y. A.; Bo, X.-Z.; Sturm, J. C.; Norris, D. J. On-chip natural assembly of silicon photonic bandgap crystals. *Nature* **2001,** *414*, 289-293.

(280) Vlasov, Y. A.; Astratov, V.; Baryshev, A.; Kaplyanskii, A.; Karimov, O.; Limonov, M. Manifestation of intrinsic defects in optical properties of self-organized opal photonic crystals. *Phys. Rev. E* **2000,** *61*, 5784.

(281) Wong, S.; Kitaev, V.; Ozin, G. A. Colloidal crystal films: advances in universality and perfection. *J. Am. Chem. Soc.* **2003,** *125*, 15589-15598.

(282) Gratson, G. M.; García‐Santamaría, F.; Lousse, V.; Xu, M.; Fan, S.; Lewis, J. A.; Braun, P. V. Direct‐write assembly of three‐dimensional photonic crystals: conversion of polymer scaffolds to silicon hollow‐woodpile structures. *Adv. Mater.* **2006,** *18*, 461-465.

(283) Seet, K. K.; Mizeikis, V.; Matsuo, S.; Juodkazis, S.; Misawa, H. Three‐dimensional spiral‐architecture photonic crystals obtained by direct laser writing. *Adv. Mater.* **2005,** *17*, 541-545.

(284) Park, J.; Moon, J.; Shin, H.; Wang, D.; Park, M. Direct-write fabrication of colloidal photonic crystal microarrays by ink-jet printing. *J. Colloid Interface Sci.* **2006,** *298*, 713-719.

(285) Al‐Milaji, K. N.; Secondo, R. R.; Ng, T. N.; Kinsey, N.; Zhao, H. Interfacial Self‐Assembly of Colloidal Nanoparticles in Dual‐Droplet Inkjet Printing. *Adv. Mater. Interfaces* **2018,** *5*, 1701561.

(286) Sowade, E.; Blaudeck, T.; Baumann, R. R. Self-assembly of spherical colloidal photonic crystals inside inkjet-printed droplets. *Cryst. Growth Des.* **2016,** *16*, 1017-1026.

(287) Shanker, R.; Sardar, S.; Chen, S.; Gamage, S.; Rossi, S.; Jonsson, M. P. Noniridescent Biomimetic Photonic Microdomes by Inkjet Printing. *Nano Lett.* **2020,** *20*, 7243-7250.

(288) Yin, Y.; Xia, Y. Growth of large colloidal crystals with their (100) planes orientated parallel to the surfaces of supporting substrates. *Adv. Mater.* **2002,** *14*, 605-608.

(289) Zhou, M.; Xing, F.; Ren, M.; Feng, Y.; Zhao, Y.; Qiu, H.; Wang, X.; Gao, C.; Sun, F.; He, Y. A Facile Method to Assemble PNIPAM‐Containing Microgel Photonic Crystals. *Chemphyschem* **2009,** *10*, 523-526.

(290) Lyon, L. A.; Meng, Z.; Singh, N.; Sorrell, C. D.; John, A. S. Thermoresponsive microgel-based materials. *Chem. Soc. Rev.* **2009,** *38*, 865-874.

(291) Wohlleben, W.; Bartels, F. W.; Boyle, M.; Leyrer, R. J. Covalent and physical cross-linking of photonic crystals with 10-fold-enhanced chemomechanical stability. *Langmuir* **2008,** *24*, 5627-5635.

(292) Weissman, J. M.; Sunkara, H. B.; Albert, S. T.; Asher, S. A. Thermally switchable periodicities and diffraction from mesoscopically ordered materials. *Science* **1996,** *274*, 959-963.

(293) Hellweg, T.; Dewhurst, C.; Brückner, E.; Kratz, K.; Eimer, W. Colloidal crystals made of poly (N-isopropylacrylamide) microgel particles. *Colloid. Polym. Sci.* **2000,** *278*, 972-978.

(294) Zhou, J.; Wang, G.; Marquez, M.; Hu, Z. The formation of crystalline hydrogel films by self-crosslinking microgels. *Soft Matter* **2009,** *5*, 820-826.

(295) Cai, Z.; Teng, J.; Wan, Y.; Zhao, X. An improved convective self-assembly method for the fabrication of binary colloidal crystals and inverse structures. *J. Colloid Interface Sci.* **2012,** *380*, 42-50.

(296) Cai, Z.; Liu, Y. J.; Lu, X.; Teng, J. Fabrication of well-ordered binary colloidal crystals with extended size ratios for broadband reflectance. *ACS Appl. Mater. Interfaces* **2014,** *6*, 10265-10273.

(297) Cai, Z.; Teng, J.; Yan, Q.; Zhao, X. Solvent effect on the self-assembly of colloidal microspheres via a horizontal deposition method. *Colloids Surf. Physicochem. Eng. Aspects* **2012,** *402*, 37-44.

(298) Wang, L.; Zhao, X. Fabrication of crack-free colloidal crystals using a modified vertical deposition method. *J. Phys. Chem. C* **2007,** *111*, 8538-8542.

(299) Guo, D.; Li, C.; Wang, Y.; Li, Y.; Song, Y. Precise assembly of particles for zigzag or linear patterns. *Angew. Chem. Int. Ed.* **2017,** *56*, 15348-15352.

(300) Guo, D.; Li, Y.; Zheng, X.; Li, F.; Chen, S.; Li, M.; Yang, Q.; Li, H.; Song, Y. Programmed coassembly of one-dimensional binary superstructures by liquid soft confinement. *J. Am. Chem. Soc.* **2018,** *140*, 18-21.

(301) Guo, D.; Zheng, X.; Wang, X.; Li, H.; Li, K.; Li, Z.; Song, Y. Formation of Multicomponent Size‐Sorted Assembly Patterns by Tunable Templated Dewetting. *Angew. Chem. Int. Ed.* **2018,** *57*, 16126-16130.

(302) Rycenga, M.; Camargo, P. H.; Xia, Y. Template-assisted self-assembly: a versatile approach to complex micro-and nanostructures. *Soft Matter* **2009,** *5*, 1129-1136.

(303) Xia, Y.; Yin, Y.; Lu, Y.; McLellan, J. Template‐assisted self‐assembly of spherical colloids into complex and controllable structures. *Adv. Funct. Mater.* **2003,** *13*, 907-918.

(304) Yin, Y.; Xia, Y. Self‐assembly of monodispersed spherical colloids into complex aggregates with well‐defined sizes, shapes, and structures. *Adv. Mater.* **2001,** *13*, 267-271.

(305) Yin, Y.; Lu, Y.; Gates, B.; Xia, Y. Template-assisted self-assembly: a practical route to complex aggregates of monodispersed colloids with well-defined sizes, shapes, and structures. *J. Am. Chem. Soc.* **2001,** *123*, 8718-8729.

(306) Yin, Y.; Xia, Y. Self-assembly of spherical colloids into helical chains with well-controlled handedness. *J. Am. Chem. Soc.* **2003,** *125*, 2048-2049.

(307) Yin, Y.; Lu, Y.; Xia, Y. A self-assembly approach to the formation of asymmetric dimers from monodispersed spherical colloids. *J. Am. Chem. Soc.* **2001,** *123*, 771-772.

(308) Yin, Y.; Li, Z.-Y.; Xia, Y. Template-directed growth of (100)-oriented colloidal crystals. *Langmuir* **2003,** *19*, 622-631.

(309) Hanske, C.; Tebbe, M.; Kuttner, C.; Bieber, V.; Tsukruk, V. V.; Chanana, M.; König, T. A.; Fery, A. Strongly coupled plasmonic modes on macroscopic areas via template-assisted colloidal self-assembly. *Nano Lett.* **2014,** *14*, 6863-6871.

(310) Lin, Q.-Y.; Mason, J. A.; Li, Z.; Zhou, W.; O'Brien, M. N.; Brown, K. A.; Jones, M. R.; Butun, S.; Lee, B.; Dravid, V. P. Building superlattices from individual nanoparticles via template-confined DNA-mediated assembly. *Science* **2018,** *359*, 669-672.

(311) Liu, D.; Aleisa, R.; Cai, Z.; Li, Y.; Yin, Y. Self-assembly of superstructures at all scales. *Matter* **2021,** *4*, 927-941.

(312) Acharya, S.; Hill, J. P.; Ariga, K. Soft Langmuir–Blodgett technique for hard nanomaterials. *Adv. Mater.* **2009,** *21*, 2959-2981.

(313) Miyashita, T. Recent studies on functional ultrathin polymer films prepared by the Langmuir-Blodgett technique. *Prog. Polym. Sci.* **1993,** *18*, 263-294.

(314) Clint, J. H.; Taylor, S. E. Particle size and interparticle forces of overbased detergents: a Langmuir trough study. *Colloids and surfaces* **1992,** *65*, 61-67.

(315) Bardosova, M.; Dillon, F. C.; Pemble, M. E.; Povey, I. M.; Tredgold, R. H. Langmuir–Blodgett assembly of colloidal photonic crystals using silica particles prepared without the use of surfactant molecules. *J. Colloid Interface Sci.* **2009,** *333*, 816-819.

(316) Parchine, M.; McGrath, J.; Bardosova, M.; Pemble, M. E. Large area 2D and 3D colloidal photonic crystals fabricated by a roll-to-roll Langmuir–Blodgett method. *Langmuir* **2016,** *32*, 5862-5869.

(317) Udayabhaskararao, T.; Altantzis, T.; Houben, L.; Coronado-Puchau, M.; Langer, J.; Popovitz-Biro, R.; Liz-Marzán, L. M.; Vuković, L.; Král, P.; Bals, S. Tunable porous nanoallotropes prepared by post-assembly etching of binary nanoparticle superlattices. *Science* **2017,** *358*, 514-518.

(318) Grillo, F.; Fernandez-Rodriguez, M. A.; Antonopoulou, M.-N.; Gerber, D.; Isa, L. Self-templating assembly of soft microparticles into complex tessellations. *Nature* **2020,** *582*, 219-224.

(319) Wu, C.; Lu, Z.; Li, Z.; Yin, Y. Assembly of Colloidal Nanoparticles into Hollow Superstructures by Controlling Phase Separation in Emulsion Droplets. *Small Struct.* **2021,** *2*, 2100005.

(320) Shang, L.; Fu, F.; Cheng, Y.; Wang, H.; Liu, Y.; Zhao, Y.; Gu, Z. Photonic crystal microbubbles as suspension barcodes. *J. Am. Chem. Soc.* **2015,** *137*, 15533-15539.

(321) Yu, Y.; Shang, L.; Guo, J.; Wang, J.; Zhao, Y. Design of capillary microfluidics for spinning cell-laden microfibers. *Nat. Protoc.* **2018,** *13*, 2557-2579.

(322) Kim, S.-H.; Park, J.-G.; Choi, T. M.; Manoharan, V. N.; Weitz, D. A. Osmotic-pressure-controlled concentration of colloidal particles in thin-shelled capsules. *Nat. Commun.* **2014,** *5*, 3068.

(323) Shang, L.; Cheng, Y.; Zhao, Y. Emerging droplet microfluidics. *Chem. Rev.* **2017,** *117*, 7964-8040.

(324) Noya, E. G.; Zubieta, I.; Pine, D. J.; Sciortino, F. Assembly of clathrates from tetrahedral patchy colloids with narrow patches. *J. Chem. Phys.* **2019,** *151*, 094502.

(325) Ducrot, É.; He, M.; Yi, G.-R.; Pine, D. J. Colloidal alloys with preassembled clusters and spheres. *Nat. Mater.* **2017,** *16*, 652-657.

(326) Chen, Q.; Yan, J.; Zhang, J.; Bae, S. C.; Granick, S. Janus and multiblock colloidal particles. *Langmuir* **2012,** *28*, 13555-13561.

(327) Gennes, P. d. Soft matter. *Science* **1992,** *256*, 495-498.

(328) Lattuada, M.; Hatton, T. A. Synthesis, properties and applications of Janus nanoparticles. *Nano Today* **2011,** *6*, 286-308.

(329) Yi, G.-R.; Pine, D. J.; Sacanna, S. Recent progress on patchy colloids and their self-assembly. *J. Phys.: Condens. Matter* **2013,** *25*, 193101.

(330) Walther, A.; Muller, A. H. Janus particles: synthesis, self-assembly, physical properties, and applications. *Chem. Rev.* **2013,** *113*, 5194-5261.

(331) Jiang, S.; Chen, Q.; Tripathy, M.; Luijten, E.; Schweizer, K. S.; Granick, S. Janus particle synthesis and assembly. *Adv. Mater.* **2010,** *22*, 1060-1071.

(332) Oh, J. S.; Lee, S.; Glotzer, S. C.; Yi, G.-R.; Pine, D. J. Colloidal fibers and rings by cooperative assembly. *Nat. Commun.* **2019,** *10*, 3936.
(333) Wang, Y.; Wang, Y.; Breed, D. R.; Manoharan, V. N.; Feng, L.; Hollingsworth, A. D.; Weck, M.; Pine, D. J. Colloids with valence and specific directional bonding. *Nature* **2012,** *491*, 51-55.
(334) Zheng, X.; Liu, M.; He, M.; Pine, D. J.; Weck, M. Shape‐shifting patchy particles. *Angew. Chem.* **2017,** *129*, 5599-5603.
(335) Liu, M.; Zheng, X.; Grebe, V.; Pine, D. J.; Weck, M. Tunable assembly of hybrid colloids induced by regioselective depletion. *Nat. Mater.* **2020,** *19*, 1354-1361.
(336) Wang, Z.; Wang, Z.; Li, J.; Tian, C.; Wang, Y. Active colloidal molecules assembled via selective and directional bonds. *Nat. Commun.* **2020,** *11*, 2670.
(337) Sindoro, M.; Granick, S. Ionic Janus liquid droplets assembled and propelled by electric field. *Angew. Chem. Int. Ed.* **2018,** *57*, 16773-16776.
(338) Ren, L. J.; Liu, H. K.; Wu, H.; Hu, M. B.; Wang, W. Toward Cluster Materials with Ordered Structures via Self‐Assembly of Heterocluster Janus Molecules. *Adv. Mater.* **2020,** *32*, 1805863.
(339) Lin, H.; Lee, S.; Sun, L.; Spellings, M.; Engel, M.; Glotzer, S. C.; Mirkin, C. A. Clathrate colloidal crystals. *Science* **2017,** *355*, 931-935.
(340) He, M.; Gales, J. P.; Ducrot, É.; Gong, Z.; Yi, G.-R.; Sacanna, S.; Pine, D. J. Colloidal diamond. *Nature* **2020,** *585*, 524-529.
(341) Oh, J. S.; Yi, G.-R.; Pine, D. J. Reconfigurable Transitions between One-and Two-Dimensional Structures with Bifunctional DNA-Coated Janus Colloids. *ACS nano* **2020,** *14*, 15786-15792.
(342) Agard, N. J.; Prescher, J. A.; Bertozzi, C. R. A strain-promoted [3+ 2] azide− alkyne cycloaddition for covalent modification of biomolecules in living systems. *J. Am. Chem. Soc.* **2004,** *126*, 15046-15047.
(343) Maldovan, M.; Thomas, E. L. Diamond-structured photonic crystals. *Nat. Mater.* **2004,** *3*, 593-600.
(344) Crocker, J. C. Elusive photonic crystals come a step closer. *Nature* **2020,** *585*, 506-507.
(345) Chen, Q.; Bae, S. C.; Granick, S. Directed self-assembly of a colloidal kagome lattice. *Nature* **2011,** *469*, 381-384.
(346) Erb, R. M.; Jenness, N. J.; Clark, R. L.; Yellen, B. B. Towards holonomic control of Janus particles in optomagnetic traps. *Adv. Mater.* **2009,** *21*, 4825-4829.
(347) Wang, Z.; Wang, Z.; Li, J.; Wang, Y. Directional and Reconfigurable Assembly of Metallodielectric Patchy Particles. *ACS nano* **2021,** *15*, 5439-5448.
(348) Sacanna, S.; Korpics, M.; Rodriguez, K.; Colón-Meléndez, L.; Kim, S.-H.; Pine, D. J.; Yi, G.-R. Shaping colloids for self-assembly. *Nat. Commun.* **2013,** *4*, 1688.
(349) Sacanna, S.; Rossi, L.; Pine, D. J. Magnetic click colloidal assembly. *J. Am. Chem. Soc.* **2012,** *134*, 6112-6115.
(350) Stein, A.; Wilson, B. E.; Rudisill, S. G. Design and functionality of colloidal-crystal-templated materials—chemical applications of inverse opals. *Chem. Soc. Rev.* **2013,** *42*, 2763-2803.
(351) Lyu, F.; Bai, Y.; Li, Z.; Xu, W.; Wang, Q.; Mao, J.; Wang, L.; Zhang, X.; Yin, Y. Self‐Templated Fabrication of CoO‐MoO2 Nanocages for Enhanced Oxygen Evolution. *Adv. Funct. Mater.* **2017,** *27*, 1702324.
(352) Holland, B. T.; Blanford, C. F.; Stein, A. Synthesis of macroporous minerals with highly ordered three-dimensional arrays of spheroidal voids. *Science* **1998,** *281*, 538-540.
(353) Velev, O.; Jede, T.; Lobo, R.; Lenhoff, A. Porous silica via colloidal crystallization. *Nature* **1997,** *389*, 447-448.
(354) Wang, D.; Caruso, F. Fabrication of polyaniline inverse opals via templating ordered colloidal assemblies. *Adv. Mater.* **2001,** *13*, 350-354.
(355) Geier, S.; Jung, R.; Peters, K.; Gasteiger, H. A.; Fattakhova-Rohlfing, D.; Fässler, T. F. A wet-chemical route for macroporous inverse opal Ge anodes for lithium ion batteries with high capacity retention. *Sustain. Energy Fuels* **2018,** *2*, 85-90.
(356) Miguez, H.; Meseguer, F.; López, C.; López‐Tejeira, F.; Sánchez‐Dehesa, J. Synthesis and photonic bandgap characterization of polymer inverse opals. *Adv. Mater.* **2001,** *13*, 393-396.

(357) Juarez, B. H.; Ibisate, M.; Palacios, J. M.; López, C. High‐Energy Photonic Bandgap in Sb2S3 Inverse Opals by Sulfidation Processing. *Adv. Mater.* **2003,** *15*, 319-323.

(358) Juárez, B. H.; García, P. D.; Golmayo, D.; Blanco, A.; Lopez, C. ZnO inverse opals by chemical vapor deposition. *Adv. Mater.* **2005,** *17*, 2761-2765.

(359) Moon, J.-H.; Cho, Y.-S.; Yang, S.-M. Room temperature chemical vapor deposition for fabrication of titania inverse opals: Fabrication, morphology analysis and optical characterization. *Bull. Korean Chem. Soc.* **2009,** *30*, 2245-2248.

(360) Rugge, A.; Becker, J. S.; Gordon, R. G.; Tolbert, S. H. Tungsten nitride inverse opals by atomic layer deposition. *Nano Lett.* **2003,** *3*, 1293-1297.

(361) King, J. S.; Graugnard, E.; Summers, C. J. TiO2 inverse opals fabricated using low‐temperature atomic layer deposition. *Adv. Mater.* **2005,** *17*, 1010-1013.

(362) Alessandri, I.; Zucca, M.; Ferroni, M.; Bontempi, E.; Depero, L. E. Tailoring the pore size and architecture of CeO2/TiO2 core/shell inverse opals by atomic layer deposition. *Small* **2009,** *5*, 336-340.

(363) Huang, L.; Wang, Z.; Sun, J.; Miao, L.; Li, Q.; Yan, Y.; Zhao, D. Fabrication of ordered porous structures by self-assembly of zeolite nanocrystals. *J. Am. Chem. Soc.* **2000,** *122*, 3530-3531.

(364) Wang, Y.; Tang, Y.; Ni, Z.; Hua, W.; Yang, W.; Wang, X.; Tao, W.; Gao, Z. Synthesis of macroporous materials with zeolitic microporous frameworks by self-assembly of colloidal zeolites. *Chem. Lett.* **2000,** *29*, 510-511.

(365) Wang, J.; Li, Q.; Knoll, W.; Jonas, U. Preparation of multilayered trimodal colloid crystals and binary inverse opals. *J. Am. Chem. Soc.* **2006,** *128*, 15606-15607.

(366) Zeng, X.; Hu, X.; Song, H.; Xia, G.; Shen, Z.-Y.; Yu, R.; Moskovits, M. Microwave synthesis of zeolites and their related applications. *Microporous Mesoporous Mater.* **2021**, 111262.

(367) Caruso, F.; Caruso, R. A.; Möhwald, H. Nanoengineering of inorganic and hybrid hollow spheres by colloidal templating. *Science* **1998,** *282*, 1111-1114.

(368) Dong, A.; Wang, Y.; Tang, Y.; Zhang, Y.; Ren, N.; Gao, Z. Mechanically stable zeolite monoliths with three‐dimensional ordered macropores by the transformation of mesoporous silica spheres. *Adv. Mater.* **2002,** *14*, 1506-1510.

(369) Hotta, Y.; Jia, Y.; Kawamura, M.; Omura, N.; Tsunekawa, K.; Sato, K.; Watari, K. Synthesis of multilayer Nano-ZrO 2 coated polystyrene spheres on fabrication of three-dimensional ordered macroporous structures. *J. Mater. Sci.* **2006,** *41*, 2779-2786.

(370) Morin, F. Oxides which show a metal-to-insulator transition at the Neel temperature. *Phys. Rev. Lett.* **1959,** *3*, 34-36.

(371) Verleur, H. W.; Barker Jr, A.; Berglund, C. Optical properties of V O 2 between 0.25 and 5 eV. *Phys. Rev.* **1968,** *172*, 788-798.

(372) Pevtsov, A.; Kurdyukov, D.; Golubev, V.; Akimov, A.; Meluchev, A.; Sel'kin, A.; Kaplyanskii, A.; Yakovlev, D.; Bayer, M. Ultrafast stop band kinetics in a three-dimensional opal-V O 2 photonic crystal controlled by a photoinduced semiconductor-metal phase transition. *Phys. Rev. B* **2007,** *75*, 153101.

(373) Jeong, U.; Xia, Y. Photonic crystals with thermally switchable stop bands fabricated from Se@ Ag2Se spherical colloids. *Angew. Chem.* **2005,** *117*, 3159-3163.

(374) Liu, F.; Zhang, S.; Jin, X.; Wang, W.; Tang, B. Thermal-Responsive Photonic Crystal with Function of Color Switch Based on Thermochromic System. *ACS Appl. Mater. Interfaces* **2019,** *11*, 39125-39131.

(375) Kubo, S.; Gu, Z.-Z.; Takahashi, K.; Fujishima, A.; Segawa, H.; Sato, O. Control of the optical properties of liquid crystal-infiltrated inverse opal structures using photo irradiation and/or an electric field. *Chem. Mater.* **2005,** *17*, 2298-2309.

(376) Kubo, S.; Gu, Z.-Z.; Takahashi, K.; Fujishima, A.; Segawa, H.; Sato, O. Tunable photonic band gap crystals based on a liquid crystal-infiltrated inverse opal structure. *J. Am. Chem. Soc.* **2004,** *126*, 8314-8319.

(377) Kubo, S.; Gu, Z.-Z.; Takahashi, K.; Ohko, Y.; Sato, O.; Fujishima, A. Control of the optical

band structure of liquid crystal infiltrated inverse opal by a photoinduced nematic–isotropic phase transition. *J. Am. Chem. Soc.* **2002,** *124*, 10950-10951.

(378) Zheng, H.; Ou, J. Z.; Strano, M. S.; Kaner, R. B.; Mitchell, A.; Kalantar‐zadeh, K. Nanostructured tungsten oxide – properties, synthesis, and applications. *Adv. Funct. Mater.* **2011,** *21*, 2175-2196.

(379) Niklasson, G. A.; Granqvist, C. G. Electrochromics for smart windows: thin films of tungsten oxide and nickel oxide, and devices based on these. *J. Mater. Chem.* **2007,** *17*, 127-156.

(380) Redel, E.; Mlynarski, J.; Moir, J.; Jelle, A.; Huai, C.; Petrov, S.; Helander, M. G.; Peiris, F. C.; von Freymann, G.; Ozin, G. A. Electrochromic bragg mirror: ECBM. *Adv. Mater.* **2012,** *24*, OP265-OP269.

(381) Shen, Y.; Zhou, J.; Liu, T.; Tao, Y.; Jiang, R.; Liu, M.; Xiao, G.; Zhu, J.; Zhou, Z.-K.; Wang, X. Plasmonic gold mushroom arrays with refractive index sensing figures of merit approaching the theoretical limit. *Nat. Commun.* **2013,** *4*, 2381.

(382) Nehl, C. L.; Liao, H.; Hafner, J. H. Optical properties of star-shaped gold nanoparticles. *Nano Lett.* **2006,** *6*, 683-688.

(383) Hao, F.; Nehl, C. L.; Hafner, J. H.; Nordlander, P. Plasmon resonances of a gold nanostar. *Nano Lett.* **2007,** *7*, 729-732.

(384) Prasad, J.; Zins, I.; Branscheid, R.; Becker, J.; Koch, A. H.; Fytas, G.; Kolb, U.; Sönnichsen, C. Plasmonic core–satellite assemblies as highly sensitive refractive index sensors. *J. Phys. Chem. C* **2015,** *119*, 5577-5582.

(385) Xiong, K.; Emilsson, G.; Maziz, A.; Yang, X.; Shao, L.; Jager, E. W.; Dahlin, A. B. Plasmonic metasurfaces with conjugated polymers for flexible electronic paper in color. *Adv. Mater.* **2016,** *28*, 9956-9960.

(386) Kim, S.; Cheng, N.; Jeong, J.-R.; Jang, S.-G.; Yang, S.-M.; Huck, W. T. Localized surface plasmon resonance (LSPR) sensitivity of Au nanodot patterns to probe solvation effects in polyelectrolyte brushes. *Chem. Commun.* **2008,** *3666*, 3666-3668.

(387) Gao, C.; Lu, Z.; Liu, Y.; Zhang, Q.; Chi, M.; Cheng, Q.; Yin, Y. Highly stable silver nanoplates for surface plasmon resonance biosensing. *Angew. Chem. Int. Ed.* **2012,** *51*, 5629-5633.

(388) Byers, C. P.; Zhang, H.; Swearer, D. F.; Yorulmaz, M.; Hoener, B. S.; Huang, D.; Hoggard, A.; Chang, W.-S.; Mulvaney, P.; Ringe, E. From tunable core-shell nanoparticles to plasmonic drawbridges: Active control of nanoparticle optical properties. *Sci. Adv.* **2015,** *1*, e1500988.

(389) Wijnhoven, J. E.; Zevenhuizen, S. J.; Hendriks, M. A.; Vanmaekelbergh, D.; Kelly, J. J.; Vos, W. L. Electrochemical assembly of ordered macropores in gold. *Adv. Mater.* **2000,** *12*, 888-890.

(390) Yan, H.; Blanford, C. F.; Holland, B. T.; Parent, M.; Smyrl, W. H.; Stein, A. A chemical synthesis of periodic macroporous NiO and metallic Ni. *Adv. Mater.* **1999,** *11*, 1003-1006.

(391) Yang, P.; Deng, T.; Zhao, D.; Feng, P.; Pine, D.; Chmelka, B. F.; Whitesides, G. M.; Stucky, G. D. Hierarchically ordered oxides. *Science* **1998,** *282*, 2244-2246.

(392) Blanco, A.; Chomski, E.; Grabtchak, S.; Ibisate, M.; John, S.; Leonard, S. W.; Lopez, C.; Meseguer, F.; Miguez, H.; Mondia, J. P. Large-scale synthesis of a silicon photonic crystal with a complete three-dimensional bandgap near 1.5 micrometres. *Nature* **2000,** *405*, 437-440.

(393) Park, S. H.; Xia, Y. Macroporous membranes with highly ordered and three‐dimensionally interconnected spherical pores. *Adv. Mater.* **1998,** *10*, 1045-1048.

(394) Johnson, S. A.; Ollivier, P. J.; Mallouk, T. E. Ordered mesoporous polymers of tunable pore size from colloidal silica templates. *Science* **1999,** *283*, 963-965.

(395) Wijnhoven, J. E.; Vos, W. L. Preparation of photonic crystals made of air spheres in titania. *Science* **1998,** *281*, 802-804.

(396) Zakhidov, A. A.; Baughman, R. H.; Iqbal, Z.; Cui, C.; Khayrullin, I.; Dantas, S. O.; Marti, J.; Ralchenko, V. G. Carbon structures with three-dimensional periodicity at optical wavelengths. *Science* **1998,** *282*, 897-901.

(397) Burgess, I. B.; Koay, N.; Raymond, K. P.; Kolle, M.; Lonˇcar, M.; Aizenberg, J. Wetting in color: colorimetric differentiation of organic liquids with high selectivity. *ACS nano* **2012,** *6*, 1427-1437.

(398) Burgess, I. B.; Mishchenko, L.; Hatton, B. D.; Kolle, M.; Loncar, M.; Aizenberg, J. Encoding complex wettability patterns in chemically functionalized 3D photonic crystals. *J. Am. Chem. Soc.* **2011,** *133*, 12430-12432.

(399) Liu, C.; Gao, G.; Zhang, Y.; Wang, L.; Wang, J.; Song, Y. The Naked‐Eye Detection of NH3‐HCl by Polyaniline‐Infiltrated TiO2 Inverse Opal Photonic Crystals. *Macromol. Rapid Commun.* **2012,** *33*, 380-385.

(400) Zhao, Y.; Zhao, X.; Tang, B.; Xu, W.; Li, J.; Hu, J.; Gu, Z. Quantum‐dot‐tagged bioresponsive hydrogel suspension array for multiplex label‐free DNA detection. *Adv. Funct. Mater.* **2010,** *20*, 976-982.

(401) Zhao, Y. J.; Zhao, X. W.; Hu, J.; Li, J.; Xu, W. Y.; Gu, Z. Z. Multiplex label‐free detection of biomolecules with an imprinted suspension array. *Angew. Chem. Int. Ed.* **2009,** *48*, 7350-7352.

(402) Khunsin, W.; Romanov, S. G.; Scharrer, M.; Aagesen, L. K.; Chang, R. P.; Torres, C. M. S. Chemosorption-related shift of a photonic bandgap in photoconductive ZnO inverse opal. *Opt. Lett.* **2008,** *33*, 461-463.

(403) Wu, Y. n.; Li, F.; Zhu, W.; Cui, J.; Tao, C. a.; Lin, C.; Hannam, P. M.; Li, G. Metal‐organic frameworks with a three‐dimensional ordered macroporous structure: dynamic photonic materials. *Angew. Chem.* **2011,** *123*, 12726-12730.

(404) Joshi, G. K.; Blodgett, K. N.; Muhoberac, B. B.; Johnson, M. A.; Smith, K. A.; Sardar, R. Ultrasensitive photoreversible molecular sensors of azobenzene-functionalized plasmonic nanoantennas. *Nano Lett.* **2014,** *14*, 532-540.

(405) Pardo, R.; Zayat, M.; Levy, D. Photochromic organic–inorganic hybrid materials. *Chem. Soc. Rev.* **2011,** *40*, 672-687.

(406) Ming, T.; Zhao, L.; Xiao, M.; Wang, J. Resonance‐Coupling‐Based Plasmonic Switches. *small* **2010,** *6*, 2514-2519.

(407) Okamoto, T.; Kamiyama, T.; Yamaguchi, I. All-optical spatial light modulator with surface plasmon resonance. *Opt. Lett.* **1993,** *18*, 1570-1572.

(408) Sasaki, K.; Nagamura, T. Ultrafast all-optical switch using complex refractive index changes of thin films containing photochromic dye. *Appl. Phys. Lett.* **1997,** *71*, 434-436.

(409) Khutoryanskiy, V.; Georgiou, T. *Temperature-Responsive Polymers*; Wiley Online Library, 2018, 1-408.

(410) De las Heras Alarcón, C.; Pennadam, S.; Alexander, C. Stimuli responsive polymers for biomedical applications. *Chem. Soc. Rev.* **2005,** *34*, 276-285.

(411) Lanzalaco, S.; Armelin, E. Poly (N-isopropylacrylamide) and copolymers: a review on recent progresses in biomedical applications. *Gels* **2017,** *3*, 36.

(412) Flory, P. J. Thermodynamics of high polymer solutions. *J. Chem. Phys.* **1942,** *10*, 51-61.

(413) Tao, H.; Galati, E.; Kumacheva, E. Temperature-Responsive Self-Assembly of Nanoparticles Grafted with UCST Polymer Ligands. *Macromolecules* **2018,** *51*, 6021-6027.

(414) Kaiser, A.; Schmidt, A. M. Phase behavior of polystyrene-brush-coated nanoparticles in cyclohexane. *J. Phys. Chem. B* **2008,** *112*, 1894-1898.

(415) Seuring, J.; Bayer, F. M.; Huber, K.; Agarwal, S. Upper critical solution temperature of poly (N-acryloyl glycinamide) in water: a concealed property. *Macromolecules* **2012,** *45*, 374-384.

(416) Fu, W.; Luo, C.; Morin, E. A.; He, W.; Li, Z.; Zhao, B. UCST-type thermosensitive hairy nanogels synthesized by RAFT polymerization-induced self-assembly. *ACS Macro Lett.* **2017,** *6*, 127-133.

(417) Haas, H. C.; Schuler, N. W. Thermally reversible homopolymer gel systems. *J. Polym. Sci. B: Polym. Phys.* **1964,** *2*, 1095-1096.

(418) Haas, H. C.; Chiklis, C. K.; Moreau, R. D. Synthetic thermally reversible gel systems. III. *J. Polym. Sci. A Polym. Chem.* **1970,** *8*, 1131-1145.

(419) Xu, Z.; Liu, W. Poly (N-acryloyl glycinamide): a fascinating polymer that exhibits a range of properties from UCST to high-strength hydrogels. *Chem. Commun.* **2018,** *54*, 10540-10553.

(420) Chen, M.; Zhou, L.; Guan, Y.; Zhang, Y. Polymerized microgel colloidal crystals: photonic hydrogels with tunable band gaps and fast response rates. *Angew. Chem. Int. Ed.* **2013,** *52*, 9961-9965.

(421) Debord, J. D.; Lyon, L. A. Thermoresponsive photonic crystals. *J. Phys. Chem. B* **2000,** *104*, 6327-6331.
(422) Matsubara, K.; Watanabe, M.; Takeoka, Y. A thermally adjustable multicolor photochromic hydrogel. *Angew. Chem.* **2007,** *119*, 1718-1722.
(423) Kumoda, M.; Watanabe, M.; Takeoka, Y. Preparations and optical properties of ordered arrays of submicron gel particles: interconnected state and trapped state. *Langmuir* **2006,** *22*, 4403-4407.
(424) Ueno, K.; Matsubara, K.; Watanabe, M.; Takeoka, Y. An electro‐and thermochromic hydrogel as a full‐color indicator. *Adv. Mater.* **2007,** *19*, 2807-2812.
(425) Hu, Z.; Lu, X.; Gao, J. Hydrogel opals. *Adv. Mater.* **2001,** *13*, 1708-1712.
(426) Luo, W.; Yan, J.; Tan, Y.; Ma, H.; Guan, J. Rotating 1-D magnetic photonic crystal balls with a tunable lattice constant. *Nanoscale* **2017,** *9*, 9548-9555.
(427) Shang, S.; Zhu, P.; Wang, H.; Li, Y.; Yang, S. Thermally Responsive Photonic Fibers Consisting of Chained Nanoparticles. *ACS Appl. Mater. Interfaces* **2020,** *12*, 50844-50851.
(428) van Heeswijk, E. P.; Meerman, T.; de Heer, J.; Grossiord, N.; Schenning, A. P. Paintable encapsulated body-temperature-responsive photonic reflectors with arbitrary shapes. *ACS Appl. Polym. Mater.* **2019,** *1*, 3407-3412.
(429) Xing, H.; Li, J.; Shi, Y.; Guo, J.; Wei, J. Thermally driven photonic actuator based on silica opal photonic crystal with liquid crystal elastomer. *ACS Appl. Mater. Interfaces* **2016,** *8*, 9440-9445.
(430) Shi, Y.; Zhu, C.; Li, J.; Wei, J.; Guo, J. A color-changing plasmonic actuator based on silver nanoparticle array/liquid crystalline elastomer nanocomposites. *New J. Chem.* **2016,** *40*, 7311-7319.
(431) Wang, Y.; Chen, G.; Yang, M.; Silber, G.; Xing, S.; Tan, L. H.; Wang, F.; Feng, Y.; Liu, X.; Li, S. A systems approach towards the stoichiometry-controlled hetero-assembly of nanoparticles. *Nat. Commun.* **2010,** *1*, 87.
(432) Han, B.; Zhang, Y. L.; Chen, Q. D.; Sun, H. B. Carbon‐Based Photothermal Actuators. *Adv. Funct. Mater.* **2018,** *28*, 1802235.
(433) Yang, Y.; Liu, Y.; Shen, Y. Plasmonic‐Assisted Graphene Oxide Films with Enhanced Photothermal Actuation for Soft Robots. *Adv. Funct. Mater.* **2020,** *30*, 1910172.
(434) Shen, X.; Viney, C.; Johnson, E. R.; Wang, C.; Lu, J. Q. Large negative thermal expansion of a polymer driven by a submolecular conformational change. *Nat. Chem.* **2013,** *5*, 1035-1041.
(435) Mukherjee, M.; Bhattacharya, M.; Sanyal, M.; Geue, T.; Grenzer, J.; Pietsch, U. Reversible negative thermal expansion of polymer films. *Phys. Rev. E* **2002,** *66*, 061801.
(436) Liu, Z.; Gao, Q.; Chen, J.; Deng, J.; Lin, K.; Xing, X. Negative thermal expansion in molecular materials. *Chem. Commun.* **2018,** *54*, 5164-5176.
(437) Mu, J.; Hou, C.; Wang, H.; Li, Y.; Zhang, Q.; Zhu, M. Origami-inspired active graphene-based paper for programmable instant self-folding walking devices. *Sci. Adv.* **2015,** *1*, e1500533.
(438) Shi, Q.; Li, J.; Hou, C.; Shao, Y.; Zhang, Q.; Li, Y.; Wang, H. A remote controllable fiber-type near-infrared light-responsive actuator. *Chem. Commun.* **2017,** *53*, 11118-11121.
(439) Cai, G.; Ciou, J.-H.; Liu, Y.; Jiang, Y.; Lee, P. S. Leaf-inspired multiresponsive MXene-based actuator for programmable smart devices. *Sci. Adv.* **2019,** *5*, eaaw7956.
(440) Ube, T.; Ikeda, T. Photomobile Polymer Materials with Complex 3D Deformation, Continuous Motions, Self‐Regulation, and Enhanced Processability. *Adv. Opt. Mater.* **2019,** *7*, 1900380.
(441) Tong, F.; Li, W.; Li, Z.; Islam, I.; Al‐Kaysi, R. O.; Bardeen, C. J. Molecular Crystal Microcapsules: Formation of Sealed Hollow Chambers via Surfactant‐Mediated Growth. *Angew. Chem.* **2020,** *132*, 23235-23239.
(442) Bisoyi, H. K.; Li, Q. Light-driven liquid crystalline materials: from photo-induced phase transitions and property modulations to applications. *Chem. Rev.* **2016,** *116*, 15089-15166.
(443) Yu, Y.; Nakano, M.; Ikeda, T. Directed bending of a polymer film by light. *Nature* **2003,** *425*, 145-145.
(444) Ercole, F.; Davis, T. P.; Evans, R. A. Photo-responsive systems and biomaterials: photochromic polymers, light-triggered self-

assembly, surface modification, fluorescence modulation and beyond. *Polym. Chem.* **2010,** *1*, 37-54.

(445) Yu, Y.; Ikeda, T. Alignment modulation of azobenzene-containing liquid crystal systems by photochemical reactions. *J. Photochem. Photobiol. C: Photochem. Rev.* **2004,** *5*, 247-265.

(446) Küpfer, J.; Finkelmann, H. Nematic liquid single crystal elastomers. *Makromol. Chem. Rapid Comm.* **1991,** *12*, 717-726.

(447) Broer, D. J.; Finkelmann, H.; Kondo, K. In‐situ photopolymerization of an oriented liquid‐crystalline acrylate. *Macromol. Chem. Phys.* **1988,** *189*, 185-194.

(448) Broer, D. J.; Boven, J.; Mol, G. N.; Challa, G. In‐situ photopolymerization of oriented liquid‐crystalline acrylates, 3. Oriented polymer networks from a mesogenic diacrylate. *Macromol. Chem. Phys.* **1989,** *190*, 2255-2268.

(449) Broer, D.; Gossink, R.; Hikmet, R. Oriented polymer networks obtained by photopolymerization of liquid‐crystalline monomers. *Angew. Makromolek. Chem.* **1990,** *183*, 45-66.

(450) Yang, Y.; Pei, Z.; Li, Z.; Wei, Y.; Ji, Y. Making and remaking dynamic 3D structures by shining light on flat liquid crystalline vitrimer films without a mold. *J. Am. Chem. Soc.* **2016,** *138*, 2118-2121.

(451) Lu, X.; Zhang, H.; Fei, G.; Yu, B.; Tong, X.; Xia, H.; Zhao, Y. Liquid‐crystalline dynamic networks doped with gold nanorods showing enhanced photocontrol of actuation. *Adv. Mater.* **2018,** *30*, 1706597.

(452) Hu, Y.; Li, Z.; Lan, T.; Chen, W. Photoactuators for direct optical‐to‐mechanical energy conversion: from nanocomponent assembly to macroscopic deformation. *Adv. Mater.* **2016,** *28*, 10548-10556.

(453) Wang, Y.; Dang, A.; Zhang, Z.; Yin, R.; Gao, Y.; Feng, L.; Yang, S. Repeatable and Reprogrammable Shape Morphing from Photoresponsive Gold Nanorod/Liquid Crystal Elastomers. *Adv. Mater.* **2020,** *32*, 2004270.

(454) Tong, F.; Chen, S.; Li, Z.; Liu, M.; Al‐Kaysi, R. O.; Mohideen, U.; Yin, Y.; Bardeen, C. J. Crystal‐to‐Gel Transformation Stimulated by a Solid‐State E→Z Photoisomerization. *Angew. Chem.* **2019,** *131*, 15575-15580.

(455) Kitagawa, D.; Nishi, H.; Kobatake, S. Photoinduced twisting of a photochromic diarylethene crystal. *Angew. Chem.* **2013,** *125*, 9490-9492.

(456) Fukaminato, T.; Ishida, S.; Métivier, R. Photochromic fluorophores at the molecular and nanoparticle levels: fundamentals and applications of diarylethenes. *NPG Asia Mater.* **2018,** *10*, 859-881.

(457) Zhu, M.; Zhou, H. Azobenzene-based small molecular photoswitches for protein modulation. *Org. Biomol. Chem.* **2018,** *16*, 8434-8445.

(458) Bandara, H. D.; Burdette, S. C. Photoisomerization in different classes of azobenzene. *Chem. Soc. Rev.* **2012,** *41*, 1809-1825.

(459) Pang, X.; Lv, J. a.; Zhu, C.; Qin, L.; Yu, Y. Photodeformable Azobenzene‐Containing Liquid Crystal Polymers and Soft Actuators. *Adv. Mater.* **2019,** *31*, 1904224.

(460) Kumar, G. S.; Neckers, D. Photochemistry of azobenzene-containing polymers. *Chem. Rev.* **1989,** *89*, 1915-1925.

(461) Griffiths, J. II. Photochemistry of azobenzene and its derivatives. *Chem. Soc. Rev.* **1972,** *1*, 481-493.

(462) Beharry, A. A.; Woolley, G. A. Azobenzene photoswitches for biomolecules. *Chem. Soc. Rev.* **2011,** *40*, 4422-4437.

(463) Zhu, J.; Lin, H.; Kim, Y.; Yang, M.; Skakuj, K.; Du, J. S.; Lee, B.; Schatz, G. C.; Van Duyne, R. P.; Mirkin, C. A. Light‐Responsive Colloidal Crystals Engineered with DNA. *Adv. Mater.* **2020,** *32*, 1906600.

(464) Ueno, K.; Sakamoto, J.; Takeoka, Y.; Watanabe, M. Electrochromism based on structural colour changes in a polyelectrolyte gel. *J. Mater. Chem.* **2009,** *19*, 4778-4783.

(465) Hong, W.; Hu, X.; Zhao, B.; Zhang, F.; Zhang, D. Tunable photonic polyelectrolyte colorimetric sensing for anions, cations and zwitterions. *Adv. Mater.* **2010,** *22*, 5043-5047.

(466) Wang, D.; Caruso, F. Lithium Niobate Inverse Opals Prepared by Templating Colloidal Crystals of Polyelectrolyte‐Coated Spheres. *Adv. Mater.* **2003,** *15*, 205-210.

(467) Hong, W.; Li, W.; Hu, X.; Zhao, B.; Zhang, F.; Zhang, D. Highly sensitive colorimetric sensing for heavy metal ions by strong polyelectrolyte photonic hydrogels. *J. Mater. Chem.* **2011,** *21*, 17193-17201.

(468) Xia, J.; Ying, Y.; Foulger, S. H. Electric‐Field‐Induced Rejection‐Wavelength Tuning of Photonic‐Bandgap Composites. *Adv. Mater.* **2005,** *17*, 2463-2467.

(469) Foulger, S. H.; Jiang, P.; Ying, Y.; Lattam, A. C.; Smith Jr, D. W.; Ballato, J. Photonic bandgap composites. *Adv. Mater.* **2001,** *13*, 1898-1901.

(470) Jiang, Y.; Xu, D.; Li, X.; Lin, C.; Li, W.; An, Q.; Tao, C.-a.; Tang, H.; Li, G. Electrothermally driven structural colour based on liquid crystal elastomers. *J. Mater. Chem.* **2012,** *22*, 11943-11949.

(471) Gallei, M.; Rüttiger, C. Recent Trends in Metallopolymer Design: Redox‐Controlled Surfaces, Porous Membranes, and Switchable Optical Materials Using Ferrocene‐Containing Polymers. *Chem. Eur. J* **2018,** *24*, 10006-10021.

(472) Arsenault, A. C.; Puzzo, D. P.; Manners, I.; Ozin, G. A. Photonic-crystal full-colour displays. *Nat. Photonics* **2007,** *1*, 468-472.

(473) Puzzo, D. P.; Arsenault, A. C.; Manners, I.; Ozin, G. A. Electroactive inverse opal: a single material for all colors. *Angew. Chem.* **2009,** *121*, 961-965.

(474) Walish, J. J.; Kang, Y.; Mickiewicz, R. A.; Thomas, E. L. Bioinspired electrochemically tunable block copolymer full color pixels. *Adv. Mater.* **2009,** *21*, 3078-3081.

(475) Lu, Y.; Meng, C.; Xia, H.; Zhang, G.; Wu, C. Fast electrically driven photonic crystal based on charged block copolymer. *J. Mater. Chem. C* **2013,** *1*, 6107-6111.

(476) Lu, Y.; Xia, H.; Zhang, G.; Wu, C. Electrically tunable block copolymer photonic crystals with a full color display. *J. Mater. Chem.* **2009,** *19*, 5952-5955.

(477) Hwang, K.; Kwak, D.; Kang, C.; Kim, D.; Ahn, Y.; Kang, Y. Electrically tunable hysteretic photonic gels for nonvolatile display pixels. *Angew. Chem.* **2011,** *123*, 6435-6438.

(478) Norton, J.; Han, M. G.; Jiang, P.; Creager, S.; Foulger, S. H. Electrochemical tuning the optical properties of crystalline colloidal arrays composed of poly (3, 4-ethylenedioxythiophene) coated silica particles. *J. Mater. Chem.* **2007,** *17*, 1149-1153.

(479) Norton, J. C. S.; Han, M. G.; Creager, S.; Foulger, S. H. Electrochemical redox of pedot-coated core-shell silica spheres stabilized in a peg-based hydrogel maxtrix: Modulation of the optical properties by doping with various oxidative mediators. *Int. J. Electrochem. Sci* **2012,** *7*, 3627-3637.

(480) Wang, D.; Li, Z.; Zhou, J.; Fang, H.; He, X.; Jena, P.; Zeng, J.-B.; Wang, W.-N. Simultaneous detection and removal of formaldehyde at room temperature: Janus Au@ ZnO@ ZIF-8 nanoparticles. *Nano-Micro Lett.* **2018,** *10*, 1-11.

(481) Fenzl, C.; Hirsch, T.; Wolfbeis, O. S. Photonic crystals for chemical sensing and biosensing. *Angew. Chem. Int. Ed.* **2014,** *53*, 3318-3335.

(482) Stewart, M. E.; Anderton, C. R.; Thompson, L. B.; Maria, J.; Gray, S. K.; Rogers, J. A.; Nuzzo, R. G. Nanostructured plasmonic sensors. *Chem. Rev.* **2008,** *108*, 494-521.

(483) Tittl, A.; Giessen, H.; Liu, N. Plasmonic gas and chemical sensing. *Nanophotonics* **2014,** *3*, 157-180.

(484) Fudouzi, H.; Xia, Y. Colloidal crystals with tunable colors and their use as photonic papers. *Langmuir* **2003,** *19*, 9653-9660.

(485) Fudouzi, H.; Xia, Y. Photonic papers and inks: color writing with colorless materials. *Adv. Mater.* **2003,** *15*, 892-896.

(486) Fenzl, C.; Hirsch, T.; Wolfbeis, O. S. Photonic crystal based sensor for organic solvents and for solvent-water mixtures. *Sensors* **2012,** *12*, 16954-16963.

(487) Endo, T.; Yanagida, Y.; Hatsuzawa, T. Colorimetric detection of volatile organic compounds using a colloidal crystal-based chemical sensor for environmental applications. *Sens. Actuators B Chem.* **2007,** *125*, 589-595.

(488) Pan, Z.; Ma, J.; Yan, J.; Zhou, M.; Gao, J. Response of inverse-opal hydrogels to alcohols. *J. Mater. Chem.* **2012,** *22*, 2018-2025.

(489) Wang, Z.; Zhang, J.; Li, J.; Xie, J.; Li, Y.; Liang, S.; Tian, Z.; Li, C.; Wang, Z.; Wang, T. Colorful detection of organic solvents based on responsive organic/inorganic hybrid one-

dimensional photonic crystals. *J. Mater. Chem.* **2011,** *21*, 1264-1270.

(490) Zhang, Y.; Qiu, J.; Gao, M.; Li, P.; Gao, L.; Heng, L.; Tang, B. Z.; Jiang, L. A visual film sensor based on silole-infiltrated SiO 2 inverse opal photonic crystal for detecting organic vapors. *J. Mater. Chem. C* **2014,** *2*, 8865-8872.

(491) Hu, Z.; Tao, C.-a.; Liu, H.; Zou, X.; Zhu, H.; Wang, J. Fabrication of an NH 2-MIL-88B photonic film for naked-eye sensing of organic vapors. *J. Mater. Chem. A* **2014,** *2*, 14222-14227.

(492) English, A. E.; Tanaka, T.; Edelman, E. R. Equilibrium and non-equilibrium phase transitions in copolymer polyelectrolyte hydrogels. *J. Chem. Phys.* **1997,** *107*, 1645-1654.

(493) English, A. E.; Tanaka, T.; Edelman, E. R. Polymer and solution ion shielding in polyampholytic hydrogels. *Polymer* **1998,** *39*, 5893-5897.

(494) Mafé, S.; Manzanares, J. A.; English, A. E.; Tanaka, T. Multiple phases in ionic copolymer gels. *Phys. Rev. Lett.* **1997,** *79*, 3086.

(495) Annaka, M.; Tanaka, T. Multiple phases of polymer gels. *Nature* **1992,** *355*, 430-432.

(496) Lee, K.; Asher, S. A. Photonic crystal chemical sensors: pH and ionic strength. *J. Am. Chem. Soc.* **2000,** *122*, 9534-9537.

(497) Fenzl, C.; Wilhelm, S.; Hirsch, T.; Wolfbeis, O. S. Optical sensing of the ionic strength using photonic crystals in a hydrogel matrix. *ACS Appl. Mater. Interfaces* **2013,** *5*, 173-178.

(498) Li, C.; Lotsch, B. V. Stimuli-responsive 2D polyelectrolyte photonic crystals for optically encoded pH sensing. *Chem. Commun.* **2012,** *48*, 6169-6171.

(499) Zhang, J.-T.; Wang, L.; Luo, J.; Tikhonov, A.; Kornienko, N.; Asher, S. A. 2-D array photonic crystal sensing motif. *J. Am. Chem. Soc.* **2011,** *133*, 9152-9155.

(500) Asher, S. A.; Kimble, K. W.; Walker, J. P. Enabling thermoreversible physically cross-linked polymerized colloidal array photonic crystals. *Chem. Mater.* **2008,** *20*, 7501-7509.

(501) Xu, X.; Goponenko, A. V.; Asher, S. A. Polymerized polyHEMA photonic crystals: pH and ethanol sensor materials. *J. Am. Chem. Soc.* **2008,** *130*, 3113-3119.

(502) Yang, Q.; Zhu, S.; Peng, W.; Yin, C.; Wang, W.; Gu, J.; Zhang, W.; Ma, J.; Deng, T.; Feng, C. Bioinspired fabrication of hierarchically structured, pH-tunable photonic crystals with unique transition. *Acs Nano* **2013,** *7*, 4911-4918.

(503) Saito, H.; Takeoka, Y.; Watanabe, M. Simple and precision design of porous gel as a visible indicator for ionic species and concentration. *Chem. Commun.* **2003**, 2126-2127.

(504) Holtz, J. H.; Asher, S. A. Polymerized colloidal crystal hydrogel films as intelligent chemical sensing materials. *Nature* **1997,** *389*, 829-832.

(505) Goponenko, A. V.; Asher, S. A. Modeling of stimulated hydrogel volume changes in photonic crystal Pb2+ sensing materials. *J. Am. Chem. Soc.* **2005,** *127*, 10753-10759.

(506) Muscatello, M. M. W.; Asher, S. A. Poly (vinyl alcohol) rehydratable photonic crystal sensor materials. *Adv. Funct. Mater.* **2008,** *18*, 1186-1193.

(507) Hu, X.; Huang, J.; Zhang, W.; Li, M.; Tao, C.; Li, G. Photonic Ionic Liquids Polymer for Naked‐Eye Detection of Anions. *Adv. Mater.* **2008,** *20*, 4074-4078.

(508) Ma, C.; Jiang, Y.; Yang, X.; Wang, C.; Li, H.; Dong, F.; Yang, B.; Yu, K.; Lin, Q. Centrifugation-induced water-tunable photonic colloidal crystals with narrow diffraction bandwidth and highly sensitive detection of SCN–. *ACS Appl. Mater. Interfaces* **2013,** *5*, 1990-1996.

(509) Hu, X.; Li, G.; Huang, J.; Zhang, D.; Qiu, Y. Construction of Self‐Reporting Specific Chemical Sensors with High Sensitivity. *Adv. Mater.* **2007,** *19*, 4327-4332.

(510) Li, J.; Zhang, Z.; Xu, S.; Chen, L.; Zhou, N.; Xiong, H.; Peng, H. Label-free colorimetric detection of trace cholesterol based on molecularly imprinted photonic hydrogels. *J. Mater. Chem.* **2011,** *21*, 19267-19274.

(511) Zhang, Y.-X.; Zhao, P.-Y.; Yu, L.-P. Highly-sensitive and selective colorimetric sensor for amino acids chiral recognition based on molecularly imprinted photonic polymers. *Sens. Actuators B Chem.* **2013,** *181*, 850-857.

(512) Guo, C.; Zhou, C.; Sai, N.; Ning, B.; Liu, M.; Chen, H.; Gao, Z. Detection of bisphenol A using an opal photonic crystal sensor. *Sens. Actuators B Chem.* **2012,** *166*, 17-23.

(513) Peng, H.; Wang, S.; Zhang, Z.; Xiong, H.; Li, J.; Chen, L.; Li, Y. Molecularly imprinted photonic hydrogels as colorimetric sensors for rapid and label-free detection of vanillin. *J. Agric. Food. Chem.* **2012,** *60*, 1921-1928.

(514) Ayyub, O. B.; Ibrahim, M. B.; Briber, R. M.; Kofinas, P. Self-assembled block copolymer photonic crystal for selective fructose detection. *Biosens. Bioelectron.* **2013,** *46*, 124-129.

(515) Holtz, J. H.; Holtz, J. S.; Munro, C. H.; Asher, S. A. Intelligent polymerized crystalline colloidal arrays: novel chemical sensor materials. *Anal. Chem.* **1998,** *70*, 780-791.

(516) Asher, S. A.; Alexeev, V. L.; Goponenko, A. V.; Sharma, A. C.; Lednev, I. K.; Wilcox, C. S.; Finegold, D. N. Photonic crystal carbohydrate sensors: low ionic strength sugar sensing. *J. Am. Chem. Soc.* **2003,** *125*, 3322-3329.

(517) Alexeev, V. L.; DAs, S.; Finegold, D. N.; AsHER, S. A. Photonic crystal glucose-sensing material for noninvasive monitoring of glucose in tear fluid. *Clin. Chem.* **2004,** *50*, 2353-2360.

(518) Alexeev, V. L.; Sharma, A. C.; Goponenko, A. V.; Das, S.; Lednev, I. K.; Wilcox, C. S.; Finegold, D. N.; Asher, S. A. High ionic strength glucose-sensing photonic crystal. *Anal. Chem.* **2003,** *75*, 2316-2323.

(519) Ben-Moshe, M.; Alexeev, V. L.; Asher, S. A. Fast responsive crystalline colloidal array photonic crystal glucose sensors. *Anal. Chem.* **2006,** *78*, 5149-5157.

(520) Sharma, A. C.; Jana, T.; Kesavamoorthy, R.; Shi, L.; Virji, M. A.; Finegold, D. N.; Asher, S. A. A general photonic crystal sensing motif: creatinine in bodily fluids. *J. Am. Chem. Soc.* **2004,** *126*, 2971-2977.

(521) Maurer, M. K.; Gould, S. E.; Scott, P. J. Cholesterol oxidase functionalization of a polymerized crystalline colloidal array. *Sens. Actuators B Chem.* **2008,** *134*, 736-742.

(522) Konopsky, V. N.; Alieva, E. V. Photonic crystal surface waves for optical biosensors. *Anal. Chem.* **2007,** *79*, 4729-4735.

(523) Li, M.; He, F.; Liao, Q.; Liu, J.; Xu, L.; Jiang, L.; Song, Y.; Wang, S.; Zhu, D. Ultrasensitive DNA detection using photonic crystals. *Angew. Chem.* **2008,** *120*, 7368-7372.

(524) Park, T. J.; Lee, S.-K.; Yoo, S. M.; Yang, S.-M.; Lee, S. Y. Development of reflective biosensor using fabrication of functionalized photonic nanocrystals. *J. Nanosci. Nanotechnol.* **2011,** *11*, 632-637.

(525) Fleischhaker, F.; Arsenault, A. C.; Peiris, F. C.; Kitaev, V.; Manners, I.; Zentel, R.; Ozin, G. A. DNA designer defects in photonic crystals: optically monitored biochemistry. *Adv. Mater.* **2006,** *18*, 2387-2391.

(526) Tokarev, I.; Minko, S. Tunable plasmonic nanostructures from noble metal nanoparticles and stimuli-responsive polymers. *Soft Matter* **2012,** *8*, 5980-5987.

(527) Pastoriza-Santos, I.; Kinnear, C.; Pérez-Juste, J.; Mulvaney, P.; Liz-Marzán, L. M. Plasmonic polymer nanocomposites. *Nat. Rev. Mater.* **2018,** *3*, 375-391.

(528) Tokareva, I.; Minko, S.; Fendler, J. H.; Hutter, E. Nanosensors based on responsive polymer brushes and gold nanoparticle enhanced transmission surface plasmon resonance spectroscopy. *J. Am. Chem. Soc.* **2004,** *126*, 15950-15951.

(529) Harimech, P. K.; Gerrard, S. R.; El-Sagheer, A. H.; Brown, T.; Kanaras, A. G. Reversible ligation of programmed DNA-gold nanoparticle assemblies. *J. Am. Chem. Soc.* **2015,** *137*, 9242-9245.

(530) Liu, D.; Fang, L.; Zhou, F.; Li, H.; Zhang, T.; Li, C.; Cai, W.; Deng, Z.; Li, L.; Li, Y. Ultrasensitive and Stable Au Dimer‐Based Colorimetric Sensors Using the Dynamically Tunable Gap‐Dependent Plasmonic Coupling Optical Properties. *Adv. Funct. Mater.* **2018,** *28*, 1707392.

(531) Shen, J.; Luan, B.; Pei, H.; Yang, Z.; Zuo, X.; Liu, G.; Shi, J.; Wang, L.; Zhou, R.; Cheng, W. Humidity‐Responsive Single‐Nanoparticle‐Layer Plasmonic Films. *Adv. Mater.* **2017,** *29*, 1606796.

(532) Kunstmann-Olsen, C.; Belić, D.; Bradley, D. F.; Grzelczak, M. P.; Brust, M. Humidity-dependent reversible transitions in gold nanoparticle superlattices. *Chem. Mater.* **2016,** *28*, 2970-2980.

(533) Endo, T.; Ikeda, R.; Yanagida, Y.; Hatsuzawa, T. Stimuli-responsive hydrogel–silver nanoparticles composite for development of localized surface plasmon resonance-based optical biosensor. *Anal. Chim. Acta* **2008,** *611*, 205-211.

(534) Liu, L.; Aleisa, R.; Zhang, Y.; Feng, J.; Zheng, Y.; Yin, Y.; Wang, W. Dynamic Color‐Switching of Plasmonic Nanoparticle Films. *Angew. Chem.* **2019,** *131*, 16453-16459.

(535) Vindevogel, J.; Sandra, P. Simultaneous pH and ionic strength effects and buffer selection in capillary electrophoretic techniques. *J. Chromatogr. A* **1991,** *541*, 483-488.

(536) Weidman, J. L.; Mulvenna, R. A.; Boudouris, B. W.; Phillip, W. A. Unusually stable hysteresis in the pH-response of poly (acrylic acid) brushes confined within nanoporous block polymer thin films. *J. Am. Chem. Soc.* **2016,** *138*, 7030-7039.

(537) Clough, J. M.; Weder, C.; Schrettl, S. Mechanochromism in Structurally Colored Polymeric Materials. *Macromol. Rapid Commun.* **2021,** *42*, 2000528.

(538) Kang, Y.; Walish, J. J.; Gorishnyy, T.; Thomas, E. L. Broad-wavelength-range chemically tunable block-copolymer photonic gels. *Nat. Mater.* **2007,** *6*, 957-960.

(539) Chan, E. P.; Walish, J. J.; Thomas, E. L.; Stafford, C. M. Block copolymer photonic gel for mechanochromic sensing. *Adv. Mater.* **2011,** *23*, 4702-4706.

(540) Yang, Y.; Kim, H.; Xu, J.; Hwang, M. S.; Tian, D.; Wang, K.; Zhang, L.; Liao, Y.; Park, H. G.; Yi, G. R. Responsive block copolymer photonic microspheres. *Adv. Mater.* **2018,** *30*, 1707344.

(541) Park, T. H.; Yu, S.; Cho, S. H.; Kang, H. S.; Kim, Y.; Kim, M. J.; Eoh, H.; Park, C.; Jeong, B.; Lee, S. W. Block copolymer structural color strain sensor. *NPG Asia Mater.* **2018,** *10*, 328-339.

(542) Kazmierczak, T.; Song, H.; Hiltner, A.; Baer, E. Polymeric one‐dimensional photonic crystals by continuous coextrusion. *Macromol. Rapid Commun.* **2007,** *28*, 2210-2216.

(543) Kolle, M.; Lethbridge, A.; Kreysing, M.; Baumberg, J. J.; Aizenberg, J.; Vukusic, P. Bio‐inspired band‐gap tunable elastic optical multilayer fibers. *Adv. Mater.* **2013,** *25*, 2239-2245.

(544) Haque, M. A.; Kurokawa, T.; Kamita, G.; Gong, J. P. Lamellar bilayers as reversible sacrificial bonds to toughen hydrogel: hysteresis, self-recovery, fatigue resistance, and crack blunting. *Macromolecules* **2011,** *44*, 8916-8924.

(545) Yang, D.; Ye, S.; Ge, J. From metastable colloidal crystalline arrays to fast responsive mechanochromic photonic gels: An organic gel for deformation‐based display panels. *Adv. Funct. Mater.* **2014,** *24*, 3197-3205.

(546) Chan, E. P.; Walish, J. J.; Urbas, A. M.; Thomas, E. L. Mechanochromic photonic gels. *Adv. Mater.* **2013,** *25*, 3934-3947.

(547) Han, X.; Liu, Y.; Yin, Y. Colorimetric stress memory sensor based on disassembly of gold nanoparticle chains. *Nano Lett.* **2014,** *14*, 2466-2470.

(548) Yu, Y.; Fu, F.; Shang, L.; Cheng, Y.; Gu, Z.; Zhao, Y. Bioinspired helical microfibers from microfluidics. *Adv. Mater.* **2017,** *29*, 1605765.

(549) Zhang, Y. S.; Aleman, J.; Shin, S. R.; Kilic, T.; Kim, D.; Shaegh, S. A. M.; Massa, S.; Riahi, R.; Chae, S.; Hu, N. Multisensor-integrated organs-on-chips platform for automated and continual in situ monitoring of organoid behaviors. *Proc. Natl. Acad. Sci. U.S.A.* **2017,** *114*, E2293-E2302.

(550) Fu, F.; Shang, L.; Chen, Z.; Yu, Y.; Zhao, Y. Bioinspired living structural color hydrogels. *Sci. Robot.* **2018,** *3*, eaar8580.

(551) Wang, H.; Liu, Y.; Chen, Z.; Sun, L.; Zhao, Y. Anisotropic structural color particles from colloidal phase separation. *Sci. Adv.* **2020,** *6*, eaay1438.

(552) Shang, L.; Shao, C.; Chi, J.; Zhao, Y. Living Materials for Life Healthcare. *Acc. Mater. Res.* **2020,** *2*, 59-70.

(553) Wang, Y.; Shang, L.; Chen, G.; Sun, L.; Zhang, X.; Zhao, Y. Bioinspired structural color patch with anisotropic surface adhesion. *Sci. Adv.* **2020,** *6*, eaax8258.

(554) Li, Y.; Jiang, X.; Fu, Z.; Huang, Q.; Wang, G.-E.; Deng, W.-H.; Wang, C.; Li, Z.; Yin, W.; Chen, B. Coordination assembly of 2D ordered organic metal chalcogenides with widely tunable electronic band gaps. *Nat. Commun.* **2020,** *11*, 261.

(555) Liu, L.; Bisri, S. Z.; Ishida, Y.; Aida, T.; Iwasa, Y. Tunable electronic properties by ligand coverage control in PbS nanocrystal assemblies. *Nanoscale* **2019,** *11*, 20467-20474.

(556) Zherebetskyy, D.; Scheele, M.; Zhang, Y.; Bronstein, N.; Thompson, C.; Britt, D.; Salmeron, M.; Alivisatos, P.; Wang, L.-W. Hydroxylation of the surface of PbS

nanocrystals passivated with oleic acid. *Science* **2014,** *344*, 1380-1384.

(557) Van Overbeek, C.; Peters, J. L.; Van Rossum, S. A.; Smits, M.; Van Huis, M. A.; Vanmaekelbergh, D. Interfacial self-assembly and oriented attachment in the family of PbX (X= S, Se, Te) nanocrystals. *J. Phys. Chem. C* **2018,** *122*, 12464-12473.

(558) Gu, X. W.; Ye, X.; Koshy, D. M.; Vachhani, S.; Hosemann, P.; Alivisatos, A. P. Tolerance to structural disorder and tunable mechanical behavior in self-assembled superlattices of polymer-grafted nanocrystals. *Proc. Natl. Acad. Sci. U.S.A.* **2017,** *114*, 2836-2841.

(559) Milner, S. T. Polymer brushes. *Science* **1991,** *251*, 905-914.

(560) Wijmans, C.; Zhulina, E. B. Polymer brushes at curved surfaces. *Macromolecules* **1993,** *26*, 7214-7224.

(561) Xue, Z.; Li, X.; Chen, X.; Huang, C.; Ye, H.; Li, A.; Wang, T. Mechanical and Tribological Performances Enhanced by Self‐Assembled Structures. *Adv. Mater.* **2020,** *32*, 2002004.

(562) Li, Y.; Wang, Q.; Zhang, L.; Hu, S.; Chen, L.; He, P.; Feng, H.; Zhang, J.; Ji, H.; Ma, X. Self-assembly of nickel: from nanoparticles to foils with tunable magnetic properties. *CrystEngComm* **2019,** *21*, 5317-5321.

(563) Liu, X.; Kent, N.; Ceballos, A.; Streubel, R.; Jiang, Y.; Chai, Y.; Kim, P. Y.; Forth, J.; Hellman, F.; Shi, S. Reconfigurable ferromagnetic liquid droplets. *Science* **2019,** *365*, 264-267.

(564) Feng, J.; Yang, F.; Wang, X.; Lyu, F.; Li, Z.; Yin, Y. Self‐aligned anisotropic plasmonic nanostructures. *Adv. Mater.* **2019,** *31*, 1900789.

(565) Xu, W.; Wang, M.; Li, Z.; Wang, X.; Wang, Y.; Xing, M.; Yin, Y. Chemical transformation of colloidal nanostructures with morphological preservation by surface-protection with capping ligands. *Nano Lett.* **2017,** *17*, 2713-2718.

(566) Hu, Y.; He, L.; Yin, Y. Magnetically responsive photonic nanochains. *Angew. Chem.* **2011,** *123*, 3831-3834.

(567) Nam, S. K.; Kim, J. B.; Han, S. H.; Kim, S.-H. Photonic Janus Balls with Controlled Magnetic Moment and Density Asymmetry. *ACS nano* **2020,** *14*, 15714-15722.

(568) Chen, X.; Ye, Z.; Yang, F.; Feng, J.; Li, Z.; Huang, C.; Ke, Q.; Yin, Y. Magnetic cellulose microcrystals with tunable magneto-optical responses. *Appl. Mater. Today* **2020,** *20*, 100749.

(569) Ge, J.; Lee, H.; He, L.; Kim, J.; Lu, Z.; Kim, H.; Goebl, J.; Kwon, S.; Yin, Y. Magnetochromatic microspheres: rotating photonic crystals. *J. Am. Chem. Soc.* **2009,** *131*, 15687-15694.

(570) Wang, M.; He, L.; Xu, W.; Wang, X.; Yin, Y. Magnetic assembly and field‐tuning of ellipsoidal‐nanoparticle‐based colloidal photonic crystals. *Angew. Chem. Int. Ed.* **2015,** *54*, 7077-7081.

(571) Wang, M.; Gao, C.; He, L.; Lu, Q.; Zhang, J.; Tang, C.; Zorba, S.; Yin, Y. Magnetic tuning of plasmonic excitation of gold nanorods. *J. Am. Chem. Soc.* **2013,** *135*, 15302-15305.

(572) Li, Z.; Jin, J.; Yang, F.; Song, N.; Yin, Y. Coupling magnetic and plasmonic anisotropy in hybrid nanorods for mechanochromic responses. *Nat. Commun.* **2020,** *11*, 2883.

(573) Zhou, S.; Bai, Y.; Xu, W.; Feng, J.; Wang, X.; Li, Z.; Yin, Y. Formation of resorcinol-formaldehyde hollow nanoshells through a dissolution–regrowth process. *Nanoscale* **2020,** *12*, 15460-15465.

(574) Li, Z.; Ye, Z.; Han, L.; Fan, Q.; Wu, C.; Ding, D.; Xin, H. L.; Myung, N. V.; Yin, Y. Polarization‐modulated multidirectional photothermal actuators. *Adv. Mater.* **2021,** *33*, 2006367.

(575) Zhang, M.; Magagnosc, D. J.; Liberal, I.; Yu, Y.; Yun, H.; Yang, H.; Wu, Y.; Guo, J.; Chen, W.; Shin, Y. J. High-strength magnetically switchable plasmonic nanorods assembled from a binary nanocrystal mixture. *Nat. Nanotechnol.* **2017,** *12*, 228-232.

(576) Jung, I.; Yoo, H.; Jang, H. J.; Cho, S.; Lee, K.; Hong, S.; Park, S. Fourier transform surface plasmon resonance (FTSPR) with gyromagnetic plasmonic nanorods. *Angew. Chem.* **2018,** *130*, 1859-1863.

(577) Kim, K.; Xu, X.; Guo, J.; Fan, D. Ultrahigh-speed rotating nanoelectromechanical system devices assembled from nanoscale building blocks. *Nat. Commun.* **2014,** *5*, 3632.

(578) Oh, B.-K.; Park, S.; Millstone, J. E.; Lee, S. W.; Lee, K.-B.; Mirkin, C. A. Separation of tricomponent protein mixtures with triblock

nanorods. *J. Am. Chem. Soc.* **2006,** *128*, 11825-11829.

(579) Lee, K. B.; Park, S.; Mirkin, C. A. Multicomponent magnetic nanorods for biomolecular separations. *Angew. Chem. Int. Ed.* **2004,** *43*, 3048-3050.

(580) Hilal, H.; Lee, S.; Jung, I.; Yoo, S.; Park, S. Scattering Fourier Transform Biosensor: Binary Mixture Consisting of Magnetic Ni Nanorings and Plasmonic Au Nanorods. *Anal. Chem.* **2020,** *92*, 10099-10107.

(581) Jung, I.; Ih, S.; Yoo, H.; Hong, S.; Park, S. Fourier transform surface plasmon resonance of nanodisks embedded in magnetic nanorods. *Nano Lett.* **2018,** *18*, 1984-1992.

(582) Lin, Y.; Hu, Z.; Zhang, M.; Xu, T.; Feng, S.; Jiang, L.; Zheng, Y. Magnetically induced low adhesive direction of nano/micropillar arrays for microdroplet transport. *Adv. Funct. Mater.* **2018,** *28*, 1800163.

(583) Drotlef, D. M.; Blümler, P.; del Campo, A. Magnetically actuated patterns for bioinspired reversible adhesion (dry and wet). *Adv. Mater.* **2014,** *26*, 775-779.

(584) Fu, L.; Liu, Y.; Wang, W.; Wang, M.; Bai, Y.; Chronister, E. L.; Zhen, L.; Yin, Y. A pressure sensor based on the orientational dependence of plasmonic properties of gold nanorods. *Nanoscale* **2015,** *7*, 14483-14488.

(585) Tang, Z.; Huang, Q.; Liu, Y.; Chen, Y.; Guo, B.; Zhang, L. Uniaxial stretching-induced alignment of carbon nanotubes in cross-linked elastomer enabled by dynamic cross-link reshuffling. *ACS Macro Lett.* **2019,** *8*, 1575-1581.

(586) Jin, L.; Bower, C.; Zhou, O. Alignment of carbon nanotubes in a polymer matrix by mechanical stretching. *Appl. Phys. Lett.* **1998,** *73*, 1197-1199.

(587) Wang, L.; Li, Y.; Chen, B.; Liu, S.; Li, M.; Zheng, L.; Wang, P.; Lu, T. J.; Xu, F. Patterning cellular alignment through stretching hydrogels with programmable strain gradients. *ACS Appl. Mater. Interfaces* **2015,** *7*, 15088-15097.

(588) Urayama, K.; Mashita, R.; Kobayashi, I.; Takigawa, T. Stretching-induced director rotation in thin films of liquid crystal elastomers with homeotropic alignment. *Macromolecules* **2007,** *40*, 7665-7670.

(589) Kim, Y.; Yeom, B.; Arteaga, O.; Yoo, S. J.; Lee, S.-G.; Kim, J.-G.; Kotov, N. A. Reconfigurable chiroptical nanocomposites with chirality transfer from the macro-to the nanoscale. *Nat. Mater.* **2016,** *15*, 461-468.

(590) Kato, T.; Uchida, J.; Ichikawa, T.; Sakamoto, T. Functional liquid crystals towards the next generation of materials. *Angew. Chem. Int. Ed.* **2018,** *57*, 4355-4371.

(591) Kumar, N.; Zhang, R.; De Pablo, J. J.; Gardel, M. L. Tunable structure and dynamics of active liquid crystals. *Sci. Adv.* **2018,** *4*, eaat7779.

(592) Mezzenga, R.; Seddon, J. M.; Drummond, C. J.; Boyd, B. J.; Schröder‐Turk, G. E.; Sagalowicz, L. Nature‐Inspired design and application of lipidic lyotropic liquid crystals. *Adv. Mater.* **2019,** *31*, 1900818.

(593) Liu, Q.; Ackerman, P. J.; Lubensky, T. C.; Smalyukh, I. I. Biaxial ferromagnetic liquid crystal colloids. *Proc. Natl. Acad. Sci. U.S.A.* **2016,** *113*, 10479-10484.

(594) Park, S.; Mundoor, H.; Fleury, B.; Davidson, P.; van de Lagemaat, J.; Smalyukh, I. I. Liquid Crystalline Order and Electric Switching of Upconversion Luminescence in Colloidal Nanorod Suspensions. *Adv. Opt. Mater.* **2019,** *7*, 1900041.

(595) Mundoor, H.; Park, S.; Senyuk, B.; Wensink, H. H.; Smalyukh, I. I. Hybrid molecular-colloidal liquid crystals. *Science* **2018,** *360*, 768-771.

(596) Hess, A. J.; Liu, Q.; Smalyukh, I. I. Optical patterning of magnetic domains and defects in ferromagnetic liquid crystal colloids. *Appl. Phys. Lett.* **2015,** *107*, 071906.

(597) Zhang, Q.; Ackerman, P. J.; Liu, Q.; Smalyukh, I. I. Ferromagnetic switching of knotted vector fields in liquid crystal colloids. *Phys. Rev. Lett.* **2015,** *115*, 097802.

(598) Mundoor, H.; Wu, J.-S.; Wensink, H. H.; Smalyukh, I. I. Thermally reconfigurable monoclinic nematic colloidal fluids. *Nature* **2021,** *590*, 268-274.

(599) Yuan, Y.; Liu, Q.; Senyuk, B.; Smalyukh, I. I. Elastic colloidal monopoles and reconfigurable self-assembly in liquid crystals. *Nature* **2019,** *570*, 214-218.

(600) Yuan, Y.; Martinez, A.; Senyuk, B.; Tasinkevych, M.; Smalyukh, I. I. Chiral liquid crystal colloids. *Nat. Mater.* **2018,** *17*, 71-79.

(601) Chaikin, P. M.; Lubensky, T. C.; Witten, T. A. *Principles of condensed matter physics*; Cambridge university press Cambridge, 1995, 1-699.
(602) De Gennes, P.-G.; Prost, J. *The physics of liquid crystals*; Oxford university press, 1993, 1-597.
(603) Freiser, M. Ordered states of a nematic liquid. *Phys. Rev. Lett.* **1970,** *24*, 1041-1043.
(604) Yu, L.; Saupe, A. Observation of a biaxial nematic phase in potassium laurate-1-decanol-water mixtures. *Phys. Rev. Lett.* **1980,** *45*, 1000-1003.
(605) Severing, K.; Saalwächter, K. Biaxial nematic phase in a thermotropic liquid-crystalline side-chain polymer. *Phys. Rev. Lett.* **2004,** *92*, 125501.
(606) Van den Pol, E.; Petukhov, A.; Thies-Weesie, D.; Byelov, D.; Vroege, G. Experimental realization of biaxial liquid crystal phases in colloidal dispersions of boardlike particles. *Phys. Rev. Lett.* **2009,** *103*, 258301.
(607) Lubensky, T.; Radzihovsky, L. Theory of bent-core liquid-crystal phases and phase transitions. *Phys. Rev. E* **2002,** *66*, 031704.
(608) Luckhurst, G. R.; Naemura, S.; Sluckin, T. J.; To, T. B.; Turzi, S. Molecular field theory for biaxial nematic liquid crystals composed of molecules with C 2 h point group symmetry. *Phys. Rev. E* **2011,** *84*, 011704.
(609) Mettout, B. Macroscopic and molecular symmetries of unconventional nematic phases. *Phys. Rev. E* **2006,** *74*, 041701.
(610) Poulin, P.; Stark, H.; Lubensky, T.; Weitz, D. Novel colloidal interactions in anisotropic fluids. *Science* **1997,** *275*, 1770-1773.
(611) Muševič, I.; Škarabot, M.; Tkalec, U.; Ravnik, M.; Žumer, S. Two-dimensional nematic colloidal crystals self-assembled by topological defects. *Science* **2006,** *313*, 954-958.
(612) Mundoor, H.; Senyuk, B.; Almansouri, M.; Park, S.; Fleury, B.; Smalyukh, I. I. Electrostatically controlled surface boundary conditions in nematic liquid crystals and colloids. *Sci. Adv.* **2019,** *5*, eaax4257.
(613) Jerome, B. Surface effects and anchoring in liquid crystals. *Rep. Prog. Phys.* **1991,** *54*, 391.
(614) Liu, Q.; Yuan, Y.; Smalyukh, I. I. Electrically and optically tunable plasmonic guest–host liquid crystals with long-range ordered nanoparticles. *Nano Lett.* **2014,** *14*, 4071-4077.
(615) Vroege, G. J.; Lekkerkerker, H. N. Phase transitions in lyotropic colloidal and polymer liquid crystals. *Rep. Prog. Phys.* **1992,** *55*, 1241-1309.
(616) Dogic, Z.; Fraden, S. Ordered phases of filamentous viruses. *Curr. Opin. Colloid Interface Sci.* **2006,** *11*, 47-55.
(617) Grelet, E. Hard-rod behavior in dense mesophases of semiflexible and rigid charged viruses. *Phys. Rev. X* **2014,** *4*, 021053.
(618) Lemaire, B.; Davidson, P.; Ferré, J.; Jamet, J.; Petermann, D.; Panine, P.; Dozov, I.; Jolivet, J. Physical properties of aqueous suspensions of goethite (α-FeOOH) nanorods. *Eur. Phys. J. E* **2004,** *13*, 291-308.
(619) de La Cotte, A.; Merzeau, P.; Kim, J. W.; Lahlil, K.; Boilot, J.-P.; Gacoin, T.; Grelet, E. Electric field induced birefringence in non-aqueous dispersions of mineral nanorods. *Soft matter* **2015,** *11*, 6595-6603.
(620) Kim, J.; de la Cotte, A.; Deloncle, R.; Archambeau, S.; Biver, C.; Cano, J. P.; Lahlil, K.; Boilot, J. P.; Grelet, E.; Gacoin, T. LaPO4 Mineral Liquid Crystalline Suspensions with Outstanding Colloidal Stability for Electro‐Optical Applications. *Adv. Funct. Mater.* **2012,** *22*, 4949-4956.
(621) Paineau, E.; Krapf, M.-E. M.; Amara, M.-S.; Matskova, N. V.; Dozov, I.; Rouzière, S.; Thill, A.; Launois, P.; Davidson, P. A liquid-crystalline hexagonal columnar phase in highly-dilute suspensions of imogolite nanotubes. *Nat. Commun.* **2016,** *7*, 10271.
(622) Castro, C. E.; Kilchherr, F.; Kim, D.-N.; Shiao, E. L.; Wauer, T.; Wortmann, P.; Bathe, M.; Dietz, H. A primer to scaffolded DNA origami. *Nat. Methods* **2011,** *8*, 221-229.
(623) Hong, F.; Zhang, F.; Liu, Y.; Yan, H. DNA origami: scaffolds for creating higher order structures. *Chem. Rev.* **2017,** *117*, 12584-12640.
(624) Han, D.; Pal, S.; Nangreave, J.; Deng, Z.; Liu, Y.; Yan, H. DNA origami with complex curvatures in three-dimensional space. *Science* **2011,** *332*, 342-346.
(625) Shen, X.; Zhan, P.; Kuzyk, A.; Liu, Q.; Asenjo-Garcia, A.; Zhang, H.; de Abajo, F. J. G.;

Govorov, A.; Ding, B.; Liu, N. 3D plasmonic chiral colloids. *Nanoscale* **2014,** *6*, 2077-2081.
(626) Lan, X.; Lu, X.; Shen, C.; Ke, Y.; Ni, W.; Wang, Q. Au nanorod helical superstructures with designed chirality. *J. Am. Chem. Soc.* **2015,** *137*, 457-462.
(627) Yan, W.; Xu, L.; Xu, C.; Ma, W.; Kuang, H.; Wang, L.; Kotov, N. A. Self-assembly of chiral nanoparticle pyramids with strong R/S optical activity. *J. Am. Chem. Soc.* **2012,** *134*, 15114-15121.
(628) Shen, X.; Asenjo-Garcia, A.; Liu, Q.; Jiang, Q.; García de Abajo, F. J.; Liu, N.; Ding, B. Three-dimensional plasmonic chiral tetramers assembled by DNA origami. *Nano Lett.* **2013,** *13*, 2128-2133.
(629) Shen, X.; Song, C.; Wang, J.; Shi, D.; Wang, Z.; Liu, N.; Ding, B. Rolling up gold nanoparticle-dressed DNA origami into three-dimensional plasmonic chiral nanostructures. *J. Am. Chem. Soc.* **2012,** *134*, 146-149.
(630) Xin, L.; Zhou, C.; Duan, X.; Liu, N. A rotary plasmonic nanoclock. *Nat. Commun.* **2019,** *10*, 1-8.
(631) Rothemund, P. W. Folding DNA to create nanoscale shapes and patterns. *Nature* **2006,** *440*, 297-302.
(632) Dietz, H.; Douglas, S. M.; Shih, W. M. Folding DNA into twisted and curved nanoscale shapes. *Science* **2009,** *325*, 725-730.
(633) Yang, Y.; Wang, J.; Shigematsu, H.; Xu, W.; Shih, W. M.; Rothman, J. E.; Lin, C. Self-assembly of size-controlled liposomes on DNA nanotemplates. *Nat. Chem.* **2016,** *8*, 476-483.
(634) Zhou, C.; Duan, X.; Liu, N. A plasmonic nanorod that walks on DNA origami. *Nat. Commun.* **2015,** *6*, 8102.
(635) Zhan, P.; Urban, M. J.; Both, S.; Duan, X.; Kuzyk, A.; Weiss, T.; Liu, N. DNA-assembled nanoarchitectures with multiple components in regulated and coordinated motion. *Sci. Adv.* **2019,** *5*, eaax6023.
(636) Zhang, D. Y.; Winfree, E. Control of DNA strand displacement kinetics using toehold exchange. *J. Am. Chem. Soc.* **2009,** *131*, 17303-17314.
(637) Machinek, R. R.; Ouldridge, T. E.; Haley, N. E.; Bath, J.; Turberfield, A. J. Programmable energy landscapes for kinetic control of DNA strand displacement. *Nat. Commun.* **2014,** *5*, 5324.
(638) Lagerwall, J. P.; Scalia, G. A new era for liquid crystal research: Applications of liquid crystals in soft matter nano-, bio-and microtechnology. *Curr. Appl. Phys.* **2012,** *12*, 1387-1412.
(639) Sasikala, S. P.; Lim, J.; Kim, I. H.; Jung, H. J.; Yun, T.; Han, T. H.; Kim, S. O. Graphene oxide liquid crystals: a frontier 2D soft material for graphene-based functional materials. *Chem. Soc. Rev.* **2018,** *47*, 6013-6045.
(640) Narayan, R.; Kim, J. E.; Kim, J. Y.; Lee, K. E.; Kim, S. O. Graphene oxide liquid crystals: discovery, evolution and applications. *Adv. Mater.* **2016,** *28*, 3045-3068.
(641) Habibi, Y.; Lucia, L. A.; Rojas, O. J. Cellulose nanocrystals: chemistry, self-assembly, and applications. *Chem. Rev.* **2010,** *110*, 3479-3500.
(642) Dumanli, A. G. m.; Van Der Kooij, H. M.; Kamita, G.; Reisner, E.; Baumberg, J. J.; Steiner, U.; Vignolini, S. Digital color in cellulose nanocrystal films. *ACS Appl. Mater. Interfaces* **2014,** *6*, 12302-12306.
(643) Onsager, L. The effects of shape on the interaction of colloidal particles. *Ann. N.Y. Acad. Sci.* **1949,** *51*, 627-659.
(644) Bates, M. A.; Frenkel, D. Nematic–isotropic transition in polydisperse systems of infinitely thin hard platelets. *J. Chem. Phys.* **1999,** *110*, 6553-6559.
(645) Xu, Z.; Gao, C. Aqueous liquid crystals of graphene oxide. *ACS nano* **2011,** *5*, 2908-2915.
(646) Arshadi Pirlar, M.; Honarmand, Y.; Rezaei Mirghaed, M.; Movahed, S. M. S.; Karimzadeh, R. Birefringent Graphene Oxide Liquid Crystals in Microchannel for Optical Switch. *ACS Appl. Nano Mater.* **2020,** *3*, 2123-2128.
(647) Shen, T.-Z.; Hong, S.-H.; Song, J.-K. Electro-optical switching of graphene oxide liquid crystals with an extremely large Kerr coefficient. *Nat. Mater.* **2014,** *13*, 394-399.
(648) He, L.; Ye, J.; Shuai, M.; Zhu, Z.; Zhou, X.; Wang, Y.; Li, Y.; Su, Z.; Zhang, H.; Chen, Y. Graphene oxide liquid crystals for reflective displays without polarizing optics. *Nanoscale* **2015,** *7*, 1616-1622.
(649) Franklin, D.; Chen, Y.; Vazquez-Guardado, A.; Modak, S.; Boroumand, J.; Xu, D.; Wu, S.-T.;

Chanda, D. Polarization-independent actively tunable colour generation on imprinted plasmonic surfaces. *Nat. Commun.* **2015,** *6*, 7337.

(650) Højlund‐Nielsen, E.; Clausen, J.; Mäkela, T.; Thamdrup, L. H.; Zalkovskij, M.; Nielsen, T.; Li Pira, N.; Ahopelto, J.; Mortensen, N. A.; Kristensen, A. Plasmonic colors: toward mass production of metasurfaces. *Adv. Mater. Technol.* **2016,** *1*, 1600054.

(651) Shao, L.; Zhuo, X.; Wang, J. Advanced plasmonic materials for dynamic color display. *Adv. Mater.* **2018,** *30*, 1704338.

(652) Jiang, M.; Siew, S. Y.; Chan, J. Y.; Deng, J.; Wu, Q. Y. S.; Jin, L.; Yang, J. K.; Teng, J.; Danner, A.; Qiu, C.-W. Patterned resist on flat silver achieving saturated plasmonic colors with sub-20-nm spectral linewidth. *Mater. Today* **2020,** *35*, 99-105.

(653) Hsu, C. W.; Zhen, B.; Qiu, W.; Shapira, O.; DeLacy, B. G.; Joannopoulos, J. D.; Soljačić, M. Transparent displays enabled by resonant nanoparticle scattering. *Nat. Commun.* **2014,** *5*, 3152.

(654) Xu, T.; Wu, Y.-K.; Luo, X.; Guo, L. J. Plasmonic nanoresonators for high-resolution colour filtering and spectral imaging. *Nat. Commun.* **2010,** *1*, 59.

(655) Gu, Y.; Zhang, L.; Yang, J. K.; Yeo, S. P.; Qiu, C.-W. Color generation via subwavelength plasmonic nanostructures. *Nanoscale* **2015,** *7*, 6409-6419.

(656) Kristensen, A.; Yang, J. K.; Bozhevolnyi, S. I.; Link, S.; Nordlander, P.; Halas, N. J.; Mortensen, N. A. Plasmonic colour generation. *Nat. Rev. Mater.* **2016,** *2*, 1-14.

(657) Li, Z.; Fan, Q.; Wu, C.; Li, Y.; Cheng, C.; Yin, Y. Magnetically Tunable Plasmon Coupling of Au Nanoshells Enabled by Space-Free Confined Growth. *Nano Lett.* **2020,** *20*, 8242-8249.

(658) Chen, T.; Reinhard, B. M. Assembling color on the nanoscale: multichromatic switchable pixels from plasmonic atoms and molecules. *Adv. Mater.* **2016,** *28*, 3522-3527.

(659) Driencourt, L.; Federspiel, F. o.; Kazazis, D.; Tseng, L.-T.; Frantz, R.; Ekinci, Y.; Ferrini, R.; Gallinet, B. Electrically tunable multicolored filter using birefringent plasmonic resonators and liquid crystals. *ACS Photonics* **2019,** *7*, 444-453.

(660) Olson, J.; Manjavacas, A.; Liu, L.; Chang, W.-S.; Foerster, B.; King, N. S.; Knight, M. W.; Nordlander, P.; Halas, N. J.; Link, S. Vivid, full-color aluminum plasmonic pixels. *Proc. Natl. Acad. Sci. U.S.A.* **2014,** *111*, 14348-14353.

(661) Liu, Y. J.; Si, G. Y.; Leong, E. S.; Xiang, N.; Danner, A. J.; Teng, J. H. Light‐driven plasmonic color filters by overlaying photoresponsive liquid crystals on gold annular aperture arrays. *Adv. Mater.* **2012,** *24*, OP131-OP135.

(662) Paik, S.; Kim, G.; Chang, S.; Lee, S.; Jin, D.; Jeong, K.-Y.; Lee, I. S.; Lee, J.; Moon, H.; Lee, J. Near-field sub-diffraction photolithography with an elastomeric photomask. *Nat. Commun.* **2020,** *11*, 805.

(663) Franklin, D.; He, Z.; Ortega, P. M.; Safaei, A.; Cencillo-Abad, P.; Wu, S.-T.; Chanda, D. Self-assembled plasmonics for angle-independent structural color displays with actively addressed black states. *Proc. Natl. Acad. Sci. U.S.A.* **2020,** *117*, 13350-13358.

(664) Franklin, D.; Frank, R.; Wu, S.-T.; Chanda, D. Actively addressed single pixel full-colour plasmonic display. *Nat. Commun.* **2017,** *8*, 15209.

(665) Lapointe, C. P.; Mason, T. G.; Smalyukh, I. I. Shape-controlled colloidal interactions in nematic liquid crystals. *Science* **2009,** *326*, 1083-1086.

(666) Fontana, J.; da Costa, G. K.; Pereira, J. M.; Naciri, J.; Ratna, B. R.; Palffy-Muhoray, P.; Carvalho, I. C. Electric field induced orientational order of gold nanorods in dilute organic suspensions. *Appl. Phys. Lett.* **2016,** *108*, 081904.

(667) Yin, T.; Wu, T.; Zhong, D.; Liu, J.; Liu, X.; Han, Z.; Yu, H.; Qu, S. Soft display using photonic crystals on dielectric elastomers. *ACS Appl. Mater. Interfaces* **2018,** *10*, 24758-24766.

(668) Kang, H. S.; Han, S. W.; Park, C.; Lee, S. W.; Eoh, H.; Baek, J.; Shin, D.-G.; Park, T. H.; Huh, J.; Lee, H. 3D touchless multiorder reflection structural color sensing display. *Sci. Adv.* **2020,** *6*, eabb5769.

(669) Qi, Y.; Niu, W.; Zhang, S.; Zhang, Z.; Wu, S.; Ma, W. Rotational Periodicity Display of the Tunable Wettability Pattern in a Photoswitch Based on a Response Bilayer Photonic Crystal.

ACS Appl. Mater. Interfaces **2020,** *12*, 9664-9672.

(670) Lee, I.; Kim, D.; Kal, J.; Baek, H.; Kwak, D.; Go, D.; Kim, E.; Kang, C.; Chung, J.; Jang, Y. Quasi‐amorphous colloidal structures for electrically tunable full‐color photonic pixels with angle‐independency. *Adv. Mater.* **2010,** *22*, 4973-4977.

(671) Wang, H.; Kerins, F.; Kamp, U.; Bonifacio, L.; Arsenault, A. C.; Ozin, G. A. Photonic‐Crystal Display Materials. *Inf. Disp.* **2011,** *27*, 26-29.

(672) Fu, Q.; Zhu, H.; Ge, J. Electrically tunable liquid photonic crystals with large dielectric contrast and highly saturated structural colors. *Adv. Funct. Mater.* **2018,** *28*, 1804628.

(673) Gao, Z.; Gao, D.; Huang, C.; Zhang, H.; Guo, J.; Wei, J. Dual‐responsive SPMA‐modified polymer photonic crystals and their dynamic display patterns. *Macromol. Rapid Commun.* **2018,** *39*, 1800134.

(674) Wang, W.; Fan, X.; Li, F.; Qiu, J.; Umair, M. M.; Ren, W.; Ju, B.; Zhang, S.; Tang, B. Magnetochromic photonic hydrogel for an alternating magnetic field‐responsive color display. *Adv. Opt. Mater.* **2018,** *6*, 1701093.

(675) Niu, W.; Zhao, K.; Qu, L.; Zhang, S. Rewritable and highly stable photonic patterns for optical storage and display enabled by direct-pressure-programmed shape memory photonic crystals. *J. Mater. Chem. C* **2018,** *6*, 8385-8394.

(676) Haque, M. A.; Kamita, G.; Kurokawa, T.; Tsujii, K.; Gong, J. P. Unidirectional alignment of lamellar bilayer in hydrogel: one‐dimensional swelling, anisotropic modulus, and stress/strain tunable structural color. *Adv. Mater.* **2010,** *22*, 5110-5114.

(677) Liao, J.; Zhu, C.; Gao, B.; Zhao, Z.; Liu, X.; Tian, L.; Zeng, Y.; Zhou, X.; Xie, Z.; Gu, Z. Multiresponsive elastic colloidal crystals for reversible structural color patterns. *Adv. Funct. Mater.* **2019,** *29*, 1902954.

(678) Wang, H.; Yang, S.; Yin, S.-N.; Chen, L.; Chen, S. Janus suprabead displays derived from the modified photonic crystals toward temperature magnetism and optics multiple responses. *ACS Appl. Mater. Interfaces* **2015,** *7*, 8827-8833.

(679) Wang, D.; Wang, X.; Li, Z.; Chi, M.; Li, Y.; Liu, Y.; Yin, Y. Migration of Iron Oxide Nanoparticle through a Silica Shell by the Redox-Buffering Effect. *ACS nano* **2018,** *12*, 10949-10956.

(680) Hao, L.-W.; Liu, J.-D.; Li, Q.; Qing, R.-K.; He, Y.-Y.; Guo, J.; Li, G.; Zhu, L.; Chen, S. Microfluidic-directed magnetic controlling supraballs with multi-responsive anisotropic photonic crystal structures. *J. Mater. Sci. Technol.* **2021,** *81*, 203-211.

(681) Kang, P.; Ogunbo, S. O.; Erickson, D. High resolution reversible color images on photonic crystal substrates. *Langmuir* **2011,** *27*, 9676-9680.

(682) Wang, M.; He, L.; Hu, Y.; Yin, Y. Magnetically rewritable photonic ink based on superparamagnetic nanochains. *J. Mater. Chem. C* **2013,** *1*, 6151-6156.

(683) Hu, H.; Tang, J.; Zhong, H.; Xi, Z.; Chen, C.; Chen, Q. Invisible photonic printing: computer designing graphics, UV printing and shown by a magnetic field. *Sci. Rep.* **2013,** *3*, 1-5.

(684) Hu, H.; Zhong, H.; Chen, C.; Chen, Q. Magnetically responsive photonic watermarks on banknotes. *J. Mater. Chem. C* **2014,** *2*, 3695-3702.

(685) Kim, H.; Ge, J.; Kim, J.; Choi, S.-e.; Lee, H.; Lee, H.; Park, W.; Yin, Y.; Kwon, S. Structural colour printing using a magnetically tunable and lithographically fixable photonic crystal. *Nat. Photonics* **2009,** *3*, 534-540.

(686) Chen, J.; Xu, L.; Yang, M.; Chen, X.; Chen, X.; Hong, W. Highly stretchable photonic crystal hydrogels for a sensitive mechanochromic sensor and direct ink writing. *Chem. Mater.* **2019,** *31*, 8918-8926.

(687) Ding, T.; Cao, G.; Schäfer, C. G.; Zhao, Q.; Gallei, M.; Smoukov, S. K.; Baumberg, J. J. Revealing invisible photonic inscriptions: images from strain. *ACS Appl. Mater. Interfaces* **2015,** *7*, 13497-13502.

(688) Ye, S.; Fu, Q.; Ge, J. Invisible photonic prints shown by deformation. *Adv. Funct. Mater.* **2014,** *24*, 6430-6438.

(689) Yang, D.; Ye, S.; Ge, J. Old relief printing applied to the current preparation of multi-color and high resolution colloidal photonic crystal patterns. *Chem. Commun.* **2015,** *51*, 16972-16975.

(690) Liu, L.; Gao, Z.; Jiang, B.; Bai, Y.; Wang, W.; Yin, Y. Reversible assembly and dynamic plasmonic tuning of Ag nanoparticles enabled by limited ligand protection. *Nano Lett.* **2018,** *18*, 5312-5318.

(691) Sierra-Martin, B.; Romero-Cano, M.; Fernandez-Nieves, A.; Fernandez-Barbero, A. Thermal control over the electrophoresis of soft colloidal particles. *Langmuir* **2006,** *22*, 3586-3590.

(692) Hayward, R.; Saville, D.; Aksay, I. A. Electrophoretic assembly of colloidal crystals with optically tunable micropatterns. *Nature* **2000,** *404*, 56-59.

(693) Park, T. J.; Hwang, S. K.; Park, S.; Cho, S. H.; Park, T. H.; Jeong, B.; Kang, H. S.; Ryu, D. Y.; Huh, J.; Thomas, E. L. Electrically tunable soft-solid block copolymer structural color. *ACS nano* **2015,** *9*, 12158-12167.

(694) Seyfoddin, A.; Chan, A.; Chen, W.-T.; Rupenthal, I.; Waterhouse, G.; Svirskis, D. Electro-responsive macroporous polypyrrole scaffolds for triggered dexamethasone delivery. *Eur. J. Pharm. Biopharm.* **2015,** *94*, 419-426.

(695) Fang, Z. H.; Punckt, C.; Leung, E. Y.; Schniepp, H. C.; Aksay, I. A. Tuning of structural color using a dielectric actuator and multifunctional compliant electrodes. *Appl. Opt.* **2010,** *49*, 6689-6696.

(696) Yin, T.; Zhong, D.; Liu, J.; Liu, X.; Yu, H.; Qu, S. Stretch tuning of the Debye ring for 2D photonic crystals on a dielectric elastomer membrane. *Soft matter* **2018,** *14*, 1120-1129.

(697) Xie, Y.; Meng, Y.; Wang, W.; Zhang, E.; Leng, J.; Pei, Q. Bistable and Reconfigurable Photonic Crystals—Electroactive Shape Memory Polymer Nanocomposite for Ink‐Free Rewritable Paper. *Adv. Funct. Mater.* **2018,** *28*, 1802430.

(698) Kang, H. S.; Lee, J.; Cho, S. M.; Park, T. H.; Kim, M. J.; Park, C.; Lee, S. W.; Kim, K. L.; Ryu, D. Y.; Huh, J. Printable and rewritable full block copolymer structural color. *Adv. Mater.* **2017,** *29*, 1700084.

(699) Wang, Z.; Zhang, J.; Xie, J.; Wang, Z.; Yin, Y.; Li, J.; Li, Y.; Liang, S.; Zhang, L.; Cui, L. Polymer Bragg stack as color tunable photonic paper. *J. Mater. Chem.* **2012,** *22*, 7887-7893.

(700) Xuan, R.; Ge, J. Invisible photonic prints shown by water. *J. Mater. Chem.* **2012,** *22*, 367-372.

(701) Wan, H.; Li, X.; Zhang, L.; Li, X.; Liu, P.; Jiang, Z.; Yu, Z.-Z. Rapidly responsive and flexible chiral nematic cellulose nanocrystal composites as multifunctional rewritable photonic papers with eco-friendly inks. *ACS Appl. Mater. Interfaces* **2018,** *10*, 5918-5925.

(702) Ye, S.; Ge, J. Soaking based invisible photonic print with a fast response and high resolution. *J. Mater. Chem. C* **2015,** *3*, 8097-8103.

(703) Xia, Y.; Chen, B.; Gao, S.; Liu, Y.; Zeng, Z.; Cao, M.; Wang, S. Tough, freestanding, and colorless photonic paper using water as ink. *Adv. Mater. Interfaces* **2019,** *6*, 1901363.

(704) Du, X.; Li, T.; Li, L.; Zhang, Z.; Wu, T. Water as a colorful ink: transparent, rewritable photonic coatings based on colloidal crystals embedded in chitosan hydrogel. *J. Mater. Chem. C* **2015,** *3*, 3542-3546.

(705) Ge, J.; Goebl, J.; He, L.; Lu, Z.; Yin, Y. Rewritable photonic paper with hygroscopic salt solution as ink. *Adv. Mater.* **2009,** *21*, 4259-4264.

(706) Arsenault, A. C.; Míguez, H.; Kitaev, V.; Ozin, G. A.; Manners, I. A Polychromic, Fast Response Metallopolymer Gel Photonic Crystal with Solvent and Redox Tunability: A Step Towards Photonic Ink (P‐Ink). *Adv. Mater.* **2003,** *15*, 503-507.

(707) Patel, B. B.; Walsh, D. J.; Kim, D. H.; Kwok, J.; Lee, B.; Guironnet, D.; Diao, Y. Tunable structural color of bottlebrush block copolymers through direct-write 3D printing from solution. *Sci. Adv.* **2020,** *6*, eaaz7202.

(708) Sienkiewicz, A.; Krasucka, P.; Charmas, B.; Stefaniak, W.; Goworek, J. Swelling effects in cross-linked polymers by thermogravimetry. *J. Therm. Anal. Calorim.* **2017,** *130*, 85-93.

(709) Ou, G.; Li, Z.; Li, D.; Cheng, L.; Liu, Z.; Wu, H. Photothermal therapy by using titanium oxide nanoparticles. *Nano Res.* **2016,** *9*, 1236-1243.

(710) Wang, Y.; Zhao, Q.; Du, X. Inkless multi-color writing and copying of laser-programmable photonic crystals. *Mater. Horiz.* **2020,** *7*, 1341-1347.

(711) Chichkov, B. N.; Momma, C.; Nolte, S.; Von Alvensleben, F.; Tünnermann, A. Femtosecond, picosecond and nanosecond

laser ablation of solids. *Appl. Phys. A* **1996,** *63*, 109-115.

(712) Zhu, X.; Vannahme, C.; Højlund-Nielsen, E.; Mortensen, N. A.; Kristensen, A. Plasmonic colour laser printing. *Nat. Nanotechnol.* **2016,** *11*, 325-329.

(713) Baù, L.; Tecilla, P.; Mancin, F. Sensing with fluorescent nanoparticles. *Nanoscale* **2011,** *3*, 121-133.

(714) Kaeser, A.; Schenning, A. P. Fluorescent nanoparticles based on self‐assembled π‐conjugated systems. *Adv. Mater.* **2010,** *22*, 2985-2997.

(715) Carter, K. P.; Young, A. M.; Palmer, A. E. Fluorescent sensors for measuring metal ions in living systems. *Chem. Rev.* **2014,** *114*, 4564-4601.

(716) Nolan, E. M.; Lippard, S. J. Small-molecule fluorescent sensors for investigating zinc metalloneurochemistry. *Acc. Chem. Res.* **2009,** *42*, 193-203.

(717) Howes, P. D.; Chandrawati, R.; Stevens, M. M. Colloidal nanoparticles as advanced biological sensors. *Science* **2014,** *346*, 1247390.

(718) Li, C.; Liu, S. Polymeric assemblies and nanoparticles with stimuli-responsive fluorescence emission characteristics. *Chem. Commun.* **2012,** *48*, 3262-3278.

(719) Huang, Y.; Li, F.; Qin, M.; Jiang, L.; Song, Y. A Multi‐stopband Photonic‐Crystal Microchip for High‐Performance Metal‐Ion Recognition Based on Fluorescent Detection. *Angew. Chem. Int. Ed.* **2013,** *52*, 7296-7299.

(720) Park, W. M.; Champion, J. A. Colloidal Assembly of Hierarchically Structured Porous Supraparticles from Flower-Shaped Protein–Inorganic Hybrid Nanoparticles. *ACS nano* **2016,** *10*, 8271-8280.

(721) Mohraz, A.; Solomon, M. J. Direct visualization of colloidal rod assembly by confocal microscopy. *Langmuir* **2005,** *21*, 5298-5306.

(722) Kim, J.; Michelin, S.; Hilbers, M.; Martinelli, L.; Chaudan, E.; Amselem, G.; Fradet, E.; Boilot, J.-P.; Brouwer, A. M.; Baroud, C. N. Monitoring the orientation of rare-earth-doped nanorods for flow shear tomography. *Nat. Nanotechnol.* **2017,** *12*, 914-919.

(723) Nagaoka, Y.; Wang, T.; Lynch, J.; LaMontagne, D.; Cao, Y. C. Binary assembly of colloidal semiconductor nanorods with spherical metal nanoparticles. *Small* **2012,** *8*, 843-846.

(724) Ding, D.; Li, K.; Liu, B.; Tang, B. Z. Bioprobes based on AIE fluorogens. *Acc. Chem. Res.* **2013,** *46*, 2441-2453.

(725) Hu, R.; Leung, N. L.; Tang, B. Z. AIE macromolecules: syntheses, structures and functionalities. *Chem. Soc. Rev.* **2014,** *43*, 4494-4562.

(726) Wang, H.; Zhao, E.; Lam, J. W.; Tang, B. Z. AIE luminogens: emission brightened by aggregation. *Mater. Today* **2015,** *18*, 365-377.

(727) Guo, R.; Wang, D.-N.; Wei, Y.-Y.; Zhang, Y.-Z.; Yang, C.-G.; Xu, Z.-R. Colloidal photonic crystal array chip based on nanoparticle self-assembly on patterned hydrophobic surface for signal-enhanced fluorescent assay of adenosine. *Microchim. Acta* **2020,** *187*, 1-10.

(728) Zhu, M.-Q.; Zhu, L.; Han, J. J.; Wu, W.; Hurst, J. K.; Li, A. D. Spiropyran-based photochromic polymer nanoparticles with optically switchable luminescence. *J. Am. Chem. Soc.* **2006,** *128*, 4303-4309.

(729) Li, C.; Wu, T.; Hong, C.; Zhang, G.; Liu, S. A general strategy to construct fluorogenic probes from charge‐generation polymers (CGPs) and AIE‐active fluorogens through triggered complexation. *Angew. Chem.* **2012,** *124*, 470-474.

(730) Rostovtsev, V. V.; Green, L. G.; Fokin, V. V.; Sharpless, K. B. A stepwise huisgen cycloaddition process: copper (I)‐catalyzed regioselective "ligation" of azides and terminal alkynes. *Angew. Chem.* **2002,** *114*, 2708-2711.

(731) Hawker, C. J.; Bosman, A. W.; Harth, E. New polymer synthesis by nitroxide mediated living radical polymerizations. *Chem. Rev.* **2001,** *101*, 3661-3688.

(732) Smith, A. E.; Xu, X.; McCormick, C. L. Stimuli-responsive amphiphilic (co) polymers via RAFT polymerization. *Prog. Polym. Sci.* **2010,** *35*, 45-93.

(733) Zhou, K.; Wang, Y.; Huang, X.; Luby‐Phelps, K.; Sumer, B. D.; Gao, J. Tunable, ultrasensitive pH‐responsive nanoparticles targeting specific endocytic organelles in living cells. *Angew. Chem. Int. Ed.* **2011,** *50*, 6109-6114.

(734) Chen, J.; Zeng, F.; Wu, S.; Zhao, J.; Chen, Q.; Tong, Z. Reversible fluorescence modulation

through energy transfer with ABC triblock copolymer micelles as scaffolds. *Chem. Commun.* **2008**, 5580-5582.

(735) Yin, J.; Hu, H.; Wu, Y.; Liu, S. Thermo-and light-regulated fluorescence resonance energy transfer processes within dually responsive microgels. *Polym. Chem.* **2011,** *2*, 363-371.

(736) Sivakumar, K.; Xie, F.; Cash, B. M.; Long, S.; Barnhill, H. N.; Wang, Q. A fluorogenic 1, 3-dipolar cycloaddition reaction of 3-azidocoumarins and acetylenes. *Org. Lett.* **2004,** *6*, 4603-4606.

(737) Tian, J.; Chen, H.; Zhuo, L.; Xie, Y.; Li, N.; Tang, B. A Highly Selective, Cell‐Permeable Fluorescent Nanoprobe for Ratiometric Detection and Imaging of Peroxynitrite in Living Cells. *Chem. Eur. J* **2011,** *17*, 6626-6634.

(738) Li, C.; Liu, S. Responsive nanogel-based dual fluorescent sensors for temperature and Hg2+ ions with enhanced detection sensitivity. *J. Mater. Chem.* **2010,** *20*, 10716-10723.

(739) Lee, S.; Ryu, J. H.; Park, K.; Lee, A.; Lee, S.-Y.; Youn, I.-C.; Ahn, C.-H.; Yoon, S. M.; Myung, S.-J.; Moon, D. H. Polymeric nanoparticle-based activatable near-infrared nanosensor for protease determination in vivo. *Nano Lett.* **2009,** *9*, 4412-4416.

(740) Uchiyama, S.; Kawai, N.; de Silva, A. P.; Iwai, K. Fluorescent polymeric AND logic gate with temperature and pH as inputs. *J. Am. Chem. Soc.* **2004,** *126*, 3032-3033.

(741) Chen, C.-Y.; Chen, C.-T. A PNIPAM-based fluorescent nanothermometer with ratiometric readout. *Chem. Commun.* **2011,** *47*, 994-996.

(742) Hu, J.; Zhang, G.; Geng, Y.; Liu, S. Micellar nanoparticles of coil–rod–coil triblock copolymers for highly sensitive and ratiometric fluorescent detection of fluoride ions. *Macromolecules* **2011,** *44*, 8207-8214.

(743) Hu, J.; Dai, L.; Liu, S. Analyte-reactive amphiphilic thermoresponsive diblock copolymer micelles-based multifunctional ratiometric fluorescent chemosensors. *Macromolecules* **2011,** *44*, 4699-4710.

(744) Li, C.; Zhang, Y.; Hu, J.; Cheng, J.; Liu, S. Reversible three‐state switching of multicolor fluorescence emission by multiple stimuli modulated FRET processes within thermoresponsive polymeric micelles. *Angew. Chem. Int. Ed.* **2010,** *49*, 5120-5124.

(745) Wang, J.; Gudiksen, M. S.; Duan, X.; Cui, Y.; Lieber, C. M. Highly polarized photoluminescence and photodetection from single indium phosphide nanowires. *Science* **2001,** *293*, 1455-1457.

(746) Hu, J.; Li, L.-s.; Yang, W.; Manna, L.; Wang, L.-w.; Alivisatos, A. P. Linearly polarized emission from colloidal semiconductor quantum rods. *Science* **2001,** *292*, 2060-2063.

(747) Forkey, J. N.; Quinlan, M. E.; Shaw, M. A.; Corrie, J. E.; Goldman, Y. E. Three-dimensional structural dynamics of myosin V by single-molecule fluorescence polarization. *Nature* **2003,** *422*, 399-404.

(748) McIntyre, C.; Sham, L. Theory of luminescence polarization anisotropy in quantum wires. *Phys. Rev. B* **1992,** *45*, 9443.

(749) Califano, M.; Zunger, A. Anisotropy of interband transitions in InAs quantum wires: An atomistic theory. *Phys. Rev. B* **2004,** *70*, 165317.

(750) Chen, H.-Y.; Yang, Y.-C.; Lin, H.-W.; Chang, S.-C.; Gwo, S. Polarized photoluminescence from single GaN nanorods: effects of optical confinement. *Opt. Express* **2008,** *16*, 13465-13475.

(751) Binnemans, K.; Görller-Walrand, C. Application of the Eu3+ ion for site symmetry determination. *J. Rare Earths* **1996,** *14*, 173-180.

(752) Brecher, C. Europium in the ultraphosphate lattice: Polarized spectra and structure of EuP5O14. *J. Chem. Phys.* **1974,** *61*, 2297-2315.

(753) Brecher, C.; Samelson, H.; Lempicki, A.; Riley, R.; Peters, T. Polarized Spectra and Crystal-Field Parameters of Eu+ 3 in YV O 4. *Phys. Rev.* **1967,** *155*, 178.

(754) Yuan, S.; Ge, F.; Yang, X.; Guang, S. Self-assembly of colloidal photonic crystals of PS@ PNIPAM nanoparticles and temperature-responsive tunable fluorescence. *J. Fluoresc.* **2016,** *26*, 2303-2310.

(755) Purcell, E. M.; Torrey, H. C.; Pound, R. V. Resonance absorption by nuclear magnetic moments in a solid. *Phys. Rev.* **1946,** *69*, 37.

(756) Tam, F.; Goodrich, G. P.; Johnson, B. R.; Halas, N. J. Plasmonic enhancement of molecular fluorescence. *Nano Lett.* **2007,** *7*, 496-501.

(757) Bauch, M.; Toma, K.; Toma, M.; Zhang, Q.; Dostalek, J. Plasmon-enhanced fluorescence biosensors: a review. *Plasmonics* **2014,** *9*, 781-799.

(758) Dong, J.; Zhang, Z.; Zheng, H.; Sun, M. Recent progress on plasmon-enhanced fluorescence. *Nanophotonics* **2015,** *4*, 472-490.

(759) Fu, Y.; Zhang, J.; Lakowicz, J. R. Plasmon-enhanced fluorescence from single fluorophores end-linked to gold nanorods. *J. Am. Chem. Soc.* **2010,** *132*, 5540-5541.

(760) Neumann, T.; Johansson, M. L.; Kambhampati, D.; Knoll, W. Surface–plasmon fluorescence spectroscopy. *Adv. Funct. Mater.* **2002,** *12*, 575-586.

(761) Bohlen, J.; Cuartero-González, Á.; Pibiri, E.; Ruhlandt, D.; Fernández-Domínguez, A.; Tinnefeld, P.; Acuna, G. P. Plasmon-assisted Förster resonance energy transfer at the single-molecule level in the moderate quenching regime. *Nanoscale* **2019,** *11*, 7674-7681.

(762) Guerrero, A. R.; Zhang, Y.; Aroca, R. F. Experimental confirmation of local field enhancement determining far‐field measurements with shell‐isolated silver nanoparticles. *Small* **2012,** *8*, 2964-2967.

(763) Gersten, J.; Nitzan, A. Spectroscopic properties of molecules interacting with small dielectric particles. *J. Chem. Phys.* **1981,** *75*, 1139-1152.

(764) Li, J.-F.; Li, C.-Y.; Aroca, R. F. Plasmon-enhanced fluorescence spectroscopy. *Chem. Soc. Rev.* **2017,** *46*, 3962-3979.

(765) Zhang, Y.-Q.; Wang, J.-X.; Ji, Z.-Y.; Hu, W.-P.; Jiang, L.; Song, Y.-L.; Zhu, D.-B. Solid-state fluorescence enhancement of organic dyes by photonic crystals. *J. Mater. Chem.* **2007,** *17*, 90-94.

(766) Vermorken, A.; Goos, C.; Hukkelhoven, M.; Coelen, M. Aluminum-coated cell for fluorescence signal enhancement. *Anal. Chem.* **1983,** *55*, 2464-2466.

(767) Qin, M.; Huang, Y.; Li, Y.; Su, M.; Chen, B.; Sun, H.; Yong, P.; Ye, C.; Li, F.; Song, Y. A Rainbow Structural‐Color Chip for Multisaccharide Recognition. *Angew. Chem. Int. Ed.* **2016,** *55*, 6911-6914.

(768) Badugu, R.; Nowaczyk, K.; Descrovi, E.; Lakowicz, J. R. Radiative decay engineering 6: Fluorescence on one-dimensional photonic crystals. *Anal. Biochem.* **2013,** *442*, 83-96.

(769) Dutta Choudhury, S.; Badugu, R.; Lakowicz, J. R. Directing fluorescence with plasmonic and photonic structures. *Acc. Chem. Res.* **2015,** *48*, 2171-2180.

(770) Lin, C.; Jiang, Y.; Tao, C.-a.; Yin, X.; Lan, Y.; Wang, C.; Wang, S.; Liu, X.; Li, G. Electrothermally driven fluorescence switching by liquid crystal elastomers based on dimensional photonic crystals. *ACS Appl. Mater. Interfaces* **2017,** *9*, 11770-11779.

(771) Sepúlveda, B.; Angelomé, P. C.; Lechuga, L. M.; Liz-Marzán, L. M. LSPR-based nanobiosensors. *nano today* **2009,** *4*, 244-251.

(772) Lin, J.; Mueller, J. B.; Wang, Q.; Yuan, G.; Antoniou, N.; Yuan, X.-C.; Capasso, F. Polarization-controlled tunable directional coupling of surface plasmon polaritons. *Science* **2013,** *340*, 331-334.

(773) Lee, S.; Mayer, K. M.; Hafner, J. H. Improved localized surface plasmon resonance immunoassay with gold bipyramid substrates. *Anal. Chem.* **2009,** *81*, 4450-4455.

(774) Huang, C.; Ye, J.; Wang, S.; Stakenborg, T.; Lagae, L. Gold nanoring as a sensitive plasmonic biosensor for on-chip DNA detection. *Appl. Phys. Lett.* **2012,** *100*, 173114.

(775) Chen, T.; Pourmand, M.; Feizpour, A.; Cushman, B.; Reinhard, B. r. M. Tailoring plasmon coupling in self-assembled one-dimensional Au nanoparticle chains through simultaneous control of size and gap separation. *J. Phys. Chem. Lett.* **2013,** *4*, 2147-2152.

(776) Shanthil, M.; Thomas, R.; Swathi, R.; George Thomas, K. Ag@ SiO2 core–shell nanostructures: distance-dependent plasmon coupling and SERS investigation. *J. Phys. Chem. Lett.* **2012,** *3*, 1459-1464.

(777) Knight, M. W.; King, N. S.; Liu, L.; Everitt, H. O.; Nordlander, P.; Halas, N. J. Aluminum for plasmonics. *ACS nano* **2014,** *8*, 834-840.

(778) Liu, N.; Hentschel, M.; Weiss, T.; Alivisatos, A. P.; Giessen, H. Three-dimensional plasmon rulers. *Science* **2011,** *332*, 1407-1410.

(779) Qian, G.-S.; Zhang, T.-T.; Zhao, W.; Xu, J.-J.; Chen, H.-Y. Single-molecule imaging of telomerase activity via linear plasmon rulers. *Chem. Commun.* **2017,** *53*, 4710-4713.

(780) Shafiei, F.; Monticone, F.; Le, K. Q.; Liu, X.-X.; Hartsfield, T.; Alù, A.; Li, X. A subwavelength plasmonic metamolecule exhibiting magnetic-based optical Fano resonance. *Nat. Nanotechnol.* **2013,** *8*, 95-99.

(781) Kuzyk, A.; Schreiber, R.; Zhang, H.; Govorov, A. O.; Liedl, T.; Liu, N. Reconfigurable 3D plasmonic metamolecules. *Nat. Mater.* **2014,** *13*, 862-866.

(782) Kuzyk, A.; Urban, M. J.; Idili, A.; Ricci, F.; Liu, N. Selective control of reconfigurable chiral plasmonic metamolecules. *Sci. Adv.* **2017,** *3*, e1602803.

(783) Wang, P.; Nasir, M. E.; Krasavin, A. V.; Dickson, W.; Jiang, Y.; Zayats, A. V. Plasmonic metamaterials for nanochemistry and sensing. *Acc. Chem. Res.* **2019,** *52*, 3018-3028.

(784) Le, N. H.; Nguyen, B. K.; Ye, G.; Peng, C.; Chen, J. I. Tuning the Sensing Performance of Multilayer Plasmonic Core–Satellite Assemblies for Rapid Detection of Targets from Lysed Cells. *ACS sensors* **2017,** *2*, 1578-1583.

(785) Armstrong, R. E.; Horáček, M.; Zijlstra, P. Plasmonic Assemblies for Real‐Time Single‐Molecule Biosensing. *Small* **2020,** *16*, 2003934.

(786) Qian, Z.; Ginger, D. S. Reversibly reconfigurable colloidal plasmonic nanomaterials. *J. Am. Chem. Soc.* **2017,** *139*, 5266-5276.

(787) Skewis, L. R.; Reinhard, B. M. Spermidine modulated ribonuclease activity probed by RNA plasmon rulers. *Nano Lett.* **2008,** *8*, 214-220.

(788) Chen, J. I.; Chen, Y.; Ginger, D. S. Plasmonic nanoparticle dimers for optical sensing of DNA in complex media. *J. Am. Chem. Soc.* **2010,** *132*, 9600-9601.

(789) Rong, G.; Wang, H.; Skewis, L. R.; Reinhard, B. r. M. Resolving sub-diffraction limit encounters in nanoparticle tracking using live cell plasmon coupling microscopy. *Nano Lett.* **2008,** *8*, 3386-3393.

(790) Lee, K.; Cui, Y.; Lee, L. P.; Irudayaraj, J. Quantitative imaging of single mRNA splice variants in living cells. *Nat. Nanotechnol.* **2014,** *9*, 474.

(791) Kim, K.; Oh, J. W.; Lee, Y. K.; Son, J.; Nam, J. M. Associating and dissociating nanodimer analysis for quantifying ultrasmall amounts of DNA. *Angew. Chem. Int. Ed.* **2017,** *56*, 9877-9880.

(792) Chen, J. I.; Durkee, H.; Traxler, B.; Ginger, D. S. Optical detection of protein in complex media with plasmonic nanoparticle dimers. *Small* **2011,** *7*, 1993-1997.

(793) Park, Y.; Shin, S.; Jin, H.; Park, J.; Hong, Y.; Choi, J.; Jung, B.; Song, H.; Seo, D. Single-molecule rotation for EGFR conformational dynamics in live cells. *J. Am. Chem. Soc.* **2018,** *140*, 15161-15165.

(794) Samai, S.; Choi, T. L. Y.; Guye, K. N.; Yan, Y.; Ginger, D. S. Plasmonic Nanoparticle Dimers with Reversibly Photoswitchable Interparticle Distances Linked by DNA. *J. Phys. Chem. C* **2017,** *122*, 13363-13370.

(795) Lee, S. E.; Chen, Q.; Bhat, R.; Petkiewicz, S.; Smith, J. M.; Ferry, V. E.; Correia, A. L.; Alivisatos, A. P.; Bissell, M. J. Reversible aptamer-Au plasmon rulers for secreted single molecules. *Nano Lett.* **2015,** *15*, 4564-4570.

(796) Tüting, L.; Ye, W.; Settanni, G.; Schmid, F.; Wolf, B. A.; Ahijado-Guzmán, R. n.; Sönnichsen, C. Potassium Triggers a Reversible Specific Stiffness Transition of Polyethylene Glycol. *J. Phys. Chem. C* **2017,** *121*, 22396-22402.

(797) Ohshima, H. *Electrical phenomena at interfaces and biointerfaces: fundamentals and applications in nano-, bio-, and environmental sciences*; John Wiley & Sons, 2012, 1-850.

(798) Liu, Q.; Liu, Y.; Yin, Y. Optical tuning by the self-assembly and disassembly of chain-like plasmonic superstructures. *Natl. Sci. Rev.* **2018,** *5*, 128-130.

(799) Lin, S.; Li, M.; Dujardin, E.; Girard, C.; Mann, S. One‐dimensional plasmon coupling by facile self‐assembly of gold nanoparticles into branched chain networks. *Adv. Mater.* **2005,** *17*, 2553-2559.

(800) Zhang, X.; Lv, L.; Ji, L.; Guo, G.; Liu, L.; Han, D.; Wang, B.; Tu, Y.; Hu, J.; Yang, D. Self-assembly of one-dimensional nanocrystal superlattice chains mediated by molecular clusters. *J. Am. Chem. Soc.* **2016,** *138*, 3290-3293.

(801) Zhou, C.; Xin, L.; Duan, X.; Urban, M. J.; Liu, N. Dynamic plasmonic system that responds to

thermal and aptamer-target regulations. *Nano Lett.* **2018,** *18*, 7395-7399.

(802) Kim, D.-Y.; Kang, D.-G.; Lee, M.-H.; Kim, J.-S.; Lee, C.-R.; Jeong, K.-U. A photo-responsive metallomesogen for an optically and electrically tunable polarized light modulator. *Chem. Commun.* **2016,** *52*, 12821-12824.

(803) Zhang, H.; Hu, Z.; Ma, Z.; Gecevičius, M.; Dong, G.; Zhou, S.; Qiu, J. Anisotropically enhanced nonlinear optical properties of ensembles of gold nanorods electrospun in polymer nanofiber film. *ACS Appl. Mater. Interfaces* **2016,** *8*, 2048-2053.

(804) Li, N.; Tittl, A.; Yue, S.; Giessen, H.; Song, C.; Ding, B.; Liu, N. DNA-assembled bimetallic plasmonic nanosensors. *Light Sci. Appl.* **2014,** *3*, e226-e226.

(805) Liu, N.; Liedl, T. DNA-assembled advanced plasmonic architectures. *Chem. Rev.* **2018,** *118*, 3032-3053.

(806) Duan, W.; Liu, A.; Li, Q.; Li, Z.; Wen, C.-y.; Cai, Z.; Tang, S.; Li, X.; Zeng, J. Toward ultrasensitive and fast colorimetric detection of indoor formaldehyde across the visible region using cetyltrimethylammonium chloride-capped bone-shaped gold nanorods as "chromophores". *Analyst* **2019,** *144*, 4582-4588.

(807) Couturier, J. P.; Sütterlin, M.; Laschewsky, A.; Hettrich, C.; Wischerhoff, E. Responsive inverse opal hydrogels for the sensing of macromolecules. *Angew. Chem. Int. Ed.* **2015,** *54*, 6641-6644.

(808) Zhang, Y.; Fu, Q.; Ge, J. Photonic sensing of organic solvents through geometric study of dynamic reflection spectrum. *Nat. Commun.* **2015,** *6*, 7510.

(809) Luo, W.; Cui, Q.; Fang, K.; Chen, K.; Ma, H.; Guan, J. Responsive hydrogel-based photonic nanochains for microenvironment sensing and imaging in real time and high resolution. *Nano Lett.* **2018,** *20*, 803-811.

(810) Liu, Y.; Han, F.; Li, F.; Zhao, Y.; Chen, M.; Xu, Z.; Zheng, X.; Hu, H.; Yao, J.; Guo, T. Inkjet-printed unclonable quantum dot fluorescent anti-counterfeiting labels with artificial intelligence authentication. *Nat. Commun.* **2019,** *10*, 2409.

(811) Li, F.; Wang, X.; Xia, Z.; Pan, C.; Liu, Q. Photoluminescence tuning in stretchable PDMS film grafted doped core/multishell quantum dots for anticounterfeiting. *Adv. Funct. Mater.* **2017,** *27*, 1700051.

(812) Abdollahi, A.; Alidaei-Sharif, H.; Roghani-Mamaqani, H.; Herizchi, A. Photoswitchable fluorescent polymer nanoparticles as high-security anticounterfeiting materials for authentication and optical patterning. *J. Mater. Chem. C* **2020,** *8*, 5476-5493.

(813) Delavari, S.; Ziadzade, S.; Rad, J. K.; Hamrang, V.; Mahdavian, A. R. Anticounterfeiting and photoluminescent cellulosic papers based on fluorescent acrylic copolymer nanoparticles containing coumarin. *Carbohydr. Polym.* **2020,** *247*, 116756.

(814) Jiang, K.; Zhang, L.; Lu, J.; Xu, C.; Cai, C.; Lin, H. Triple‐mode emission of carbon dots: applications for advanced anti‐counterfeiting. *Angew. Chem.* **2016,** *128*, 7347-7351.

(815) Liu, X.; Wang, Y.; Li, X.; Yi, Z.; Deng, R.; Liang, L.; Xie, X.; Loong, D. T.; Song, S.; Fan, D. Binary temporal upconversion codes of Mn 2+-activated nanoparticles for multilevel anti-counterfeiting. *Nat. Commun.* **2017,** *8*, 899.

(816) Ni, R.; Qian, B.; Liu, C.; Liu, X.; Qiu, J. 3D printing of resin composites doped with upconversion nanoparticles for anti-counterfeiting and temperature detection. *Opt. Express* **2018,** *26*, 25481-25491.

(817) He, L.; Feng, L.; Cheng, L.; Liu, Y.; Li, Z.; Peng, R.; Li, Y.; Guo, L.; Liu, Z. Multilayer dual-polymer-coated upconversion nanoparticles for multimodal imaging and serum-enhanced gene delivery. *ACS Appl. Mater. Interfaces* **2013,** *5*, 10381-10388.

(818) Abdollahi, A.; Roghani-Mamaqani, H.; Razavi, B.; Salami-Kalajahi, M. Photoluminescent and Chromic Nanomaterials for Anticounterfeiting Technologies: Recent Advances and Future Challenges. *ACS nano* **2020,** *14*, 14417-14492.

(819) Diaz, R.; Palleau, E.; Poirot, D.; Sangeetha, N.; Ressier, L. High-throughput fabrication of anti-counterfeiting colloid-based photoluminescent microtags using electrical nanoimprint lithography. *Nanotechnology* **2014,** *25*, 345302.

(820) Liu, Y.; Zheng, Y.; Zhu, Y.; Ma, F.; Zheng, X.; Yang, K.; Zheng, X.; Xu, Z.; Ju, S.; Zheng, Y. Unclonable Perovskite Fluorescent Dots with

Fingerprint Pattern for Multilevel Anticounterfeiting. *ACS Appl. Mater. Interfaces* **2020,** *12*, 39649-39656.

(821) Zhang, C.; Wang, B.; Li, W.; Huang, S.; Kong, L.; Li, Z.; Li, L. Conversion of invisible metal-organic frameworks to luminescent perovskite nanocrystals for confidential information encryption and decryption. *Nat. Commun.* **2017,** *8*, 1138.

(822) Huang, W.; Xu, M.; Liu, J.; Wang, J.; Zhu, Y.; Liu, J.; Rong, H.; Zhang, J. Hydrophilic Doped Quantum Dots "Ink" and Their Inkjet‐Printed Patterns for Dual Mode Anticounterfeiting by Reversible Cation Exchange Mechanism. *Adv. Funct. Mater.* **2019,** *29*, 1808762.

(823) Da Luz, L. L.; Milani, R.; Felix, J. F.; Ribeiro, I. R.; Talhavini, M.; Neto, B. A.; Chojnacki, J.; Rodrigues, M. O.; Júnior, S. A. Inkjet printing of lanthanide–organic frameworks for anti-counterfeiting applications. *ACS Appl. Mater. Interfaces* **2015,** *7*, 27115-27123.

(824) Sangeetha, N. M.; Moutet, P.; Lagarde, D.; Sallen, G.; Urbaszek, B.; Marie, X.; Viau, G.; Ressier, L. 3D assembly of upconverting NaYF4 nanocrystals by AFM nanoxerography: creation of anti-counterfeiting microtags. *Nanoscale* **2013,** *5*, 9587-9592.

(825) Morales, D.; Teulon, L.; Palleau, E.; Alnasser, T.; Ressier, L. Single-step binary electrostatic directed assembly of active nanogels for smart concentration-dependent encryption. *Langmuir* **2018,** *34*, 1557-1563.

(826) Gan, L.; Feng, N.; Liu, S.; Zheng, S.; Li, Z.; Huang, J. Assembly‐Induced Emission of Cellulose Nanocrystals for Hiding Information. *Part. Part. Syst. Charact.* **2019,** *36*, 1800412.

(827) Gao, R.; Yan, D.; Evans, D. G.; Duan, X. Layer-by-layer assembly of long-afterglow self-supporting thin films with dual-stimuli-responsive phosphorescence and antiforgery applications. *Nano Res.* **2017,** *10*, 3606-3617.

(828) Li, J.; Yu, P.; Cheng, H.; Liu, W.; Li, Z.; Xie, B.; Chen, S.; Tian, J. Optical polarization encoding using graphene‐loaded plasmonic metasurfaces. *Adv. Opt. Mater.* **2016,** *4*, 91-98.

(829) Franklin, D.; Modak, S.; Vázquez-Guardado, A.; Safaei, A.; Chanda, D. Covert infrared image encoding through imprinted plasmonic cavities. *Light Sci. Appl.* **2018,** *7*, 1-8.

(830) Zhang, T.; Blair, S. Gray level image encoding in plasmonic metasurfaces. *Plasmonics* **2020,** *15*, 1305-1311.

(831) Heydari, E.; Sperling, J. R.; Neale, S. L.; Clark, A. W. Plasmonic Color Filters as Dual‐State Nanopixels for High‐Density Microimage Encoding. *Adv. Funct. Mater.* **2017,** *27*, 1701866.

(832) Smith, J. D.; Reza, M. A.; Smith, N. L.; Gu, J.; Ibrar, M.; Crandall, D. J.; Skrabalak, S. E. Plasmonic Anticounterfeit Tags with High Encoding Capacity Rapidly Authenticated with Deep Machine Learning. *ACS nano* **2021,** *15*, 2901-2910.

(833) Liu, H.; Zhang, B.; Gao, T.; Wu, X.; Cui, F.; Xu, W. 3D chiral color prints for anti-counterfeiting. *Nanoscale* **2019,** *11*, 5506-5511.

(834) Frese, D.; Wei, Q.; Wang, Y.; Huang, L.; Zentgraf, T. Nonreciprocal asymmetric polarization encryption by layered plasmonic metasurfaces. *Nano Lett.* **2019,** *19*, 3976-3980.

(835) Li, X.; Lan, T.-H.; Tien, C.-H.; Gu, M. Three-dimensional orientation-unlimited polarization encryption by a single optically configured vectorial beam. *Nat. Commun.* **2012,** *3*, 998.

(836) McGorty, R.; Fung, J.; Kaz, D.; Manoharan, V. N. Colloidal self-assembly at an interface. *Mater. Today* **2010,** *13*, 34-42.

(837) Liu, B.; Lu, X.; Qiao, Z.; Song, L.; Cheng, Q.; Zhang, J.; Zhang, A.; Huang, Y.; Chen, T. pH and temperature dual-responsive plasmonic switches of gold nanoparticle monolayer film for multiple anticounterfeiting. *Langmuir* **2018,** *34*, 13047-13056.

(838) Chen, X.; Chen, Y.; Yan, M.; Qiu, M. Nanosecond photothermal effects in plasmonic nanostructures. *ACS nano* **2012,** *6*, 2550-2557.

(839) Xu, L.; Feng, Y.; Yu, D.; Zheng, Z.; Chen, X.; Hong, W. Recoverable Photolithographic Patterning for Polarized Display and Encryption. *Adv. Mater. Technol.* **2020,** *5*, 2000373.

(840) Song, L.; Qiu, N.; Huang, Y.; Cheng, Q.; Yang, Y.; Lin, H.; Su, F.; Chen, T. Macroscopic Orientational Gold Nanorods Monolayer Film with Excellent Photothermal

Anticounterfeiting Performance. *Adv. Opt. Mater.* **2020,** *8*, 1902082.

(841) Fukuoka, T.; Yamaguchi, A.; Hara, R.; Matsumoto, T.; Utsumi, Y.; Mori, Y. 2015 International Conference on Electronics Packaging and iMAPS All Asia Conference (ICEP-IAAC), 2015; p 432-435.

(842) Si, K. J.; Sikdar, D.; Yap, L. W.; Foo, J. K. K.; Guo, P.; Shi, Q.; Premaratne, M.; Cheng, W. Dual‐Coded Plasmene Nanosheets as Next‐Generation Anticounterfeit Security Labels. *Adv. Opt. Mater.* **2015,** *3*, 1710-1717.

(843) Gu, Y.; He, C.; Zhang, Y.; Lin, L.; Thackray, B. D.; Ye, J. Gap-enhanced Raman tags for physically unclonable anticounterfeiting labels. *Nat. Commun.* **2020,** *11*, 516.

(844) Zhou, Y.; Zhao, G.; Bian, J.; Tian, X.; Cheng, X.; Wang, H.; Chen, H. Multiplexed SERS Barcodes for Anti-Counterfeiting. *ACS Appl. Mater. Interfaces* **2020,** *12*, 28532-28538.

(845) Liu, Y.; Lee, Y. H.; Lee, M. R.; Yang, Y.; Ling, X. Y. Flexible three-dimensional anticounterfeiting plasmonic security labels: Utilizing z-axis-dependent SERS readouts to encode multilayered molecular information. *ACS Photonics* **2017,** *4*, 2529-2536.

(846) Tang, L.; Huang, J.; Zhang, H.; Yang, T.; Mo, Z.; Qu, J. Multi-stimuli responsive hydrogels with shape memory and self-healing properties for information encryption. *Eur. Polym. J.* **2020,** *140*, 110061.

(847) Wang, X.; Feng, J.; Yu, H.; Jin, Y.; Davidson, A.; Li, Z.; Yin, Y. Anisotropically shaped magnetic/plasmonic nanocomposites for information encryption and magnetic-field-direction sensing. *Research* **2018,** *2018*, 7527825.

(848) Li, Y.; Zhou, X.; Yang, Q.; Li, Y.; Li, W.; Li, H.; Chen, S.; Li, M.; Song, Y. Patterned photonic crystals for hiding information. *J. Mater. Chem. C* **2017,** *5*, 4621-4628.

(849) Wang, C.; Lin, X.; Schäfer, C. G.; Hirsemann, S.; Ge, J. Spray Synthesis of Photonic Crystal Based Automotive Coatings with Bright and Angular‐Dependent Structural Colors. *Adv. Funct. Mater.* **2020**, 2008601.

(850) Wu, S.; Liu, T.; Tang, B.; Li, L.; Zhang, S. Different structural colors or patterns on the front and back sides of a multilayer photonic structure. *ACS Appl. Mater. Interfaces* **2019,** *11*, 27210-27215.

(851) Wu, S.; Huang, B.; Wu, Y.; Meng, Z.; Zhang, S. Reflection and transmission two-way structural colors. *Nanoscale* **2020,** *12*, 11460-11467.

(852) Xuan, R.; Ge, J. Photonic printing through the orientational tuning of photonic structures and its application to anticounterfeiting labels. *Langmuir* **2011,** *27*, 5694-5699.

(853) Peng, C.-Y.; Hsu, C.-W.; Li, C.-W.; Wang, P.-L.; Jeng, C.-C.; Chang, C.-C.; Wang, G.-J. Flexible photonic crystal material for multiple anticounterfeiting applications. *ACS Appl. Mater. Interfaces* **2018,** *10*, 9858-9864.

(854) Nam, H.; Song, K.; Ha, D.; Kim, T. Inkjet printing based mono-layered photonic crystal patterning for anti-counterfeiting structural colors. *Sci. Rep.* **2016,** *6*, 1-9.

(855) Wu, P.; Shen, X.; Schäfer, C. G.; Pan, J.; Guo, J.; Wang, C. Mechanochromic and thermochromic shape memory photonic crystal films based on core/shell nanoparticles for smart monitoring. *Nanoscale* **2019,** *11*, 20015-20023.

(856) Chang, P.; Niu, W.; Qu, L.; Zhang, S. Two-way rewritable and stable photonic patterns enabled by near-infrared laser-responsive shape memory photonic crystals. *J. Mater. Chem. C* **2019,** *7*, 1896-1903.

(857) Liu, F.; Zhang, S.; Meng, Y.; Tang, B. Thermal Responsive Photonic Crystal Achieved through the Control of Light Path Guided by Phase Transition. *Small* **2020,** *16*, 2002319.

(858) Qi, Y.; Chu, L.; Niu, W.; Tang, B.; Wu, S.; Ma, W.; Zhang, S. New encryption strategy of photonic crystals with bilayer inverse heterostructure guided from transparency response. *Adv. Funct. Mater.* **2019,** *29*, 1903743.

(859) Chen, K.; Zhang, Y.; Ge, J. Highly invisible photonic crystal patterns encrypted in an inverse opaline macroporous polyurethane film for anti-counterfeiting applications. *ACS Appl. Mater. Interfaces* **2019,** *11*, 45256-45264.

(860) Wang, Z.; Meng, F.; Zhang, S.; Meng, Y.; Wu, S.; Tang, B. Robust, Portable, and Specific Water-Response Silk Film with Noniridescent Pattern Encryption for Information Security.

ACS Appl. Mater. Interfaces **2020,** *12*, 56413-56423.

(861) He, X.; Gu, Y.; Yu, B.; Liu, Z.; Zhu, K.; Wu, N.; Zhao, X.; Wei, Y.; Zhou, J.; Song, Y. Multi-mode structural-color anti-counterfeiting labels based on physically unclonable amorphous photonic structures with convenient artificial intelligence authentication. *J. Mater. Chem. C* **2019,** *7*, 14069-14074.

(862) Zhou, C.; Qi, Y.; Zhang, S.; Niu, W.; Wu, S.; Ma, W.; Tang, B. Bilayer Heterostructure Photonic Crystal Composed of Hollow Silica and Silica Sphere Arrays for Information Encryption. *Langmuir* **2020,** *36*, 1379-1385.

(863) Gao, Z.; Huang, C.; Yang, D.; Zhang, H.; Guo, J.; Wei, J. Dual-mode multicolored photonic crystal patterns enabled by ultraviolet-responsive core-shell colloidal spheres. *Dyes Pigm.* **2018,** *148*, 108-117.

(864) Park, K.; Park, M.; Jang, H. S.; Park, J. H.; Kim, J.; Cho, Y.; Han, I. K.; Byun, D.; Ko, H. Highly secure plasmonic encryption keys combined with upconversion luminescence nanocrystals. *Adv. Funct. Mater.* **2018,** *28*, 1800369.

(865) Zheng, Y.; Jiang, C.; Ng, S. H.; Lu, Y.; Han, F.; Bach, U.; Gooding, J. J. Unclonable Plasmonic Security Labels Achieved by Shadow‐Mask‐Lithography‐Assisted Self‐Assembly. *Adv. Mater.* **2016,** *28*, 2330-2336.

(866) Tsai, W.-K.; Lai, Y.-S.; Tseng, P.-J.; Liao, C.-H.; Chan, Y.-H. Dual colorimetric and fluorescent authentication based on semiconducting polymer dots for anticounterfeiting applications. *ACS Appl. Mater. Interfaces* **2017,** *9*, 30918-30924.

(867) Miriyev, A.; Stack, K.; Lipson, H. Soft material for soft actuators. *Nat. Commun.* **2017,** *8*, 596.

(868) Bahramzadeh, Y.; Shahinpoor, M. A review of ionic polymeric soft actuators and sensors. *Soft Robot.* **2014,** *1*, 38-52.

(869) Nie, M.; Huang, C.; Du, X. Recent advances in colour-tunable soft actuators. *Nanoscale* **2021,** *13*, 2780-2791.

(870) Niku, S. B. *Introduction to robotics: analysis, systems, applications*; Prentice hall New Jersey, 2001, 1-339.

(871) Ratna, D.; Karger-Kocsis, J. Recent advances in shape memory polymers and composites: a review. *J. Mater. Sci.* **2008,** *43*, 254-269.

(872) Cianchetti, M.; Laschi, C.; Menciassi, A.; Dario, P. Biomedical applications of soft robotics. *Nat. Rev. Mater.* **2018,** *3*, 143-153.

(873) Chung, H. J.; Parsons, A. M.; Zheng, L. Magnetically controlled soft robotics utilizing elastomers and gels in actuation: A review. *Adv. Intell. Syst.* **2021,** *3*, 2000186.

(874) Hu, W.; Lum, G. Z.; Mastrangeli, M.; Sitti, M. Small-scale soft-bodied robot with multimodal locomotion. *Nature* **2018,** *554*, 81-85.

(875) Kim, Y.; Parada, G. A.; Liu, S.; Zhao, X. Ferromagnetic soft continuum robots. *Sci. Robot.* **2019,** *4*, eaax7329.

(876) Cui, J.; Huang, T.-Y.; Luo, Z.; Testa, P.; Gu, H.; Chen, X.-Z.; Nelson, B. J.; Heyderman, L. J. Nanomagnetic encoding of shape-morphing micromachines. *Nature* **2019,** *575*, 164-168.

(877) Kim, Y.; Yuk, H.; Zhao, R.; Chester, S. A.; Zhao, X. Printing ferromagnetic domains for untethered fast-transforming soft materials. *Nature* **2018,** *558*, 274-279.

(878) Kim, J.; Chung, S. E.; Choi, S.-E.; Lee, H.; Kim, J.; Kwon, S. Programming magnetic anisotropy in polymeric microactuators. *Nat. Mater.* **2011,** *10*, 747-752.

(879) Huang, H.-W.; Sakar, M. S.; Petruska, A. J.; Pané, S.; Nelson, B. J. Soft micromachines with programmable motility and morphology. *Nat. Commun.* **2016,** *7*, 12263.

(880) Song, H.; Lee, H.; Lee, J.; Choe, J. K.; Lee, S.; Yi, J. Y.; Park, S.; Yoo, J.-W.; Kwon, M. S.; Kim, J. Reprogrammable ferromagnetic domains for reconfigurable soft magnetic actuators. *Nano Lett.* **2020,** *20*, 5185-5192.

(881) Han, D. D.; Zhang, Y. L.; Ma, J. N.; Liu, Y. Q.; Han, B.; Sun, H. B. Light‐mediated manufacture and manipulation of actuators. *Adv. Mater.* **2016,** *28*, 8328-8343.

(882) Irie, M.; Fukaminato, T.; Matsuda, K.; Kobatake, S. Photochromism of diarylethene molecules and crystals: memories, switches, and actuators. *Chem. Rev.* **2014,** *114*, 12174-12277.

(883) Tian, H.; Yang, S. Recent progresses on diarylethene based photochromic switches. *Chem. Soc. Rev.* **2004,** *33*, 85-97.

(884) Guo, S.; Matsukawa, K.; Miyata, T.; Okubo, T.; Kuroda, K.; Shimojima, A. Photoinduced bending of self-assembled azobenzene–

siloxane hybrid. *J. Am. Chem. Soc.* **2015,** *137*, 15434-15440.

(885) Liu, D.; Liu, L.; Onck, P. R.; Broer, D. J. Reverse switching of surface roughness in a self-organized polydomain liquid crystal coating. *Proc. Natl. Acad. Sci. U.S.A.* **2015,** *112*, 3880-3885.

(886) Palffy-Muhoray, P. Printed actuators in a flap. *Nat. Mater.* **2009,** *8*, 614-615.

(887) Kim, T.; Zhu, L.; Mueller, L. J.; Bardeen, C. J. Mechanism of photoinduced bending and twisting in crystalline microneedles and microribbons composed of 9-methylanthracene. *J. Am. Chem. Soc.* **2014,** *136*, 6617-6625.

(888) Zhu, L.; Al-Kaysi, R. O.; Bardeen, C. J. Reversible photoinduced twisting of molecular crystal microribbons. *J. Am. Chem. Soc.* **2011,** *133*, 12569-12575.

(889) Ohshima, A.; Momotake, A.; Arai, T. Photochromism, thermochromism, and solvatochromism of naphthalene-based analogues of salicylideneaniline in solution. *J. Photochem. Photobiol. A: Chem.* **2004,** *162*, 473-479.

(890) Koshima, H.; Takechi, K.; Uchimoto, H.; Shiro, M.; Hashizume, D. Photomechanical bending of salicylideneaniline crystals. *Chem. Commun.* **2011,** *47*, 11423-11425.

(891) Harada, J.; Uekusa, H.; Ohashi, Y. X-ray analysis of structural changes in photochromic salicylideneaniline crystals. Solid-state reaction induced by two-photon excitation. *J. Am. Chem. Soc.* **1999,** *121*, 5809-5810.

(892) Klajn, R. Spiropyran-based dynamic materials. *Chem. Soc. Rev.* **2014,** *43*, 148-184.

(893) Kortekaas, L.; Browne, W. R. The evolution of spiropyran: fundamentals and progress of an extraordinarily versatile photochrome. *Chem. Soc. Rev.* **2019,** *48*, 3406-3424.

(894) Buback, J.; Kullmann, M.; Langhojer, F.; Nuernberger, P.; Schmidt, R.; Würthner, F.; Brixner, T. Ultrafast bidirectional photoswitching of a spiropyran. *J. Am. Chem. Soc.* **2010,** *132*, 16510-16519.

(895) Tong, F.; Xu, W.; Guo, T.; Lui, B. F.; Hayward, R. C.; Palffy-Muhoray, P.; Al-Kaysi, R. O.; Bardeen, C. J. Photomechanical molecular crystals and nanowire assemblies based on the [2+ 2] photodimerization of a phenylbutadiene derivative. *J. Mater. Chem. C* **2020,** *8*, 5036-5044.

(896) Shoji, H.; Kitagawa, D.; Kobatake, S. Alkyl substituent effects in photochemical and thermal reactions of photochromic thiophene-S, S-dioxidized diarylethenes. *New J. Chem.* **2014,** *38*, 933-941.

(897) Gupta, P.; Panda, T.; Allu, S.; Borah, S.; Baishya, A.; Gunnam, A.; Nangia, A.; Naumov, P. e.; Nath, N. K. Crystalline acylhydrazone photoswitches with multiple mechanical responses. *Cryst. Growth Des.* **2019,** *19*, 3039-3044.

(898) Kobatake, S.; Takami, S.; Muto, H.; Ishikawa, T.; Irie, M. Rapid and reversible shape changes of molecular crystals on photoirradiation. *Nature* **2007,** *446*, 778-781.

(899) Morimoto, M.; Irie, M. A diarylethene cocrystal that converts light into mechanical work. *J. Am. Chem. Soc.* **2010,** *132*, 14172-14178.

(900) Kitagawa, D.; Tsujioka, H.; Tong, F.; Dong, X.; Bardeen, C. J.; Kobatake, S. Control of photomechanical crystal twisting by illumination direction. *J. Am. Chem. Soc.* **2018,** *140*, 4208-4212.

(901) Zhu, L.; Al‐Kaysi, R. O.; Bardeen, C. J. Photoinduced Ratchet‐Like Rotational Motion of Branched Molecular Crystals. *Angew. Chem.* **2016,** *128*, 7189-7192.

(902) Uchida, E.; Azumi, R.; Norikane, Y. Light-induced crawling of crystals on a glass surface. *Nat. Commun.* **2015,** *6*, 7310.

(903) Tong, F.; Al-Haidar, M.; Zhu, L.; Al-Kaysi, R. O.; Bardeen, C. J. Photoinduced peeling of molecular crystals. *Chem. Commun.* **2019,** *55*, 3709-3712.

(904) Naumov, P.; Sahoo, S. C.; Zakharov, B. A.; Boldyreva, E. V. Dynamic single crystals: kinematic analysis of photoinduced crystal jumping (the photosalient effect). *Angew. Chem.* **2013,** *125*, 10174-10179.

(905) Lahikainen, M.; Zeng, H.; Priimagi, A. Reconfigurable photoactuator through synergistic use of photochemical and photothermal effects. *Nat. Commun.* **2018,** *9*, 4148.

(906) Wei, W.; Zhang, Z.; Wei, J.; Li, X.; Guo, J. Phototriggered Selective Actuation and Self‐

Oscillating in Dual‐Phase Liquid Crystal Photonic Actuators. *Adv. Opt. Mater.* **2018,** *6*, 1800131.

(907) Hong, G.; Diao, S.; Antaris, A. L.; Dai, H. Carbon nanomaterials for biological imaging and nanomedicinal therapy. *Chem. Rev.* **2015,** *115*, 10816-10906.

(908) Dai, L.; Chang, D. W.; Baek, J. B.; Lu, W. Carbon nanomaterials for advanced energy conversion and storage. *small* **2012,** *8*, 1130-1166.

(909) Jariwala, D.; Sangwan, V. K.; Lauhon, L. J.; Marks, T. J.; Hersam, M. C. Carbon nanomaterials for electronics, optoelectronics, photovoltaics, and sensing. *Chem. Soc. Rev.* **2013,** *42*, 2824-2860.

(910) Yu, X.; Cheng, H.; Zhang, M.; Zhao, Y.; Qu, L.; Shi, G. Graphene-based smart materials. *Nat. Rev. Mater.* **2017,** *2*, 1-13.

(911) Ji, J.; Sui, G.; Yu, Y.; Liu, Y.; Lin, Y.; Du, Z.; Ryu, S.; Yang, X. Significant improvement of mechanical properties observed in highly aligned carbon-nanotube-reinforced nanofibers. *J. Phys. Chem. C* **2009,** *113*, 4779-4785.

(912) Deng, J.; Li, J.; Chen, P.; Fang, X.; Sun, X.; Jiang, Y.; Weng, W.; Wang, B.; Peng, H. Tunable photothermal actuators based on a pre-programmed aligned nanostructure. *J. Am. Chem. Soc.* **2016,** *138*, 225-230.

(913) Peng, H.; Sun, X.; Cai, F.; Chen, X.; Zhu, Y.; Liao, G.; Chen, D.; Li, Q.; Lu, Y.; Zhu, Y. Electrochromatic carbon nanotube/polydiacetylene nanocomposite fibres. *Nat. Nanotechnol.* **2009,** *4*, 738-741.

(914) Aliev, A. E.; Guthy, C.; Zhang, M.; Fang, S.; Zakhidov, A. A.; Fischer, J. E.; Baughman, R. H. Thermal transport in MWCNT sheets and yarns. *Carbon* **2007,** *45*, 2880-2888.

(915) Chen, L.; Weng, M.; Zhou, P.; Zhang, L.; Huang, Z.; Zhang, W. Multi-responsive actuators based on a graphene oxide composite: intelligent robot and bioinspired applications. *Nanoscale* **2017,** *9*, 9825-9833.

(916) Gao, D.; Lin, M.-F.; Xiong, J.; Li, S.; Lou, S. N.; Liu, Y.; Ciou, J.-H.; Zhou, X.; Lee, P. S. Photothermal actuated origamis based on graphene oxide–cellulose programmable bilayers. *Nanoscale Horiz.* **2020,** *5*, 730-738.

(917) Gao, Y.-Y.; Zhang, Y.-L.; Han, B.; Zhu, L.; Dong, B.; Sun, H.-B. Gradient Assembly of Polymer Nanospheres and Graphene Oxide Sheets for Dual-Responsive Soft Actuators. *ACS Appl. Mater. Interfaces* **2019,** *11*, 37130-37138.

(918) Link, S.; El-Sayed, M. A. Spectral properties and relaxation dynamics of surface plasmon electronic oscillations in gold and silver nanodots and nanorods. *J. Phys. Chem. B* **1999,** *103*, 8410-8426.

(919) Meder, F.; Naselli, G. A.; Sadeghi, A.; Mazzolai, B. Remotely Light‐Powered Soft Fluidic Actuators Based on Plasmonic‐Driven Phase Transitions in Elastic Constraint. *Adv. Mater.* **2019,** *31*, 1905671.

(920) Chen, J.; Feng, J.; Yang, F.; Aleisa, R.; Zhang, Q.; Yin, Y. Space‐Confined Seeded Growth of Cu Nanorods with Strong Surface Plasmon Resonance for Photothermal Actuation. *Angew. Chem.* **2019,** *131*, 9376-9382.

(921) Kim, H.; Kang, J. H.; Zhou, Y.; Kuenstler, A. S.; Kim, Y.; Chen, C.; Emrick, T.; Hayward, R. C. Light‐Driven Shape Morphing, Assembly, and Motion of Nanocomposite Gel Surfers. *Adv. Mater.* **2019,** *31*, 1900932.

(922) Nishiyama, H.; Odashima, S.; Asoh, S. Femtosecond laser writing of plasmonic nanoparticles inside PNIPAM microgels for light-driven 3D soft actuators. *Opt. Express* **2020,** *28*, 26470-26480.

(923) Sun, Z.; Yamauchi, Y.; Araoka, F.; Kim, Y. S.; Bergueiro, J.; Ishida, Y.; Ebina, Y.; Sasaki, T.; Hikima, T.; Aida, T. An Anisotropic Hydrogel Actuator Enabling Earthworm‐Like Directed Peristaltic Crawling. *Angew. Chem. Int. Ed.* **2018,** *57*, 15772-15776.

(924) Füllbrandt, M.; Ermilova, E.; Asadujjaman, A.; Hölzel, R.; Bier, F. F.; von Klitzing, R.; Schönhals, A. Dynamics of linear poly (N-isopropylacrylamide) in water around the phase transition investigated by dielectric relaxation spectroscopy. *J. Phys. Chem. B* **2014,** *118*, 3750-3759.

(925) Kim, Y. S.; Liu, M.; Ishida, Y.; Ebina, Y.; Osada, M.; Sasaki, T.; Hikima, T.; Takata, M.; Aida, T. Thermoresponsive actuation enabled by permittivity switching in an electrostatically anisotropic hydrogel. *Nat. Mater.* **2015,** *14*, 1002-1007.

(926) Jiang, S.; Liu, F.; Lerch, A.; Ionov, L.; Agarwal, S. Unusual and superfast temperature‐triggered actuators. *Adv. Mater.* **2015,** *27*, 4865-4870.

(927) Behl, M.; Kratz, K.; Noechel, U.; Sauter, T.; Lendlein, A. Temperature-memory polymer actuators. *Proc. Natl. Acad. Sci. U.S.A.* **2013,** *110*, 12555-12559.

(928) Yang, Y.; Tian, F.; Wang, X.; Xu, P.; An, W.; Hu, Y.; Xu, S. Biomimetic color-changing hierarchical and gradient hydrogel actuators based on salt-induced microphase separation. *ACS Appl. Mater. Interfaces* **2019,** *11*, 48428-48436.

(929) Agarwal, S.; Jiang, S.; Chen, Y. Progress in the field of water‐and/or temperature‐triggered polymer actuators. *Macromol. Mater. Eng.* **2019,** *304*, 1800548.

(930) Du, X.; Cui, H.; Xu, T.; Huang, C.; Wang, Y.; Zhao, Q.; Xu, Y.; Wu, X. Reconfiguration, Camouflage, and Color‐Shifting for Bioinspired Adaptive Hydrogel‐Based Millirobots. *Adv. Funct. Mater.* **2020,** *30*, 1909202.

(931) Li, Z.; Liu, Y.; Marin, M.; Yin, Y. Thickness-dependent wrinkling of PDMS films for programmable mechanochromic responses. *Nano Res.* **2020,** *13*, 3.

(932) Srinivasan, V.; Pamula, V. K.; Fair, R. B. An integrated digital microfluidic lab-on-a-chip for clinical diagnostics on human physiological fluids. *Lab Chip* **2004,** *4*, 310-315.

(933) Rogers, J. A.; Someya, T.; Huang, Y. Materials and mechanics for stretchable electronics. *Science* **2010,** *327*, 1603-1607.

(934) Kaasik, F.; Must, I.; Baranova, I.; Poldsalu, I.; Lust, E.; Johanson, U.; Punning, A.; Aabloo, A. Scalable fabrication of ionic and capacitive laminate actuators for soft robotics. *Sens. Actuators B Chem.* **2017,** *246*, 154-163.

(935) Hassani, F. A.; Shi, Q.; Wen, F.; He, T.; Haroun, A.; Yang, Y.; Feng, Y.; Lee, C. Smart materials for smart healthcare–moving from sensors and actuators to self-sustained nanoenergy nanosystems. *Smart Mater. Med.* **2020,** *1*, 92-124.

(936) Chen, S.; Pang, Y.; Yuan, H.; Tan, X.; Cao, C. Smart Soft Actuators and Grippers Enabled by Self‐Powered Tribo‐Skins. *Adv. Mater. Technol.* **2020,** *5*, 1901075.

(937) Kim, S. J.; Kim, O.; Park, M. J. True low‐power self‐locking soft actuators. *Adv. Mater.* **2018,** *30*, 1706547.

(938) Li, W.; Li, F.; Li, H.; Su, M.; Gao, M.; Li, Y.; Su, D.; Zhang, X.; Song, Y. Flexible circuits and soft actuators by printing assembly of graphene. *ACS Appl. Mater. Interfaces* **2016,** *8*, 12369-12376.

(939) Chen, L.; Weng, M.; Zhang, W.; Zhou, Z.; Zhou, Y.; Xia, D.; Li, J.; Huang, Z.; Liu, C.; Fan, S. Transparent actuators and robots based on single-layer superaligned carbon nanotube sheet and polymer composites. *Nanoscale* **2016,** *8*, 6877-6883.

(940) Taccola, S.; Greco, F.; Sinibaldi, E.; Mondini, A.; Mazzolai, B.; Mattoli, V. Toward a new generation of electrically controllable hygromorphic soft actuators. *Adv. Mater.* **2015,** *27*, 1668-1675.

(941) Yao, S.; Cui, J.; Cui, Z.; Zhu, Y. Soft electrothermal actuators using silver nanowire heaters. *Nanoscale* **2017,** *9*, 3797-3805.

(942) Rothemund, P.; Kirkman, S.; Keplinger, C. Dynamics of electrohydraulic soft actuators. *Proc. Natl. Acad. Sci. U.S.A.* **2020,** *117*, 16207-16213.

(943) Yan, Y.; Santaniello, T.; Bettini, L. G.; Minnai, C.; Bellacicca, A.; Porotti, R.; Denti, I.; Faraone, G.; Merlini, M.; Lenardi, C. Electroactive ionic soft actuators with monolithically integrated gold nanocomposite electrodes. *Adv. Mater.* **2017,** *29*, 1606109.

(944) Li, K.; Shao, Y.; Yan, H.; Lu, Z.; Griffith, K. J.; Yan, J.; Wang, G.; Fan, H.; Lu, J.; Huang, W. Lattice-contraction triggered synchronous electrochromic actuator. *Nat. Commun.* **2018,** *9*, 4798.

(945) Zhao, Q.; Dunlop, J. W.; Qiu, X.; Huang, F.; Zhang, Z.; Heyda, J.; Dzubiella, J.; Antonietti, M.; Yuan, J. An instant multi-responsive porous polymer actuator driven by solvent molecule sorption. *Nat. Commun.* **2014,** *5*, 4293.

(946) Dawson, C.; Vincent, J. F.; Rocca, A.-M. How pine cones open. *Nature* **1997,** *390*, 668-668.

(947) Reyssat, E.; Mahadevan, L. Hygromorphs: from pine cones to biomimetic bilayers. *J. R. Soc. Interface.* **2009,** *6*, 951-957.

(948) Elbaum, R.; Zaltzman, L.; Burgert, I.; Fratzl, P. The role of wheat awns in the seed dispersal unit. *Science* **2007,** *316*, 884-886.

(949) Teyssier, J.; Saenko, S. V.; Van Der Marel, D.; Milinkovitch, M. C. Photonic crystals cause active colour change in chameleons. *Nat. Commun.* **2015,** *6*, 6368.

(950) Erb, R. M.; Sander, J. S.; Grisch, R.; Studart, A. R. Self-shaping composites with programmable bioinspired microstructures. *Nat. Commun.* **2013,** *4*, 1712.

(951) Armon, S.; Efrati, E.; Kupferman, R.; Sharon, E. Geometry and mechanics in the opening of chiral seed pods. *Science* **2011,** *333*, 1726-1730.

(952) Gladman, A. S.; Matsumoto, E. A.; Nuzzo, R. G.; Mahadevan, L.; Lewis, J. A. Biomimetic 4D printing. *Nat. Mater.* **2016,** *15*, 413-418.

(953) Aharoni, H.; Sharon, E.; Kupferman, R. Geometry of thin nematic elastomer sheets. *Phys. Rev. Lett.* **2014,** *113*, 257801.

(954) van Doorn, W. G.; Van Meeteren, U. Flower opening and closure: a review. *J. Exp. Bot.* **2003,** *54*, 1801-1812.

(955) Wegst, U. G.; Bai, H.; Saiz, E.; Tomsia, A. P.; Ritchie, R. O. Bioinspired structural materials. *Nat. Mater.* **2015,** *14*, 23-36.

(956) Cao, J.; Zhou, Z.; Song, Q.; Chen, K.; Su, G.; Zhou, T.; Zheng, Z.; Lu, C.; Zhang, X. Ultrarobust Ti3C2T x MXene-Based Soft Actuators via Bamboo-Inspired Mesoscale Assembly of Hybrid Nanostructures. *ACS nano* **2020,** *14*, 7055-7065.

(957) Jeong, K.-U.; Jang, J.-H.; Koh, C. Y.; Graham, M. J.; Jin, K.-Y.; Park, S.-J.; Nah, C.; Lee, M.-H.; Cheng, S. Z.; Thomas, E. L. Colour-tunable spiral photonic actuators. *J. Mater. Chem.* **2009,** *19*, 1956-1959.

(958) Zhang, Z.; Qi, Y.; Ma, W.; Zhang, S. Wettability-Controlled Directional Actuating Strategy Based on Bilayer Photonic Crystals. *ACS Appl. Mater. Interfaces* **2020,** *13*, 2007-2017.

(959) Yue, Y.; Kurokawa, T. Designing responsive photonic crystal patterns by using laser engraving. *ACS Appl. Mater. Interfaces* **2019,** *11*, 10841-10847.

(960) Yang, N.; Ji, X.; Sun, J.; Zhang, Y.; Xu, Q.; Fu, Y.; Li, H.; Qin, M.; Yuan, Z. Photonic actuators with predefined shapes. *Nanoscale* **2019,** *11*, 10088-10096.

(961) Fang, Y.; Ni, Y.; Choi, B.; Leo, S. Y.; Gao, J.; Ge, B.; Taylor, C.; Basile, V.; Jiang, P. Chromogenic photonic crystals enabled by novel vapor‐responsive shape‐memory polymers. *Adv. Mater.* **2015,** *27*, 3696-3704.

(962) Shin, S. R.; Shin, C.; Memic, A.; Shadmehr, S.; Miscuglio, M.; Jung, H. Y.; Jung, S. M.; Bae, H.; Khademhosseini, A.; Tang, X. Aligned carbon nanotube–based flexible gel substrates for engineering biohybrid tissue actuators. *Adv. Funct. Mater.* **2015,** *25*, 4486-4495.

(963) Shin, S. R.; Jung, S. M.; Zalabany, M.; Kim, K.; Zorlutuna, P.; Kim, S. B.; Nikkhah, M.; Khabiry, M.; Azize, M.; Kong, J. Carbon-nanotube-embedded hydrogel sheets for engineering cardiac constructs and bioactuators. *ACS nano* **2013,** *7*, 2369-2380.

(964) Cheng, L.; Wang, C.; Feng, L.; Yang, K.; Liu, Z. Functional nanomaterials for phototherapies of cancer. *Chem. Rev.* **2014,** *114*, 10869-10939.

(965) Zeng, J.; Gong, M.; Wang, D.; Li, M.; Xu, W.; Li, Z.; Li, S.; Zhang, D.; Yan, Z.; Yin, Y. Direct Synthesis of Water-Dispersible Magnetic/Plasmonic Heteronanostructures for Multimodality Biomedical Imaging. *Nano Lett.* **2019,** *19*, 3011-3018.

(966) Shi, Y.; Van der Meel, R.; Chen, X.; Lammers, T. The EPR effect and beyond: Strategies to improve tumor targeting and cancer nanomedicine treatment efficacy. *Theranostics* **2020,** *10*, 7921.

(967) Yang, G.; Gong, H.; Qian, X.; Tan, P.; Li, Z.; Liu, T.; Liu, J.; Li, Y.; Liu, Z. Mesoporous silica nanorods intrinsically doped with photosensitizers as a multifunctional drug carrier for combination therapy of cancer. *Nano Res.* **2015,** *8*, 751-764.

(968) Song, X.; Gong, H.; Yin, S.; Cheng, L.; Wang, C.; Li, Z.; Li, Y.; Wang, X.; Liu, G.; Liu, Z. Ultra‐small iron oxide doped polypyrrole nanoparticles for in vivo multimodal imaging guided photothermal therapy. *Adv. Funct. Mater.* **2014,** *24*, 1194-1201.

(969) Yin, S.; Li, Z.; Cheng, L.; Wang, C.; Liu, Y.; Chen, Q.; Gong, H.; Guo, L.; Li, Y.; Liu, Z. Magnetic PEGylated Pt 3 Co nanoparticles as a novel MR contrast agent: in vivo MR imaging and long-term toxicity study. *Nanoscale* **2013,** *5*, 12464-12473.

(970) Kim, M.; Lee, J. H.; Nam, J. M. Plasmonic photothermal nanoparticles for biomedical applications. *Adv. Sci.* **2019,** *6*, 1900471.

(971) Liu, T.; Wang, C.; Cui, W.; Gong, H.; Liang, C.; Shi, X.; Li, Z.; Sun, B.; Liu, Z. Combined photothermal and photodynamic therapy delivered by PEGylated MoS2 nanosheets. *Nanoscale* **2014,** *6*, 11219-11225.

(972) Ge, X.; Fu, Q.; Su, L.; Li, Z.; Zhang, W.; Chen, T.; Yang, H.; Song, J. Light-activated gold nanorod vesicles with NIR-II fluorescence and photoacoustic imaging performances for cancer theranostics. *Theranostics* **2020,** *10*, 4809.

(973) Chen, Y.-S.; Yoon, S. J.; Frey, W.; Dockery, M.; Emelianov, S. Dynamic contrast-enhanced photoacoustic imaging using photothermal stimuli-responsive composite nanomodulators. *Nat. Commun.* **2017,** *8*, 15782.

(974) Zhou, C.; Zhang, L.; Sun, T.; Zhang, Y.; Liu, Y.; Gong, M.; Xu, Z.; Du, M.; Liu, Y.; Liu, G. Activatable NIR‐II Plasmonic Nanotheranostics for Efficient Photoacoustic Imaging and Photothermal Cancer Therapy. *Adv. Mater.* **2021,** *33*, 2006532.

(975) Karg, M.; König, T. A.; Retsch, M.; Stelling, C.; Reichstein, P. M.; Honold, T.; Thelakkat, M.; Fery, A. Colloidal self-assembly concepts for light management in photovoltaics. *Mater. Today* **2015,** *18*, 185-205.

(976) Gong, C.; Sun, S.; Zhang, Y.; Sun, L.; Su, Z.; Wu, A.; Wei, G. Hierarchical nanomaterials via biomolecular self-assembly and bioinspiration for energy and environmental applications. *Nanoscale* **2019,** *11*, 4147-4182.

(977) Wang, D.; Kou, R.; Choi, D.; Yang, Z.; Nie, Z.; Li, J.; Saraf, L. V.; Hu, D.; Zhang, J.; Graff, G. L. Ternary self-assembly of ordered metal oxide− graphene nanocomposites for electrochemical energy storage. *ACS nano* **2010,** *4*, 1587-1595.

(978) Qiu, P.; Zhao, T.; Fang, Y.; Zhu, G.; Zhu, X.; Yang, J.; Li, X.; Jiang, W.; Wang, L.; Luo, W. Pushing the Limit of Ordered Mesoporous Materials via 2D Self‐Assembly for Energy Conversion and Storage. *Adv. Funct. Mater.* **2021,** *31*, 2007496.

(979) Song, S.; Xue, Y.; Feng, L.; Elbatal, H.; Wang, P.; Moorefield, C. N.; Newkome, G. R.; Dai, L. Reversible self‐assembly of terpyridine‐functionalized graphene oxide for energy conversion. *Angew. Chem.* **2014,** *126*, 1439-1443.

(980) Zeng, X.; Song, H.; Shen, Z.-Y.; Moskovits, M. Progress and challenges of ceramics for supercapacitors. *J. Materiomics* **2021**, doi.org/10.1016/j.jmat.2021.1003.1001.

(981) Armstrong, E.; O'Dwyer, C. Artificial opal photonic crystals and inverse opal structures–fundamentals and applications from optics to energy storage. *J. Mater. Chem. C* **2015,** *3*, 6109-6143.

(982) Liu, N.; Lu, Z.; Zhao, J.; McDowell, M. T.; Lee, H.-W.; Zhao, W.; Cui, Y. A pomegranate-inspired nanoscale design for large-volume-change lithium battery anodes. *Nat. Nanotechnol.* **2014,** *9*, 187-192.

(983) Lu, D.; Li, J.; Lin, C.; Liao, J.; Feng, Y.; Ding, Z.; Li, Z.; Liu, Q.; Li, H. A Simple and Scalable Route to Synthesize CoxCu1− xCo2O4@ CoyCu1− yCo2O4 Yolk–Shell Microspheres, A High‐Performance Catalyst to Hydrolyze Ammonia Borane for Hydrogen Production. *Small* **2019,** *15*, 1805460.

(984) Ergang, N. S.; Lytle, J. C.; Yan, H.; Stein, A. Effect of a macropore structure on cycling rates of LiCoO2. *J. Electrochem. Soc.* **2005,** *152*, A1989.

(985) Lu, J.; Tang, Z.; Zhang, Z.; Shen, W. Preparation of LiFePO4 with inverse opal structure and its satisfactory electrochemical properties. *Mater. Res. Bull.* **2005,** *40*, 2039-2046.

(986) Lu, J.; Tang, Z.; Zhang, Z.; Shen, W. Structural and electrochemical properties of multihollow LiFePO4 for lithium battery cathodes. *J. Electrochem. Soc.* **2005,** *152*, A1441.

(987) Lee, K. T.; Lytle, J. C.; Ergang, N. S.; Oh, S. M.; Stein, A. Synthesis and rate performance of monolithic macroporous carbon electrodes for lithium‐ion secondary batteries. *Adv. Funct. Mater.* **2005,** *15*, 547-556.

(988) Kang, D.-Y.; Kim, S.-O.; Chae, Y. J.; Lee, J. K.; Moon, J. H. Particulate inverse opal carbon electrodes for lithium-ion batteries. *Langmuir* **2013,** *29*, 1192-1198.

(989) Kavan, L.; Zukalová, M.; Kalbáč, M.; Graetzel, M. Lithium insertion into anatase inverse opal. *J. Electrochem. Soc.* **2004,** *151*, A1301.

(990) Wu, M.-S.; Lin, Y.-P. Monodispersed macroporous architecture of nickel-oxide film as an anode material for thin-film lithium-ion batteries. *Electrochim. Acta* **2011,** *56*, 2068-2073.

(991) Xu, W.; Lu, Z.; Sun, X.; Jiang, L.; Duan, X. Superwetting electrodes for gas-involving electrocatalysis. *Acc. Chem. Res.* **2018,** *51*, 1590-1598.

(992) Lu, Z.; Zhu, W.; Yu, X.; Zhang, H.; Li, Y.; Sun, X.; Wang, X.; Wang, H.; Wang, J.; Luo, J. Ultrahigh hydrogen evolution performance of under‐water "superaerophobic" MoS2 nanostructured electrodes. *Adv. Mater.* **2014,** *26*, 2683-2687.

(993) Song, Q.; Xue, Z.; Liu, C.; Qiao, X.; Liu, L.; Huang, C.; Liu, K.; Li, X.; Lu, Z.; Wang, T. General strategy to optimize gas evolution reaction via assembled striped-pattern superlattices. *J. Am. Chem. Soc.* **2019,** *142*, 1857-1863.

(994) Brongersma, M. L.; Cui, Y.; Fan, S. Light management for photovoltaics using high-index nanostructures. *Nat. Mater.* **2014,** *13*, 451-460.

(995) Stratakis, E.; Kymakis, E. Nanoparticle-based plasmonic organic photovoltaic devices. *Mater. Today* **2013,** *16*, 133-146.

(996) Atwater, H.; Polman, A. Plasmonics for improved photovoltaic devices. *Nat. Mater.* **2010,** *9*, 205-213.

(997) Kiriarachchi, H. D.; Awad, F. S.; Hassan, A. A.; Bobb, J. A.; Lin, A.; El-Shall, M. S. Plasmonic chemically modified cotton nanocomposite fibers for efficient solar water desalination and wastewater treatment. *Nanoscale* **2018,** *10*, 18531-18539.

(998) Awad, F. S.; Kiriarachchi, H. D.; AbouZeid, K. M.; Özgür, U. m.; El-Shall, M. S. Plasmonic graphene polyurethane nanocomposites for efficient solar water desalination. *ACS Appl. Energy Mater.* **2018,** *1*, 976-985.

(999) Gao, C.; Hu, Y.; Wang, M.; Chi, M.; Yin, Y. Fully alloyed Ag/Au nanospheres: combining the plasmonic property of Ag with the stability of Au. *J. Am. Chem. Soc.* **2014,** *136*, 7474-7479.

(1000) Qin, H. L.; Wang, D.; Huang, Z. L.; Wu, D. M.; Zeng, Z. C.; Ren, B.; Xu, K.; Jin, J. Thickness-controlled synthesis of ultrathin Au sheets and surface plasmonic property. *J. Am. Chem. Soc.* **2013,** *135*, 12544-12547.

(1001) Zhou, L.; Tan, Y.; Ji, D.; Zhu, B.; Zhang, P.; Xu, J.; Gan, Q.; Yu, Z.; Zhu, J. Self-assembly of highly efficient, broadband plasmonic absorbers for solar steam generation. *Sci. Adv.* **2016,** *2*, e1501227.

(1002) Chen, C.; Zhou, L.; Yu, J.; Wang, Y.; Nie, S.; Zhu, S.; Zhu, J. Dual functional asymmetric plasmonic structures for solar water purification and pollution detection. *Nano Energy* **2018,** *51*, 451-456.

(1003) Chen, J.; Feng, J.; Li, Z.; Xu, P.; Wang, X.; Yin, W.; Wang, M.; Ge, X.; Yin, Y. Space-confined seeded growth of black silver nanostructures for solar steam generation. *Nano Lett.* **2018,** *19*, 400-407.

(1004) Ghasemi, H.; Ni, G.; Marconnet, A. M.; Loomis, J.; Yerci, S.; Miljkovic, N.; Chen, G. Solar steam generation by heat localization. *Nat. Commun.* **2014,** *5*, 4449.

(1005) Xu, N.; Hu, X.; Xu, W.; Li, X.; Zhou, L.; Zhu, S.; Zhu, J. Mushrooms as efficient solar steam‐generation devices. *Adv. Mater.* **2017,** *29*, 1606762.

(1006) Shang, W.; Deng, T. Solar steam generation: steam by thermal concentration. *Nat. Energy* **2016,** *1*, 1-2.

(1007) Lu, D.; Zhou, J.; Hou, S.; Xiong, Q.; Chen, Y.; Pu, K.; Ren, J.; Duan, H. Functional Macromolecule‐Enabled Colloidal Synthesis: From Nanoparticle Engineering to Multifunctionality. *Adv. Mater.* **2019,** *31*, 1902733.

(1008) Deng, R.; Xu, J.; Yi, G. R.; Kim, J. W.; Zhu, J. Responsive colloidal polymer particles with ordered mesostructures. *Adv. Funct. Mater.* **2021,** *31*, 2008169.

(1009) Jones, M. R.; Macfarlane, R. J.; Lee, B.; Zhang, J.; Young, K. L.; Senesi, A. J.; Mirkin, C. A. DNA-nanoparticle superlattices formed from anisotropic building blocks. *Nat. Mater.* **2010,** *9*, 913-917.

(1010) Samanta, D.; Iscen, A.; Laramy, C. R.; Ebrahimi, S. B.; Bujold, K. E.; Schatz, G. C.; Mirkin, C. A. Multivalent Cation-Induced Actuation of DNA-Mediated Colloidal Superlattices. *J. Am. Chem. Soc.* **2019,** *141*, 19973-19977.

(1011) Wang, S.; Park, S. S.; Buru, C. T.; Lin, H.; Chen, P.-C.; Roth, E. W.; Farha, O. K.; Mirkin, C. A.

Colloidal crystal engineering with metal–organic framework nanoparticles and DNA. *Nat. Commun.* **2020,** *11*, 2495.

(1012) Xu, H.; Wu, P.; Zhu, C.; Elbaz, A.; Gu, Z. Z. Photonic crystal for gas sensing. *J. Mater. Chem. C* **2013,** *1*, 6087-6098.

(1013) Parreira, R.; Özelçi, E.; Sakar, M. S. Remotely Controlled Colloidal Assembly of Soft Microrobotic Artificial Muscle. *Adv. Intell. Syst.* **2020,** *2*, 2000062.

TOC

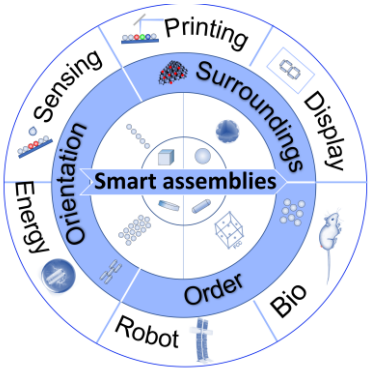
Printing
Surroundings
Display
Sensing
Orientation
Smart assemblies
Energy
Order
Bio
Robot